DISS. ETH NO. 19342

Tectono-metamorphic evolution of the Gruf Complex
(Swiss and Italian Central Alps)

A dissertation submitted to

ETH ZURICH

for the degree of

DOCTOR OF SCIENCES

presented by

Andrea Galli

Dipl. Natw. ETH

born on March 26th, 1980

citizen of Bioggio (TI)

Accepted on the recommendation of:

Examiner: Prof. Dr. M.W. Schmidt   ETH Zurich
Co-examiner: Prof. Dr. J.-P. Burg   ETH Zurich
Co-examiner: Dr. E.C. Reusser   ETH Zurich
Co-examiner: Dr. A. Möller   University of Kansas

2010

Acknowledgements

First I would like to thank Prof. Dr. Max W. Schmidt for bringing me the opportunity to do a PhD thesis at the Institute of Mineralogy and Petrology at the ETH and for the freedom he gave me as a Doktorvater. Thanks to Prof. Dr. J.-P. Burg for the always stimulating and helpfull discussions about the Gruf. Thanks to Dr. E. Reusser for the years spent together at the ETH. You have been much more than a supervisor for me...a right "Nji". Also thanks to Prof. Dr. A. Möller for being co-supervisor of my thesis.

A special thank goes to all the people who helped me during these years: L. Zhender, M. Caddick, J. Connoly, Pulmi, Peter Brack (unserer Konservator), N. Mancktelow and, in particular, P. Nievergelt. Thank you Nievi!!! Thanks to F. Pirovino for the huge amount of first class quality thin sections. Thank you very much also to the "SHRIMP team" in Saint-Petersbourg for introducing me to the amazing micro-world of the zircons.

My best thanks go to the family Biavaschi, Mr. Cotola, Mr. Rochin and Mr. Ranzeta for the fundamental and spontaneous help they gave me during the hart field seasons. Grazie di cuore! A special thank go to S. Ghizzoni for motivating me to climb every day the steep flanks of Val Codera.

Thanks a lot to all the PhD students and office mates: Angelika, Bona, Daniele, Dave, Davide, Esther, Ettore, Giulio, Luca, Marteen, Paola, Pippo and Claudio, Rohit, Tobias, Tamara, Ute and Wuong. In particular, I would like to thank "gli artisti" Ettore and Nene for sharing four wonderfull years in Zurich. Thank you also to Santiago for the pleasant and long chats through the corridors.

A special thank goes to all the friends of the Gruf: Monika, Nene (again), Omar, Stefy, Giuliano and Pierre. I apologyse for the tough days you spent in the Gruf helping me...

My heartfelt thanks go to family Negrini. Grazie Siff; grazie Menga; grazie Marianne. Siete riusciti a darmi quello che la vita mi aveva tolto.

My best thanks go to Ben Le Bayon for the time spent together walking up and down through our Gruf, climbing and climbing, discussing and discussing, or just dreaming a grotto. Thank you Grufiste!!!

Finally, I would like to thank my fantastic wife Mariana for the patience and the constant support she gave me during the thesis.

Abstract

Aim of this study is to map the Gruf Complex (eastern Central Alps) and to constrain its tectono-metamorphic evolution. The Gruf Complex, exposed between the Tertiary calc-alkaline Bergell Intrusion and the ophiolitic rocks of the Chiavenna Unit and the Adula Nappe, is prevalently constituted of migmatitic metagranitoids and partly migmatitic pelitic to psammitic metasediments associated with leucosomes and leucogranites. Lenses of charnockites, granulites, meta-ultramafic, -basic and -calcareous rocks occur within these two major groups.

Metagranitoids consist of coarse-grained, massive to slightly foliated, metaluminous to slightly peraluminous migmatitic biotite-orthogneisses, characterised by a disorganised and fluidal texture. In the northernmost part of the Gruf Complex, the migmatitic biotite-orthogneiss contains numerous, decimetric to metric enclaves of mostly mafic composition which are geochemically similar to the Chiavenna amphibolites. Internally boudinaged, 8 km long and 0.5 km thick, sheet-like bodies of opx-bearing charnockite associated to up to 50 m large lenses of websterite to gabbronorite occur within migmatitic metagranitoids. Charnockites are leucocratic, medium- to coarse-grained and metaluminous to peraluminous. Charnockites are separated from the host orthogneisses by thin mylonites. Their internal structure is marked by irregular flow structures and the occurrence of metric granulite schlieren and enclaves. Granulites occur as garnet-orthopyroxene-biotite-alkalifeldspar-bearing schlieren ($\pm$ sapphirine, sillimanite, cordierite, corundum, spinel, plagioclase, quartz) within charnockites and as residual enclaves both in the charnockites and the migmatitic orthogneisses. Webstrerites to gabbronorites are greenish-brownish, middle- to coarse-grained, massive and mainly composed of clinopyroxene, orthopyroxene and interstitial biotite and plagioclase. The contacts to the enclosing orthogneisses are intrusive.

Metasediments are composed of alternating garnet-bearing paragneisses and garnet-cordierite-bearing sillimanite-biotite-schists. Both rock types display a migmatitic banding of quartzo-feldspatic leucosomes and biotite-garnet-($\pm$ sillimanite)-rich melanosomes to mesosomes. This banding is prevalently parallel to the main foliation. However, where the degree of anatexis is stronger, leucosomes migrate discordantly to the main fabric and collect in dykes and pockets. Massive, fine- to coarse-grained, peraluminous garnet-sillimanite two-mica leucogranites occur spatially associated to migmatitic metasediments. Leucogranites display sharp and irregular intrusive contacts to the metasediments and more diffuse contacts to the migmatitic metagranitoids.

Lenses of metaperidotite associated to amphibolites and calcsilicates are contained both in the metagranitoids and metasediments. Metaperidotites exhibit alternating lherzolite, dunite, pyroxenite and chromite layers crosscutted by several metarodingite and ferro-gabbro dykes. Compositional banding and dykes are overgrown by a penetrative foliation mainly defined by oriented orthopyroxene. Talc-chlorite-bearing veins cut across this main foliation. Metaperidotites display mylonitic contacts to the metasediments. In contrast, leucosomes from the biotite-orthogneisses are intrusive, with decimetric leucocratic veins intruding fractures at the rim of ultramafic lenses and related amphibolites.

The regional structure of the Gruf Complex is dominated by an ENE-WSW trending, steeply

dipping attitude underlined by bulk orientation of lithological contacts and the parallel main foliation. The regional fabric dips to the NNW in the northern and central Gruf and prevalently to the SSE in the southern part, suggesting a dome-like architecture for the Gruf Complex. The regional mineral elongation plunges 30-40° between E and NE. In contrast, charnockites and meta-peridotites display a separate internal foliation and lineation with no clear regional trend. Intensity and style of deformation strongly depend on the rock type and degree of anatexis. In the metagranitoids the deformation generally concentrate in ductile shear zones. Three main sets of conjugated shear zones have been recognised which describe a syn- to late migmatitic or magmatic vertical flattening and a marked top-to-the NE dextral-normal movement documenting the upward movement of the Gruf Complex with respect to the surrounding units. Metasediments are characterised by a more regular and penetrative foliation. However, these rocks often display a more complex deformation pattern marked by the contorted refolding of the main foliation.

Stromatic structures, melt-filled shear zones, veinlets, patches, pockets and dykes of leucosomes crosscutting the main foliation, magmatic breccias and back veining of Gruf leucosomes into the base of the Bergell Intrusion indicate that migmatization was coeval with the main Alpine deformation and with the emplacement of the Bergell Pluton. The occurrence of sillimanite + alkali feldspar and the scarcity or lack of syn-kinematic muscovite observed in most of the regionally-dominant migmatitic micaschists of the Gruf Complex suggest that partial melting was mostly induced by the breakdown of muscovite at about 700-750 °C and 6-7 kbar.

Charnockites and granulites show a more complex metamorphic evolution. Thermobarometric calculations, P–T pseudosections and orthopyroxene Al content, indicate that both charnockites and granulites equilibrated at ultrahigh-temperature (UHT) metamorphic peak conditions of T = 920–940 °C and P = 8.5–9.5 kbar. Peak assemblages were subsequently overprinted by intergrowth, symplectite and corona textures involving orthopyroxene, sapphirine, cordierite and spinel at T = 720–740 °C and P = 7–7.5 kbar. Garnet diffusion modelling suggests that metamorphic peak assemblages and post-peak reaction textures always involving cordierite developed during two separate metamorphic cycles. Fluid-absent partial melting of pelitic and psammitic sediments during the UHT event lead to the formation of charnockitic magmas and granulitic residuals. Intense melt loss and thorough dehydration of the granulites (although retaining biotite) favoured the partial preservation of peak mineral assemblages during Alpine regional metamorphism.

To understand the geotectonic significance of charnockites and granulites, in particular in the context of the Alpine migmatisation, zircons from 15 high grade samples have been U-Pd dated by SHRIMP II analysis. The age of the granulite metamorphism results to 282-261 Ma and is obtained from oscillatory zoned zircons from charnokite sheets. Furthermore, some of these zircons contain inclusions of the complete suite of granulite facies minerals, rendering a Permian age of the granulites unequivocal. Two samples from an enclave-rich biotite-orthogneiss sheet yield Cambrian and Ordovician zircon cores, while two deformed leucogranites and six ortho- and augengneisses, which compose two thirds of the Gruf complex, give zircon ages of 290-260 Ma. Most zircons have milky rims with ages ranging from 34-30 Ma. These rims date the Alpine amphibolite facies migmatisation, an interpretation confirmed by directly dating a leucosome pocket

from the upper amphibolite facies migmatitic metapelites also common in the Gruf.

The Gruf charnokites associated with boudins of granulites and websterites to gabbronorites are identified as part of the post-Variscan European lower crust. A geotectonic reconstruction reveals that this piece of lower crust must have been stranded in the (European) North upon rifting of the Neothetis and that exhumation of this lower crust occurred during migmatisation and formation of the Bergell Pluton in the aftermath of the breakoff of the European slab. During its ascent, the dynamics of the uprising Bergell Pluton helped the exhumation of the Gruf Complex as a pluton-related migmatitic dome. As a corollary, the Gruf Complex has to be treated independently from the other Penninic units.

The joint exhumation of the Bergell with the hot Gruf Complex also explain the increase of metamorphic temperatures across the Chiavenna Unit and the Tambo Nappe towards the contact with the Gruf Complex. The differential movement of the Gruf Complex did not occur along a well defined Gruf Line but was accommodated in a wide zone within the enclave-rich biotite-orthogneiss. The enclaves embedded within the orthogneiss are relics of the Chiavenna ophiolites sheared into the orthogneiss during its syn-kinematic partial melting.

Riassunto

Lo scopo di questo studio consiste nel mappare il Complesso del Gruf (parte orientale delle Alpi Centrali) e caratterizzarne l' evoluzione tettono-metamorfica. Il Complesso del Gruf affiora tra il plutone calcalcalino della Bregaglia e le rocce ofiolitiche mesozoiche dell'Unità di Chiavenna. Il Gruf è costituito in prevalenza da rocce migmatitiche metagranitoidiche e da migmatiti di origine sedimentaria a composizione pelitica e psammitica. Quest'ultime sono associate a leucosomi e graniti leucocratici. Lenti di charnockiti, granuliti, rocce metamorfiche ultramafiche, basiche e carbonatiche sono contenute nelle migmatiti.

Le rocce metagranitoidiche sono formate da orthogneiss migmatitici a biotite, a grana grossolana, compatte o debolmente foliate, caratterizzate da una tessitura disorganizzata e fluidale. La loro composizione varia da metaluminosa a peraluminosa. Nella parte più settentrionale del Complesso del Gruf, questi orthogneiss contengono numerose enclavi a composizione basica geochimicamente molto simili alle anfiboliti di Chiavenna. Corpi budinati (8 x 0.5 km) di charnockiti a ortopirosseno associate a lenti (< 50m) di websteriti/gabbronoriti affiorano nelle migmatiti. Le charnockiti sono leucocratiche, a granulometria da media a grossolana e a composizione da metaluminosa a peraluminosa. Queste rocce sono separate dagli orthogneiss migmatitici incassanti da sottili zone milonitiche centimetriche. La loro struttura interna è caratterizzata da strutture di flusso irregolari e da schlieren e enclavi granulitiche. Granuliti a granato, ortopirosseno, biotite e felspato potassico (± saffirina, sillimanite, cordierite, corindone, spinello, plagioclasio e quarzo) formano schlieren nelle charnockiti o enclavi restitiche sia nelle charnockiti sia negli orthogneiss migmatitici. Le websteriti/gabbronoriti sono di color verde-marrone, presentano una granulometria da media a grossolana, sono compatte e prevalentemente composte da clinopirosseno, ortopirosseno e biotite e plagioclasio interstiziali. I contatti con gli orthogneiss incassanti sono di natura intrusiva.

I metasedimenti migmatitici sono caratterizzati dall'alternanza di paragneiss a granato e scisti biotitici a sillimanite, granato e cordierite. Entrambe le litologie presentano una bancatura migmatitica definita dall'alternanza di leucosomi quarzo-felspatici e mesosomi/melanosomi richi in biotite, granato e sillimanite. Questa bancatura è prevalentemente parallela alla scistosità dominante. Ciononostante, dove il grado di fusione parziale è più elevato, i leucosomi migrano in maniera discordante rispetto alla scistosità formando filoni e tasche centimetriche. Associati a questi metasedimenti migmatitici si osservano graniti leucocratici a due miche, granato e sillimanite, compatti, a granulometria da fine a grossolana e di composizione peraluminosa. Questi graniti presentano contatti intrusivi netti e irregolari con i metasedimenti e contatti più diffusi con gli orthogneiss migmatitici.

Lenti di metaperidotiti, spesso associate ad anfiboliti e calcsilicati, sono contenute sia nelle rocce metagranitoidiche sia nei metasedimenti. Queste metaperidotiti sono caratterizzate dall'alternanza composizionale di layer lerzolitici, dunitici, pirossenitici e cromitici. Il layering è tagliato da numerosi filoni metarodingitici e ferrogabbroici. Layering e filoni presentano una scistosità penetrativa comune, prevalentemente definita dall'orientazione preferenziale degli ortopirosseni. Vene

tardive a talco e clorite ritagliano questa scistosità. I contatti tra le metaperidotiti e i metasedimenti migmatitici sono di natura milonitica. Al contrario, i contatti tra le metaperidotiti e le rocce meta-granitoidiche sono di natura intrusiva e caratterizzati da filoni decimetrici di leucosomi granitici che intrudono e fratturano i bordi delle lenti metaperidotitiche.

La struttura regionale del Complesso del Gruf è dominata da un trend strutturale della scistosità e dei contatti litologici orientato ENE-WSW. Nella parte settentrionale e centrale del Gruf, la fabbrica regionale si immerge verso NNW; nella parte più meridionale, al contrario, verso SSE. Ciò suggerisce che l'architettura dell'intero complesso sia definita da un duomo strutturale. L'elongazione dei minerali a livello regionale si immerge con un angolo di 30-40° verso E e NE. Eccezioni sono rappresentate dalle charnockiti e dalle metaperidotiti, le quali presentano scistosità e lineazioni differenti e irregolari, senza un chiaro trend regionale. Lo stile e l'intensità della deformazione dipende dalla litologia e dal suo grado di fusione. Nelle rocce metagranitoidiche la deformazione si concentra prevalentemente in zone di scorrimento duttili. Sono stati identificati tre tipi principali di zone di scorrimento, coniugati tra loro, che descrivono un appiattimento verticale syn-migmatitico e un marcato movimento destrale e normale con senso di scorrimento top-to-the NE. Questo movimento rispecchia la risalita del Gruf rispetto alle unità limitrofe. I metasedimenti sono generalmente interessati da una scistosità più regolare e penetrativa. Queste rocce possono tuttavia localmente presentare una deformazione più complessa, marcata dalla ripiegatura apparentemente caotica della scistosità.

Strutture stromatiche, zone di scorrimento riempite con magmi, venette, tasche e filoni di leucosomi ritaglianti la scistosità, breccie magmatiche e fenomeni di back-veining di leucosomi del Gruf alla base dell'intrusione della Bregaglia indicano che il processo di migmatizzazione è avvenuto contemporaneamente alla deformazione Alpina regionale e alla la messa in posto del plutone. La presenza di sillimanite + felspato potassico e la scarsità o completa mancanza di muscovite syn-cinematica riscontrate a livello regionale nei micascisti migmatitici del Gruf suggeriscono che la fusione parziale regionale è stata indotta dal breakdown della muscovite a T = 700-750 °C e P = 6-7 kbar.

Le charnockiti e le granuliti, invece, presentano un'evoluzione metamorfica più complessa. Calcoli termobarometrici, P-T pseudosections e il contenuto di Al negli ortopirosseni indicano che queste rocce si sono formate a condizioni metamorfiche di UHT a T = 920-940 °C e P = 8.5-9.5 kbar. La paragenesi formatasi al picco metamorfico è stata in seguito parzialmente cancellata da tessiture simplettitiche e corone di ortopirosseno, saffirina, cordierite e spinello a T = 720-740 °C e P = 7-7.5 kbar. Modelli di diffusione nel granato suggeriscono che la paragenesi formatasi al picco metamorfico e le tessiture simplettitiche e corone sono il frutto di due differenti eventi metamorfici. La fusione secca di sedimenti pelitici e psammitici a condizioni di UHT ha generato magmi charnockitici e restiti granulitici. L'intensa perdita di magma e la deidratazione delle granuliti hanno favorito la preservazione (anche se in parte solo parziale) delle paragenesi del picco metamorfico durante il metamorfismo regionale alpino.

Per comprendere il significato geotettonico delle charnockiti e delle granuliti, in particolare nel contesto della migmatizzazione alpina, sono stati datati con la SHRIMP II zirconi separati da 15

campioni di alto grado metamorfico. L'età del metamorfismo granulitico è 282-261 Ma ed è stata ottenuta datando le zonazioni oscillatorie degli zirconi separati dalle charnockiti. Le inclusioni di minerali di facies granulitica trovate in alcuni degli zirconi datati confermano inequivocabilmente l'età permiana delle granuliti. I nuclei magmatici degli zirconi separati da due campioni di orthogneiss biotitico a enclavi basiche hanno età cambriane e ordoviciane. Gli zirconi separati da due leucograniti e sei orthogneiss, che aassieme formano due terzi del Gruf, hanno età comprese tra 290 e 260 Ma. La maggior parte degli zirconi presentano bordi omogenei di età comprese tra 34 e 30 Ma. Questi bordi rispecchiano la migmatizzazione alpina di facies anfibolitica, interpretazione direttamente confermata dalla datazione di una tasca di leucosoma discordante nei metasedimenti migmatitici del Gruf.

Charnockiti, granuliti e websteriti/gabbronoriti formano parte della croste inferiore europea post-varistica. Una ricostruzione geotettonica suggerisce che un pezzo di crosta inferiore appartenente alla crosta europea è stato esumato durante la migmatizzazione e la contemporanea formazione del plutone della Bregaglia, in seguito alla rottura della placca europea subducente. Durante la sua risalita, la dinamica verticale dell'intrusione ha aiutato l'esumazione del Complesso del Gruf quale duomo migmatitico direttamente associato al plutone. Quale corollario, il Complesso del Gruf deve essere inteso come indipendente dalle altre unità penniniche.

L'esumazione comune del Gruf e del plutone della Bregaglia spiega l'aumento delle temperature metamorfiche osservato nelle rocce dell'Unità di Chiavenna e della falda Tambo verso il Gruf. Il movimento differenziale del Gruf non è avvenuto lungo una linea tettonica ben definita ma, al contrario, è stato accomodato in un'ampia zona dentro l'orthogneiss a enclavi. Le enclavi basiche contenute in queta litologia sono da considerarsi relitti delle anfiboliti di Chiavenna inglobate nell'orthogneiss durante la fusione parziale sin-cinematica.

x

Contents

Chapter 1

Introduction

1.1 Geological overview

1.1.1 Central Alps

Architecture

The Alps result from the convergence between the European and Adriatic paleo-margins which led to the closure of two oceanic basins, the Piemont-Ligurian Ocean and the Valaisan Trough (Milnes and Pfiffner, 1980; Schmid *et al.*, 1996a). The Penninic nappe stacking of the Central Alps originated from the south-vergent subduction of the European margin and the subsequent continental collision. Five main paleogeographic domains are recognized in the Eastern part of the Central Alps (Fig. 1.1). These are from the bottom to the top:

  (i) the Lower Penninic Leventina, Simano and Adula Nappes, ascribed to the distal part of the European continental margin (Trümpy, 1960; Schmid *et al.*, 1990, 1996a);

 (ii) the North Penninic ophiolitic rocks of the Misox Zone and Chiavenna Unit, interpreted as remnants of the Valais Trough (Schmid *et al.*, 1996a; Steinmann and Stille, 1999);

(iii) the Middle Penninic Tambo and Suretta Nappes, representing the former Briançonnnais micro-plate (Schmid *et al.*, 1990);

 (iv) the South Penninic ophiolitic units Malenco-Forno-Lizun-Avers, assigned to the Piemont-Ligurian Ocean (Staub, 1946; Schmid *et al.*, 1990, 1996a);

  (v) the overthrusted Austroalpine units, corresponding to the distal Adriatic continental margin (Handy *et al.*, 1993; Froitzheim *et al.*, 1994).

In this nappe stack, coherent basement thrust sheets such as the Leventina, Simano, Tambo and Suretta nappes can be discerned from more heterogeneous units as the Adula-Cima Lunga Nappe Complex, Gruf Complex and Bellinzona-Dascio Zone formed from the imbrication of various rock types (Berger *et al.*, 2005). These heterogeneous units were defined by Trommsdorff (1990) as "Alpine lithospheric mélange" and interpreted as parts of a "tectonic accretion channel" (TAC), accreted along the European plate during subduction (Engi *et al.*, 2001).

Metamorphic evolution

The metamorphic pattern of the Central Alps is characterised by two major metamorphic events:

  (i) **a low- to medium-temperature, high-pressure metamorphism** preserved as relics of blueschist- and eclogite-facies mineral assemblages in metasediments of domains (ii) and (iii) (Ring, 1992; Baudin and Marquer, 1993; Nussbaum *et al.*, 1998; Bousquet *et al.*, 2002) and as eclogites of mainly metabasaltic and peridotitic composition in the Adula-Cima Lunga Nappe Complex, Orselina Zone, Arbedo-Mergoscia Zone and Someo Zone (Heinrich, 1983, 1986; Meyre *et al.*, 1999; Nimis and Trommsdorff, 2001; Dale and Holland, 2003; Berger *et al.*, 2005; Brouwer *et al.*, 2005; Zulbati, 2008). This first metamorphic event is related to the subduction stage;

(ii) a **Barrovian-type "Lepontine metamorphism"** related to the thermal relaxation after the nappe stacking.
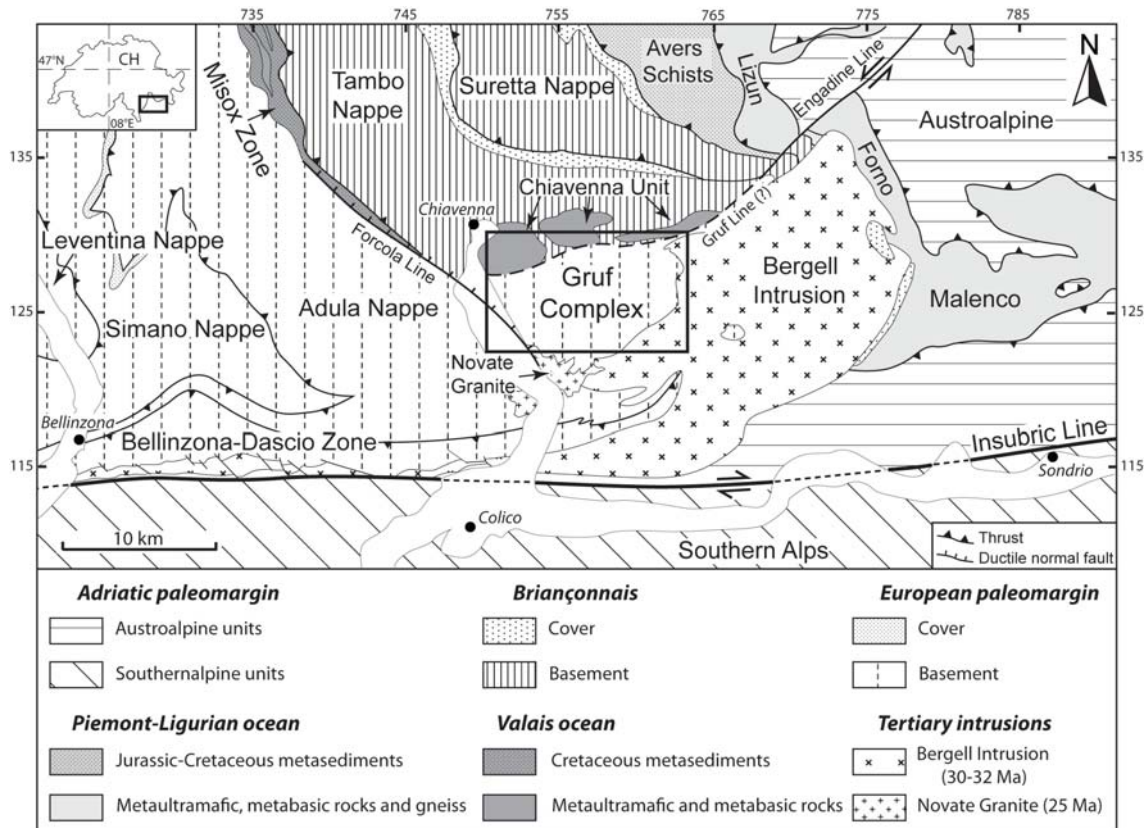
Figure 1.1: *Simplified tectonic map of the eastern Central Alps. The main units are organised according to their paleogeographical origin. Framed: location of the studied area. Swiss co-ordinates are given with units in kilometres.*

This latter temperature-dominated event strongly overprinted the pre-existing mineral assemblages. Concentric isograds, isotherms and isobars define the Lepontine Metamorphic Dome (Wenk, 1955; Todd and Engi, 1997). Contrasting the high-pressure metamorphism, this pattern cuts across nappe boundaries, suggesting that Barrovian peak-conditions were achieved after nappe stacking (Niggli and Niggli, 1965; Trommsdorff, 1966; Wenk, 1970; Bernotat and Bambauer, 1982; Todd and Engi, 1997). Lepontine metamorphic conditions increase southwards from upper greenschist- to upper amphibolite-facies. In the southernmost part, the Lepontine Dome is characterised by intense migmatization (Berger *et al.*, 2005; Burri *et al.*, 2005) which took place through fluid-assisted melting (Berger *et al.*, 2008) at about 700 °C and 6-8 kbar (Nagel *et al.*, 2002; Burri *et al.*, 2005) between 32 and 22 Ma (Hänny *et al.*, 1975; Köppel *et al.*, 1981; Gebauer, 1996; Berger *et al.*, 2009; Rubatto *et al.*, 2009). Further to the south, the Lepontine Dome is truncated by the Insubric Line (Fig. 1.1), a major tectonic boundary separating the high-grade Central Alps from the Southern Alps, which record only minor Alpine metamorphism (Schmid *et al.*, 1987, 1989; Steck and Hunziker, 1994).

1.1.2 Gruf Complex

The Gruf Complex, about 20 x 10 km in extension, is located in the southeastern part of the Lepontine Dome. To the north, the so-called (but fairly putative) Gruf Line separates the Gruf from the Chiavenna ophiolitic Unit and from the Tambo Nappe. The Gruf Linie is described as a vertical, strongly recrystallised mylonite zone (Schmutz, 1976). To the east, the Gruf is cut by the calc-alkaline Bergell Pluton. To the west and south, the Gruf is bordered by the Adula Nappe and Novate Granite, which in turn are followed by the Bellinzona-Dascio Zone (Fig. 1.1).

The tectonic position of the Gruf Complex in the sequence of the Pennine nappes is still uncertain. Three interpretations have been proposed:

(i) the Gruf Complex is equivalent to the Bellinzona-Dascio Zone (Wenk, 1973; Wenk and Cornelius, 1977; Milnes and Pfiffner, 1980);

(ii) the Gruf Complex constitutes the eastern continuation of the Adula-Cima Lunga Nappe Complex (Schmid *et al.*, 1996b; Davidson *et al.*, 1996; Frey and Ferreiro Mählmann, 1999; Liati and Gebauer, 2003) forming part of the Gruf-Bodengo subunit (Berger *et al.*, 2005);

(iii) the Gruf Complex is an independent unit (Staub, 1946; Hänny *et al.*, 1975);

The Gruf Complex consists prevalently of migmatitic quartzo-feldspatic orthogneisses, parag- neisses and sillimanit-garnet-($\pm$ cordierite)-bearing micaschists. Two generations of migmatites have been recognised: i) pre-Alpine migmatites related to Variscan intrusives (Gulson, 1973; Hänny *et al.*, 1975) and ii) migmatites of Alpine age (Hänny, 1972; Hänny *et al.*, 1975; Hafner, 1993; Davidson *et al.*, 1996; Berger *et al.*, 1996; Rubatto *et al.*, 2007). Alpine regional metamor- phic peak conditions occurred at ca. 32 Ma (Liati and Gebauer, 2003) at upper amphibolite-facies conditions (Bucher-Nurminen and Droop, 1983; Reusser, 1987b; Nagel *et al.*, 2002). In contrast to the adjacent Adula-Cima Lunga Nappe Complex which contains numerous eclogites, no high- pressure relics have been reported in the Gruf Complex.

Several lenses (up to 100 m in size) and centimetric nodules of ultramafic, mafic, calcareous and pelitic composition occur regionally within the migmatites (Artus, 1959; Moticska, 1970; Wenk, 1973, 1982, 1986; Diethelm, 1989; Wenk, 1992). These lenses and nodules are prevalently concentrated in proximity of the Bergell Pluton (Moticska, 1970; Wenk and Cornelius, 1977) and are regarded as remnants of the North Penninic Suture connecting the ophiolitic Chiavenna Unit and Misox Zone in the north with the Mesozoic ophiolitic rocks contained in the migmatites of the Bellinzona-Dascio Zone in the south (Diethelm, 1989; Davidson *et al.*, 1996; Schmid *et al.*, 1996b).

Dark, Mg-Al-rich, sapphirine-orthopyroxene-bearing granulites are the peculiarity of the Gruf Complex and represent a long-standing enigma in Alpine geology. These rocks were discovered by Cornelius (1916) and subsequently by Wenk *et al.* (1974) in form of blocks from two talus slopes in Val Codera (locations indicated in Wenk and Cornelius, 1977), but have never been found in their geological context, in part because of the hostile topography of the Gruf area. Estimates of

metamorphic peak-conditions by conventional thermobarometry yielded $T \geq 800\,^{\circ}C$ and $P = 8\text{-}10$ kbar, conditions pre-dating the formation of symplectitic textures and coronae at about $T = 750\,^{\circ}C$ and $P = 5$ kbar (Barker, 1964; Ackermand and Seifert, 1969; Droop and Bucher-Nurminen, 1984). The latter authors suggested that the Gruf granulites formed during a single Alpine metamorphic cycle characterised by nearly isothermal decompression and proposed that granulitic conditions affected the entire Gruf Complex and were preserved exclusively in the Mg-Al richest rock types. In contrast, Huber (1999); Huber *et al.* (1999); Burri *et al.* (2005) on structural and petrological arguments envisaged a Permian age for the granulitic event.

Zircon grains separated from the Gruf granulites yielded SHRIMP ages of 272.0 ± 4.1 Ma for oscillatory zoned cores, interpreted as crystallisation time of a presumably magmatic precursor, and 32.7 ± 0.5 Ma for the homogeneous rims, inferred to represent the age of the granulite facies metamorphism (Liati and Gebauer, 2003). Similar ages of 33 ± 4.4 Ma have been reported from monazite grains included by or as intergrowth with high temperature minerals such as sapphirine and aluminous orthopyroxene (Schmitz *et al.*, 2009). However, metamorphic conditions of $T \geq 800\,^{\circ}C$ and $P = 10 \pm 2$ kbar do not fit any known metamorphic event of regional significance in the Central Alps questioning the inferred Alpine age for the granulites.

1.1.3   Chiavenna Unit

Tectonically, the Chiavenna Unit lies above the Gruf Complex and below the Tambo Nappe (Wenk, 1955). The Chiavenna Unit is composed of metamorphic ultramafic rocks which overlie mafic rocks and rare metacarbonates and is interpreted as an incomplete, overturned, ophiolitic sequence (Schmutz, 1976). Geochemically, the rocks are similar to other North Penninic ophiolites exposed in the Central Alps (Dürr *et al.*, 1993). Metaultramafic rocks consist of former lherzolites showing a composite mantle history of partial melting, cryptic metasomatism and serpentinisation (Talerico, 2000). Mafic rocks comprise both banded and massive amphibolites and rodingite dykes, all of them of tholeitic composition and strong affinity to N-type MORB basalts (Dürr *et al.*, 1993; Talerico, 2000). Metacarbonates are composed of calcite-marbles, calcsilicates and rare ophicarbonates (Schmutz, 1976).

Paleogeographically, the Chiavenna Unit is regarded as the eastern prolongation of the Misox Zone and is interpreted as the North Penninic Suture (Schmid *et al.*, 1996a). Huber and Marquer (1998) and Talerico (2000) propose that the Chiavenna Unit represents former denuded subcontinental mantle at the thinned northern margin of the Briançonnais terrain, whereby subcontinental mantle rocks instead of "typical" oceanic lithosphere were exposed on the ocean floor along deep seated normal fault and were covered with tholeitic N-type MORB basalts and carbonatic sediments. This interpretation is supported by geochronological data. Co-magmatic zircon domains of grains separated from the Chiavenna amphibolites yielded an age of 93 Ma, interpreted as the time of intrusion of the magmatic precursor during the late spreading of the Valais Through. Metamorphic zircon rims display an Eocene age of about 37 Ma (Liati *et al.*, 2003), which is similar to the age attributed to the metamorphism in other Valais domains (e.g. Antrona ophiolite, Liati and Gebauer (2001)).

The rocks of the Chiavenna Unit show a strong metamorphic gradient characterised by an isobaric increase of the temperatures from north to south. Towards the contact with the Gruf Complex, higher-grade mineral assemblages progressively substitute low-grade metamorphic assemblages (Schmutz, 1976). In the north, ultramafic rocks are composed of antigorite, olivine, magnetite, tremolite, chlorite and relictic diopside, while amphibolites are epidote-bearing. Towards the south, in the metaperidotites the diopside-out, talc-in, antigorite-out, talc-out, enstatite-in and spinel-in isograds are progressively crossed (Figs. 1.2a and b), whereas in the amphibolites epidote-bearing assemblages are replaced by hornblende- and diopside-bearing assemblages (Fig. 1.2a). In proximity of the Gruf Complex, amphibolites are partially molten (Huber and Marquer, 1998).
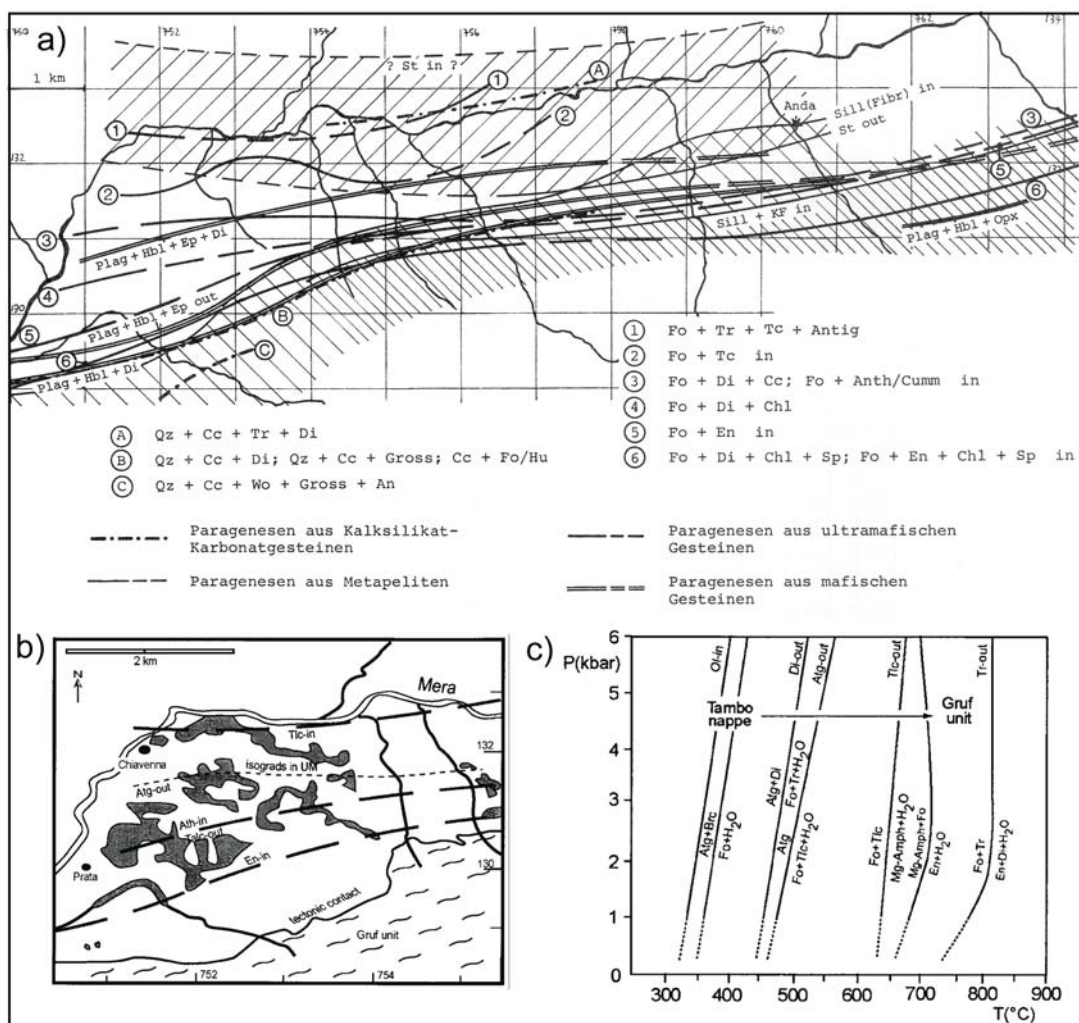
Figure 1.2: *(a) Map of the Alpine metamorphic isograds in the rocks of the Chiavenna Unit and Tambo Nappe, showing the locations of mineral isograds and the occurring main mineral assemblages in metaperidotites, amphibolites, metacarbonates and metapelites (after Schmutz (1976)); (b) isograds in metaperidotites from the Chiavenna Unit (modified after Schmutz (1976)); (c) phase-diagram for the ultramafic CMSH system, showing the estimated metamorphic evolution from the Tambo Nappe to the Gruf Complex (Talerico, 2000).*

6

Thermobarometric calculations (Fig. 1.2c) yielded metamorphic conditions of P = 3-4 kbar and T = 500 °C in the north and T = 700 °C in the southern part of the unit (Schmutz, 1976; Talerico, 2000), corresponing to a metamorphic field gradient of about 80 °C/km. Talerico (2000) recognised two distinct metamorphic events: i) a dynamic metamorphism at greenschist facies conditions interpreted as the regional metamorphism; ii) a static thermal overprint imputed to the juxtapositiont of the hot Gruf Complex along the Gruf Line leading to the anomalously strong temperature gradient (Fig. 1.3). Ar/Ar ages indicate that the greenschist facies regional meta-morphism occurred at 45-47 Ma, while the static thermal overprint occurred between 30 and 33 Ma (Talerico, 2000), contemporaneously to the metamorphic peak in the Gruf Complex (Liati and Gebauer, 2003) and to the emplacement of the Bergell Pluton (Von Blanckenburg, 1992).
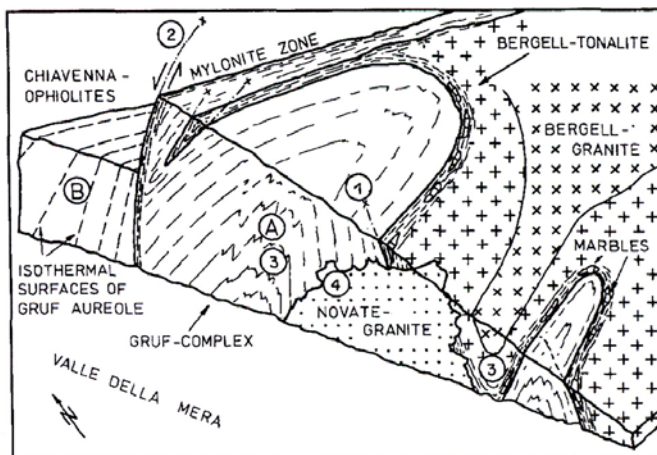
Figure 1.3: *Schematic block diagram of the Gruf Complex area (Bucher-Nurminen and Droop, 1983). The rocks of the Gruf Complex and Bergell Intrusion (A) experienced a strong and rapid differential uplift in respect of the Chiavenna ophiolites and the surrounding Penninic nappe system (B). Succession of geological events: (1) emplacement of the Bergell Pluton above the Gruf Complex; (2) strong differential uplift along the Gruf Line and formation of contact aureole in (B), (3) folding of the pluton basis, (4) intrusion of the Novate Granite dated at ca. 24-25 Ma (Liati et al., 2000).*

1.1.4   Adula-Cima Lunga Nappe Complex

The Adula-Cima Lunga Nappe Complex forms the uppermost part of the lower Penninic nappes and paleogeographically represents the distal margin of the former European continent (Schmid *et al.*, 1990, 1996a). The complex is internally heterogeneous and is composed of several slices and thrust sheets (Berger *et al.*, 2005). The structurally lower part is marked by uniform orthogneiss lithologies without high pressure relics. In contrast, the higher part shows an imbricated structure of basement slices intercalated with metacarbonates of probably Mesozoic age, mafic and ultra-mafic lenses and is interpreted as "lithospheric mélange" (Trommsdorff, 1990). Ultramafic, mafic and metapelitic rocks preserve eclogitic assemblages (Heinrich, 1983, 1986; Meyre *et al.*, 1997; Partzsch, 1998; Meyre *et al.*, 1999; Nimis and Trommsdorff, 2001). High pressure conditions increase southwards from 10-17 kbar and 450-640 °C in the north, to 25 kbar and 750-800 °C in the south (Heinrich, 1986; Meyre *et al.*, 1997; Partzsch, 1998; Dale and Holland, 2003). Brouwer *et al.* (2005) show that the HP rocks of the southern Adula, and more in general of the entire "Southern Steep Belt", have no systematics in their metamorphic paths, implying greater relative mobility between different slices forming the nappe complex.

The age of the HP metamorphism has been a matter of debate. Heinrich (1983), Heinrich (1986), Löw (1987), Meyre *et al.* (1997) and Nagel *et al.* (2002), based on petrological evidences, proposed that the Adula-Cima Lunga Nappe Complex experienced a single, Alpine, high pressure event of regional importance. This interpretation is supported by Oligocene Rb-Sr and Ar-Ar ages on phengite from gneisses and eclogites (Jäger *et al.*, 1967; Muralt, 1986; Santini, 1992) and by Paleocene up to Oligocene Lu-Hf ages of eclogites (Brouwer *et al.*, 2005). However, a recent geochronological investigation on zircons separated from eclogite lenses and their country rocks (Liati *et al.*, 2009) showed that the northern part of the nappe were affected by HP metamorphism both in Mid-Carboniferous time (ca. 330-340 Ma) and probably in Alpine time. In the central Adula, HP metamorphism occurred in Devonian time (ca. 370 Ma) but no HP Alpine event has been recorded by the zircons. In the southern Adula, HP metamorphism is instead reported at ca. 35 Ma (Gebauer, 1994, 1996; Hermann *et al.*, 2006).

Between 33 and 25 Ma (Hänny *et al.*, 1975; Gebauer, 1994, 1996; Rubatto *et al.*, 2007; Berger *et al.*, 2009; Liati *et al.*, 2009), the entire Adula-Cime Lunga Nappe Complex was overprinted by the Lepontine regional metamorphism, marked by amphibolite-facies conditions. Detailed petrological investigations showed that metamorphic temperatures increased southwards from 550°C up to ca. 700°C during decompression up to 5-8 kbar (Nagel *et al.*, 2002).

1.1.5 Zone of Bellinzona-Dascio

The zone of Bellinzona-Dascio (BDZ) represents the southernmost Penninic unit of the Central Alps. It is a steeply dipping, east-west striking zone marked by the intercalation of different rock types. Similarly to the Adula-Cima Lunga Nappe Complex, the BDZ is interpreted as lithospheric mélange formed in the TAC (Schmid *et al.*, 1996a; Engi *et al.*, 2001).

Migmatitic orthogneisses, paragneisses and sillimanite-garnet-bearing micachists are the predominant rock types. Marbles, calcsilicates, amphibolites and ultramafic rocks are subordinate and occur as lenses and layers within the migmatitic gneisses (Knoblauch, 1939; Moticska, 1970; Fumasoli, 1974; Heitzmann, 1975). Migmatisation occurred at upper amphibolite facies conditions of T = 650-750 °C and P ± 7 kbar (Fumasoli, 1974; Heitzmann, 1975; Schmidt, 1989; Buob, 1997; Gianettoni, 1997; Stucki, 2001). No relics of an earlier HP event have been reported.

Ultramafic rocks represent fertile to moderately depleted, serpentinised metalherzolites, regarded as former subcontinental mantle (Stucki *et al.*, 2003). Generally, UM lenses are rimmed by amphibolites. Boudinaged, mostly rodingitised mafic dikes and rare plagiogranites occur within the metalherzolites. Mafic dykes show different degrees of rodingitisation and a wide range of composition, varying from primitive Mg-gabbro to more evolved Fe-Ti-gabbro.

Serpentinised ultramafic rocks and the occurrence of both metarodingite and plagiogranite dykes suggest an ophiolitic origin for the UM-mafic suite (Stucki *et al.*, 2003). Diethelm (1989) and Schmid *et al.* (1996a) proposed that the ophiolites of the BDZ correspond to those of the Chiavenna Unit and Misox Zone, representing relics of the North Penninic Suture within the "Southern Steep Belt". However, magmatic zircon ages of 142 ± 5 Ma and 149 ± 3 Ma displayed by two plagiogranite dykes (Stucki *et al.*, 2003) argue for the appartenance of the BDZ ophiolites to

the Piemont-Ligurian Ocean.

The contact between the Zone of Bellinzona-Dascio and the Gruf Complex is difficult to define. Moticska (1970) mapped it in the central part of Valle dei Ratti, between leucocratic gneisses, supposed to belong to the Gruf Complex, and more biotite-rich schists in the south, interpreted as part of the Bellinzona-Dascio Zone.

1.1.6 Tertiary igneous rocks: Bergell Pluton and Novate Granite

Bergell Pluton

The Bergell Pluton is a calc-alkaline intrusion composed of tonalite, granodiorite and minor amount of gabbro, hornblendite, diorite and both aplite and pegmatite dykes (Wenk, 1973; Wenk and Cornelius, 1977; Reusser, 1987b; Diethelm, 1989). The pluton shows a compositional zoning, in that rare gabbroic rocks and the main tonalite are located at the margin, while granodiorite forms the core of the intrusion. A zone of mingling and mixing, the "Übergangszone" of Moticska (1970) and Wenk and Cornelius (1977), occurs between granodiorite and tonalite.

Von Blanckenburg (1992) measured crystallisation ages at the eastern pluton margin of 31.88 ± 0.09 Ma for the tonalite and 30.13 ± 0.17 Ma for the granodiorite, respectively. Oberli *et al.* (2004) showed that the western part of the intrusion experienced a more protracted cooling history from 33 to 28 Ma. Gregory *et al.* (2009) estimated 32.4 ± 0.4 Ma as crystallisation age of magmatic allanite from a Bergell gabbro.

Geometrically, the Bergell Pluton has a nappe-like shape (Fig. 1.4). The western contact represents the floor of the magmatic body. The foliation in the intrusion lies parallel to both the contact and the foliation in the country rock. Davidson *et al.* (1996) showed that the floor of the intrusion was folded concordantly together with the country rock while the pluton was still partially molten. The southwestern tail of the pluton is a E-W striking, steeply north dipping, tabular body of tonalite, oriented parallel to the country rock and to the Insubric mylonite belt. It represents the deepest part of the intrusion (Reusser, 1987b) and is interpreted as the "feeder" of the main intrusive body (Rosenberg *et al.*, 1995). In contrast, the eastern and the northern contacts show intrusive discordant contacts to the country rocks and represent the side and the roof of the intrusion, respectively (Rosenberg *et al.*, 1995).
Two models for the genesis of the magma have been proposed:

   (i) is-situ granitisation of the country rock (Drescher-Kaden, 1940; Artus, 1959; Wenk, 1973, 1982; Wenk *et al.*, 1977), implying the subsolidus metasomatic mixing of amphibolitic and granitic country rock to generate gabbro and tonalite;

  (ii) Bergell as an intrusive massiv (Staub, 1918; Trommsdorff and Nievergelt, 1983; Diethelm, 1985; Reusser, 1987b).

Geochemical investigations (Diethelm, 1989) showed that the mafic country rocks are tholeiitic in composition and therefore different from calc alkaline gabbros belonging to the pluton margin, excluding the possibility of in-situ granitization as mechanism for the magma genesis.
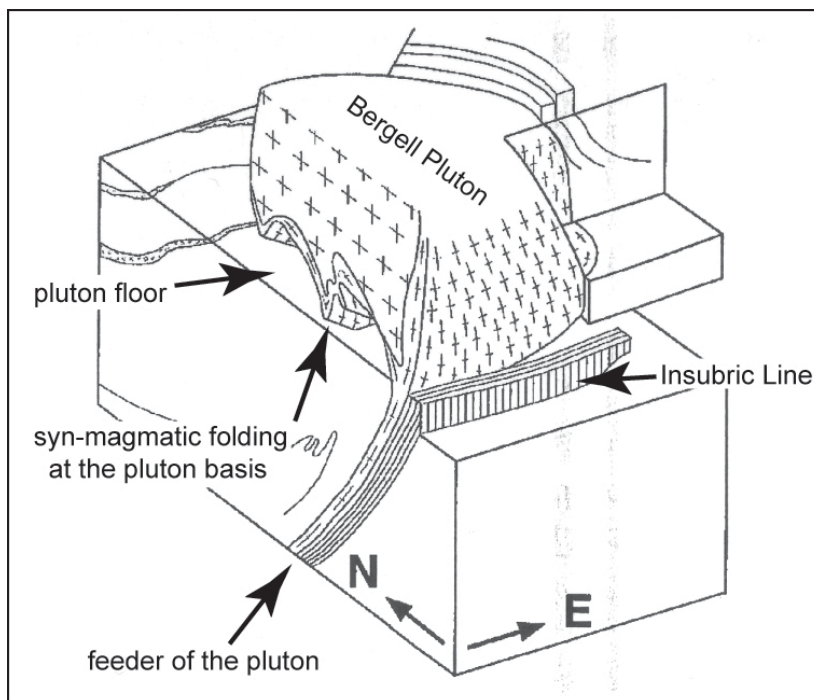
Figure 1.4: *Sketch of the shape of the Bergell Intrusion (modified after Froitzheim et al. (1994)), showing the pluton geometry and its relation to the Insubric Line. The tonalite tail extending westernward to Bellinzona represents the pluton "feeder". The western contact to the Gruf Complex corresponds to the floor of the pluton, while the northern and eastern margins are the side and the roof of the intrusions, respectively.*

Isotopical investigations (Von Blanckenburg *et al.*, 1992) demonstrated that the magma originated from an enriched lithospheric mantle and was subsequently modified by fractional crystallisation and crustal contamination during its uprise. Von Blanckenburg and Davies (1995), Davies and von Blanckenburg (1995) and Von Blanckenburg *et al.* (1998) suggested that the thermal anomaly responsible for the melting of the lithospheric mantle was produced by the break off of the subducting European slab. Berger *et al.* (1996) showed that ascent and final emplacement of the pluton occurred in a transpressive scenario controlled by N-S compression and orogen-parallel extension. Magma ascent, similarly to other Periadriatic plutons (Rosenberg, 2004), was channelled in the pre-existing Periadriatic Fault System. Pluton emplacement occurred during differential displacement of the Tambo and Suretta Nappes to the north and not during nappe stacking (Figs. 1.5a and b). Final emplacement was characterised by syn-magmatic folding of the pluton basis together with the country rock (Fig. 1.5c) during backthrusting along the Insubric Line (Berger *et al.*, 1996; Davidson *et al.*, 1996), and by tectonic-induced ballooning of the side and roof of the intrusion (Rosenberg *et al.*, 1995). Post-emplacement tilting of the pluton is suggested by barometric investigations (Reusser, 1987; Davidson, 1996), which showed an increase of the crystallisation pressure from 4.5-5 kbar at the eastern margin (Val Sissone) up to 8 kbar at the westernmost end (near Bellinzona).

   The Bergell Pluton intruded rocks of different metamorphic grade. At the western margin, the country rocks of the Gruf Complex were at upper amphibolite facies conditions (Bucher-Nurminen and Droop, 1983). No evidences of contact metamorphism are present nor in the Gruf migmatites, nor in the gneisses of the Bellinzona-Dascio Zone (squezzed between the southern tail and the central portion of the Bergell Pluton), nor in the Bergell Intrusion, suggesting that the T difference between regional metamorphic conditions and temperatures of pluton crystallisation was ≤ 200

°C. In contrast, at the eastern intrusion margin the Forno and Malenco Units were at greenschist facies conditions and were consequently contact metamorphosed to about 700 °C at 3-3.5 kbar (Trommsdorff and Evans, 1972, 1977; Trommsdorff and Connolly, 1996).
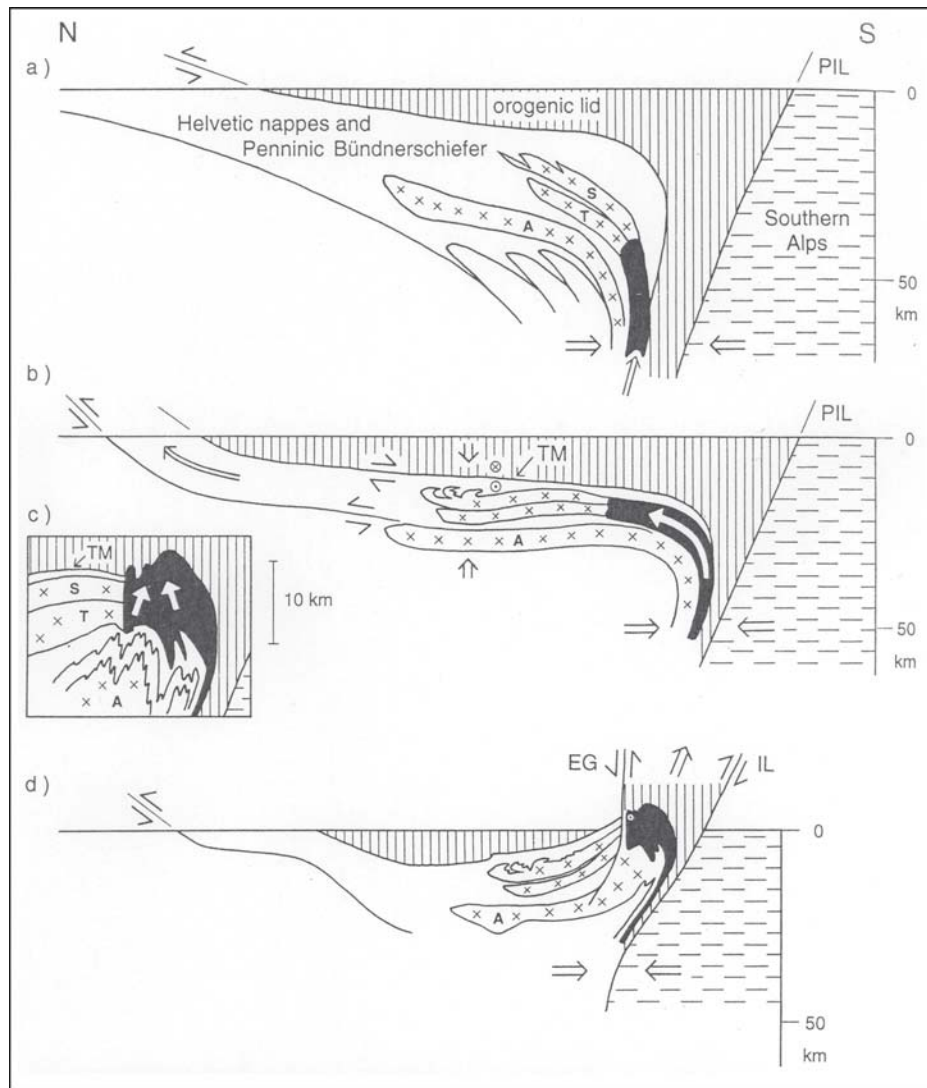
Figure 1.5: *Schematic profiles showing ascent, emplacement and exhumation of the Bergell Pluton (after Schmid et al. (1996a) and Davidson et al. (1996)). a) Situation at 35 Ma: magma ascent occurred into a pre-existing steep zone north of a precursor of the Insubric Line; b) situation at 32 Ma: final pluton emplacement leads to differential northwards displacement of the Tambo and Suretta Nappes accompanied by a top-to-east normal faulting along the Turba Mylonite Zone; c) Inset: situation at 30 Ma: final emplacement of the Bergell Pluton was characterised by syn-magmatic shortening at the base of the intrusion and contemporaneous ballooning of the intrusion roof; d) situation at 19 Ma: differential uplift of the Bergell area between the Engadine-Gruf Line and the Insubric Line.*

Novate Granite

The Novate Granite (also called "San Fedelino" Granite) is a two-mica, fine- to medium-grained leucogranite, mainly composed of quartz, plagioclase, alkali feldspar, muscovite, biotite and small garnets (Repossi, 1915; Piccoli, 1961). The granite is not a diapir but occurs as stock of aplite and pegmatite dykes which cut across the fabric of the surrounding rocks, including the Bergell Tonalite. In general, the dykes intruded after the main regional stage of deformation and partial melting. Only rare Novate-related dykes are contemporaneous to folding and migmatization in the country rock (Hafner, 1993).

The peraluminous rock composition (Callegari and Monese, 1961; Moticska, 1970; Wenk *et al.*, 1977; Mottana *et al.*, 1978) and the Sr-initials and Sm/Nd ratios (Von Blanckenburg *et al.*, 1992) suggest that the Novate Granite is not genetically related to the calc alkaline Bergell Intrusion, but rather is the result of partial melting of crustal rocks. The formation of the granite probably is related to the late-Alpine decompression associated to the exhumation of the Bergell area and the backthrusting of the Penninic units along the Insubric Line (Reusser, 1987b; Oschidari and Ziegler, 1992; Von Blanckenburg *et al.*, 1992).

Radiometric zircon data showed that the Novate Granite intruded at approximately 24-25 Ma (Liati *et al.*, 2000), simultaneously to the intrusion of numerous pegmatite and aplite dykes through the entire "Southern Steep Belt" (review in Burri *et al.* (2005)). Apatite fission-tracks data showed that the granite cooled down to temperatures of 300-350 °C at about 23-21 Ma and crossed the brittle-ductile transition at ca. 18-20 Ma (Hansmann, 1996).

The granite is heterogeneously deformed. The deformation decreases from north to south and is usually localised in arrays of anastomosing ductile shear zones (Ciancaleoni and Marquer, 2006). In the southern part, the rock is almost undeformed. Numerous blocks of Bergell tonalite embedded in the granite show no preferred orientation. In contrast, in the northern part, xenoliths of Gruf migmatite are stretched parallel to the N-E dipping foliation (Schmid *et al.*, 1996b). Analysis of the kinematics of the shear zones showed that the Novate Granite was probably emplaced along the southern tip of the Forcola Fault (Ciancaleoni and Marquer, 2006) .

1.2   Problem setting

In respect of other units that form the Central Alps, the Gruf Complex has been only poorly investigated. This is principally due to the extrem inaccessibility and the steep morphology that characterise the entire complex. Just a few studies exist and many geological problems remain still unresolved. The manuscript has been divided in 6 chapters, each of them adressing a specific topic. The major issues investigated in this study are:

- *Mapping:* neither detailed maps nor field information exist for the most part of the Gruf Complex and a coherent structural scheme of the whole complex is still missing. The geological map presented in this study represents the starting point of the thesis. The description of the different rock types and their field relations, the analysis of the deformation and the comprehension of the contacts between the Gruf Complex and the adjacent units are fundamental to understand the architecture of the Gruf Complex;

- *Geochemistry:* only a few and non-systematic geochemical data for the rocks of the Gruf Complex are available (Gulson, 1973; Droop and Bucher-Nurminen, 1984; Diethelm, 1989). An intense geochemical campaign has been conduct in order to characterise the major and trace element characteristics of migmatitic metagranitoid rocks, granulites and metabasic rocks;

- *Metamorphism:* the metamorphic evolution of the Gruf Complex is still a matter of debates. It is important to determine the exact regional metamorphic conditions and it is necessary to compare the Gruf granulites to the close-by migmatitic metapelites, understanding whether the same metamorphic history should texturally apply to a coherent unit;

- *Geochronology:* the interpretation of the geodynamic evolution of Gruf Complex can not prescind from reliable geochronological data. In this sense, the major questions to be answered concern: i) the age of the charnockitic magmatism and the timing of the granulite facies metamorphism; ii) the protolith age of the migmatitic granitoids and iii) the age of the regionally widespread partial melting;

- *Granulites:* it is crucial to identify the granulites in-situ, to understand their local extension, abundance and relations to the country rock. It is also fundamental to estimate the metamorphic granulite peak-conditions and the post-peak evolution using modern thermodynamic tools;

- *Tectono-metamorphic evolution:* the combination of all the previous data would lead to the reconstruction of the tectono-metamorphic history for the Gruf Complex, which is the final and major goal of this thesis. Particular emphasis will be put on the metamorphic evolution and exhumation history of the Gruf Complex in relation to the adjacent Bergell Pluton and Chiavenna Unit.

Chapter 2

Mapping of the Gruf Complex

2.1   Introduction

2.1.1   Geological map of the Gruf Complex: Why?

The Gruf Complex, mostly because of its hostile topography and inaccessibility, is one of the less investigated areas of the entire Alpine chain. The existing geological maps cover only small parts of the complex (northern-eastern part provided by Wenk and Cornelius (1977), Schefer (2005) and Ruzicka (1997); southernmost part by Moticska (1970)) and neither detailed maps nor field information exist for most of the complex. The few available petrological (Bucher-Nurminen and Droop, 1983; Droop and Bucher-Nurminen, 1984; Diethelm, 1989) and geochronological (Gulson, 1973; Liati and Gebauer, 2003; Schmitz *et al.*, 2009) investigations are mostly based on fallen rock blocks, i.e. without direct tectonic and geological context. Moreover, the lack of intense campaigns of detailed mapping results in the lack of a coherent structural scheme. The understanding and interpretation of the geology of the Gruf without a solide field knowledge are merely illusory. A detailed geological map and a coherent structural investigation are thus indispensable.

2.1.2   Geological map of the Gruf Complex: Where?

During this study, an area of ca. 50 km^2 and 2800 m altitude difference has been mapped on the 1:25'000 scale. The studied area comprises the central and northern part of Val Codera, the eastern flank of Valle della Mera and the southern flanks of Val Chiavenna and Val Bondasca (Fig. 2.1).

Figure 2.1: *Location of the study area. Red line: boundary of the mapped area.*

2.2 Lithological characterisation of the mapped rocks

The Gruf Complex is mostly constituted of two groups of rocks (Fig. I.1):

  (i) migmatitic metagranitoids;

  (ii) partly migmatitic pelitic to psammitic metasediments associated with leucosomes and leucogranites.

Small lenses of meta-ultramafic, -basic and -carbonatitic rocks occur within these two major groups. All the rock types described below are intruded by up to 5 m thick aplite and pegmatite dykes common within the entire Gruf Complex. Aplites and pegmatites are mostly composed of quartz, plagioclase, alkali feldspar and variable amounts of muscovite, biotite and garnet. Tourmaline and beryl are locally common rock constituents (Ghizzoni and Mazzoleni, 2005). These dikes will not be discussed further.

Metagranitoids and rock types contained therein

2.2.1 Migmatitic biotite-orthogneiss

Macroscopic description and field occurrence

The migmatitic biotite-orthogneiss is the predominant rock type of the Gruf Complex. It occurs along the southern upper flank of Val Chiavenna and forms the main part of Val Codera. The rock is greysh, coarse-grained and mainly constituted of quartz, plagioclase, alkali feldspar and biotite. Commonly, decimetric to metric, leucocratic bands alternate to more melanocratic, biotite-rich bands or, rarely, to coarse-grained bands marked by up to 2.5 cm large "Augen" of alkali feldspar (Figs. 2.2b and c). Locally, undeformed and slightly rotated enclaves of basic, ultramafic, calcareous and pelitic composition occur within the orthogneiss (Fig. 2.2d). Generally, the migmatitic biotite-orthogneiss is massive or weakly foliated and shows a disorganized and fluidal texture. No penetrative foliation occurs (Fig. 2.2a). However, particularly in upper Val Aurosina, Valle del Conco and around Bivacco Vaninetti, the rock is intensely deformed in arrays of centimetric ductile shear zones (Fig. 2.2e). Often, undeformed to locally strong sheared aplitic and pegmatitic dykes occur within the plane of shearing, suggesting that the dykes intruded contemporaneously to the deformation (Fig. 2.2f).

Contacts: the contact to the enclave-rich biotite-orthogneiss is diffuse and marked by the increase in the grain-size and number of enclaves. The contact to the leucogranites is diffuse and characterised by the progressive occurrence of both millimetric garnet and muscovite instead of biotite. The contact to the charnockites is sharp and outlined by centimetric mylonites or ultramylonites (Fig. 2.6a). The contact to the migmatitic paragneiss and micaschist is generally submylonitic. However, north of Bivacco Vaninetti, the migmatitic biotite-orthogneiss is intrusive into the micaschist (Fig. J.1). Both contacts to the metaperidotites and the websterite to gabbronorite lenses
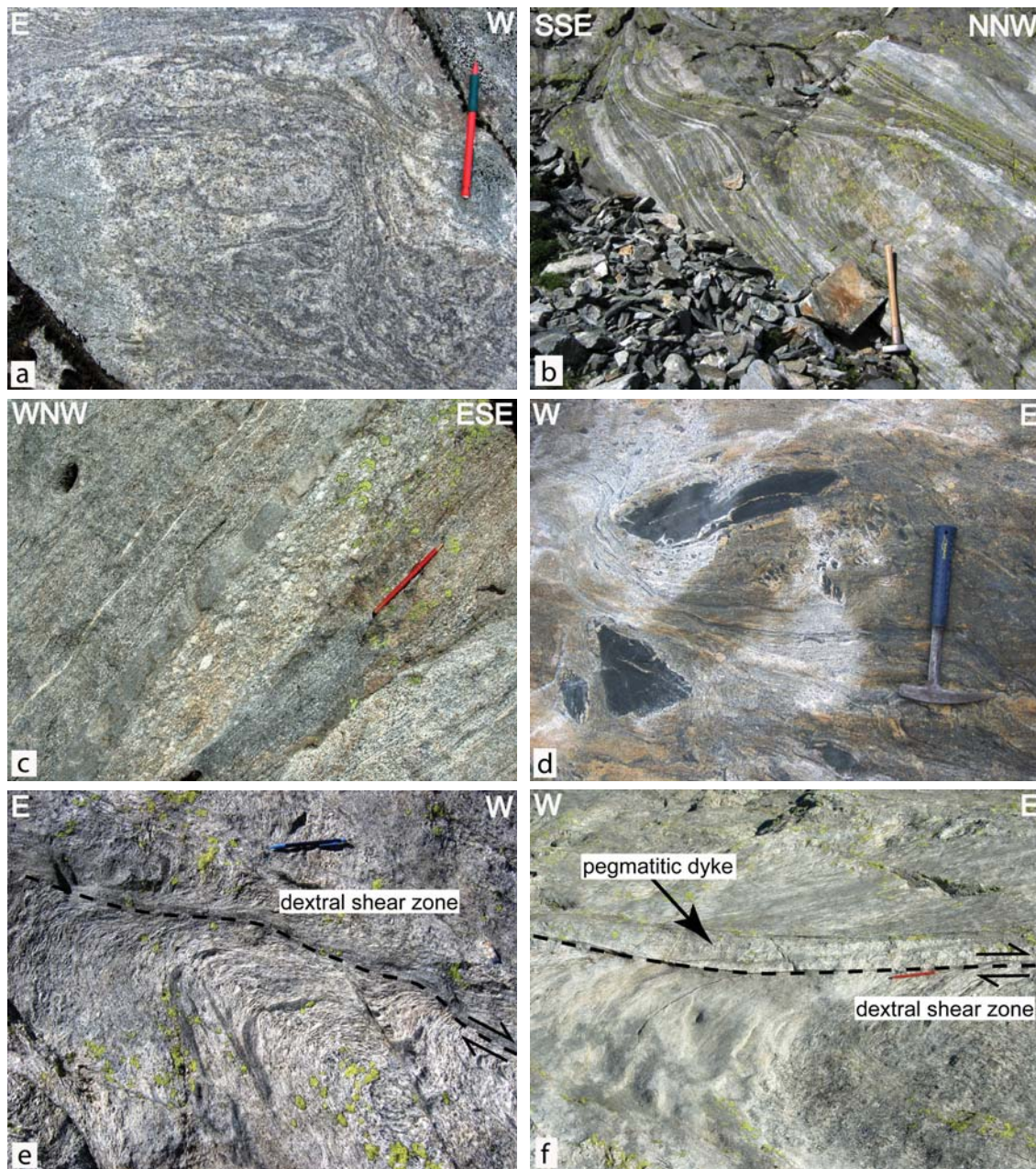
Figure 2.2: *(a) Field aspect of migmatitic biotite-orthogneiss, characterised by the coarse-grained and fluidal texture (upper Val Codera, 763'681/128'963); (b) irregular alternance of leucocratic and melanocratic bands (Val Aurosina, 757'251/128'256); (c) bands with cm-sized "Augen"' of alkali feldspar (Val Casnaggina, 762'543/130'674); (d) undeformed and slightly rotated basic enclaves (Bivacco Vaninetti, 764'168/129'059); (e) dextral ductile shear zone within the migmatitic biotite-orthogneiss (Val Aurosina, 758'314/128'576); (f) almost undeformed pegmatite dyke intrudes through the plane of a dextral ductile shear zone (Val Aurosina, 758'314/128'576).*

are prevalently intrusive. The migmatitic biotite-orthogneiss injects into the enclosed rocks brecciating the margin of the lenses (Fig. 2.16c and Figs. 2.8a, c and d). A detailed description of the contact between the migmatitic biotite-orthogneiss and the rocks of the Bergell Intrusion is treated separately and presented in section 2.4.2.

Microscopic description

Main phases: quartz, plagioclase, alkali feldspar, biotite.
Accessories: muscovite, chlorite, epidote, apatite, rutile, titanite, zircon, opaques.

The migmatitic biotite-orthogneiss displays an equigranular to inequigranular, interlobate texture formed by slightly elongated and oriented quartz, plagioclase and alkali feldspar grains (Fig. 2.3a). Quartz forms subhedral to anhedral, undulose extinguishing grains, up to 1 mm in size. Plagioclase occurs as subhedral, up to 2 mm large grains. Frequently, plagioclase displays both albite and deformation twins and shows undulose extinction. Alkali feldspar is euhedral to subhedral, perthitic and up to 1.5 cm in size. Locally, aggregates of coarse-grained alkali feldspar and millimetric quartz grains form cm-sized "Augen" (Fig. 2.3b). Biotite occurs as acicular, millimetric flakes displaying a moderate preferred orientation that define the main foliation.
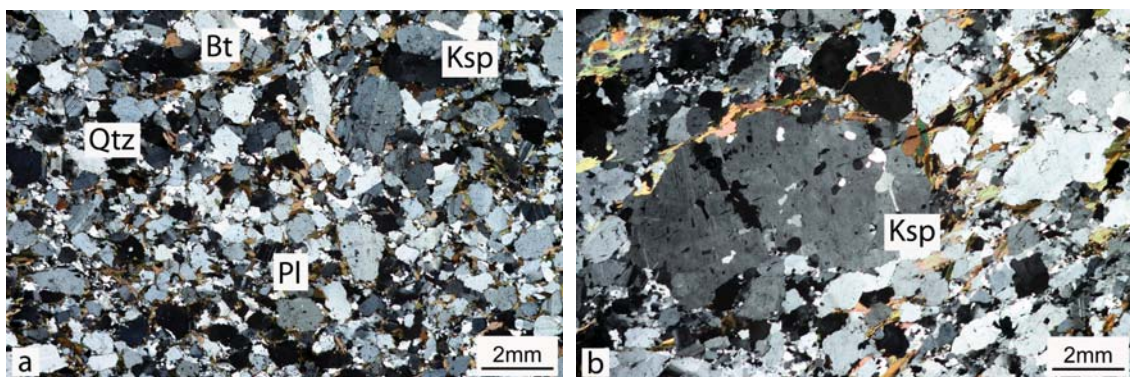
Figure 2.3: *Photomicrograph of the migmatitic biotite-orthogneiss (crossed polarised light). (a) Inequigranular-interlobate texture formed by quartz, plagioclase, alkali feldspar and almost unoriented biotite flakes; (b) detail of a coarse-grained "Augen" of alkali feldspar.*

2.2.2   Enclave-rich biotite-orthogneiss

Macroscopic description and field occurrence

The enclave-rich biotite-orthogneiss constitutes the northernmost part of the Gruf Complex and occurs as a coherent unit of variable thickness (200-1200 m) on the southern flank of Val Chiavenna, between Prata Camportaccio and Val Bondasca. Compared to the migmatitic biotite-orthogneiss, the rock is coarser grained, contains more biotite and less alkali feldspar. Generally, this orthogneiss is massive or weakly foliated (Fig. 2.4a). Exclusively in the northernmost part ap-

proaching the contact with the ophiolitic rocks of the Chiavenna Unit, the planar fabric is stronger developed and more penetrative (section 2.4.1).

The characteristic feature of this metagranitoid are the numerous, decimetric to metric, internally undeformed or well foliated, rounded to weakly elongated enclaves of prevalently mafic and, in rare cases, pelitic and calcareous composition (Fig. 2.4a-d). Commonly, the enclaves are slightly rotated and intruded by leucocratic granitic veinlets (Fig. 2.4d). Locally, these enclaves may constitute up to 5-10 %, on the other extreme, enclaves are only observed every few meters.

Contacts: the contacts to the migmatitic paragneisses and micaschists are sharp and outlined by centimetric thick mylonites. In contrast, the contact to the migmatitic biotite-orthogneiss, which is exposed exclusively in the upper part of Val Casnaggina, is diffuse and marked by grain-size reduction, particularly of biotite, and the progressive disappearance of the enclaves towards the enlcave-free biotite-orthogneiss.
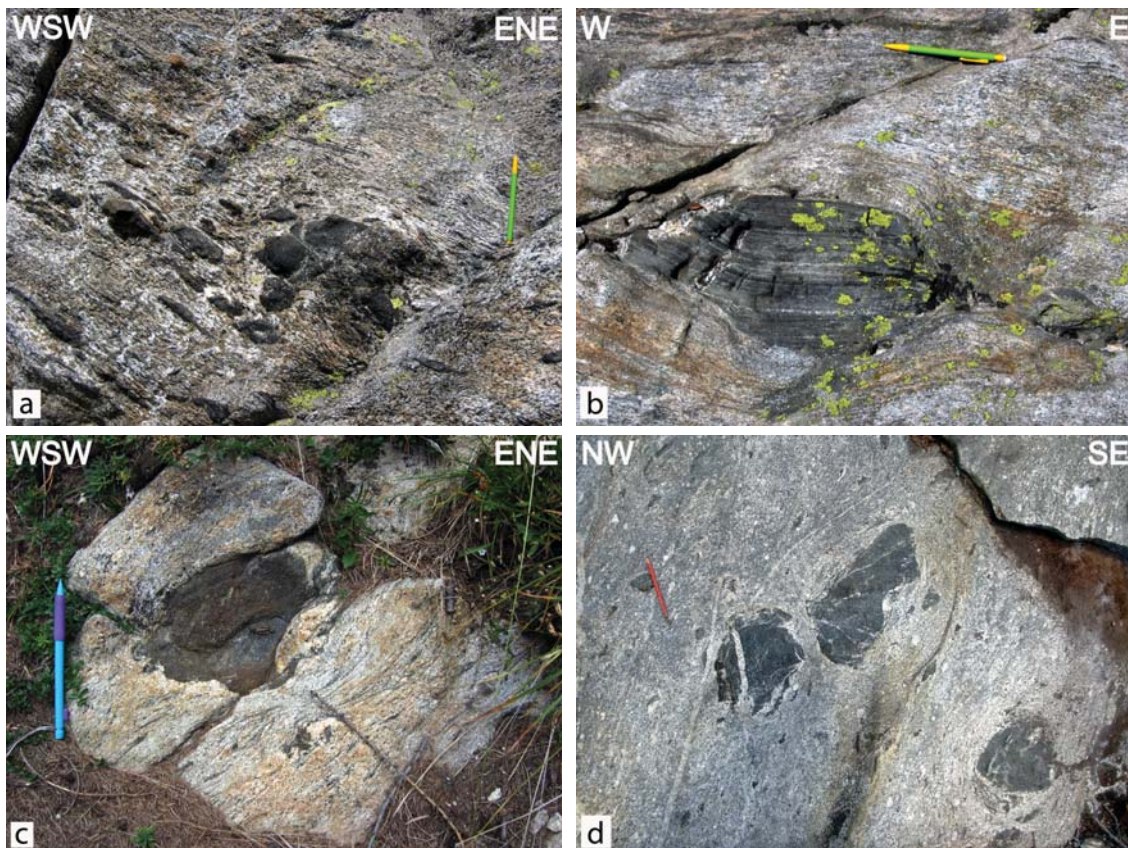
Figure 2.4: *Field aspect of the enclave-rich biotite-orthogneiss. (a) Main field characteristics of the rock are the coarse-grained and slightly deformed texture, the centimetric biotite flakes and the occurrence of decimetric to meteric enclaves (Cantac, 762'556/130'925); (b) basic enclave showing a well developed internal foliation cutted by the less penetrative foliation of the hostrock (Cantac, 761'800/131'140); (c) strain shadow in the enclave-rich biotite-orthogneiss occurring around a massive and rounded basic enclave (Il Mottaccio, 755'172/129'433); (d) massive, rounded to slightly elongated basic enclaves intruded by millimetric to centimetric granitic veinlets (Corno di Droso, 758'153/129'875).*

Microscopic description

Main phases: quartz, plagioclase, alkali feldspar, biotite.
Accessories: muscovite, chlorite, apatite, epidote, titanite, zircon, opaques.

The enclave-rich biotite-orthogneiss, depending on the intensity of the deformation, present an equigranular- to inequigranular-interlobate texture (Fig. 2.5a). Quartz grains are subhedral to anhedral, $\leq$ 1 mm in size, undulose extinguishing and display a weak developed shape prefered orientation. Plagioclase forms subhedral, up to 2.5 mm large, slightly elongated grains. Alkali feldspar is less frequent than quartz and plagioclase and occurs as subhedral, up to 7 mm in size, perthitic grains with a weak shape preferred orientation. Biotite is present as acicular, up to 1 mm large flakes with a moderate preferred orientation which define the weak main foliation of the rock.
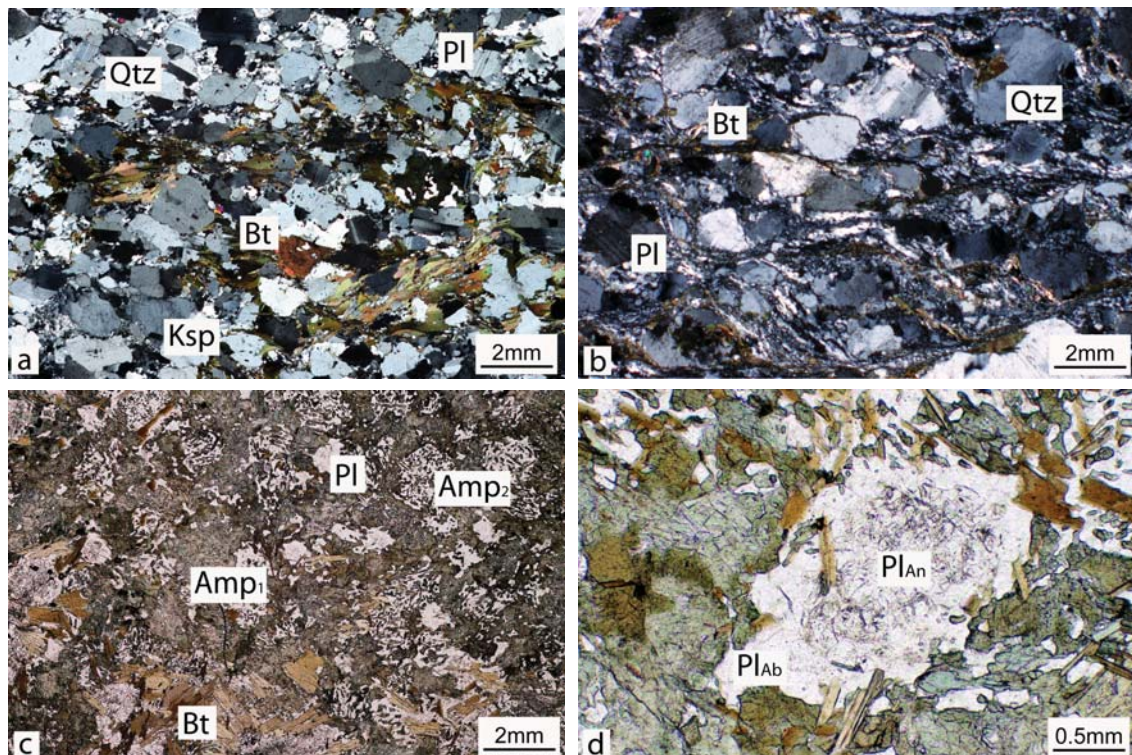
Figure 2.5: *(a) Photomicrograph of the enclave-rich biotite-orthogneiss showing an equigranular-interlobate texture formed by up to 1 mm quartz, plagioclase, rare alkali feldspar and commonly almost unoriented biotite flakes (crossed polarised light); (b) in the northernmost part, the biotite-orthogneiss is marked by a stronger developed fabric, shear bands and dynamic recrystallisation of the main mineral assemblage (crossed polarised light); (c) photomicrograph of a basic enclave, mainly composed of massive, up to 2 mm green amphibole$_1$, unoriented biotite flakes and plagioclase (plane polarised light); (d) rounded aggregate of plagioclase, characterised by anorthite-richer grains with slightly higher relief surrounded by albite-richer grains (plane polarised light).*

Description of the basic enclaves

Main phases: amphibole, plagioclase, biotite.
Accessories: chlorite, apatite, epidote, rutile, titanite.

Enclaves of basic composition are mostly composed of unoriented green amphibole, plagioclase and biotite (Fig. 2.5c). Two different amphibole generations are distinguishable. Coarse-grained, up to 2 mm, optical zoned amphibole$_1$ occurs as subhedral relict grains. A second generation of finer-grained, symplectitic, up to 0.2 mm amphibole$_2$ replaces the rims of amphibole$_1$ or, associated with plagioclase, forms rounded symplectitic aggregates (Fig. 2.5c). Plagioclase is present in the rock matrix as equigranular-interlobate, euhedral to subhedral. Locally, plagioclase forms rounded aggregates marked by anorthite-richer cores surrounded by albite-richer outer coronae (Fig. 2.5d). Biotite occurs as unoriented, poikilitic, up to 2-3 mm, acicular flakes, in rare cases replaced by chlorite. The appearance and textural occurrence of biotite suggests that the original mineral assemblage of the basic enclaves may have react with granitic melts from the host orthogneiss.

2.2.3   Charnockite

Macroscopic description and field occurrence

Charnockite constitute internally boudinaged, sheet-like bodies within the regionally dominant migmatitic biotite-orthogneisses (Fig. 2.6a). Two major, east-west striking, up to 0.5 km thick and 8 km long bodies occur in the core of the Gruf Complex, near the crest between Val Codera and Val Chiavenna. Intermediate size lenses (to 500 m) occur in Val Piana, Valle del Conco, Val Scarione and Val Aurosina.

Charnockite are leucocratic with a strong brownish weathering colour, medium- to coarse-grained, almost undeformed and mostly composed of quartz, plagioclase, alkali feldspar, orthopyroxene, biotite, ilmenite ± garnet and sillimanite. Orthopyroxene is heterogeneously distributed and often almost completely replaced by secondary biotite, amphibole and chlorite. Garnet is usually partly resorbed and displays green coronae of chlorite and biotite (Figs. 2.6b and c).

The internal structure of the charnockitic boudins is characterised by irregular flow structures wrapping around decimetric biotite-rich enclaves and meter-size schlieren (Fig. 2.6b). The schlieren are melanocratic and mainly composed of millimetric garnets and fine-grained biotite. In lower Val Piana, Valle del Conco and upper Val Aurosina, sapphirine-orthopyroxene-garnet-bearing granulitic schlieren occur within the charnockites. A detailed petrographical investigation of the granulites is provided in chapter 4.1.4.

Contacts: the contacts to the host orthogneisses are always delineated by up to 50 cm thick mylonites (Figs. 2.6a, d and e). Commonly, partially mylonitized aplite and pegmatite dykes occur within the mylonitic planes, suggesting that the intrusion of the dykes occurred simultaneously to the shearing.
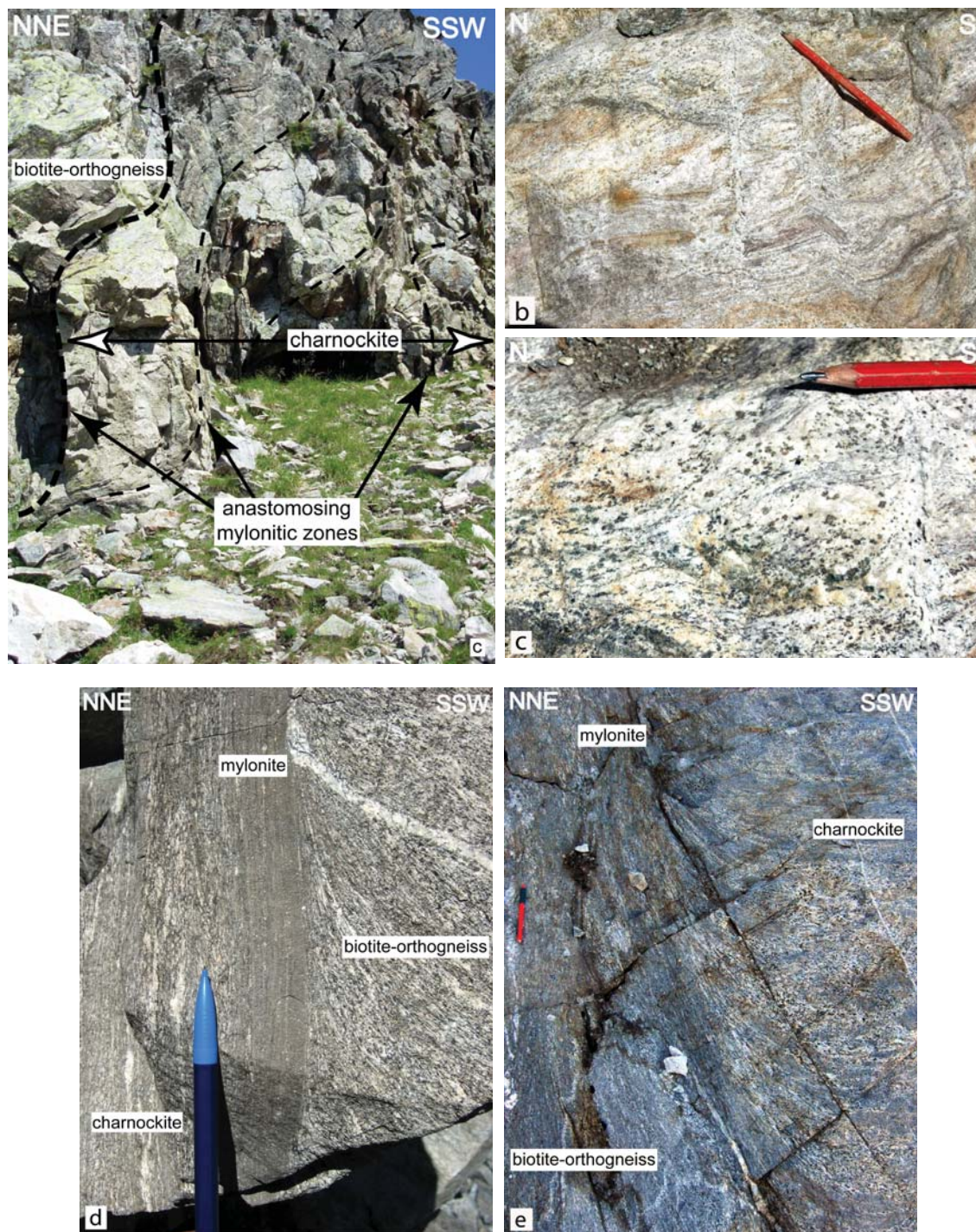
Figure 2.6: *Field aspect of charnockite. (a) Internally boudinaged, sheet-like body of charnockite within migmatitic biotite-orthogneiss. Centimetric thick mylonites occur at the contacts between charnockites and biotite-orthogneiss, bold dashed line, and between charnockitic boudins, thin dashed lines (Cantac, 762'644/130'526); (b) inhomogeneous internal structure of charnockite, marked by magmatic flow structures and numerous, cm-size, melanocratic "schlieren" of biotite and garnet (Cantac, 762'635/130'659); (c) detail of the internal structure of charnockite. Red garnets are commonly surrounded or completely replaced by biotite and chlorite (Cantac, 762'635/130'659); (e-f) detail of the contact between charnockites and migmatitic biotite-orthogneiss, marked by up to 50 cm thick mylonites (Val Aurosina, 758'535/128'617 and Cantacc, 762'724/130426, respectively).*

Microscopic description

Main phases: quartz, plagioclase, alkali feldspar, orthopyroxene, biotite $\pm$ garnet, sillimanite.
Accessories: amphibole, muscovite, chlorite, apatite, epidote, rutile, titanite, zircon, ilmenite.

Charnockite shows an equigranular-interlobate texture formed by quartz, plagioclase and perthitic alkali feldspar. The grains are slightly elongated and, together with rare biotite, define a weakly developed foliation. Garnet occurs as up to 0.5 mm large, rounded, hypidiomorphic porphyroblast with irregular edges. Garnet rims are usually in part replaced by biotite and chlorite. Orthopyroxene occurs as up to 0.5 mm, hypidiomorphic porphyroblasts (Fig. 2.7a). Generally, orthopyroxene are partly replaced by coronae of biotite, amphibole and ilmenite (Figs. 2.7b and c) or completely substituted by symplectitic aggregates of biotite and quartz (Fig 2.7d). Biotite occurs in three textural types: $biotite_1$ is present in the matrix as rare, slightly oriented, up to 0.5 mm large flakes. $Biotite_2$ grows at the expense of garnet or, together with amphibole and ilmenite, surrounding orthopyroxene. $Biotite_3$, together with quartz, replaces orthopyroxene porphyroblasts (Fig. 2.7d). Amphibole is texturally late and occurs exclusively replacing orthopyroxene.
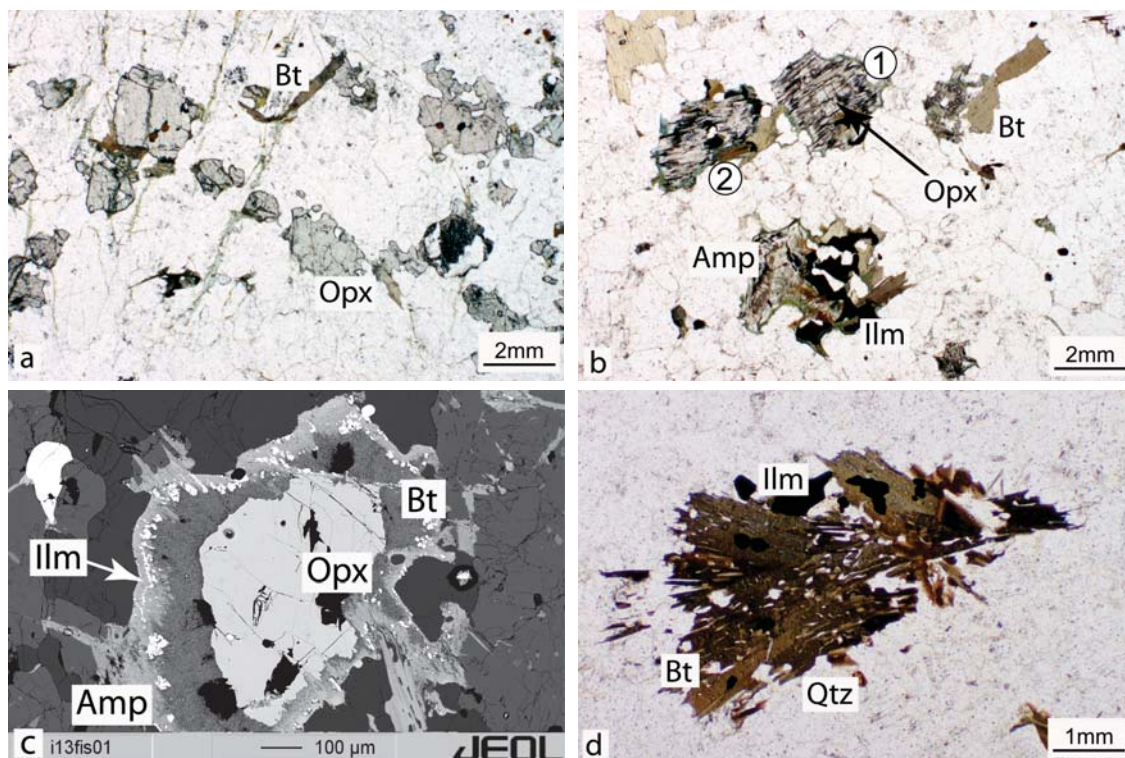
Figure 2.7: *(a) Orthopyroxene in a leucocratic matrix of quartz, plagioclase, alkali feldspar and rare biotite (plane polarised light); (b) orthopyroxene grains display different degrees of retrogression. 1: relict orthopyroxene with amphibole-biotite$_2$-ilmenite coronae; 2: amphibole-biotite$_2$-ilmenite pseudomorph after orthopyroxene (plane polarised light); (c) back-scatter image of an amphibole-biotite$_2$-ilmenite corona mantling orthopyroxene; (d) orthopyroxene replaced by symplectitic aggregates of biotite$_3$ and quartz (plane polarised light).*

2.2.4 Websterite to gabbronorite

Macroscopic description and field occurrence

Between Motto dell'Orso and Trubinasca, up to 50 m large lenses of websterite to gabbronorite occur within migmatitic biotite-orthogneisses, often associated with charnockites. Websterite to gabbronorite display a greenish-brownish colour of alteration, are massive, middle- to coarse-grained and composed of clinopyroxene, minor orthopyroxene, biotite and variable amount of plagioclase (Fig. 2.8a).

Figure 2.8: *Field aspect of websterite. (a) Greenish lense of websterite intruded by leucocratic veinlets of granitic composition (Val Deserto, 758'643/127'405); (b) websterite lense intruded by pegmatitic dykes (Valle dei Vanni, 763'283/130'461); (c) intrusive relation between websterite and migmatitic biotite-orthogneiss (Motto dell'Orso, 753'244/126'636); (d) brecciated lense of websterite with granitic matrix (Valle dei Vanni, 763'283/130'461).*

Contacts: the contacts to the enclosing orthogneisses are prevalently intrusive (Figs. 2.8a and c). Leucosomes from the host migmatites intrude and brecciate the margin of the websterite to gabbronorite lenses (Figs. 2.8a-d).

Microscopic description

Main phases: clinopyroxene, orthopyroxene, biotite, plagioclase, green amphibole.
Accessories: talc, chlorite, rutile, titanite, opaque.

Fresh websterite to gabbronorite display an equigranular texture dominated by clinopyroxene and less abundant orthopyroxene (Fig. 2.9a). Clinopyroxene is present as euhedral to subhedral, up to 1 mm large grains. Orthopyroxene occurs as slightly porphyritic grains with numerous tiny inclusions of plagioclase and biotite (Fig.2.9b). Up to 0.5 mm large, polygonal plagioclase and biotite are interstitial and in textural equilibrium with both pyroxenes (Fig. 2.9b). The amount of plagioclase varies from sample to sample. In the strongly altered websterites to gabbronorites clinopyroxene and orthopyroxene are typically replaced by slightly elongated, centimetric, poikilitic green amphibole and aggregates of fine-grained talc, respectively (Figs. 2.9c and d).
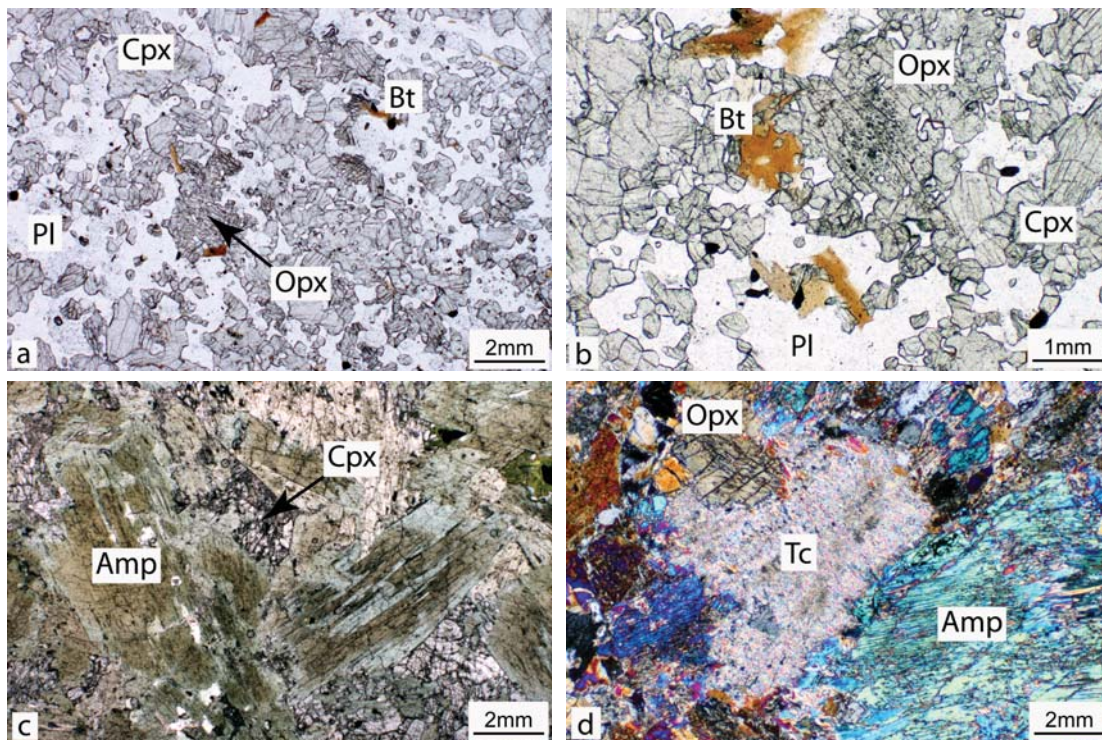
Figure 2.9: *Photomicrographs of websterite to gabbronorite. (a) Equigranular, polygonal texture formed by clinopyroxene and orthopyroxene porphyroblasts and interstitial plagioclase and biotite; (b) orthopyroxene rich of inclusions in contact with interstitial biotite; (c) relict clinopyroxene replaced by optical zoned amphibole; (d) orthopyroxene replaced by fine-grained aggregates of talc.*

Migmatitic metasediments and rock types contained therein

2.2.5   Migmatitic paragneiss and micaschist

Macroscopic description and field occurrence

Metasediments consist of partially molten paragneisses and micaschists. Gradational boundaries between these two lithologies suggest alternating pelitic and psammitic layers. These rocks have a brown weathering colour and occur along two major, east-west oriented, up to 10 km long and about 1 km thick zones, one between Casello Allaio and the southwestern part of Val Casnaggina, and the other along the northern flank of Val Codera. Smaller lenses (up to 1 km in length) are exposed around Bivacco Vaninetti, in the upper part of Val Averta and along the northern contact of the Gruf Complex, between the enclave-rich biotite-orthogneiss and the Chiavenna Unit.

Garnet- and garnet-cordierite-bearing sillimanite-biotite schist (Fig. 2.10a) predominate and alternate with less frequent, quartz- and plagioclase-rich garnet-bearing paragneiss and fine-grained bands of garnet- and sillimanite-free biotite schists. Around Bivacco Vaninetti, in proximity of the contact with the Bergell Pluton, migmatitic micaschists bear rare relic corundum grains.
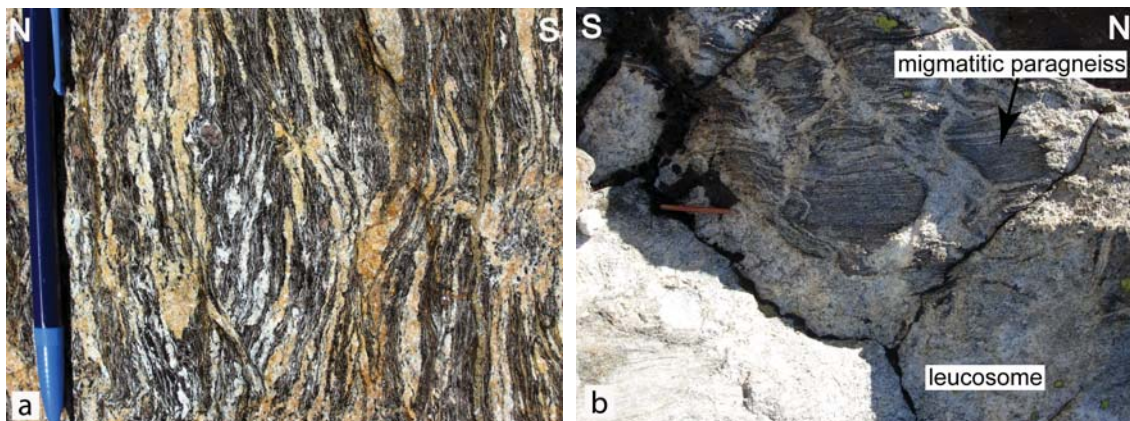
Figure 2.10: *(a) Field appearance of a garnet-bearing sillimanite-biotite schist, characterised by leucocratic bands of quartz and feldspars alternated to melanocratic bands of biotite and sillimanite (Alpesella, 758'458/129'444); (b) intense partial melting of a garnet-bearing paragneiss, causing the migration and collection of leucosomes in discordant dykes and pockets (Alpe Rossaccio, 758'872/129'928).*

Both paragneisses and micaschists are characterised by a migmatitic banding of millimetric to centimetric, leucocratic, granoblastic layers of quartz, plagioclase $\pm$ alkali feldspar $\pm$ cordierite (leucosomes) and millimetric, melanocratic lepidoblastic bands of mainly biotite, fibrolitic sillimanite, rare muscovite, garnet and quartz $\pm$ plagioclase $\pm$ corundum which represent the residual melanosome to mesosome (Figs. 2.10a). Generally, leucosomes are parallel to the main foliation (Fig. 2.10a). However, where the degree of partial melting is stronger, leucosomes migrate discordantly to the main foliation and collect in meter-sized dykes and pockets (Fig. 2.10b).

Contacts: contacts between migmatitic metasediments and both the biotite-orthogneiss and enclave-rich biotite-orthogneiss are sharp and marked by centimetric to decimetric mylonites. Exclusively

north by Bivacco Vaninetti, the leucosomes from the migmatitic biotite-orthogneiss intrude discordantly the base of a large (up to 1 km in length) lense of migmatitic metasediments (Fig. J.1). The contact to the leucogranite is generally discordant (intrusive) or characterised by the progressive increase of the amount of leucosomes within the metasediments towards the leucogranites. Only in few cases, centimetric mylonites separate these two rock types.
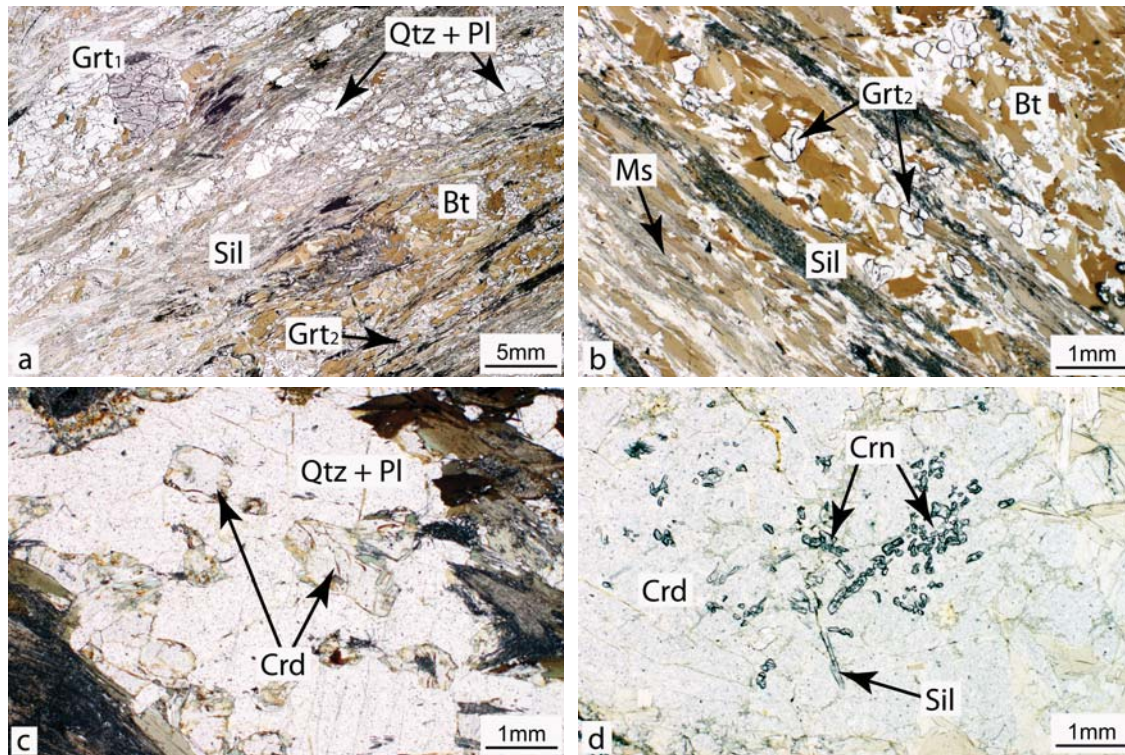
Figure 2.11: *Photomicrographs of migmatitic paragneiss and micaschist. (a) Alternance of millimetric granoblastic bands of quartz and plagioclase and lepidoblastic bands of biotite and fibrolitic sillimanite. Large, pre-kinematic garnet₁ shows an inclusion-rich core and an inclusion-free rim (plane polarised light); (b) Post-kinematic, millimetric garnet₂ overgrow the main foliation composed of oriented biotite flakes, fibrolitic sillimanite and rare muscovite grains (plane polarised light); (c) subhedral cordierite grains within granoblastic bands of quartz and feldspars distinguishible from the slightly higher relief and alteration to fine-grained whita mica (plane polarised light); (d) relictic corundum and sillimanite grains embayed in polygonal aggregate of cordierite (plane polarised light).*

Microscopic description

Main phases: quartz, plagioclase, biotite, sillimanite, garnet, ± cordierite, alkali feldspar, corundum.

Accessories: muscovite, chlorite, apatite, epidote, titanite, zircon, opaques.

In leucosomes, quartz grains are slightly elongated, subhedral, up to 2 mm large, with undulose extinction. Plagioclase forms subhedral to anhedral, up to 2 mm large grains. Alkali feldspar constitutes subhedral, up to 2.5 mm large, perthitic grains. Myrmekite is frequent along alkali feldspar-plagioclase grain boundaries. Cordierite forms subhedral, rounded, up to 1 mm large

grains (Fig. 2.11c). In the melano- to mesosomes, elongated and oriented, up to 2 mm large biotite flakes form aggregates that define the main foliation together with fibrolitic sillimanite and rare, up to 0.5 mm large muscovite flakes (Fig. 2.11b). Garnet occupies two texturally different sites. $Garnet_1$ forms centimetric, pre-kinematic porphyroblasts deflecting the main foliation and is associated with pressure fringes. $Garnet_1$ displays an equant and subhedral habitus and generally has inclusion-rich cores and inclusion-free rims. $Garnet_2$ forms up to 1 mm, post-kinematic, rounded and subhedral grains overgrowing the main foliation (Fig. 2.11b). Quartz is rare as subhedral, 0.1 mm large grains. Plagioclase forms, poikilitic, centimetric porphyroblasts overgrowing biotite, garnet, quartz and muscovite; it is therefore post-kinematic. Corundum forms agrregates of millimetric, relictic grains, related to sillimanite and surrounded by polygonal cordierite (Fig. 2.11d).

2.2.6   Leucogranite

Macroscopic description and field occurrence

Leucogranites are spatially associated with the migmatitic paragneisses and micaschists (Fig. 2.12a) and occur in two major zones, one located between San Cassiano and Baita di Garzone, and the other between Somaggia and Valle del Conco. In both areas, the thickness of leucogranites strongly decreases towards the east. Smaller bodies of leucogranite (up to 100 m in size) occur in the upper parts of Val Beleniga, Val Piana, Val Averta and around Bivacco Vaninetti.

Leucogranite is mainly composed of quartz, plagioclase, alkali feldspar, muscovite and biotite ± garnet and sillimanite. The rock is massive to slightly foliated, fine- to coarse-grained and contains cm- up to meter-size, biotite-rich, residual enclaves and "schlieren" of pelitic and, less frequent, basic and ultramafic composition (Figs. 2.13a and b).

Figure 2.12:   *Field relation between leucogranites and migmatitic metasediments, showing the irregular occurrence of discordant leucogranites within the migmatitic paragneiss and micaschist (east of Bivacco Vaninetti).*

Contacts: the contacts to the migmatitic paragneisses and micaschists are intrusive, irregular and sharp (Fig. 2.13c). Conversely, the contacts to the migmatitic biotite-orthogneiss are diffuse and marked by the progressive disappearance of biotite and the simultaneous appearance of both muscovite and millimetric garnets.
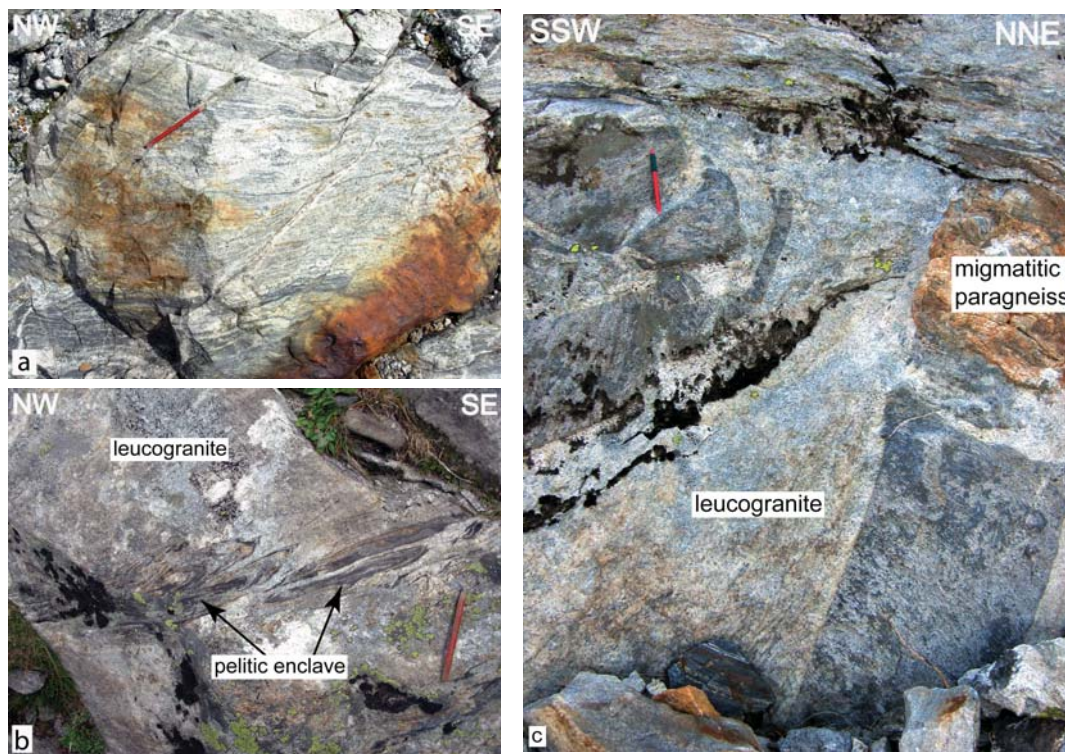
Figure 2.13: *(a) Field appearance of a slightly foliated leucogranite with centimetric, biotite-rich schlieren (Bivacco Vaninetti, 764'349/129'114); (b) deformed enclaves of pelitic composition within leucogranite (Val Schiesone, 755'919/128'394); (c) intrusive relation between leucogranite and migmatitic metasediments (Alpe Rossaccio, 758'823/129'870).*

Microscopic description

Main phases: quartz, plagioclase, alkali feldspar, biotite, muscovite $\pm$ garnet, sillimanite.
Accessories: apatite, chlorite, titanite, rutile, ilmenite, zircon.

The almost undeformed domains of the leucogranite are fine-grained and display an equigranular-interlobate texture characterised by rounded, subhedral to anhedral, up to 0.2 mm large quartz, plagioclase and perthitic alkali feldspar (Fig. 2.14a). In contrast, the moderate foliated domains are more inequigranular and constituted of slightly elongated quartz, plagioclase and alkali feldspar grains with variable grain-size (Fig. 2.14b). Biotite forms elongated, up to 1 mm large flakes with a weak shape preferred orientation. Muscovite occurs in two generations. Muscovite$_1$ forms part of the matrix and occurs as elongated, up to 1.5 mm long, acicular flakes, preferentially concentrated in the sillimanite-free and garnet-poorer domains. Together with biotite, muscovite$_1$ defines the main rock foliation. Muscovite$_2$ is present exclusively as corona mantling sillimanite (Fig. 2.14d). Garnet occurs as rounded, xenomorphic, up to 0.3 mm large grains and is more abundant in the finer-grained leucogranite, in particular between Monte Matoldo and Corna di Garzone (Fig. 2.14c). Sillimanite forms prismatic, up to 1 mm long grains within the main foliation. Generally, sillimanite is partly replaced by coronae of fine-grained muscovite$_2$ (Fig. 2.14d).

30
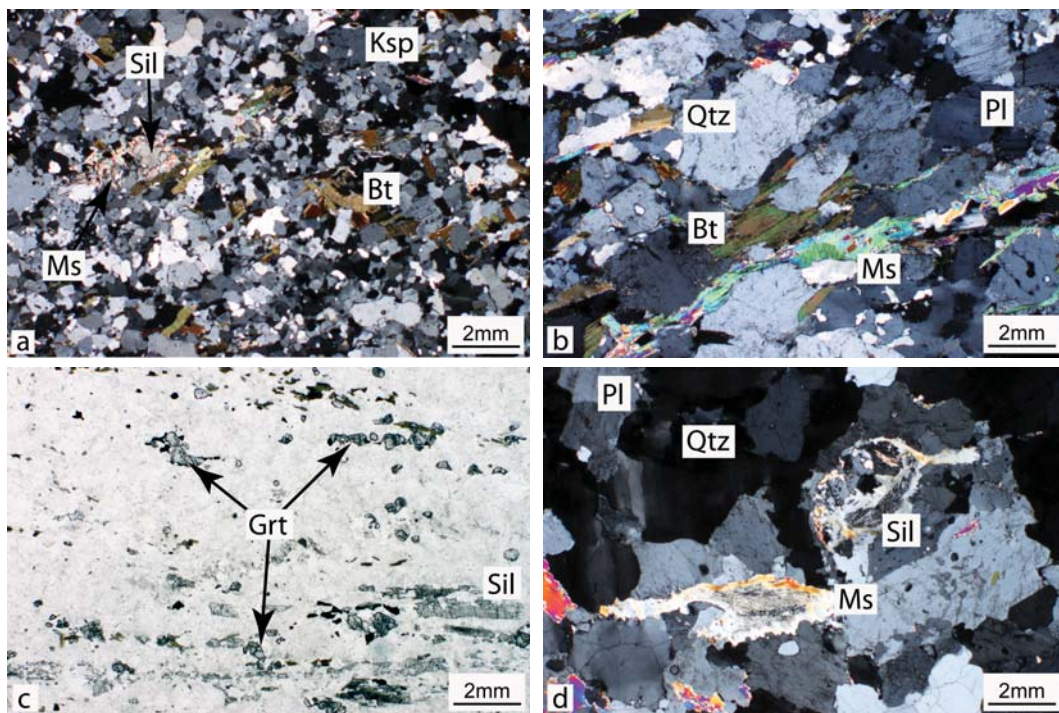
Figure 2.14: *(a) Fine-grained, undeformed sil-grt-bearing leucogranite with equigranular-interlobate texture defined by quartz, plagioclase and alkali feldspar (crossed polarised light); (b) slightly foliated, coarse-grained muscovite-bearing leucogranite, marked by elongated and oriented muscovite and biotite flakes (crossed polarised light); (c) garnet-rich leucogranite occurring between Monte Matoldo and Corna di Garzone (plane polarised light); (d) muscovite$_2$ coronae surrounding sillimanite (crossed polarised light).*

2.2.7   Augengneiss

Macroscopic description and field occurrence

The augengneiss occurs exclusively as up to 20 m thick granitoid sheet intercalated within the migmatitic paragneisses and micaschists at Bivacco Vaninetti (see detail map on Fig. J.1) and on the western flank of Cima di Droso. This rock is coarse-grained, grossly foliated, constituted of quartz, plagioclase, alkali feldspar, biotite and muscovite and characterised by cm-size "augen" of quartz and alkali feldspar (Fig. 2.15a). Biotite-free, leucocratic veinlets mainly composed of quartz and feldspars cut across the main foliation or concentrate in centimetric ductile shear zones, suggesting that partial melting of the Augengneiss occurred contemporaneously with the deformation (Fig. 2.15b).

Contacts: Augengneisses display sharp, discordant, intrusive contacts to the host migmatitic metasediments (Fig. 2.15a).
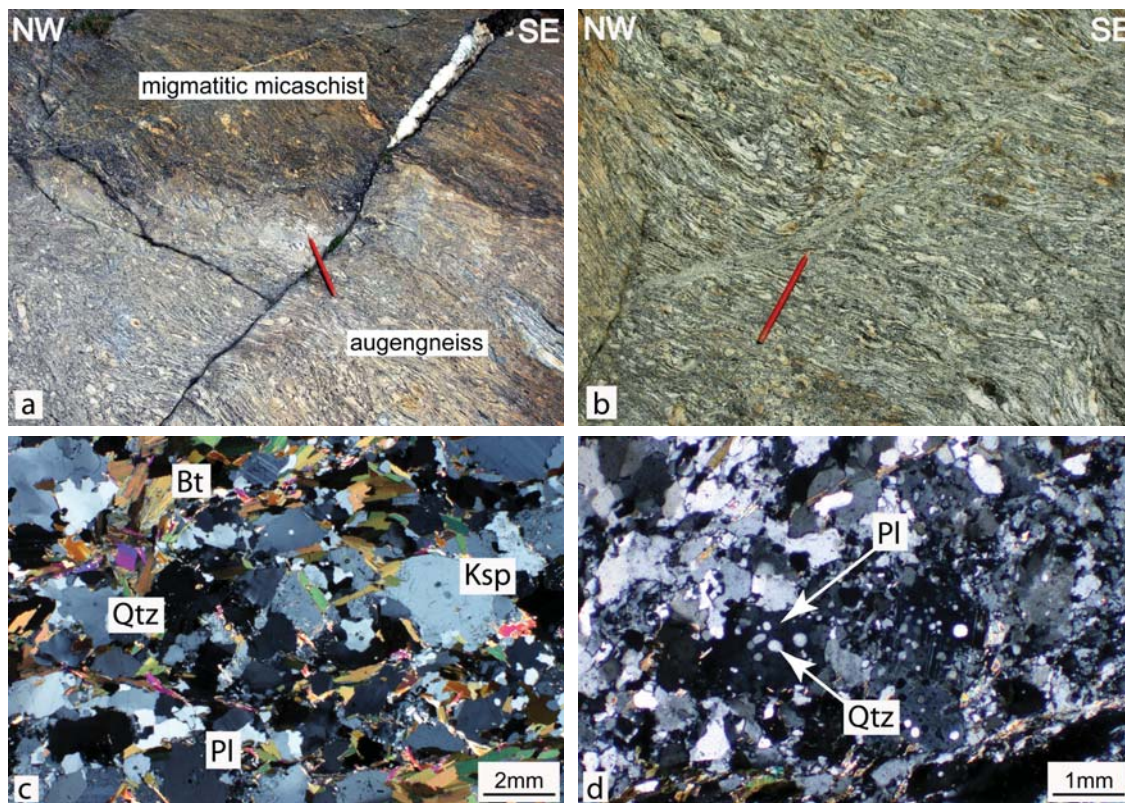
Figure 2.15: *(a) Primary intrusive relationship between augengneiss and migmatitic metasediments (Bivacco Vaninetti, 763'960/129'377); (b) leucocratic veinlets, interpreted as product of partial melting, collected within a ductile shear zone, suggesting that migmatization occurred during deformation (Bivacco Vaninetti, 763'960/129'377); (c) Photomicrograph of the augengneiss showing the coarse-grained and almost undeformed texture formed by equigranular-interlobate aggregates of quartz, plagioclase, alkali feldspar and unoriented biotite flakes (crossed polarised light); (b) detail of a leucocratic, biotite-free domain (crossed polarised light).*

Microscopic description

Main phases: quartz, plagioclase, alkali feldspar, biotite, muscovite.
Accessories: muscovite, chlorite, apatite, rutile, titanite, ilmenite, zircon.

Augengneiss displays an equigranular-interlobate texture constituted by quartz, plagioclase and alkali feldspar (Fig. 2.15c). Quartz forms subhedral, up to 2 mm large, undulose extinguishing grains. Plagioclase occurs as subhedral to anhedral, up to 1.5 mm large grains usually partly replaced by fine-grained muscovite. Perthitic alkali feldspar is present as subhedral to anhedral, up to 2 mm large grain. Both biotite and muscovite occur as unoriented, up to 1 mm, elongated flakes. The discordant leucocratic, biotite-free domains are constituted of fine-grained, inequigranular-interlobate quartz, plagioclase and alkali feldspar. Commonly, plagioclase contains numerous, fine-grained, rounded inclusions of quartz (Fig. 2.15d). The occurrence of millimetric pools of melt developed and crystallised to a micrographic intergrowth of quartz and alkali feldspar and thin films of anatectic melt on some grain boundaries prove that the rocks underwent partial melting.

Lithological units contained both in the metagranitoids and metasediments

2.2.8 Chlorite-spinel-enstatite-olivine fels (metaperidotites)

Macroscopic description and field occurrence

Up to 500 m large lenses of chlorite-spinel-enstatite-olivine fels often associated to amphibolite occur between Bivacco Vaninetti and Alpe Sivigia, south of Alpe Spluga and between Val Piana and Valle del Conco within migmatitic metasediments and leucogranites (Fig. 2.16a). Smaller lenses (up to 5 m in size) of the same rock type occur in Val Piana, at Alpesella and at the basis of Valle dell'Orco as clusters of enclaves within the migmatitic biotite-orthogneiss (Fig. 2.16b and Fig. 2.17d). Discontinous bands of metaperidotites, together with amphibolites, calcsilicates and migmatitic paragneisses and micaschists, occur also within the Bergell Tonalite along the contact with Gruf Complex.
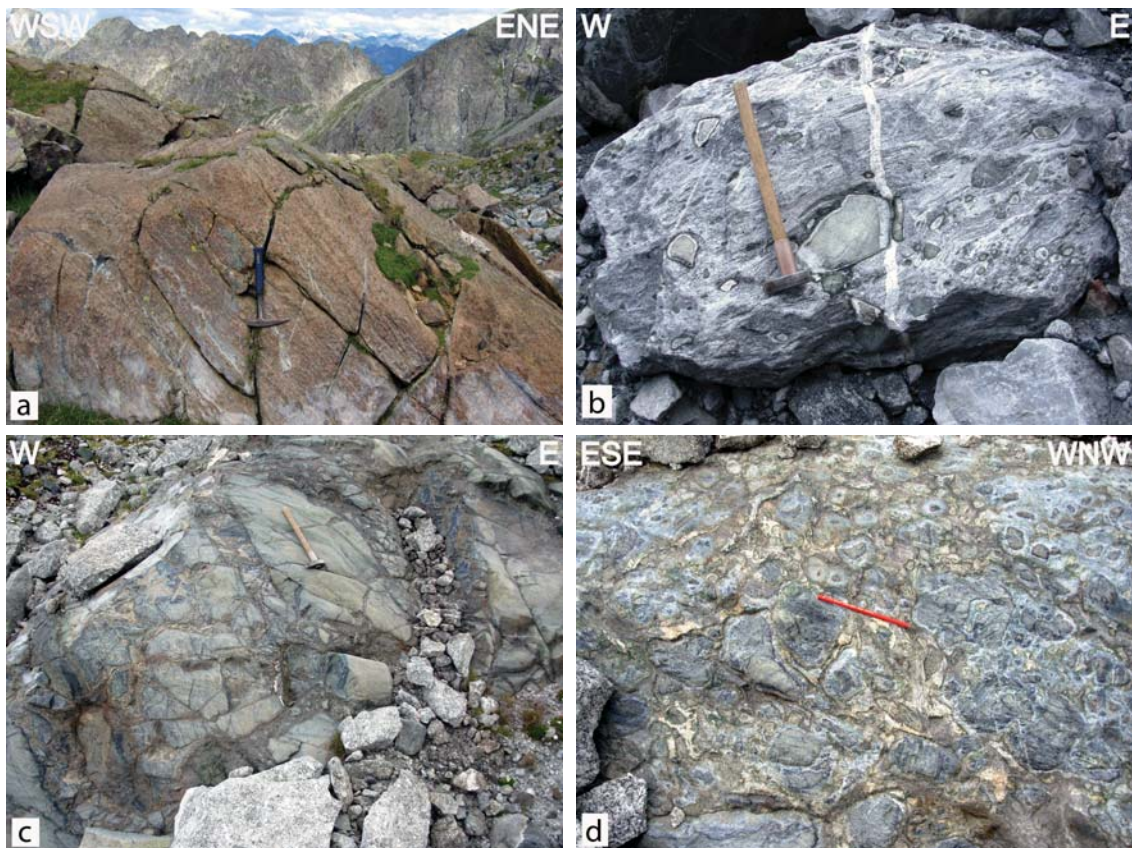
Figure 2.16: *(a) Field aspect of the metaperidotites, characterised by the alternance of lherzolitic and dunitic layers and the strong orange-brownish colour of alteration (Bivacco Vaninetti, 763'915/129'362); (b) block of migmatitic biotite-orthogneiss enclosing a partly altereted metaperidotite enclave (Val Salubiasca); (c) rim of a metaperidotite lense brecciated by leucosomes from the migmatitic biotite-orthogneiss (Bivacco Vaninetti, 764'188/129'078); (d) leucosome intruding and brecciating the rim of a metaperidotite lense (Bivacco Vaninetti, 764'265/129'082).*

The chlorite-spinel-enstatite-olivine fels weathers to an intense orange-brownish colour and exhibits alternating and sometimes isoclinally folded lherzolite, dunite, pyroxenite and chromite layers (Fig. 2.16a and Figs. 2.17a and b). Metaperidotites display a well developed foliation mostly defined by oriented enstatite. This foliation overgrows the compositional banding and is generally not parallel to the regional foliation. Within the large ultramafic lenses around Bivacco Vaninetti, several meter-thick metarodingite and ferrogabbro dykes are discordant to the banding in the metaperidotites (section 2.2.9), whereas numerous light greyish veins of talc, chlorite and rare titano-clinohumite generlly cut across the main foliation (Figs. 2.17b and c).
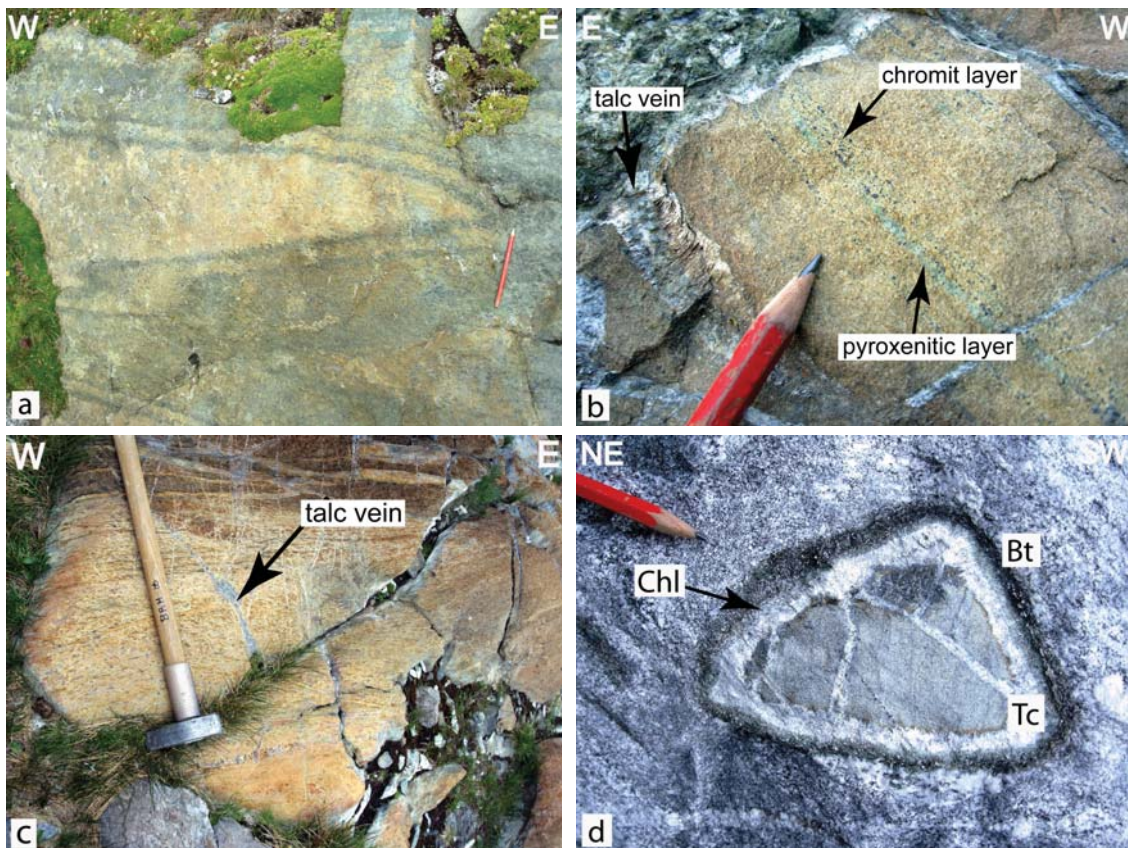
Figure 2.17: *(a) Isoclinally folded primary layering of dunitic, lherzolitic and chromitic composition (Bivacco Vaninetti, 764'045/129'117); (b) millimetric layers of chromitic and pyroxenitic composition and talc vein within a chlorite-spinel-enstatite-olivine fels (southern of Alpe Spluga, 760'342/129'718); (C) centimetric veins of talc and chlorite cutting the main foliation marked by aligned orthopyroxene crystals within the chlorite-spinel-enstatite-olivine fels (Bivacco Vaninetti, 763'940/129'339); (d) ultramafic enclave within migmatitic biotite-orthogneiss showing composite metasomatic rims of talc, chlorite and biotite (Val Salubiasca, 759'479/124'986).*

Contacts: contacts to the migmatitic metasediments are concordant and sub-mylonitic. In contrast, leucosomes from the biotite-orthogneisses are intrusive, with decimetric leucocratic veins intruding fractures at the rim of ultramafic lenses and related metabasic rocks (4 and 5 in Fig. 2.29). Different brecciation stages are observed: i) angular, up to 1.5 m large, still matching together blocks separated by centimeters thin, granitic veins (4 in Fig. 2.29); ii) more disconnected,

centimetric up to decimetric, rounded enclaves separated by up to 20-30 cm thick leucosomes (5 in Fig. 2.29) and iii) isolated, sub-ellipsoidal enclaves within the migmatitic biotite-orthogneisses (Fig. 2.16b and 6 in Fig. 2.29) and iv) swarm of enclaves embedded and brecciated by the migmatitic biotite-orthogneiss, particularly concentrated close to Alpe Sivigia, in the so-called Sivigia-Zug. In general, ultramafic and basic components of the breccias develop polymineralic reaction rims of talc-chlorite-actinolite-hornblende-biotite and green amphibole (Fig. 2.17d), respectively, while the granitic matrix displays centimetric crystals of labradorite in the vicinity of these enclaves.
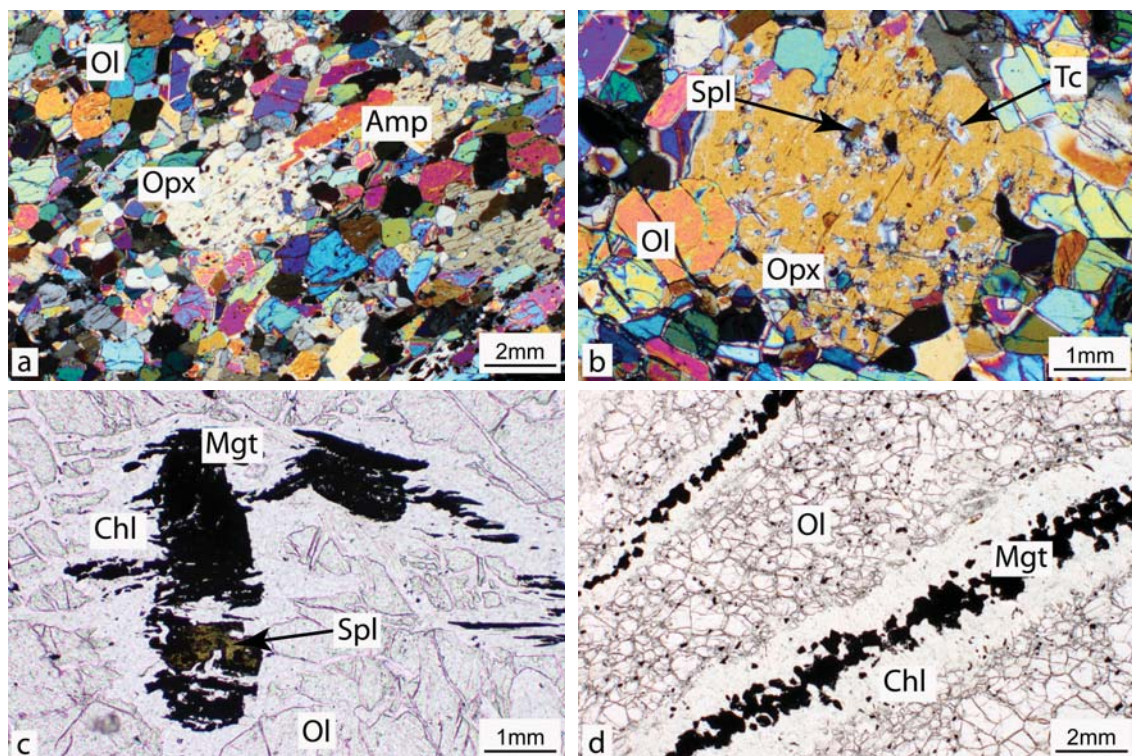
Figure 2.18: *(a) Equigranular, polygonal groundmass formed by olivine, enstatite porphyroblasts, elongated amphibole and rare chlorite (crossed polarised light); (b) inclusion-rich enstatite porphyroblast (crossed polarised light); (c) lamellar aggregate of magnetite and spinel surrounded by chlorite (plane polarised light); (d) magnetite-chlorite veins crosscutting the polygonal groundmass (plane polarised light).*

Microscopic description

Main phases: olivine, orthopyroxene, spinel, chlorite, tremolite, talc, serpentine.
Accessories: magnetite.

The rock has an equigranular, neoblastic texture constituted of olivine and less frequent orthopyroxene, amphibole and chlorite (Fig. 2.18a). Grain boundaries are generally straight, suggesting textural equilibrium. Olivine occurs as anhedral, up to 0.2 mm large grains, often prtly replaced by aggregates of acicular serpentine. Enstatite forms elongated, up to 2 mm long por-

phyroblasts showing undulose extinction and a slightly preferred shape orientation. Generally, enstatite contains many tiny inclusions of talc, spinel and magnetite (Fig. 2.18b) and may be replaced by fine-grained talc. Up to 0.4 mm long elongate chlorite and amphibole are parallel to the main foliation (Fig. 2.18a). Spinel is present in greenish to brownish, fine ($\pm$ 0.1 mm), rounded grains or as green spinel-magnetite lamellar aggregates surrounded by chlorite (Fig. 2.18c). Chlorite-magnetite veins cut across the main foliation (Fig. 2.18d).

2.2.9 Metarodingite

Macroscopic description and field occurrence

Metarodingites occur exclusively as up to 1.5-2 m thick dykes within two large ultramafic lenses around Bivacco Vaninetti (see detail map, Fig. J.1), discordant to the banding in the metaperidotites. The cores of metarodingite dykes are fine-grained, undeformed and mostly composed of pinkish garnet, epidote, clinopyroxene, hornblende and titanite. The rims of the dykes are darker and constituted of black amphibole, diopside and spinel. At the contact to the host metaperidotites, the dykes display greenish reaction rims mainly composed of actinolite, while the ultramafic rocks are rich in talc. These metarodingite dykes are similar to metarodingite dykes described from the Chiavenna Unit (Talerico, 2000) and show that ultramafic host metaperidotites underwent an oceanic stage during their evolution.
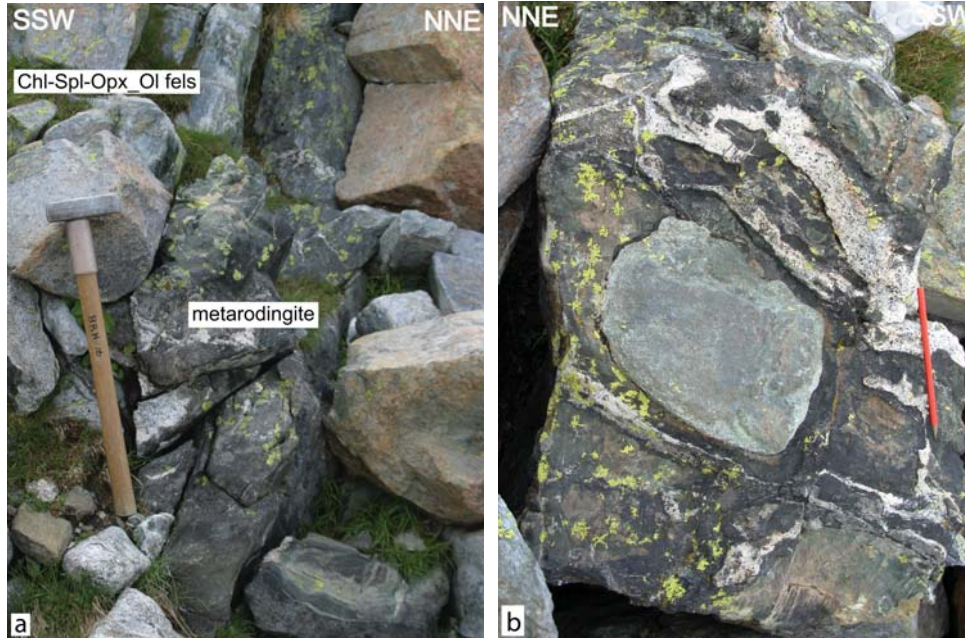
Figure 2.19: *(a) About 50 cm thick metarodingite dyke cut across compositional banding of metaperidotites (Bivacco Vaninetti, 764'039/129'190); (b) detail of metarodingitic dyke, showing a lighter core mostly constituted of diopside, epidote and garnet and a darker margin (black wall) of dark amphibole, diopside and spinel (Bivacco Vaninetti, 763'944/129'330).*

2.2.10   Amphibolite

Macroscopic description and field occurrence

Regularly boudinaged, up to 20 m thick bands of amphibolite usually associated to metaperidotite lenses occur within migmatitic paragneisses and micaschists around Bivacco Vaninetti, between Val Piana and Valle del Conco, southern of Alpe Spluga and Alpe Rossaccio, by Corno di Droso and all along the contact between the Gruf Complex and the Bergell Tonalite. Isolated enclaves (up to 1 m large) or groups of enclaves occur within the migmatitic biotite-orthogneiss, particularly concentrated in the northernmost part of the Gruf Complex (description in section 2.2.2).

Amphibolite is fine-grained, foliated and mostly composed of black/dark green amphibole, plagioclase, biotite $\pm$ clinopyroxene. Locally, amphibolites display centimetric, discordant and amphibole-bearing pockets of leucosome (Fig. 2.20a). Texturally, these leucosomes appear to be derived from the amphibolites, suggesting in-situ partial melting of the latter. These leucosomes are in sharp contrast to granitic/sediment derived leucosomes which never bear amphibole. Due to their inaccessibility, scarceness and maximal thickness of 2 cm, they have not been analysed and a geochemical verification of their probably trondhjemitic character has been left open.

Contacts: the contacts to the country rocks are generally sharp and marked by centimetric ($\leq$ 5cm) mylonites. Where the host rock is strong migmatitic, as for example close to the contact with the Bergell Tonalite at Bivacco Vaninetti, the contacts are more irregular. In this case, leucosomes from migmatitic metasediments cut across the amphibolite bands, isolating amphibolite enclaves in leucosomes (Fig. 2.20b).
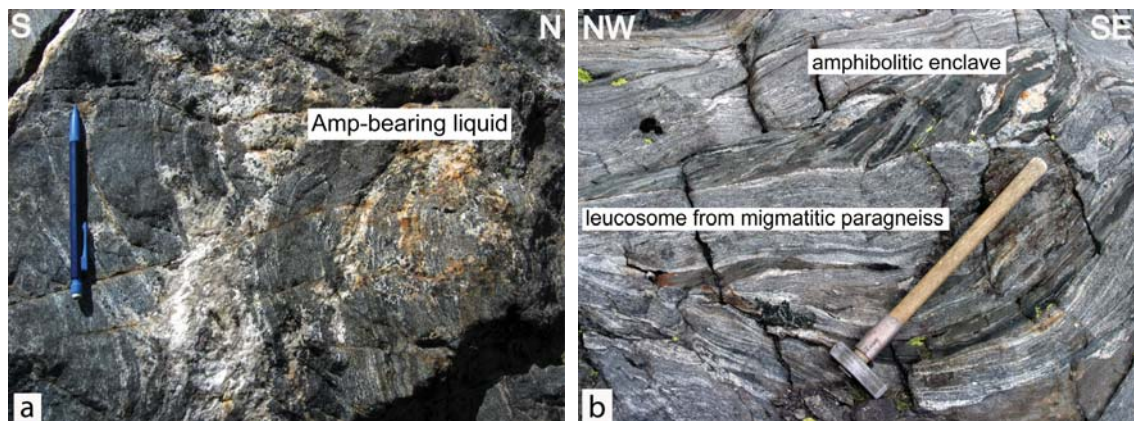
Figure 2.20: *Field aspect of amphibolite. (a) Dark amphibolite crosscutted by undeformed, leucocratic veinlets, probably originated by in-situ partial melting (southern of Alpe Spluga, 760'342/129'718); (b) isolated, internally foliated amphibolite enclaves crosscutted by leucosomes from strongly migmatitic metasediments (Bivacco Vaninetti, 764'045/129'117).*

Microscopic description

Main phases: amphibole, plagioclase, biotite, clinopyroxene.
Accessories: chlorite, titanite, rutile, opaques.

Amphibolite displays a nemoblastic, equigranular texture formed by green amphibole and plagioclase (Fig. 2.21a). Elongated, millimetric amphibole is the most abundant phase of the rock. Amphibole grains show a well developed preferred orientation and define the main foliation. Plagioclase occurs as equigranular, euhedral, up to 0.1 mm large grains which form polygonal aggregates (Fig. 2.21a). Biotite is present as rare elongated flakes oriented parallel to the main foliation. Biotite is usually more abundant at the contacts between amphibolite and leucocratic veinlets (Fig. 2.21c). Exclusively in rare samples from Alpe Spluga, millimetric, subhedral clinopyroxene grains surrounded by brownish amphibole occur (Fig. 2.21b).

Leucocratic veinlets are equigranular-euhedral and mostly constituted of quartz, plagioclase, biotite and amphibole (Fig. 2.21d). These veinlets display a weak foliation defined by slightly elongated quartz and plagioclase grains and orientd biotite and amphibole .
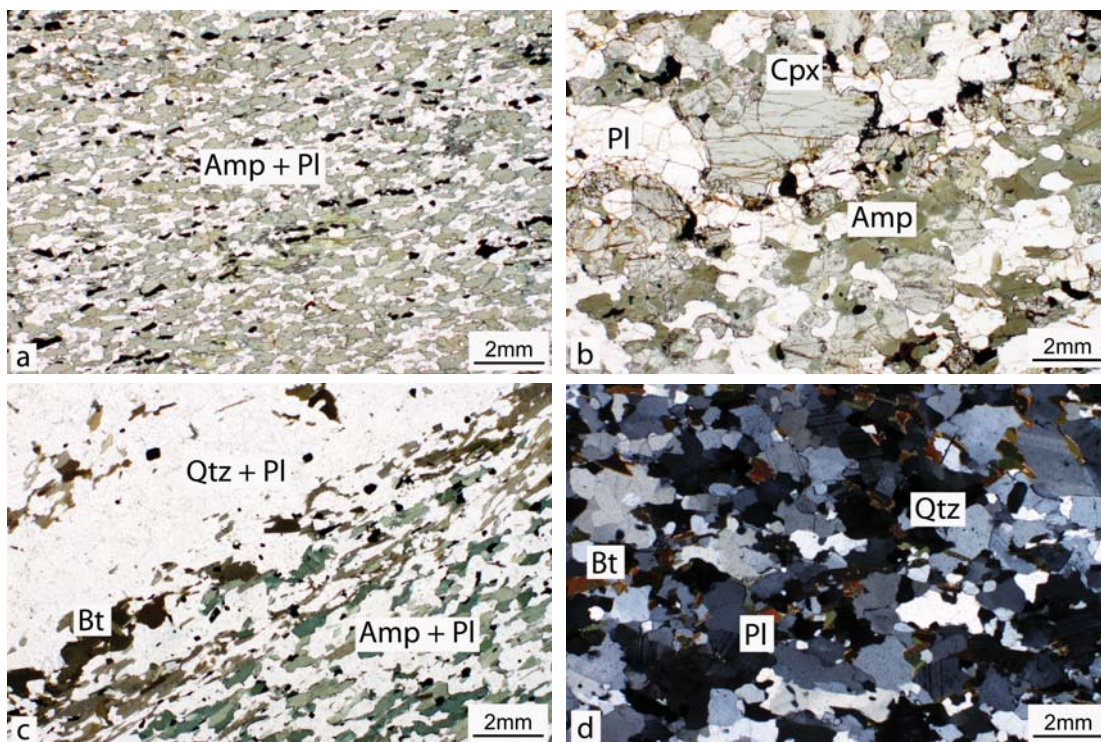
Figure 2.21: *Photomicrographs of amphibolite and leucocratic veinlets. (a) In the amphibolites, amphibole and plagioclase define a nemoblastic equigranular texture. The preferred shape orientation of amphibole outlines a well developed foliation (plane polarised light); (b) clinopyroxene relics surrounded by amphibole (plane polarised light); (c) detail of the contact between amphibolite and leucocratic veinlets, marked by slightly oriented biotite flakes (plane polarised light); (d) equigranular-euhedral texture of quartz, plagioclase and unoriented biotite typical of leucocratic veinlets within amphibolite (crossed polarised light).*

2.2.11   Calcsilicate

Macroscopic description and field occurrence

Rare calc-silicates usually associated to metaperidotites and amphibolites occur as up to 20 m long and 1 m thick lenses and boudins within both migmatitic metasediments and migmatitic biotite-orthogneiss south of Alpe Rossaccio and all along the contact between the Gruf Complex and the Bergell tonalite (Figs. 2.22a and b). Commonly, these lenses form also xenoliths in the Bergell tonalite. Calcsilicates are coarse-grained, foliated and constituted by alternating garnet-, epidote-, diopside-, calcite- and quartz-plagioclase-rich layers (Fig. 2.22c). Vesuvian, spinel, titanite, wollastonite, brucite and green amphibole occur in minor amounts. Scapolite has been locally reported (Trommsdorff, 1966; Oterdoom, 1980) but not identified in this study.
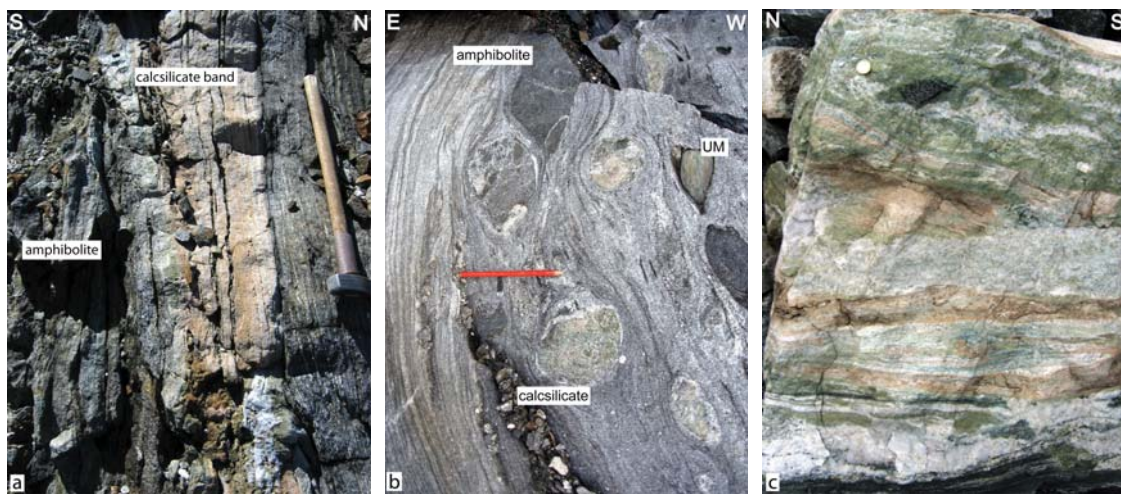
Figure 2.22: *(a) Lense of calcsilicate related to amphibolitic lenses occurring within migmatitic paragneiss and micaschist (Alpe Rossaccio, 759'749/129'494); (b) calcsilicate, amphibolite and ultramafic enclaves within strongly migmatitic biotite-orthogneiss at the contact with the Bergell Pluton (Passo Porcellizzo, 764'231/128'434); (c) calcsilicate block displaying a banded structure composed by bands of light green epidote, pink garnet, white calcite and quartz and dark green diopside.*

Microscopic description

Main phases: calcite, diopside, garnet, epidote, vesuvian, quartz, plagioclase.
Accessories: titanite, spinel, green amphibole, brucite, biotite, wollastonite.

Calcsilicates are marked by a heterogranular texture mostly constituted by idiomorphic, up to 1mm large quartz and plagioclase grains, idiomorphic to rounded and poikilitic garnet ($<$ 0.5 mm large), slightly greenish, idiomorphic diopside ($<$ 1 mm large) and partly resorbed, poikilitic epidote grains ($<$ 8 mm).

2.3   Structural characterisation of the Gruf Complex

2.3.1   Orientation and geometry of the main structures

The regional structure of the Gruf Complex is dominated by an ENE-WSW trending, steeply dipping attitude underlined by the bulk orientation of lithological contacts and the roughly parallel main foliation (see geological map of the Gruf Complex, Fig. I.1, cross sections, Fig. K.1 and Fig. 2.23). The regional fabric dips to the NNW in the northern and central parts of the Gruf and prevalently to the SSE in the southern part (Fig. 2.23). These divergent attitudes suggest two flanks of a dome-like structure for the Gruf Complex. A different geometry is observed between Sivigia and Bivacco Vaninetti, where the main foliation in biotite-orthogneisses changes in less than 100 meters from ENE-WSW to a NNW-SSE strike, parallel to the contact with the approximately 850 m large agglomerate of metaperidotite lenses (see detailed geological map of the area around Bivacco Vaninetti, Fig. J.1). Such deflections of the main foliation also occur near and at the contacts with other ultramafic lenses and in the Bergell tonalite (Fig. 2.23). Since NNW-SSE foliations have the same mineral characteristics as the regional ones, and owing to map continuity from one direction to the other in a shear zone like manner, we consider this deflection as the result of local wrapping of the foliation around rocks of different competence. The different orientations do not document a regional fold that would necessarily fold the earlier foliation, which is not observed.
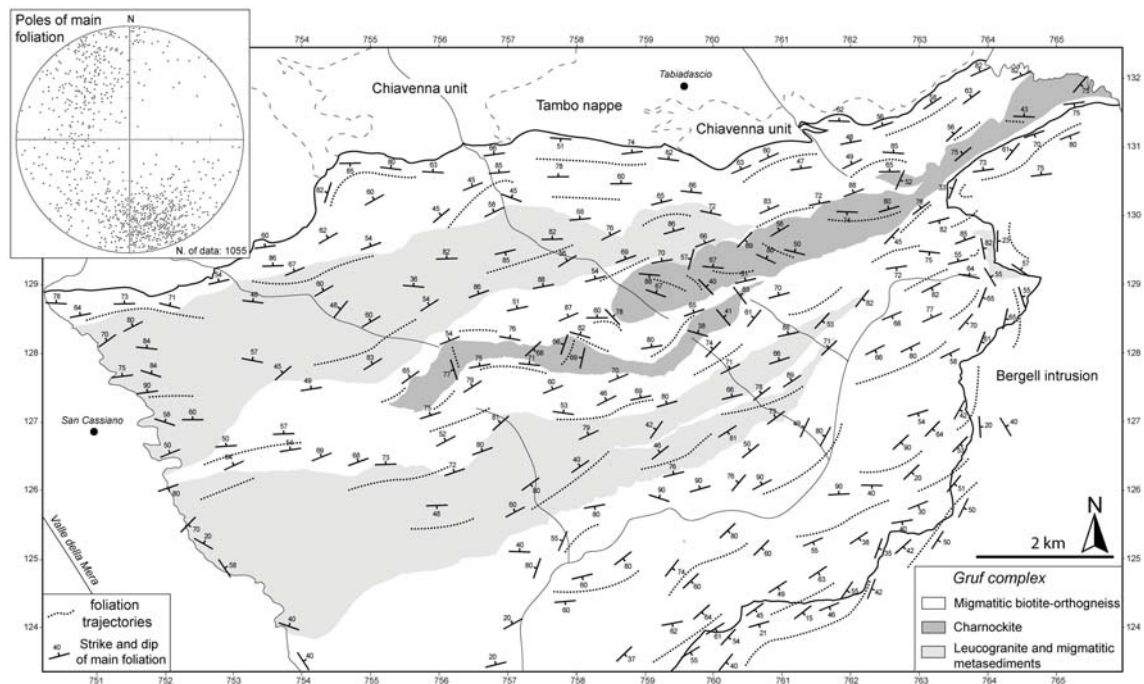
Figure 2.23: *Foliation map showing strinke and dip of main foliation and foliation trajectories.*

Lenses of charnockite and chlorite-spinel-enstatite-olivine fels display a separate internal foliation which, compared to the country rock, is apparently jumbled with no clear regional trend

(Fig. 2.23). Metaperidotite lenses enclosed within migmatitic metasediments are strongly foliated, but their internal foliation is distinct and discordant to that of the country rock, suggesting that the internal foliation of the metaperidotites formed during an earlier stage of deformation. This discrepancy in orientation is typical for boudinaged structures and cannot be used to infer regional information.
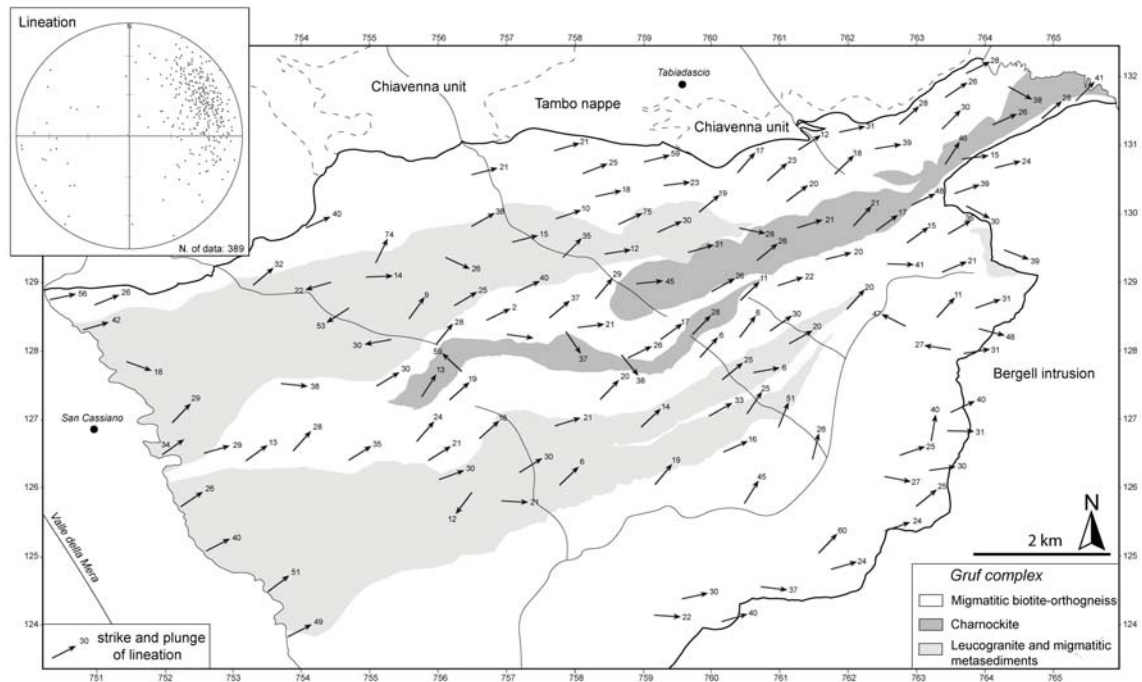
Figure 2.24: *Lineation map showing strinke and plunge of main lineation.*

The main mineral elongation lineation is regionally defined by the preferred orientation of biotite flakes in the migmatitic metagranitoids and by biotite and sillimanite grains in the migmatitic metasediments. In general, the lineation plunges 30-40° between E and NE (Fig. 2.24). However, within charnockitic and ultramafic lenses, mineral lineations have strongly variable orientations (Fig. 2.24). As for foliations, these within-boudin structures reflect local strain complexity due to rheological contrasts, (possibly a disrupted old event). Again, these latter lineations do not bear useful information on the regional, finite structure.

2.3.2   Intensity and style of deformation

Whereas the orientation and geometry of the structures are similar throughout the Gruf Complex, intensity and style of deformation are markedly heterogeneous and depend on the rock type and the degree of partial melting.

The migmatitic biotite-orthogneisses and leucogranites are either weakly foliated or characterised by an unsystematic fabric (Fig. 2.2a). The main foliation is mostly a spaced migmatitic banding folded in contorted manners that are reminiscent of magmatic flow to solid-state fabrics.
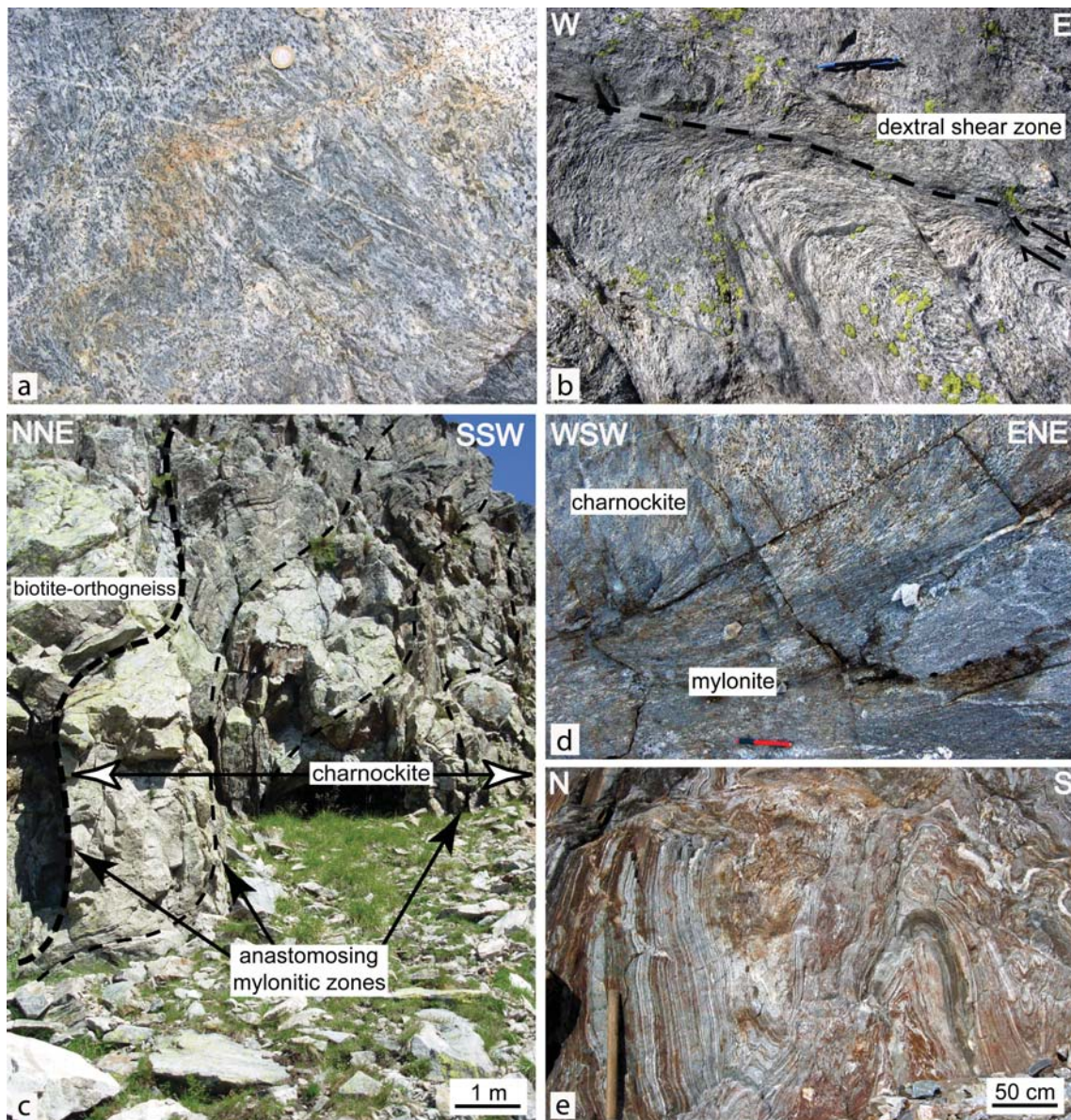
Figure 2.25: *Style of deformation in the Gruf Complex. (a) Magmatic foliation within migmatitic biotite-orthogneiss, characterised by crosscutting relationship between plane of foliation (upper Val Schiesone); (b) strain localisation within a ductile shear zones characterise the deformation within migmatitic biotite-orthogneiss (upper Val Aurosina); (c) internally boudinaged, sheet-like body of charnockite within migmatitic biotite-orthogneiss. Few cm-thin mylonitic zones occur at the contacts between charnockite and biotite-orthogneiss (bold dashed line) and between charnockitic boudins (thin dashed lines) (upper Val Casnaggina); (d) detail of the contact between charnockite and migmatitic biotite-orthogneiss, marked by up to 50 cm thin mylonite (upper Val Casnaggina); (e) apparently chaotical, ductile deformation within partly migmatitic paragneiss and micaschist (upper Val Aurosina).*
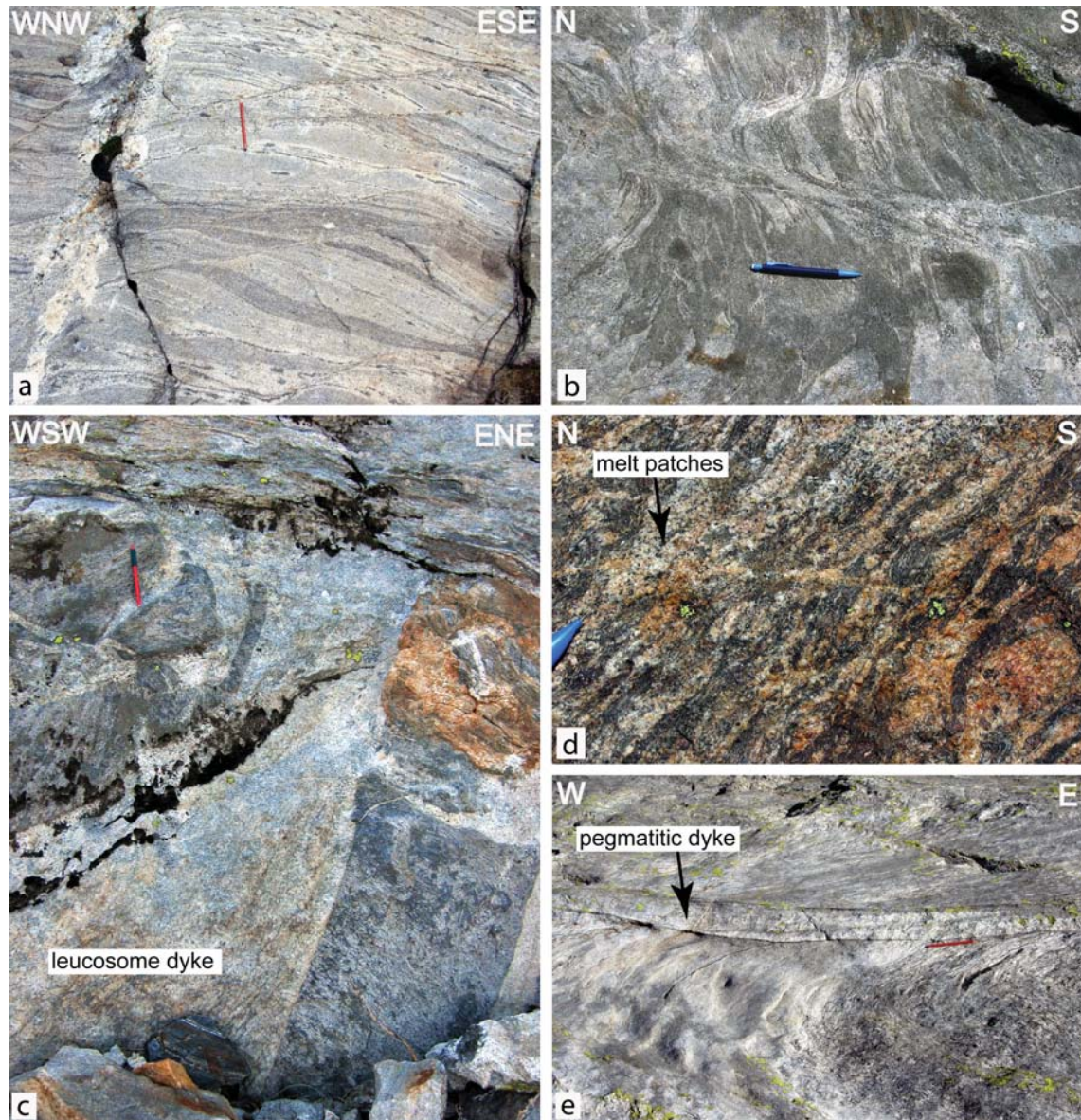
Figure 2.26: *(a) Leucosome-filled ductile shear zone within leucogranite cut by a pegmatitic vein. The boundaries of the pegmatite are cusp and lobate, which means that some flattening on the foliation of the country rock has taken place after pegmatitic veining (east of Bivacco Vaninetti); (b) partly discordant and sheared leucosomes within conjugate shear zones with opposite senses of shear (shear zones 1 and 2 in the text) in migmatitic biotite-orthogneiss (upper Val Aurosina); (c) discordant leucosome dykes within migmatitic metasediments (upper Val Casnaggina); (d) discordant melt patches cutting the main foliation within partly migmatitic micaschist (upper Val Casnaggina); (e) partly sheared pegmatitic dyke intruded into a ductile shear zone (upper Val Codera).*

This observation is consistent with the fact that minerals defining the regional foliation and lineation do not display features of crystalline plasticity to the level one might expect in strongly foliated rocks, which sometimes transist into a macroscopically mylonitic texture. A dynamic, fluidal environment is also suggested by cross cutting relationships of foliations with the same mineralogical characteristics, a magmatic feature described in several plutonic environments (Hutton, 1988; Paterson *et al.*, 1989; Vernon, 2000). Late leucosome veins cutting such foliation unconformities attest for their syn-magmatic to migmatitic character (Fig. 2.25a).

Up to 20-30 cm thin ductile shear zones are abundant, particularly in the upper part of Val Aurosina, Valle del Conco, Val Piana, Val Schiesone and west of Bivacco Vaninetti (Fig. 2.25b). The typical S shape of foliations on both sides of planar mylonite zones indicates that the migmatitic country rock was still ductile at the time of shearing, and mineral parageneses across shear zones (e.g. recrystallised biotite, quartz and feldspars) document that shearing took place at amphibolite facies metamorphic conditions. These shear zones are commonly accompanied and intruded by relatively less sheared aplitic and pegmatitic dykes and leucosomes (Figs. 2.26a, b and e), which again points to shearing in presence of melt.
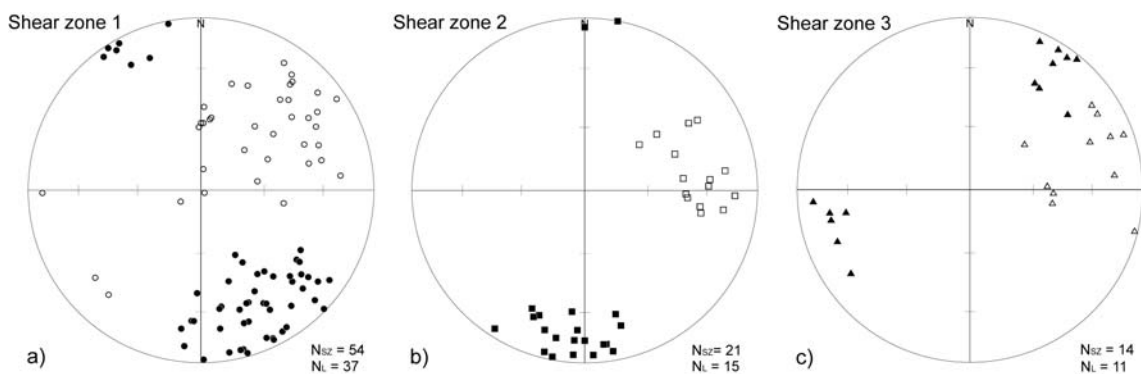
Figure 2.27: *Stereographic projections of poles of shear zones (filled symbols) and stretching lineations (open symbols) for type 1, 2 and 3 shear zone (lower hemispheres, equal area plots, NSZ = number of measurements of shear planes; NL = number of measurements of stretching lineation).*

Three main sets of ductile shear zones have been observed. The first set is striking ENE-WSW, steeply dipping towards the NNW or rarely the SSE, with an associated mineral-stretching lineation plunging from 20 to 80° between NNE and E and a top-to-the SW (reverse-sinistral) shear sense (Figs. 2.26b and 2.27a). The second set is marked by steeply N-dipping shear zones with a stretching lineation plunging 20-60° to the NE and a top-to-the NE (dextral-normal) sense of shear (Figs. 2.26b and 2.27b). The third set consists of NW-SE shear zones steeply dipping towards the NE with a stretching lineation plunging 10-50° towards the ENE and a top-to-the NE dextral-normal movement (Fig. 2.27c). All three sets of shear zones are conjugate to each other, suggesting that they developed contemporaneously. Similar shear zone patterns have been described in the Novate Granite (Ciancaleoni and Marquer, 2006) and in the Adula nappe (Meyre *et al.*, 1998). Together, they describe a syn- to late migmatitic or magmatic vertical flattening and

a marked top-to-the NE dextral-normal movement that documents the upward movement of the Gruf Complex with respect to the surrounding units.

As mentioned above, the heterogeneous deformation in charnockite bodies is visible in arrays of centimeter to several decimeter thick, anastomosing shear zones surrounding almost undeformed, meter-sized rock domains with preserved magmatic structures (e.g. schlieren or a disordered network of crosscutting melts and dykes) and in up to 50 cm thick mylonites at the contacts with the country rocks (Figs. 2.25c and d). Shear zones at charnockite contacts dip steeply towards the NNW and carry a NE plunging mineral-stretching lineation, in accordance with the regional fabric. Less sheared aplitic and pegmatitic dykes occur within these shear zones and show that the intrusion of the dykes was not the last event in the tectonometamorphic history of the region.

Partly migmatitic paragneisses, micaschists and amphibolites are characterised by a more penetrative foliation and often display a more complex deformation pattern marked by the complex refolding of the main foliation (Fig. 2.25e). Refolded folds do neither display any coherent regional trend of fold axes nor a locally coherent trend of axial planes on an outcrop-scale. This is a characteristic feature of partially molten rocks in which folds cannot be ascribed to a specific regional phase of deformation.

2.3.3 Timing of migmatization

Similar foliation and lineation orientations in the Gruf Complex and in the Bergell Intrusion (Figs. 2.23 and 2.24) suggest that the main deformation of the Gruf Complex is Alpine and provides the chance to relate deformation to partial melting. Stromatic structures, melt-filled shear zones, veinlets, patches, pockets and dykes of leucosomes crosscutting the main foliation, as well as magmatic breccias (4 and 5 in Fig. 2.29 and Fig. 2.26) and back veining of Gruf leucosomes into the base of the Bergell Pluton (1 in Fig. 2.29) suggest that migmatization was coeval with the main Alpine deformation, while syn-migmatitic recrystallization has largely reset strain and crystalline fabrics during metamorphism and melting.

Structural investigations in the south-eastern part of the Valle della Mera showed that final emplacement and crystallization of the Bergell Pluton occurred during Oligocene regional deformation (Davidson *et al.*, 1996). We therefore infer that partial melting in the Gruf Complex occurred during emplacement of the Bergell Intrusion, between 32 and 30 Ma (Von Blanckenburg, 1992). This field-based interpretation is consistent with geochronological data yielding a 29-32 Ma age for metamorphic rims of zircon grains separated from granulites, charnockites, metagranitoids and leucosomes from migmatitic metasediments (Liati and Gebauer, 2003; chapter 5) and from monazites contained in the Gruf granulites (Schmitz *et al.*, 2009). This interpretation is also consistent with the Oligocene age of the upper amphibolite-facies metamorphism in the southern and south-eastern parts of the Lepontine Dome (Hänny *et al.*, 1975; Köppel *et al.*, 1981; Gebauer, 1996; Berger *et al.*, 2009; Rubatto *et al.*, 2009).

45

2.4 Analysis of the contacts to the Chiavenna Unit and Bergell Pluton

2.4.1 Contact to the Chiavenna Unit

The northern contact of the Gruf Complex with the ophiolitic rocks of the Chiavenna Unit is only exposed south of Prata Camportaccio in the central part of Val Schiesone near Alpe Prato del Conte, and around Denc dal Luf (see geological map of the Gruf Complex. At this latter locality, the Chiavenna Unit is < 200 m thick and a continuous cross section Gruf Complex - Chiavenna Unit - Tambo Nappe is observable (Fig. 2.28).

The enclave-rich biotite-orthogneiss forms the northern part of the Gruf Complex. The rock is generally massive to slightly foliated and contains up to 50 cm large, rounded or angular mafic enclaves which are commonly intruded by millimetric leucocratic veins (1 in Fig. 2.28). Locally, in particular close to its northernmost limit, the enclave-rich orthogneiss exhibits a stronger fabric and elongated enclaves. The main foliation strikes ENE-WSW and displays a NE-plunging stretching lineation with shear bands indicating a top-to-the NE (normal dextral) sense of shear (2 in Fig. 2.28). To the north, a 5-10 cm thick mylonitic horizont with top-to-the NE sense of shear separates the enclave-rich orthogneiss from strongly migmatitic, irregularly foliated, sillimanite-bearing (garnet, cordierite) biotite-schists. These metasediments present centimetric leucosomes, parallel or discordant to the foliation, and are associated to 10-15 m thick bands of massive, garnet-bearing leucogranite, which commonly crosscut the main fabric. Within metasediments and leucogranites, lenses of metaperidotite and amphibolites occur (Fig. 2.28). Immediately north of Denc dal Luf, the migmatitic metasediments are in contact with the metaperidotites of the Chiavenna Unit. At the contact, massive leucosomes from the metasediments intrude strongly serpentinised metaperidotites, brecciating their margin (4 in Fig. 2.28). Locally, the leucosomes are sheared along < 5 cm thick mylonites. To the north, the rocks of the Chiavenna Unit form a homogeneous mass of about 200 m thickness marked by the strong orange-brownish colour of alteration. Similarly to metaperidotitic lenses within the Gruf Complex, these metaultramafic rock are mostly constituted of olivine, enstatite, chlorite and spinel, are slightly foliated and contain metarodingitic dykes. Further to the north, metaperidotites are in contact with migmatitic, strongly and regularly foliated metasediments of psammitic to pelitic composition belonging to the Tambo Nappe.

The investigation of the northern contact between Gruf Complex and Chiavenna ophiolites does not confirm the existence of a Gruf Line as was previously postulated by Schmutz (1976). This putative line has been interpreted as the tectonic horizon where the differential uplift of the Gruf Complex in respect to the Chiavenna Unit has been accommodated (Bucher-Nurminen and Droop, 1983). However, detailed mapping of the northern contact of the Gruf Complex revealed the occurrence of only locally developed, centimetric mylonite horizons. No wide mylonitic zone(s) have been observed. This suggests that the deformation accompanying the raise of the Gruf Complex with respect to the northern Chiavenna and Tambo units was not concentrated along a specific contact plane but has been somewhat distributed into the Gruf Complex itself, albeit only in the northernmost part of the contact lithologies.

46
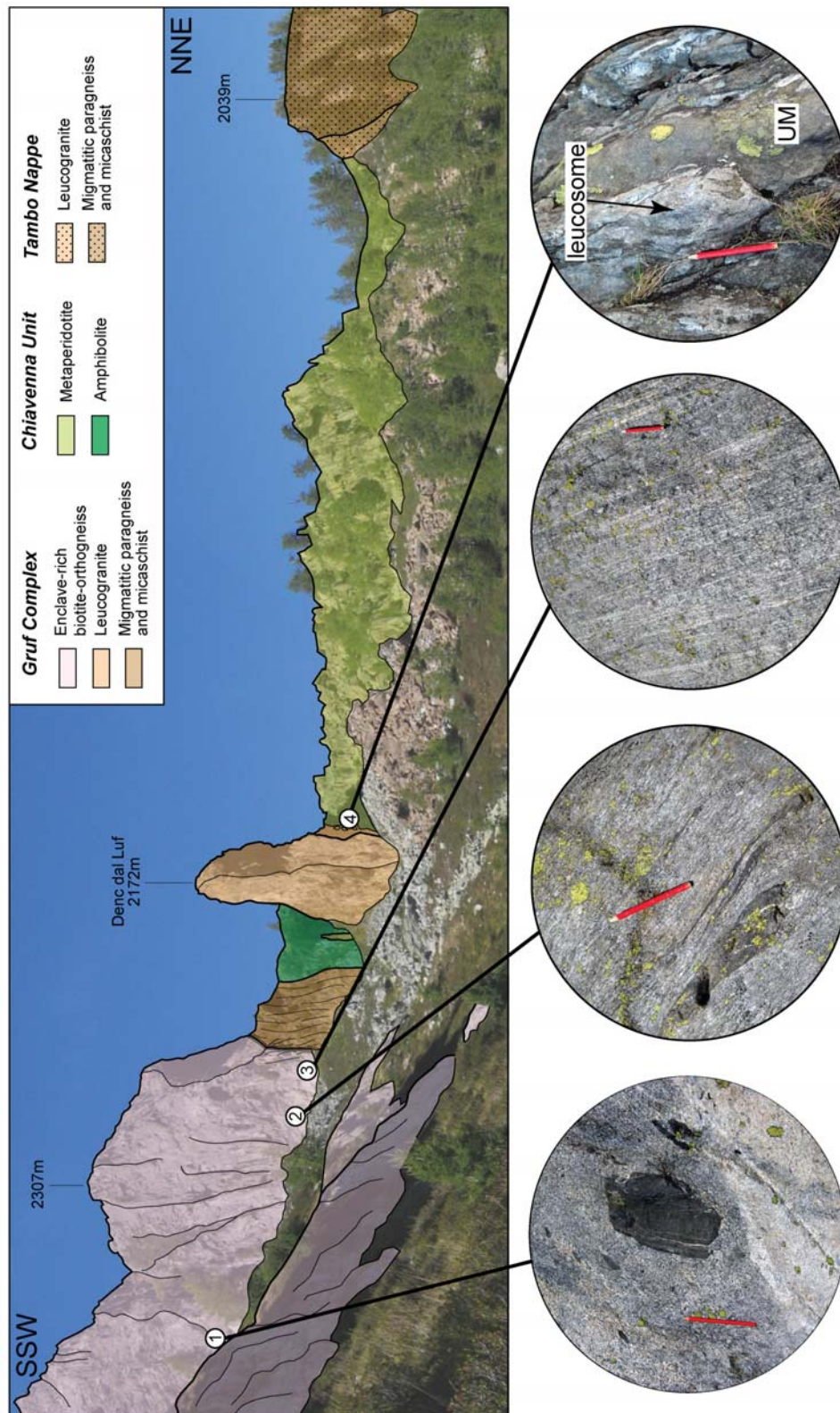
Figure 2.28: *Contact of Gruf Complex and Chiavenna Unit around Denc dal Luf (Val Bondasca). 1: undeformed mafic enclave in massive enclave-rich biotite-orthogneiss; 2: elongated mafic enclaves in foliated enclave-rich biotite-orthogneiss; 3: strongly foliated biotite-orthogneiss; 4: undeformed leucosomes from the migmatitic metasediments brecciate the margin of the Chiavenna metaperidotites.*

Hence, we propose that the enclave-rich biotite-orthogneiss, or at least its northernmost part, acted as low viscosity, partly molten granite sheet which accommodated the exhumation of the Gruf Complex. During this movement fragments of the Chiavenna amphibolites have been sheared of and incorporated into the biotite-orthogneiss, thus becoming enclave-rich. This interpretation is in accordance with the occurrence of shear bands indicating a top-to-the NE (normal dextral) sense of shear within this orthogneiss.

2.4.2   Contact to the Bergell Pluton

Along the south-eastern and southern flanks of Val Codera and Val Bondasca, respectively, the rocks of the Gruf Complex are in contact with the base of the central part of the Bergell Intrusion (Davidson *et al.*, 1996). Here, the pluton is composed of a 50-100 m thick, slightly foliated outermost tonalite with minor amounts of diorite, gabbros and hornblendites at its margin and of a voluminous, coarse-grained, almost undeformed granodiorite with up to 10 cm large alkali feldspar megacrysts in its more internal part. An up to 150 m thick zone of magma mingling and mixing, often referred to as "transitional zone" (Moticska, 1970; Wenk and Cornelius, 1977), is commonly present between these two lithologies. Up to 10 m thick, discontinuous bands and meter-size lenses of ultramafic rocks, amphibolites, calc-silicates and rare metapelites occur along the contact, preferentially contained within the Bergell tonalite, but often also in the adjacent migmatitic biotite-orthogneiss of the Gruf Complex.

For the most part, the Bergell tonalite is in contact with the migmatitic biotite-orthogneiss (Fig. I.1). Both rock types lie sub-parallel and dip gently to the SE (Fig. 2.23). Commonly, the migmatitic biotite-orthogneiss displays a stronger developed foliation than the Bergell tonalite. The contact is not defined by a regular, straight plane but rather is characterised by the irregular compenetration of sub-parallel leucosome veins from the Gruf migmatites and the tonalite.

East of Bivacco Vaninetti, the Bergell tonalite is in contact with migmatitic metasediments containing numerous basic enclaves. Towards the intrusion, migmatitic metasediments present a markedly increased content in leucosome and bear centimetric cordierite grains and relict corundum (Fig. 2.11d). At the contact, the metasediments progressively pass into a coarse-grained fluidal leucogranite, while the numerous basic enclaves are intruded by leucogranite veins (2 on Fig. 2.29). Leucogranites texturally derived from the migmatitic metasediments and veins of the Bergell Intrusion are generally sub-parallel to each other. The boundary between leucogranites and Bergell tonalite is a diffuse transition, with concordant leucocratic veins from the Gruf and more melanocratic veins from the Bergell tonalite (3 on Fig. 2.29). However, NNE of Bivacco Vaninetti (1 on Fig. 2.29), networks of up to 20-30 cm thick, leucosome veins from the Gruf metasediments intruded dark dioritic to gabbroic and tonalitic rocks at the border of the Bergell Pluton. This feature suggests that brecciation of the border of the intrusion resulted from the back veining of Gruf-derived leucosomes.
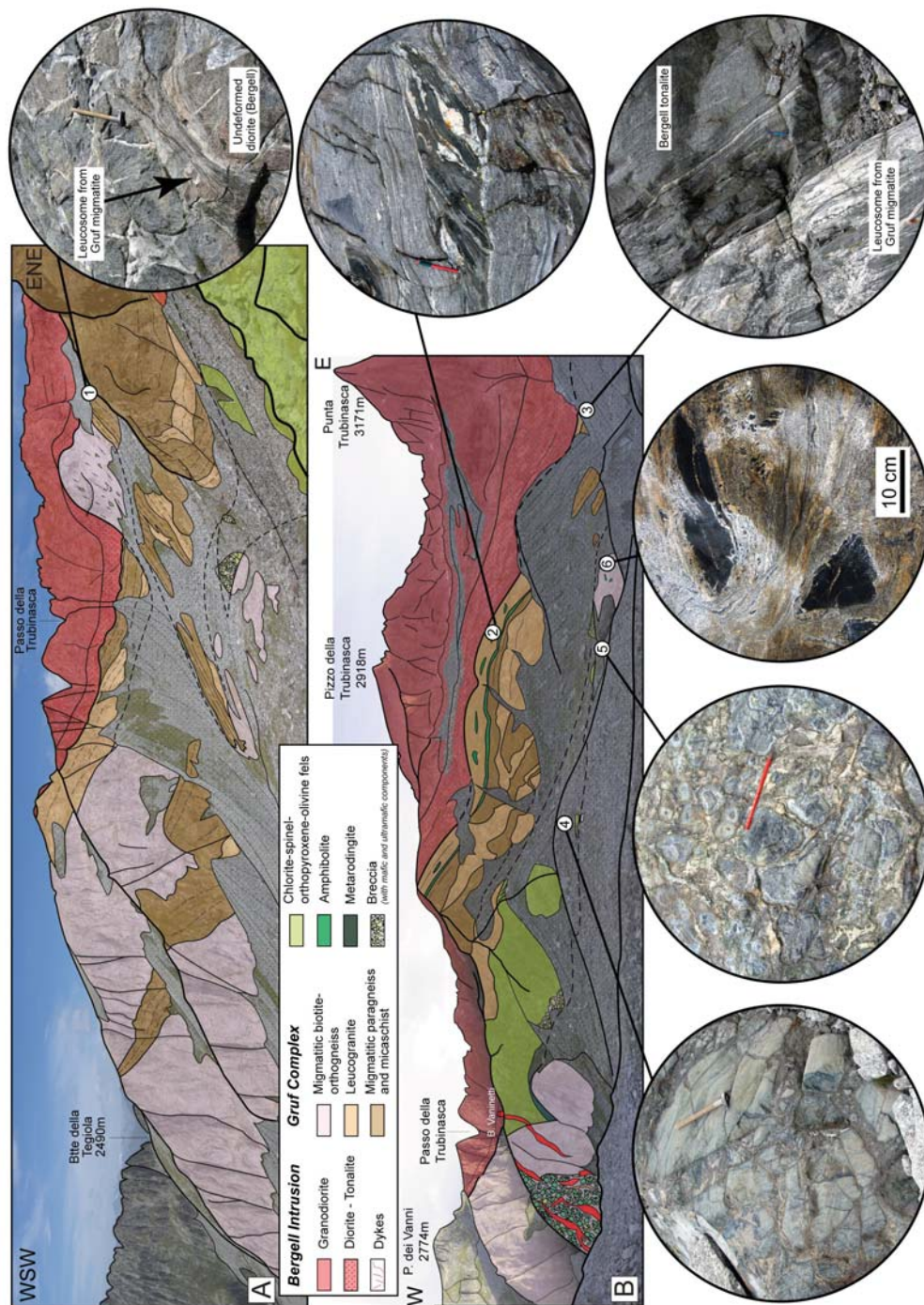
Figure 2.29: *Contact of the Gruf Complex with the Bergell Intrusion in the uppermost Val Codera. (a) Panorama between Bocchetta della Teggiola and Pizzo Trubinasca; (b) Panorama between Passo della Trubinasca and Punta Trubinasca. 1: back veining of leucosomes from the partly migmatitic metasediments of the Gruf Complex intruding diorite of the Bergell Pluton; 2: Highly contorted folding of migmatitic metasediments and enclosed mafic layers; 3: foliated mafic enclave cut by leucosome of Gruf migmatites; 4: injection of leucosomes from the migmatitic biotite orthogneiss into the base of a chlorite-spinel-orthopyroxene-olivine fels; 5: injection of leucosomes from Gruf migmatites and formation of magmatic breccias with granitoidic matrix and ultramafic components; 6: almost undeformed and slightly rotated mafic enclave within migmatitic biotite orthogneiss.*

49

Chapter 3

Geochemistry

3.1 Introduction

Two main problems are addressed in this chapter:

(i) characterise the bulk rock compositions of the metagranitoid lithologies composing the most part of the Gruf Complex;

(ii) compare the geochemical characteristics of the mafic enclaves contained in the northernmost migmatitic biotite-orthogneisses (described in section 2.2.2) with the adjacent amphibolites of the Chiavenna Unit.

Sixty-nine samples representing biotite-orthogneisses (18 migmatitic biotite-orthogneisses and 6 enclave-rich biotite-orthogneisses), leucogranites (23 samples), charnockites (3 garnet-sillimanite-absent samples, 6 garnet-bearing, sillimanite-absent samples and 2 garnet-sillimanite-bearing samples), augengneisses (2 samples) and mafic enclaves contained within the enclave-rich biotite-orthogneisses (9 samples) were collected from the whole Gruf Complex and were analysed for major elements. Six mafic enclaves and three enclave-rich biotite-orthogneisses were also analysed for trace elements. Bulk rock compositions were obtained using a Panalytical Axios wavelength dispersive XRF spectrometer (WDXRF, 2.4 kV) at ETH Zurich, while trace elements were measured with a Elan 6000 laser-ablation microsampler coupled to an inductively plasma mass spectrometer at ETH Zurich. Bulk rock compositions and trace element data are given in Appendix E and F.

3.2 Granitoidic rocks

3.2.1 Major elements

From a geochemical point of view, metagranitoids can be divided into two major compositional groups. The first group comprises the migmatitic biotite-orthogneisses, the enclave-rich biotite-orthogneisses, garnet-sillimanite-absent charnockites, garnet-bearing, sillimanite-absent charnockites and the augengneisses. The second group is formed by the leucogranites and garnet-sillimanite-bearing charnockites.

The rocks of the first group display a variable SiO_2 content ranging between 59 and 70.5 wt%, are relatively poor in K_2O (1.51-3.85 wt%) but rich in Al_2O_3 (14.54-18.87 wt%), FeO (2.24-6.68 wt%), MgO (0.66-3.39 wt%), CaO (2.22-4.78 wt%), MnO (0.04-0.11 wt%) and TiO_2 (0.29-0.94 wt%) (Fig. 3.3). Generally, the rocks of the first group are slightly peraluminous (Fig. 3.1a), only two samples slightly metaluminous. Garnet-bearing charnockites (A/CKN: 1.048-1.171) and augengneisses (A/CKN: 1.074-1.136) have slightly higher alumina saturation value (A/CKN) than the biotite-orthogneisses (A/CKN: 0.993-1.067) and the garnet-sillimanite-absent chanockites (A/CKN: 0.977-1.026), in accordance with the occurrence of garnet in these charnockites and muscovite in the augengneisses.

The second group is considerably richer in SiO_2 (71-75.3 wt%) and K_2O (2.04-6.16 wt%) but poorer in Al_2O_3 (13.35-15.42 wt%), FeO (0.94-2.82 wt%), MgO (0.15-2.32 wt%), CaO (0.46-2.78 wt%), MnO (0.02-0.07 wt%) and TiO_2 (0.06-0.34 wt%) (Fig. 3.3). This second group is significantly more peraluminous (A/CKN: 1.057-1.351) than the first group (Fig. 3.1a), in agreement with the observed high amount of muscovite + garnet $\pm$ sillimanite in the leucogranites and garnet + sillimanite in the charnockites belonging to the second group.

On a Fe^{tot} + MgO vs. SiO_2 (wt%) diagram (Fig 3.1b), the samples show an inverse correlation, rocks of the first group being poorer in silica and richer in FeO and MgO than those of the second group. The two compositional groups are also well discernable on an AFM ternary diagram projected from quartz and feldspar components (Fig. 3.1c). The rocks of the first group plot on the Fe-Mg rich side of the triangle, while the rocks of the second group plot closer to the Al-rich corner.

Comparisons with the calc-alkaline Bergell Pluton and with the S-type Novate Granite show that the rocks of the first group are similar to the Bergell Granodiorite, while rocks of the second group are similar to the peraluminous Novate Granite.
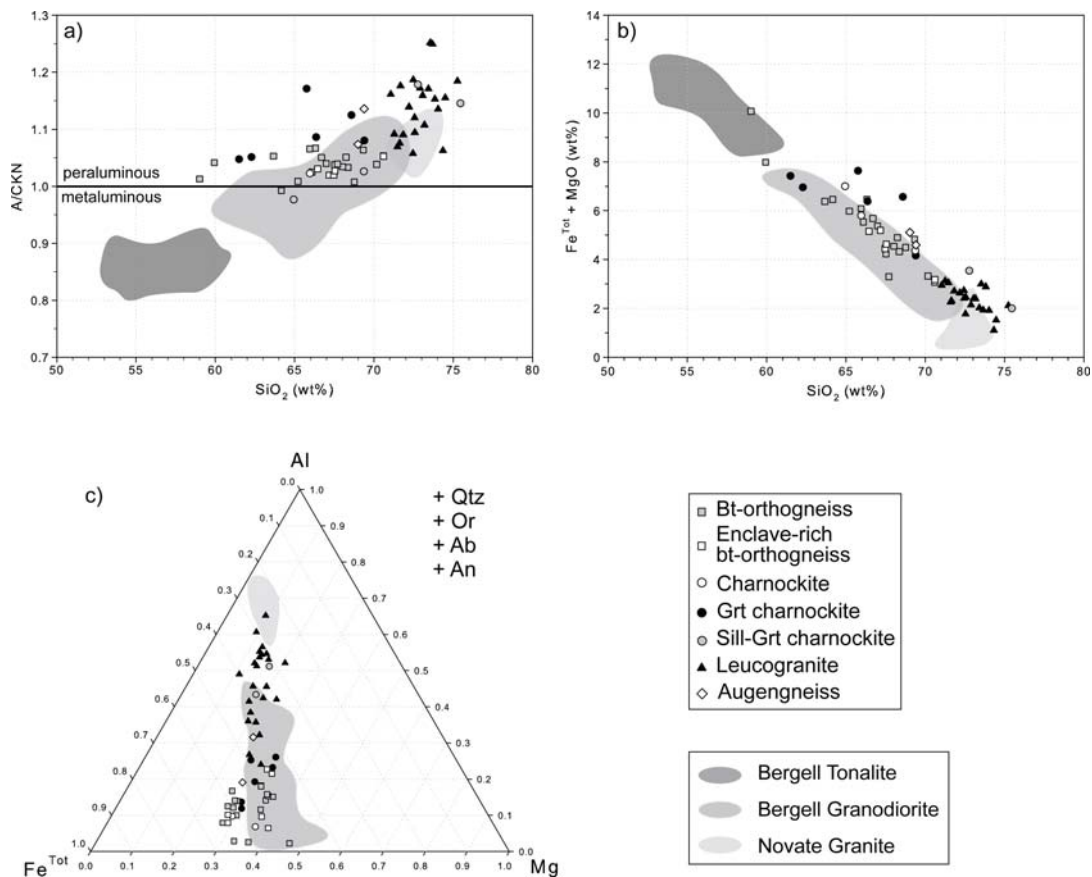
Figure 3.1: *(a) A/CKN vs. SiO_2 (wt%) diagram; (b) FeO^{Tot} + MgO (wt%) vs. SiO_2 (wt%) diagram; (c) AFM diagram projected from quartz and feldspar components. Coposition fields of Bergell Tonalite (Moticska, 1970; Reusser, 1987b), Bergell Granodiorite (Moticska, 1970; Wenk et al., 1977; Reusser, 1980, 1987b) and Novate Granite (Moticska, 1970; Wenk et al., 1977; Reusser, 1987b; Hafner, 1993) are plotted for comparison.*

3.3   Mafic enclaves: comparison to the Chiavenna amphibolites

The results presented in this section arise from the collaboration with Giuliano Krättli as part of his "Bachelorarbeit".

3.3.1   Major elements

In terms of major elements, the mafic encalves contained in the enclave-rich biotite orthogneiss (petrographical description in section 2.2.2) show higher SiO_2, K_2O and TiO_2, similar MgO, Al_2O_3, Na_2O and MnO, as well as slightly lower FeO^{tot} and CaO values than the Chiavenna amphibolites (data from Talerico, 2000; Fig. 3.3). Generally, the composition of the enclaves plot between those of the Chiavenna amphibolites and the host orthogneisses.

The SiO_2 enrichment exhibited by the enclaves in respect of the Chiavenna amphibolites may be explained by granitic melt infiltration during the embedding of the enclaves into the migmatitic orthogneiss. The observed growth of texturally late biotite in the enclaves (section 2.2.2) may account for the slightly higher K_2O and TiO_2 compositions.

3.3.2   Trace elements

Except for the HREE, the n-MORB nornalysed trace element patterns of the mafic enclaves (Figs. 3.4 a,b) are similar to the trends exhibited by the host enclave-rich biotite-orthogneisses (Figs. 3.4 e,f). Both rock types are strongly enriched in LILE and moderately enriched in HFSE and LREE, with a strong positive Pb anomaly (Fig. 3.4). In contrast, similarly to the Chiavenna amphibolites (Figs. 3.4 c,d), the mafic enclaves show a flat HREE pattern similar to n-MORB (Figs. 3.4 a,b).

3.3.3   Discussion

The petrology, the major element composition and the HREE pattern displayed from the mafic enclaves are similar to those of the Chiavenna amphibolites. Nevertheless, these enclaves seem to have been strongly contaminated by the host biotite-orthogneisses, as shown by the similar LILE, HSFE and LREE characteristics. From this picture, we suggest that the mafic enclaves largely contained in the northernmost biotite-orthogneiss of the Gruf Complex at the contact to the Chiavenna ophiolites were fragments of Chiavenna amphibolite trapped and embedded into the host orthogneisses during migmatization. This in in accordance with the interpretation that the enclave-rich biotite-orthogneiss acted as low viscosity, partly molten granite sheet which accommodated the exhumation of the Gruf Complex (section 2.4.1). During this movement pieces of the Chiavenna amphibolites have been probably incorporated into the biotite-orthogneiss.
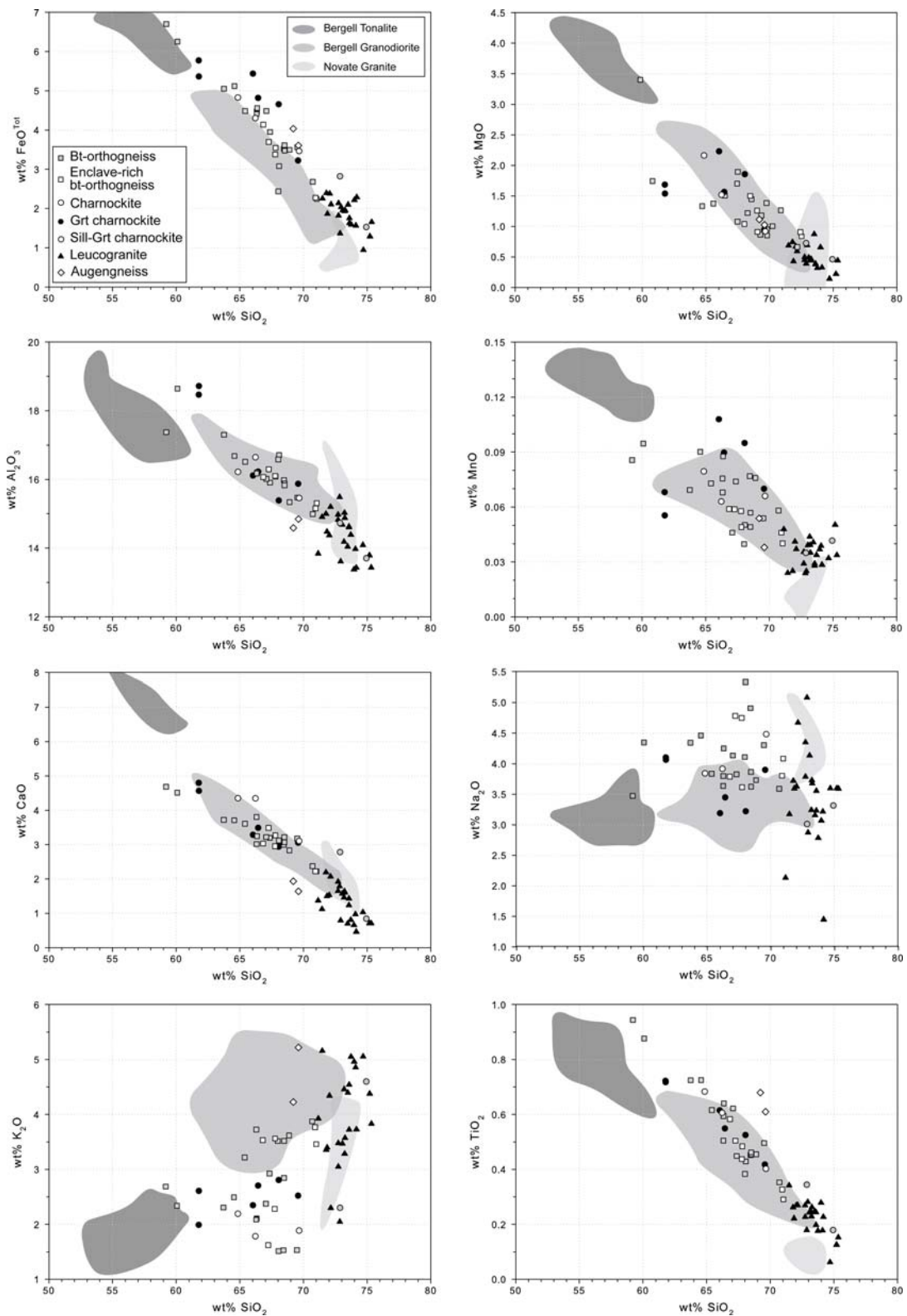
Figure 3.2: *Major element variation diagrams of Gruf metagranitoids. Coposition fields of Bergell Tonalite (Moticska, 1970; Reusser, 1987b), Bergell Granodiorite (Moticska, 1970; Wenk et al., 1977; Reusser, 1980, 1987b) and Novate Granite (Moticska, 1970; Wenk et al., 1977; Reusser, 1987b; Hafner, 1993) are plotted for comparison.*
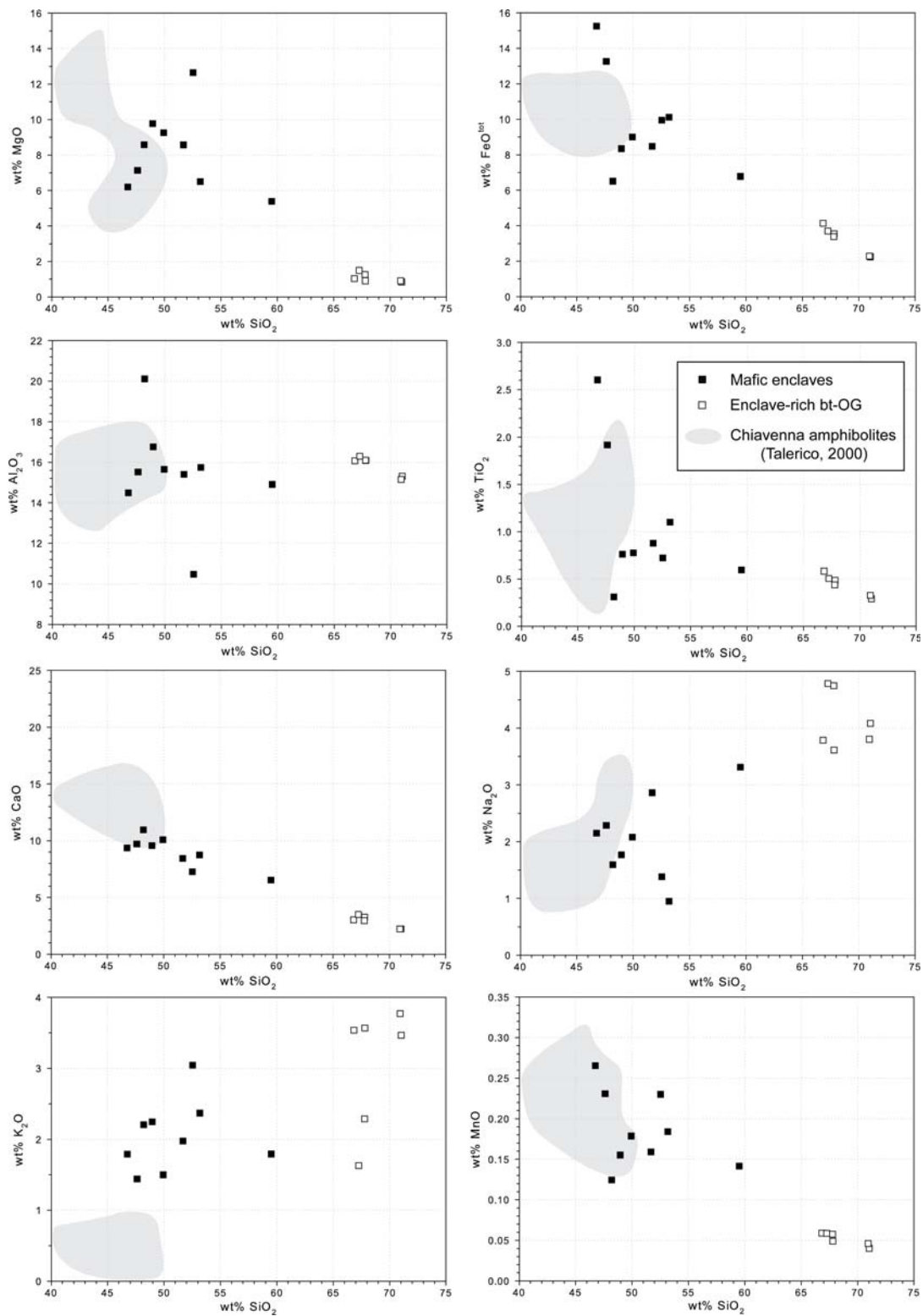
Figure 3.3: *Representative major element variation diagrams for mafic enclaves (this work), enclave-rich biotite-orthogneiss (this work) and Chiavenna amphibolites (after Talerico, 2000).*
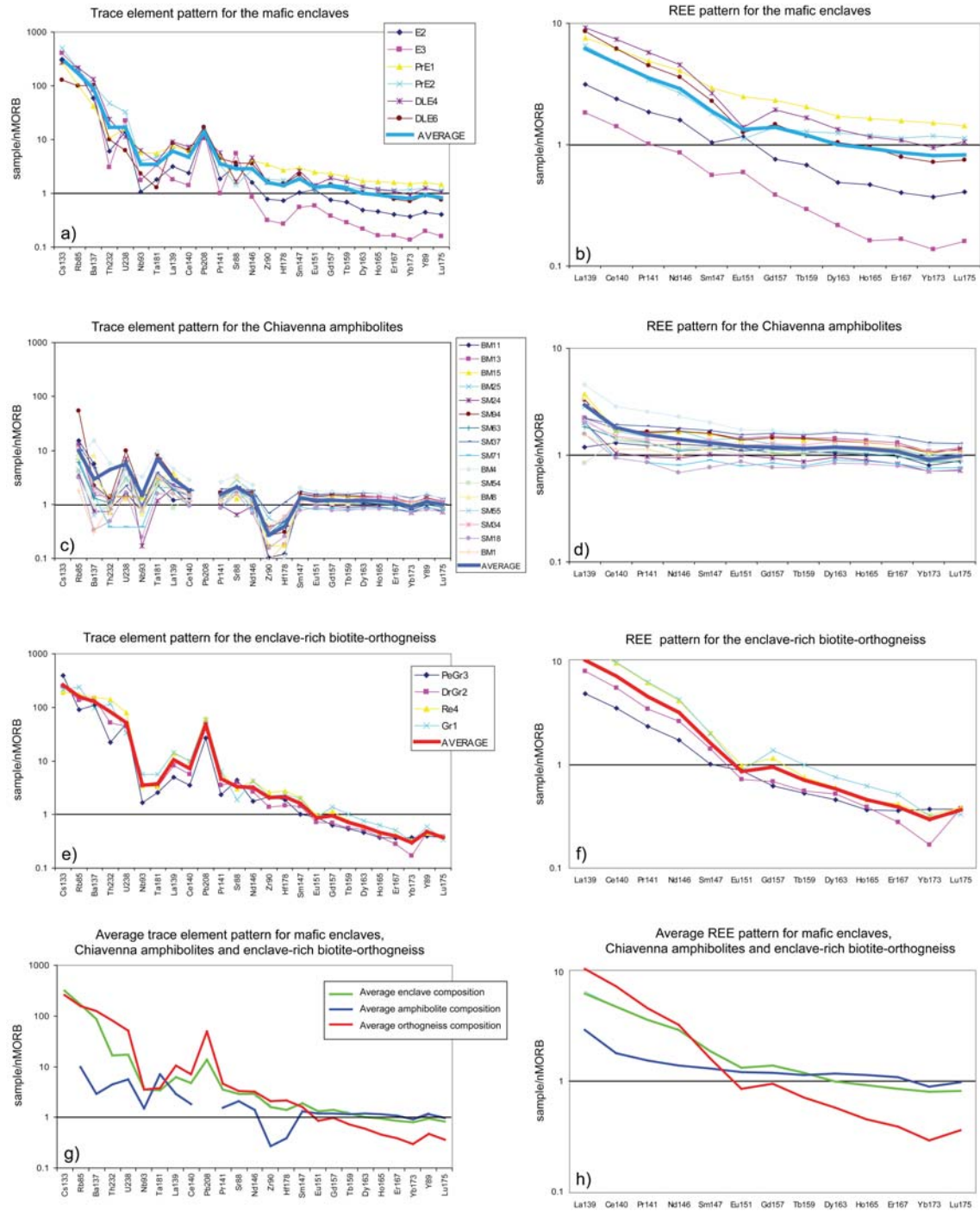
Figure 3.4: *(a-b) N-MORB normalysed trace elements and REE patterns for mafic enclaves (this work); (c-d) n-MORB normalysed trace elements and REE patterns for Chiavenna amphibolites (data after Talerico, 2000); (e-f) n-MORB normalysed trace elements and REE patterns for the enclave-rich biotite-orthogneisses (this study); (g-h) avergae trace elements and REE patterns for the enclaves, amphibolites and orthogneisses. N-MORB composition after Sun and McDonough (1989). Trace element data are given in Appendix F.*

Chapter 4

Metamorphic evolution of the Gruf Complex

4.1 Granulites and charnockites

4.1.1 Introduction

Understanding ultrahigh-temperature (UHT) metamorphism at crustal levels, defined by temperatures in excess of 900 °C and typical pressures of 7-13 kbar (Harley, 1998b), is one of the most challenging tasks in metamorphic petrology (Harley, 2004, 2008; Kelsey, 2008). Most commonly, very high-grade mineral assemblages including sapphirine, aluminous orthopyroxene, garnet, sillimanite, spinel, cordierite or corundum, and post-peak reaction-textures such as moats and symplectites are preserved in Mg-Al-rich metapelites (Harley *et al.*, 1990; Mouri *et al.*, 1996; Raith *et al.*, 1997; Moraes *et al.*, 2002; Kelsey *et al.*, 2003; Sajeev and Osanai, 2004; Barbosa *et al.*, 2006; Santosh and Sajeev, 2006; Tong and Wilson, 2006; Brandt *et al.*, 2007; Leite *et al.*, 2009). Thus, despite being volumetrically rare, such rock types are the most appropriate for investigating UHT conditions, and are fundamental for reconstructing the tectono-metamorphic history of high-grade terrains because of their multitude of mineral possible reactions.

During the last two decades, our ability to better determine the metamorphic conditions of high-grade metamorphic rocks has improved significantly. Advances have been made in the accuracy of conventional thermometers (for review see Harley, 2008), the use of Al-solubility in orthopyroxene (Harley and Green, 1982; Aranovich and Berman, 1997; Harley, 1998a; Harley and Motoyoshi, 2000), retrieval methods in order to overcome the diffusive effect of resetting of mineral composition during cooling and/or retrograde metamorphism (Fitzsimons and Harley, 1994; Pattison and Begin, 1994; Pattison *et al.*, 2003), and the development of internally-consistent thermodynamic datasets (Powell and Holland, 1988; Holland and Powell, 1990, 1998; Berman and Aranovich, 1996). As a result of these advances, more than 40 UHT localities have been identified worldwide (Brown, 2006, 2007; Kelsey, 2008).

In this study, we focus on the granulites and charnockites of the Gruf Complex (Central Alps), representing a long-standing enigma in Alpine geology. In the Gruf Complex, rare blocks of dark Mg-Al-rich sapphirine-bearing granulites were discovered by Cornelius (1916) and Wenk *et al.* (1974) in two talus slopes in Val Codera (locations indicated in Wenk and Cornelius, 1977), but have never been found in-situ, in part because of the hostile topography of the Gruf area. Estimates of metamorphic peak-conditions suggested T > 800 °C and P = 10 ± 2 kbar, conditions predating the formation of symplectitic textures and coronae at T = 750 °C and P = 5 kbar (Barker, 1964; Ackermand and Seifert, 1969; Droop and Bucher-Nurminen, 1984). Droop and Bucher-Nurminen (1984) suggested that the Gruf granulites formed during a single Alpine metamorphic cycle characterised by nearly isothermal decompression. Zircons from the Gruf granulites (Liati and Gebauer, 2003) yielded SHRIMP ages of 272.0 ± 4.1 Ma for oscillatory cores, interpreted as a magmatic crystallization age, and 32.7 ± 0.5 Ma for the homogeneous rims, inferred to represent the age of the granulite facies metamorphism. Similar ages of 33 ± 4.4 Ma (Schmitz *et al.*, 2009) have been reported from monazite grains included in or intergrown with high-temperature minerals (e.g. sapphirine, orthopyroxene).

However, metamorphic conditions of T > 800 °C and P = 10 ± 2 kbar do not fit any known

metamorphic event of regional significance in the Central Alps, questioning a close correlation of the Gruf Complex with other Alpine tectonic units. Furthermore, the strong refractory character, the occurrence of sapphirine-quartz inclusions in garnet (Droop and Bucher-Nurminen, 1984) and the highly aluminous character of orthopyroxene porphyroblasts (Al2O3opx $\sim$ 9 wt%), strongly suggest that the Gruf granulites might have formed at higher temperature than previous estimates, namely at UHT conditions, making their regional metamorphic significance even more puzzling.

The aims of this study are:

   (i) to place the Gruf granulites in their geological context and characterise the different granulite types;

  (ii) to understand the regional extent, abundance and relations to the country rocks of these granulites;

 (iii) to refine the estimates of peak PT conditions and the post-peak history with modern thermodynamic tools (PT pseudosections, conventional thermobarometry accounting for Fe-Mg back-diffusion, Al-solubility in orthopyroxene);

 (iv) to integrate these granulites within the tectonic and metamorphic evolution of the Central Alps.

4.1.2   Field relations

Rock types

Detailed mapping (1:25'000) of the Gruf Complex has revealed the occurrence of charnockite sheets and six different types of granulite (Fig. 4.1):

- dark, massive sapphirine-orthopyroxene-cordierite-garnet granulite (type A),

- dark, massive sapphirine-bearing orthopyroxene-sillimanite-cordierite-garnet granulite (type B),

- dark, massive orthopyroxene-cordierite-garnet granulite (type C),

- dark, foliated sapphirine-orthopyroxene-garnet granulite (type D),

- felsic, foliated sapphirine-bearing orthopyroxene-garnet granulite (type E),

- felsic, foliated sapphirine-orthopyroxene granulite (type F).

Type A and B granulites correspond to the sapphirine-bearing samples described in boulders from the debris scree to the east of Bresciadega in Val Codera (Cornelius, 1916), and investigated by Droop and Bucher-Nurminen (1984). Type C to F granulites and charnockites have not been previously identified
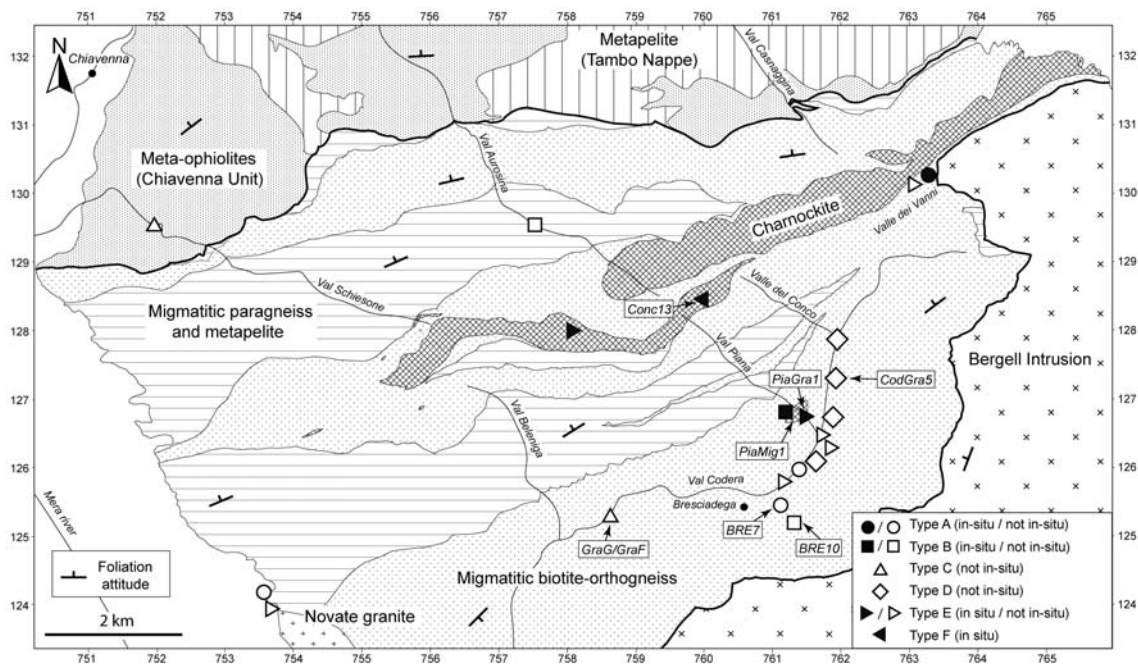
Figure 4.1: *Simplified geological map of the Gruf unit and locations of charnockites and different types of granulites in simplified geological map of the Gruf Complex. Location of the investigated samples is also indicated.*

Occurrence

The different types of granulite are widespread throughout the entire Gruf Complex (Fig. 4.1). Types A and B have been identified as cm- to meter-size enclaves (Fig. 4.2a), both within migmatitic biotite-rich orthogneisses (Valle dei Vanni, Swiss coordinates 763'000/130'200) and within charnockites (Val Piana, 761'050/127'070). However, no type A or B granulite has been found in outcrops at the historical locality near Bresciadega. Type C granulites have been found exclusively as meter-size boulders in the main rivers of Val Codera (758'650/125'400) and Val Schiesone (752'180/129'340). Type D, E and F granulites form up to 1 m long and 40 cm thick "schlieren" within charnockites (Fig. 4.2b) in Val Piana (761'000/127'100), Valle del Conco (760'160/128'540), and Val Aurosina (758'030/128'140), also occuring as boulders in the main river of Val Codera. Large (< 0.5 km wide and < 8 km long), east-west striking charnockites constitute internally boudinaged, sheet-like bodies within the regionally dominant migmatitic biotite-rich orthogneisses (Fig. 4.2c). Two major bodies have been mapped in the core of the Gruf Complex, near the crest between Val Codera and Val Chiavenna (Fig. 4.1). Several smaller lenses (< 500 m long) occur in Val Piana, Valle del Conco and Val Aurosina. In general, the charnockitic boudins and lenses are internally undeformed or preserve magmatic flow structures. Up to 50 cm wide mylonites commonly separate charnockites from the adjacent rocks.

62
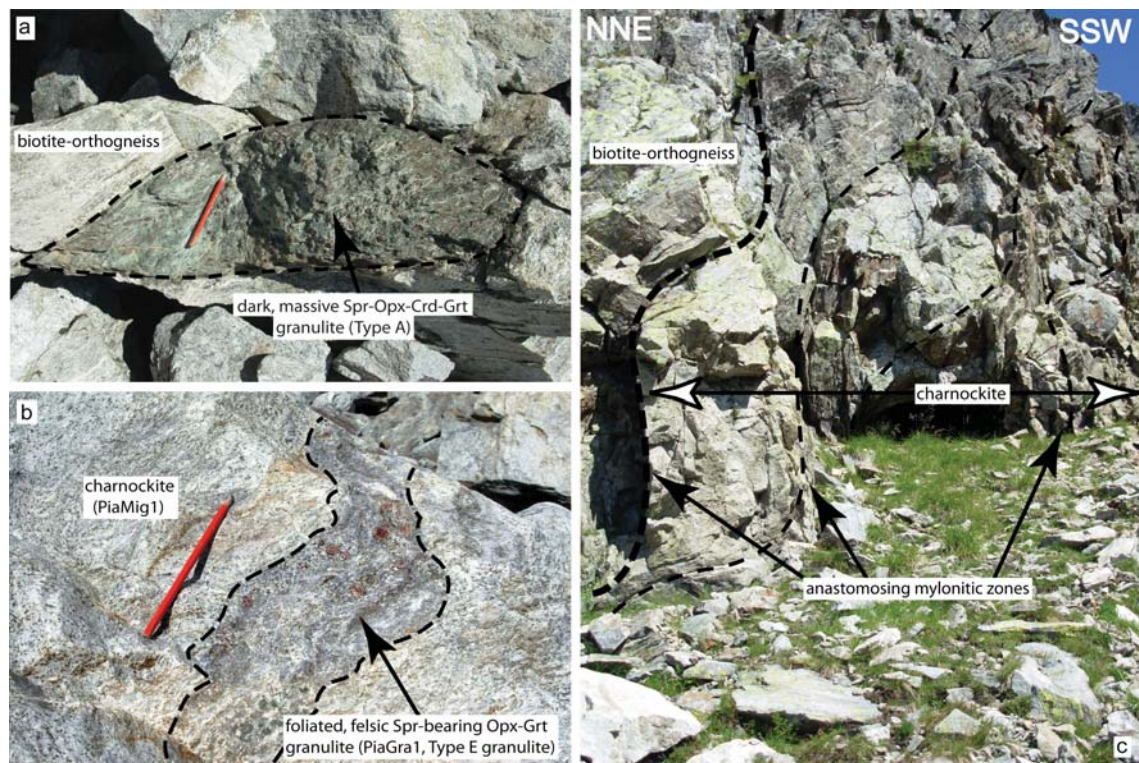
Figure 4.2: *Field aspects of granulites and charnockites. (a) Retrogressed type A granulite enclave within migmatitic biotite-orthogneiss (Valle dei Vanni, 763'024/130'193); (b) type E granulite schlieren (sample PiaGra1) within charnockite (sample PiaMig1, Val Piana, 761'118/127'060); (c) internally boudinaged, sheet-like body of charnockite within migmatitic biotite-rich orthogneiss (upper Val Casnaggina, 762'644/130'526). Few cm-thin mylonitic zones occur at the contacts between charnockite and migmatitic biotite-orthogneiss (bold dashed line) and between charnockitic boudins (thin dashed lines).*

4.1.3   Whole rock composition and chemographic analysis

Based on their peak mineral assemblages (Tab. 4.1.3), the six types of granulite and charnockites can be classified into four major groups. Types A and D are sapphirine-bearing, sillimanite- and quartz-absent; type B and the coarse-grained domains of type C are sillimanite-bearing, quartz- and sapphirine-absent; type E and F are quartz- and sapphirine-bearing, sillimanite-absent; fine-grained domains of type C and the charnockites are quartz-bearing, sillimanite- and sapphirine-absent. All rock types are garnet-, orthopyroxene- and biotite-bearing.

Bulk compositions of homogeneous charnockites and type A, B, C and F granulites were obtained using a Panalytical Axios wave-length dispersive XRF spectrometer (WDXRF, 2.4 kW) at ETH Zürich. Granulite types D and E, occurring as irregular schlieren in charnockites, were not analysed because they could not be separated from the host rock. Representative rock compositions are given in Tab. E and discussed in terms of X_{Mg}, A/AFM [A = Al_2O_3 - (K_2O + Na_2O + CaO)] and S/SFM [S = SiO_2 - Al_2O_3 - CaO - 5 * (K_2O + Na_2O) + FeO + MgO], following the approach of Harley (2008). The relationships between rock compositions and peak mineral assemblages are displayed via MFAS ((Mg + Fe)O - SiO_2 - Al_2O_3) diagrams projected from the

Table 1
Main mineral assemblages and textural features in Gruf granulites and charnockite investigated in this study

Rock type	Type A	Type B	Type C-coarse	Type C-fine	Type D	Type E	Type F	Charnockite
Sample name	BRE7	BRE10	GraG	GraF	CodGra5	PiaGra1	Conc13	PiaMig1
Location	Bresciadega	Bresciadega	Codera river	Codera river	Codera River	Val Piana	Valle del Conco	Val Piana
Minerals								
Garnet								
matrix porphyroblast	P	P	P	P	P	P	P	P
included in	opx	opx	opx	-	-	-	-	-
Orthopyroxene								
matrix porphyroblast	P	P	P	P	P	P	P	P
sym around Grt	pP	pP	pP	pP	pP	-	-	-
sym around Opxpor	pP	pP	-	-	pP	-	-	-
inclusion	grt,bt	grt,bt	grt	-	grt	grt	-	-
Sapphirine								
matrix porphyroblast	P	-*	-	-	P	-	-	-
sym around Grt	-	pP	-	-	pP	-	-	-
sym around Sil	-	pP	pP	-	-	P	P	-
sym around Crn	-	-	-	-	-	P	-	-
inclusion	grt,opx,bt	grt,opx	grt	grt	grt	grt	-	-
Sillimanite								
matrix porphyroblast	-	P	P	-	-	prP	prP	-
inclusion	grt,spr,ksp	grt,ksp,spr	grt,opx	grt	grt	grt	-	grt
Biotite								
matrix	P	P	P	P	P	P	P	P
coronae around opx	pP	pP	pP	pP	pP	pP	pP	pP
inclusion	grt,opx	grt,opx,sil	grt,opx	grt,opx	grt,opx	grt	grt,opx	grt,opx
Cordierite								
coronae	pP	pP	pP	pP	pP	-	-	-
Corundum								
matrix	-	-	-	-	-	prP	-	-
inclusion	grt	-	grt	-	-	-	-	-
Spinel								
sym around Grt	-	pP	-	-	pP	-	-	-
sym around Sil	-	pP	pP	-	-	pP	pP	pP
sym around Crn	prP	-	-	-	-	pP	-	-
inclusion	grt,opx,spr	grt,spr	grt,opx	grt	opx,spr	grt	grt	-
Alkali feldspar								
matrix	P	P	-	P	P	P	P	P
inclusion	grt	grt,opx,sil	-	-	grt,opx	grt	-	grt
Plagioclase								
matrix	-	P	-	P	P	P	P	P
sym around opx	pP							
inclusion	grt	grt,opx	grt	grt	grt,spr	grt	-	grt,opx
Quartz								
matrix	-	-	-	P	-	P	P	P
inclusion	grt	grt,opx	grt	grt,opx	-	grt	-	grt,opx

P: part of the metamorphic peak assemblage; prP: part of the metamorphic pre-peak assemblage; pP: part of the metamorphic post-peak assemblage. List of abbreviations for inclusions: grt – in garnet; opx – in orthopyroxene; spr – in sapphirine; sil – in sillimanite; ksp – in alkalifeldspar; bt – in biotite. *Prismatic sapphirine occurs in type B granulite exclusively in micro-domains of different bulk-rock composition and are therefore not considered part of the peak assemblage representative for type B granulite (see text).

three feldspar components (Figs. 4.3a and b). Relations in quartz-saturated rock types are also represented by an AFM (Al_2O_3 - FeO - MgO) diagram projected from quartz and the three feldspar components (Fig. 4.3c). We note here that slight discrepancies between bulk compositions and the triangles defined by mineral tie-lines are most likely related to the oxidation state of Fe: all Fe is calculated as Fe^{2+}, thus overestimating the (Mg,Fe)O-component and underestimating the Al_2O_3 component, to which ferric iron would be added.
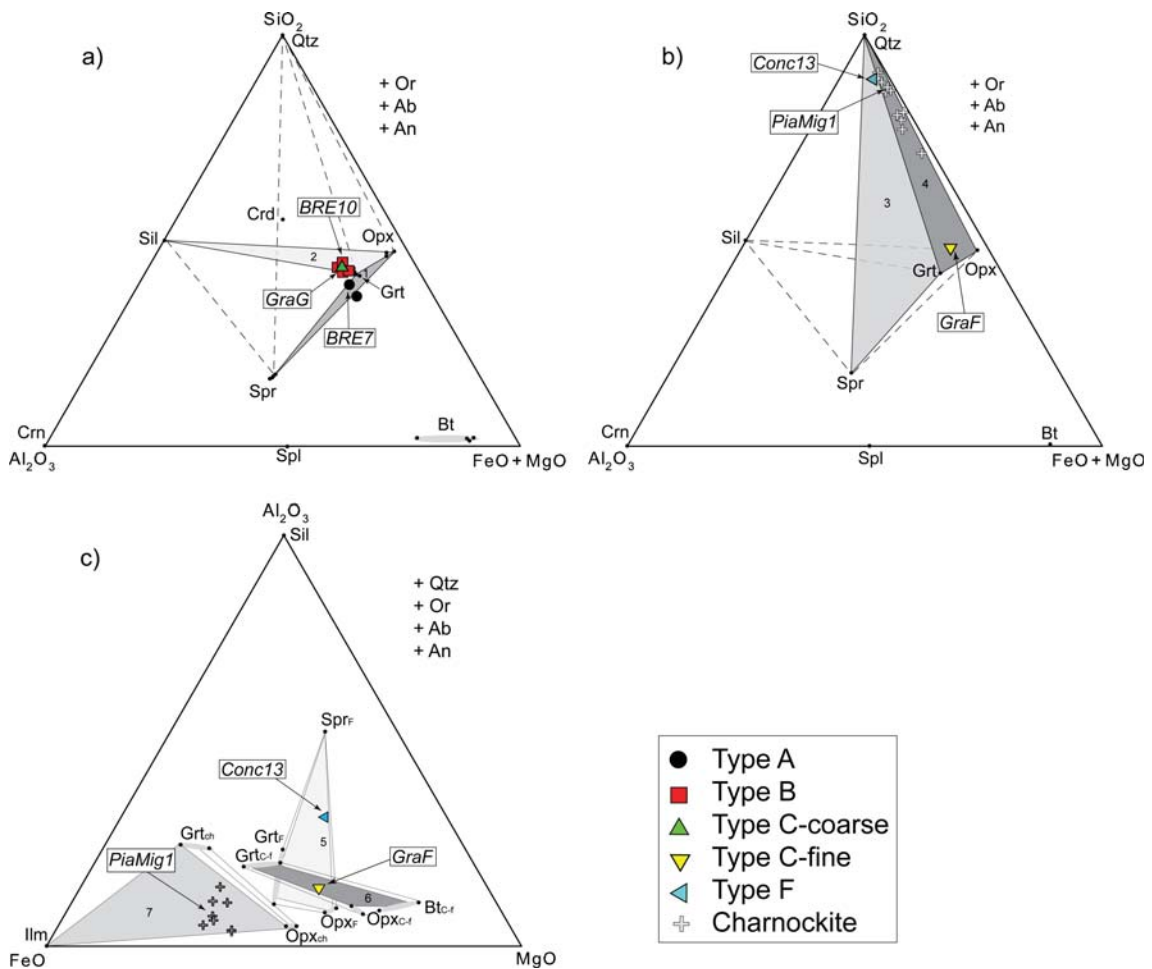
Figure 4.3: *(a-b) MFAS (MgO + FeO - Al_2O_3 - SiO_2) diagram projected from the three feldspar components representing bulk compositions and analysed peak mineral assemblages. Total iron as FeO. This ternary diagram does not display Fe-Mg relations between phases. a) for type A, B granulites and coarse-grained domains of type C; b) for fine-grained domains of type C and F granulites and charnockites; c) AFM (Al_2O_3 - FeO - MgO) diagram projected from quartz and the three feldspar components representing bulk compositions and analysed peak mineral assemblages of type C-fine and F granulites and charnockites.*

Granulite type A is quartz undersaturated (40-42 wt% SiO_2, S/SFM: 59-60), rich in alumina (24-25 wt% Al_2O_3, A/AFM: 25-27) and highly magnesian ($X_{Mg} \sim 0.74$). In a MFAS diagram, (Fig. 4.3a), type A compositions plot on the silica-poor side of the sillimanite-orthopyroxene tie-line, within the sapphirine-garnet-orthopyroxene field (field 1 in Fig. 4.3a).

Type B and *C-coarse granulites* are slightly richer in silica than type A (43-46 wt% SiO_2, S/SFM: 62-63), again containing high alumina contents (23-26 wt% Al_2O_3, A/AFM: 25-29). Type B granulites are more magnesian (X_{Mg}: 0.72-0.76) than type C-coarse ($X_{Mg} \sim 0.58$). In MFAS space, they plot within the sillimanite-garnet-orthopyroxene field (field 2 in Fig. 4.3a), in accordance with the observed sillimanite-bearing, sapphirine-absent peak assemblage.

Type F granulite is considerably richer in silica (~ 71 wt% SiO_2, S/SFM: 92) and poorer in alumina (~ 15 wt% Al_2O_3, A/AFM: 32) than types A, B and C-coarse, with $X_{Mg} \sim 0.63$. In a MFAS diagram, this plots on the alumina-rich side of the garnet-quartz tie-line, within the sapphirine-garnet-quartz triangle (field 3 in Fig. 4.3b). It falls in the sapphirine-orthopyroxene-garnet triangle of an AFM diagram (field 5 in Fig. 4.3c).

Type C-fine granulites and *charnockite* are quartz saturated. However, type C-fine granulites are poorer in silica (~ 49 wt% SiO_2, S/SFM: 65) than charnockite (61-75 wt% SiO_2, S/SFM: 78-95), and are considerably poorer in silica and richer in both iron and magnesium than the type F granulite. Alumina content (~ 16 wt% Al_2O_3) and X_{Mg} (~ 0.60) of type C-fine granulites are similar to type F, but the A/AFM value is lower (A/AFM: 16). Charnockites display variable alumina content (13-19 wt% Al_2O_3, A/AFM: 4-34) and are less magnesian than all granulites (X_{Mg}: 0.30-0.44). In a FMAS diagram, the compositions of both C-fine granulite and charnockite lie on the alumina-poor side of the garnet-quartz tie-line, within the quartz-garnet-orthopyroxene field (labelled 4 in Fig. 4.3b). Type C-fine granulite plots close to the garnet-orthopyroxene tie-line, in accordance with the high proportion of garnet and orthopyroxene in the rock, while charnockites plot much closer to quartz, in agreement with the high amount of quartz observed. In an AFM diagram, type C-fine plots within the orthopyroxene-garnet-biotite field (labelled 6 in Fig. 4.3c), while charnockites plot within the orthopyroxene-garnet-ilmenite triangle (7 in Fig. 4.3c), again in accordance with the observed peak mineral assemblages.

4.1.4   Mineralogical description of granulite types and charnockites

Mineral assemblages and textural relations for the different types of granulites and charnockite are summarized in Tab. 4.1.3. The average relative abundance of the main mineral phases present in each investigated sample is given in the text as vol%.

Dark, massive sapphirine-orthopyroxene-cordierite-garnet granulite (Type A, sample BRE7)

The rock is melanocratic, coarse-grained and massive. The peak metamorphic assemblage contains garnet (20 %), brownish, prismatic orthopyroxene (12 %), dark blue, prismatic sapphirine (20 %), biotite (17 %), and alkali feldspar (8 %). Garnet occurs as large (< 2.5 cm), rounded porphyroblasts with irregular lobate shapes (Fig. 4.4a). Rims are generally replaced by late biotite or lamellar orthopyroxene-cordierite symplectites (Fig. 4.4b). Orthopyroxene (opx_1) forms idiomorphic porphyroblasts up to 4 mm across, with lobate and corroded grain boundaries (Fig. 4.4a). Opx_1 may be intergrown with sapphirine and partially replaced by late biotite. Prismatic sapphirine occurs as idiomorphic porphyroblasts up to 3 mm long (Fig. 4.4a), with inclusions of

sillimanite and spinel (Fig. 4.4c). Generally, sapphirine is separated from the matrix by a thin moat of cordierite or is embayed by orthopyroxene porphyroblasts (Fig. 4.4c). Droop and Bucher-Nurminen (1984) reported rare sapphirine-quartz inclusions in the rims of garnet porphyroblasts. Biotite occurs as millimetric, unoriented flakes in the matrix as part of the peak assemblage or as fine-grained inclusions in garnet and opx_1 porphyroblasts. Alkali feldspar forms microperthitic, xenomorphic porphyroblasts up to 5 mm in size.

Lamellar orthopyroxenes (3 %), cordierite (10 %), plagioclase (2 %) and a late biotite generation (8 %) characterise the post-peak assemblage. Lamellar orthopyroxene (opx_2), together with cordierite, forms symplectitic coronae around garnet porphyroblasts (Fig. 4.4b). Opx_3 with thin interstitial plagioclase patches forms lamellar symplectites at the opx_1-alkali feldspar interface (Fig. 4.4d). Cordierite mantles prismatic sapphirine or, together with opx_2, forms symplectites around garnet (Fig. 4.4b). Plagioclase occurs as interstitial patches between opx_1 and alkali feldspar, rimming opx_3 lamellar symplectites. New biotite flakes grow partly replacing the rims of opx and garnet porphyroblasts.

Spinel and sillimanite are exclusively included in the cores of both prismatic sapphirine and garnet porphyroblasts, and are absent from the matrix. Spinel inclusions, in contact with quartz, as well as spinel-sapphirine-corundum composite inclusions, occur in the rim of garnet porphyroblasts. Corundum, quartz, staurolite, titanite and rutile occur only as inclusions in garnet porphyroblasts.

Dark, massive sapphirine-bearing orthopyroxene-sillimanite-cordierite-garnet granulite (Type B, sample BRE10)

The rock is melanocratic, coarse-grained and massive. The metamorphic peak assemblage is comprised of garnet porphyroblasts (20 %), brownish, prismatic orthopyroxene (12 %), light greyish, prismatic sillimanite (15 %), biotite (20 %), alkali feldspar (10 %) and plagioclase (2 %). Compared to type A granulites, the peak assemblage includes sillimanite but is sapphirine-absent. Garnet occurs as large (< 2.0 cm), xenomorphic, strongly corroded porphyroblasts with irregular shapes. Frequently, garnet is almost completely replaced by opx porphyroblasts or is preserved as disrupted and relict inclusions. Garnet is commonly surrounded by polymineralic post-peak symplectitic coronae of orthopyroxene and cordierite $\pm$ sapphirine and/or spinel. Prismatic orthopyroxene (opx_1) forms large (< 3mm), hypidiomorphic porphyroblasts, in part replaced by late biotite. Common inclusions in prismatic opx_1 are biotite, sillimanite, relicts of garnet porphyroblasts, as well as perthitic alkali feldspar rimmed by a thin film of plagioclase. Opx_1 frequently surrounds garnet porphyroblasts. Coarse prismatic sillimanite porphyroblasts (up to 2-3 mm) are abundant in the matrix. Sillimanite grains are corroded and exhibit an inner symplectitic corona of sapphirine $\pm$ spinel, and an outer moat of cordierite (Fig. 4.4e). Less frequently, relict sillimanite grains are preserved as inclusions in opx porphyroblasts (Fig. 4.4f). Biotite is part of the matrix and occurs as millimetric flakes with a only weak preferred orientation. Alkali feldspar and plagioclase occur as isolated, xenomorphic grains within the matrix. Locally, in silica-poorer micro-domains similar to type A granulite, rare prismatic sapphirine occurs instead of silliman-
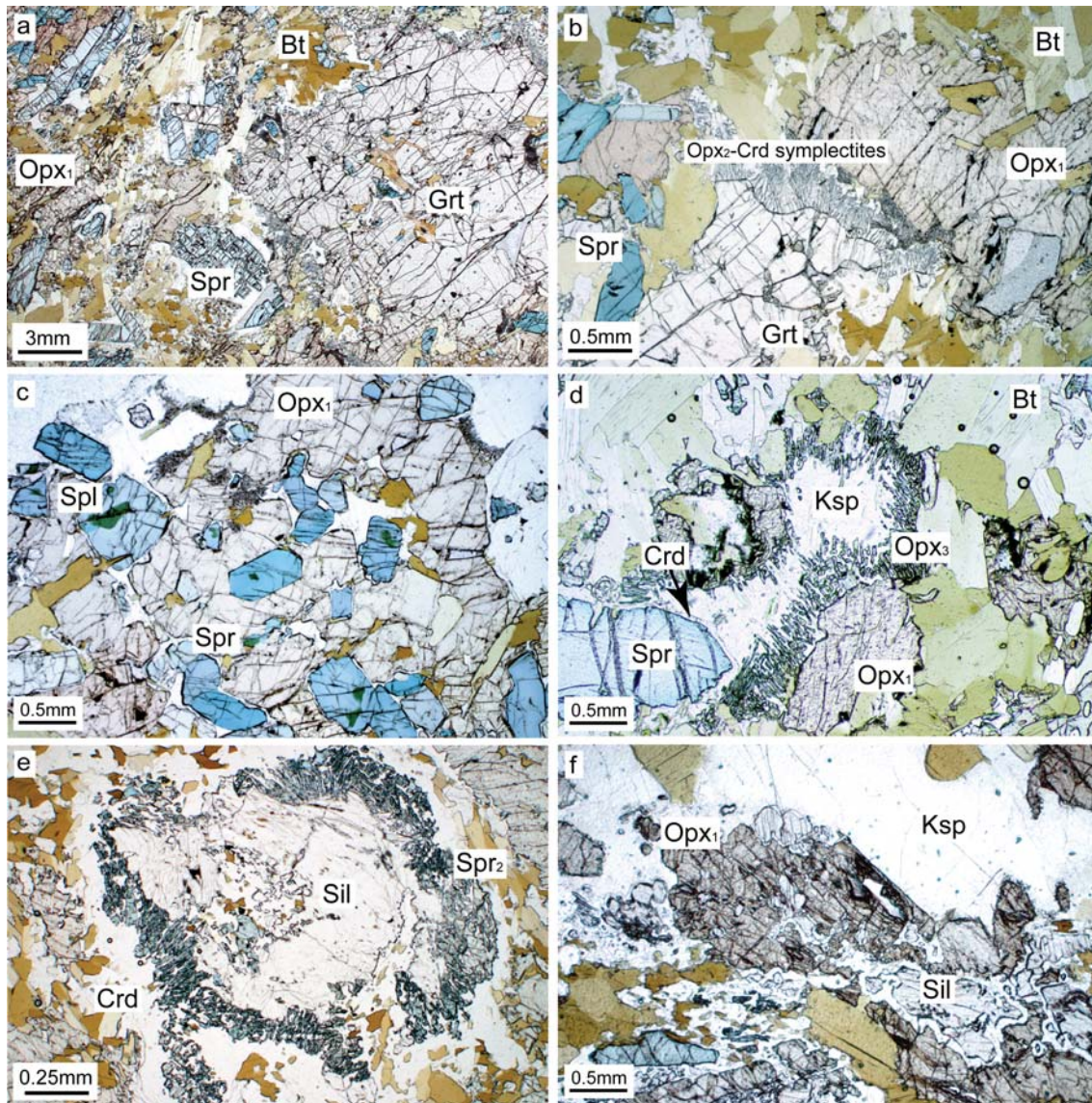
Figure 4.4: *: Photomicrographs of representative mineral assemblages and textural relationships in type A and B granulites: (a) xenomorphic garnet porphyroblast, bluish, prismatic sapphirine and pinkish orthopyroxene porphyroblasts (opx$_1$) and biotite (sample BRE7); (b) opx$_2$-cordierite symplectites replacing mostly garnet porphyroblasts (BRE7); (c) sapphirine grains with spinel inclusions embayed by large opx porphyroblasts (BRE7); (d) orthopyroxene-plagioclase symplectites (opx$_3$) around perthitic alkali feldspar and orthopyroxene porphyroblasts and thin moat of cordierite mantling sapphirine porphyroblast (BRE7); (e) double corona of sapphirine-cordierite symplectites (inner) and cordierite (outer) partially replacing prismatic sillimanite formed via reaction 15 (sample BRE10); (f) relict sillimanite overgrown by orthopyroxene porphyroblasts (BRE10).*

ite as part of the peak assemblage. Such domains are treated as type A granulite and are not representative of type B granulite.

Lamellar sapphirine (4 %), spinel (1 %), orthopyroxene (3 %), cordierite (13 %) and late biotite mark the post-peak assemblage. Sapphirine occurs as symplectitic sapphirine-cordierite ($\pm$ spinel) corona surrounding prismatic sillimanite (Fig. 4.4e). Sapphirine$_2$, together with opx$_2$, spinel and cordierite, forms part of complex symplectites partly replacing garnet. Rare, lamellar spinel grains compose symplectitic coronae around garnet and sillimanite porphyroblasts. Lamellar orthopyroxene shows the same textural pattern as opx$_2$ and opx$_3$ in type A granulites. Cordierite occurs within symplectitic corona around garnet or as corona surrounding sillimanite-sapphirine ($\pm$ spinel) aggregates (Fig. 4.4e). Late biotite shows the same textural relations as in type A granulite. Quartz, titanite and rutile are accessories and occur only as inclusion in garnet porphyroblasts.

Dark, massive orthopyroxene-cordierite-garnet granulite (Type C, samples GraG and GraF)

The rock is melanocratic, massive and characterised by domains of different grain-size and mineral assemblage (Fig. 4.5a). In this study, the coarser-grained rock domains are referred as type C-coarse granulite (sample GraG), while the finer-grained domains are referred as type C-fine granulite (sample GraF).

The metamorphic peak assemblage of type C-coarse granulite consists of garnet (30 %), brownish, prismatic orthopyroxene (28 %), prismatic sillimanite (8 %) and biotite (9 %). Garnet ($<$ 2.0 cm) occurs as rounded grains with lobate shapes and is commonly partly replaced by orthopyroxene, cordierite and late biotite, or occurs as inclusions in opx (Fig. 4.5b). Garnet rarely has symplectitic opx-cordierite coronae. Prismatic orthopyroxene (opx$_1$) forms large ($<$ 1.5 cm), hypidiomorphic porphyroblasts overgrowing sillimanite and garnet (Fig. 4.5b). Prismatic sillimanite is common in the matrix or as needle-like inclusions in opx$_1$ and garnet. The grains generally exhibit an inner symplectitic corona of spinel-cordierite $\pm$ rare sapphirine and an outer corona of cordierite (Fig. 4.5c). Biotite occurs in the matrix as unoriented flakes.

Lamellar orthopyroxene (2 %), spinel (2 %), rare sapphirine (1 %), cordierite (14 %) and late biotite (6 %) form the post-peak mineral assemblage. Lamellar orthopyroxene (opx$_2$), together with cordierite, occurs in symplectites around garnet. Lamellar spinel and rare sapphirine form polymineralic spinel-sapphirine-cordierite coronae, partially or completely replacing prismatic sillimanite, or occurring as tiny inclusions in garnet. Cordierite surrounds garnet porphyroblasts and prismatic sillimanite, while late biotite partly replaces the rims of garnet and orthopyroxene porphyroblasts. Corundum, staurolite, rutile, titanite, apatite, quartz and plagioclase are exclusively observed as inclusions in garnet porphyroblasts. Rarely, sapphirine and quartz included in garnet are in mutual contact (Fig. 4.5d).

The peak mineral assemblage of type C-fine granulite comprises garnet (35 %), orthopyroxene (18 %), biotite (10 %), quartz (10 %), plagioclase (10 %) and alkali feldspar (3 %). Garnet generally occurs as small ($<$ 1 mm), rounded porphyroblasts showing lamellar symplectites of orthopyroxene and cordierite (Figs. 4.5e and 4.5f). Scarce larger garnet grains ($<$ 4 mm) are also present. Orthopyroxene forms hypidiomorphic porphyroblasts, partially replaced by late bi-
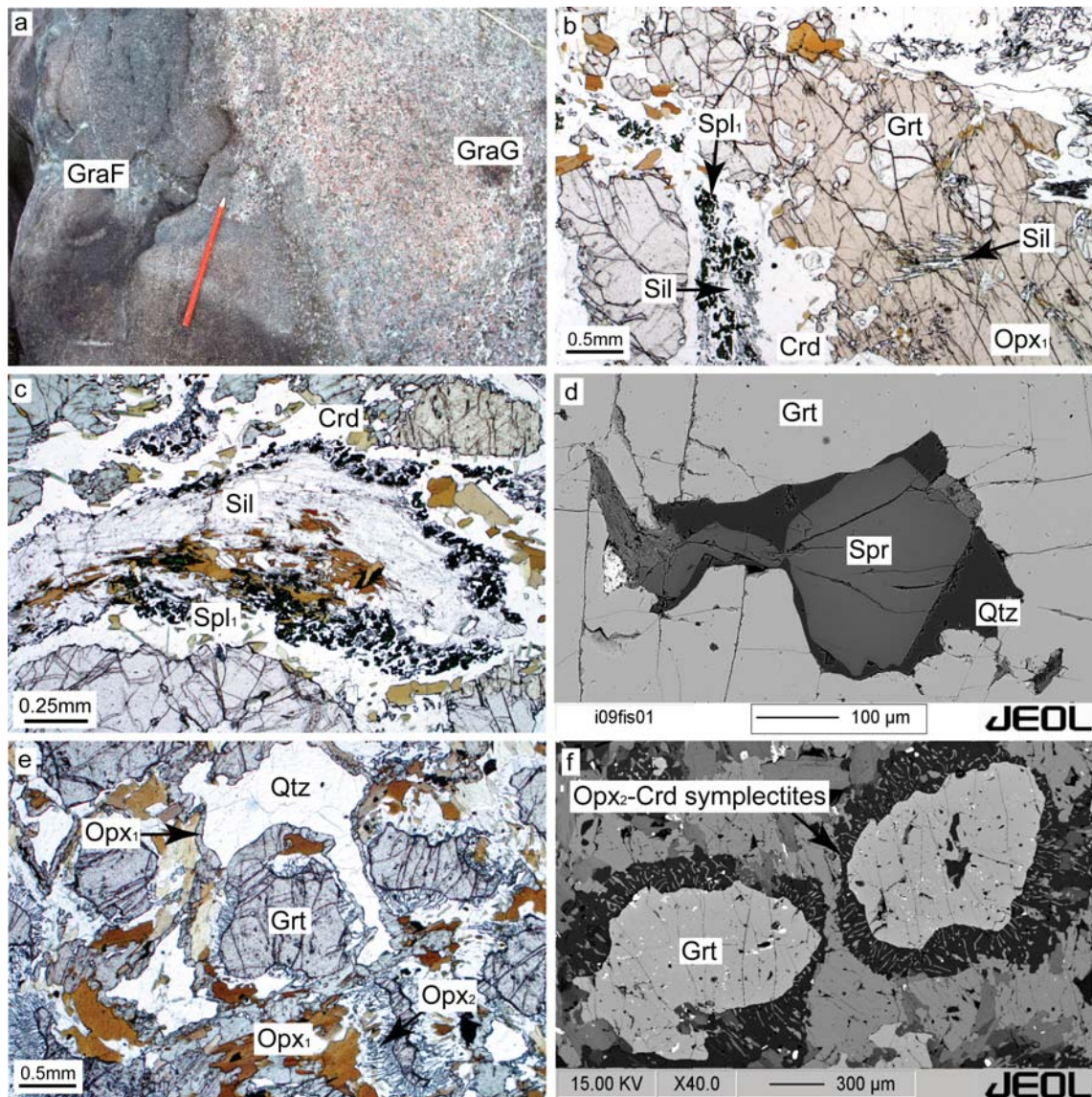
Figure 4.5: *Field aspect and photomicrographs of representative mineral assemblages and textural relationships in type C granulites: (a) boulder of type C granulite showing coarse-grained (type C-coarse, sample GraG, to the right) and finer-grained (type C-fine, sample GraF) domains; (b) orthopyroxene porphyroblast overgrowing garnet and sillimanite grains and spinel-cordierite corona around sillimanite (GraG); (c) sapphirine-spinel-biotite-cordierite corona mantling prismatic sillimanite formed via reaction 15 (GraG); (d) back-scatter image of quartz-sapphirine inclusion in garnet porphyroblast (GraG); (e) opx_1 porphyroblasts partly replaced by biotite, symplectitic opx_2-cordierite mantling garnet formed via reaction 11 and opx_3 coronae around quartz grain formed probably by fluid-absent biotite melting via reaction 2 (GraF); (f) back-scatter image of opx_2-cordierite symplectites around garnet formed via reaction 11 (GraF).*

otite. Commonly, opx mantles quartz grains, separating quartz from biotite (Fig. 4.5e). Biotite forms unoriented flakes. Unlike the type C-coarse granulite, fine-grained domains contain quartz, plagioclase, and alkali feldspar, as part of the matrix.

Lamellar orthopyroxene (4 %), cordierite (5 %) and late biotite (5 %) form the post-peak mineral assemblage. Lamellar orthopyroxene (opx_2), together with cordierite, develops as symplectite around garnet (Fig. 4.5f). Cordierite displays the same textural features as in the type C-coarse granulites. Sapphirine, spinel, sillimanite, apatite, titanite and rutile occur exclusively as inclusions in garnet porphyroblasts.

Dark, foliated sapphirine-orthopyroxene-garnet granulite (Type D, sample CodGra5)

The rock is melanocratic, fine- to medium-grained and weakly foliated. Garnet (15 %), prismatic orthopyroxene (10 %), sapphirine (4 %), biotite (36 %), rare alkali feldspar (2 %) and antipertithic plagioclase (9 %) form the peak mineral assemblage. Garnet occurs as rounded, xenomorphic porphyroblasts (3-4 mm in size). These exhibit irregular, lobate-shaped rims and are strongly replaced by symplectitic aggregates of orthopyroxene, cordierite and plagioclase $\pm$ sapphirine, spinel (Fig. 4.6a). Prismatic orthopyroxene is present as up to 4 mm long and 3 mm wide, hypidiomorphic porphyroblasts, generally embayed by late biotite. Sapphirine (spr_1) occurs in the matrix as prismatic grain strongly replaced by symplectitic aggregates of spinel and plagioclase surrounded by an outer corona of cordierite. Biotite flakes are part of the matrix. Biotite shows a well-developed preferred orientation and defines the main rock foliation. Alkali feldspar and plagioclase compose the matrix.

The post-peak mineral assemblage is marked by lamellar orthoyproxene (5 %), lamellar sapphirine (6 %), spinel (4 %), cordierite (5 %) and late biotite (4 %). Lamellar orthopyroxene (opx_2) forms part of lobate opx_2-cordierite-plagioclase $\pm$ sapphirine$_2$ $\pm$ spinel symplectites, mantling and partly replacing garnet porphyroblasts. Opx_2 is often surrounded by a thin film of plagioclase. Intergrowths of opx_2-plagioclase-cordierite-sapphirine$_2$ can completely replace garnet porphyroblasts (Fig. 4.6b). Opx_3 forms lamellar aggregates between porphyroblastic opx_1 and plagioclase. Lamellar sapphirine$_2$ is part of opx_2-cordierite-plagioclase-sapphirine$_2$ $\pm$ spinel symplectites around garnet porphyroblasts. Spinel, together with sapphirine$_2$, plagioclase, opx_2 and cordierite, forms lamellar symplectites surrounding garnet porphyroblasts and, together with plagioclase and cordierite partly replaces spr_1. Cordierite occurs in coronae around garnet porphyroblasts and sapphirine$_1$-plagioclase-spinel symplectites. Late biotite partly replaces garnet and orthopyroxene porphyroblasts. Apatite, sillimanite and rutile are accessories and occur as inclusions in garnet porphyroblasts.

Felsic, foliated sapphirine-bearing orthopyroxene-garnet granulite (Type E, sample PiaGra1)

The rock is more leucocratic than other granulite types and is foliated. Garnet porphyroblasts (10 %), prismatic orthopyroxene (10 %), sapphirine (1 %), biotite (32 %), quartz (15 %), plagioclase (15 %) and perthitic alkali feldspar (10 %) compose the metamorphic peak mineral assemblage.
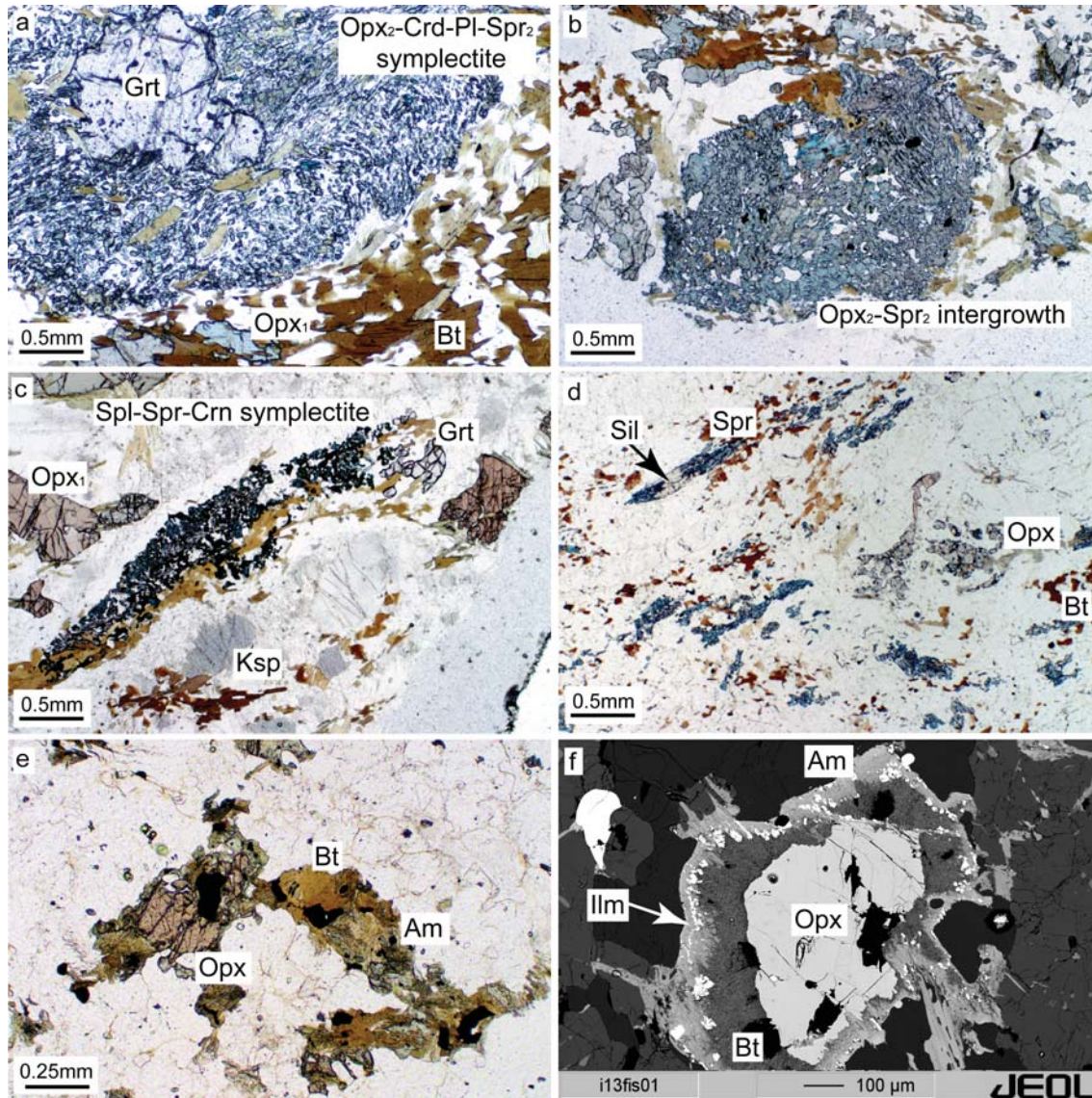
Figure 4.6: *Photomicrographs of representative mineral assemblages and textural relationships in type D, E and F granulites and in charnockites: (a) opx-cordierite-plagioclase-sapphirine symplectite replacing garnet porphyroblast via reaction 12 (sample CodGra5); (b) orthopyroxene-sapphirine intergrowth pseudomorph after garnet formed via reaction 12 (CodGra5); (c) spinel-sapphirine-corundum symplectites formed via reaction 9 (sample PiaGra1); (d) sillimanite replaced by sapphirine-plagioclase symplectites and relictic opx (Conc13); (e) orthopyroxene porphyroblast displaying biotite-amphibole coronae (sample PiaMig1); (f) back-scatter image of biotite-ilmenite-amphibole coronae surrounding orthopyroxene (PiaMig1).*

Garnet occurs in two generations. $Garnet_1$ consists in coarse-grained, up to 1.5 cm across, atoll-like, hypidiomorphic porphyroblasts wrapped by the foliation. The grains are rounded and show irregular lobate shapes. Late biotite and chlorite coronae commonly surround the porphyroblasts. $Garnet_2$ occurs as < 0.2 mm, xenomorphic grains overgrowing the main foliation. Orthopyroxene forms hypidiomorphic porphyroblasts, commonly surrounded by late biotite coronae or partially replaced by lamellar symplectites of biotite-quartz. The grains are weakly oriented subparallel to the main foliation. Sapphirine occur in lobate sapphirine-plagioclase symplectites, mantled by equant spinel grains. These aggregates are elongated within the rock foliation and partly or completely replace former relict sillimanite or corundum (Fig. 4.6c). Biotite is abundant in the rock matrix occuring as fine-grained flakes (< 0.2 mm) that delineate a pronounced preferred orientation defining the main rock foliation. Slightly oriented quartz, plagioclase and perthitic alkali feldspar are present in the rock matrix as fine-grained (< 0.2 mm) interstitial aggregates.

Spinel (2 %), late biotite (4 %) and chlorite (2 %) form the post-peak mineral assemblage. Spinel occurs in sapphirine-plagioclase-spinel symplectites, mantling sapphirine grains. Late biotite and chlorite develop at the garnet and orthopyroxene rims. Relict corundum and sillimanite are preserevd in minor amount as strongly replaced pre-peak mineral phases displaying sapphirine-plagioclase-spinel symplectites (Fig. 4.6c). titanite, zircon and monazite are accessories.

Felsic, foliated sapphirine-orthopyroxene granulite (Type F, sample Conc13)

These granulites are leucocratic, medium- to coarse-grained and foliated. The metamorphic peak mineral assemblage comprises garnet (3 %), orthopyroxene (3 %), sapphirine (5 %), biotite (4 %), quartz (36 %), plagioclase (31 %) and alkali feldspar (10 %). Garnet and orthopyroxene occur as 1-2 mm large, strongly corroded, xenomorphic porphyroblasts displaying irregular lobate shapes (Fig. 4.6d). Sapphirine forms up to 1 mm long lamellar aggregates which partially or completely substitute prismatic sillimanite (Fig. 4.6d). The aggregates are elongated within the main foliation and commonly display symplectitic coronae of equant spinel and plagioclase. Biotite forms rare brownish, fine-grained (< 0.1 mm) patches in the matrix showing a weak preferred shape orientation. Elongated and oriented quartz grains up to 3 mm in length and 1 mm in width, granoblastic aggregates of plagioclase and subordinate perthitic alkali feldspar compose the rock matrix.

Spinel (2 %), late biotite (1 %) and a second plagioclase generation (4 %) form the post-peak mineral assemblage. Lamellar spinel and late plagioclase form symplectitic aggregates around sapphirine. Late biotite partly replaces orthopyroxene and garnet porphyroblasts. Prismatic sillimanite (1 %) occasionally preserved in the cores of sapphirine and rare, fine-grained spinel inclusions in garnet are interpreted as relics of the pre-peak mineral assemblage. Ilmenite, apatite, monazite and zircon are accessories.

Charnockite

Charnockites are leucocratic, medium- to coarse-grained and weakly foliated. These rocks are composed of quartz (40 %), plagioclase (30 %), perthitic alkali feldspar (15 %), rounded garnet

(5 %), brownish orthopyroxene (5 %), rare biotite (3 %) and ilmenite (1 %). Amphibole, rutile, apatite and zircon are accessories.

Garnet is present as tiny (< 0.5 mm), subrounded, hypidiomorphic grains showing irregular edges. Garnet is commonly partly substituted by late biotite. Orthopyroxene occurs as small (up to 0.5 mm), hypidiomorphic porphyroblasts. The grains are frequently corroded or partially replaced by polymineralic coronae of late biotite, amphibole and late ilmenite (Figs. 4.6e and f). Biotite forms part of the metamorphic peak mineral assemblage and occurs as rare, slightly oriented, small flakes (up to 0.5 mm). Ilmenite occurs as xenomorphic grains in the matrix. Late $biotite_2$ grows at the expense of garnet or, together with amphibole and $ilmenite_2$, surrounding opx porphyroblasts. Amphibole occurs exclusively as post-peak phase partly replacing opx. Quartz, plagioclase and perthitic alkali feldspar form the rock matrix. Generally, grains are slightly elongated and, together with rare biotite1, define the main rock foliation.

4.1.5 Mineral chemistry

Mineral chemical compositions were obtained using the electron microprobe JEOL-8200 at ETH Zurich. Operating conditions for spot analyses were 15 kV accelerating voltage, 20 nA sample current, 40s counting time and beam size < 5 μm. Natural and synthetic standards were used for calibration. Minerals were analysed for SiO_2, TiO_2, Cr_2O_3, Al_2O_3, FeO, MnO, MgO, CaO, Na_2O, K_2O. Fe^{3+} was calculated from charge balance. Ferric iron in sapphirine was estimated using the approach of Higgins *et al.* (1979): $^{VI}Fe^{3+} = {}^{IV}Al^{3+} - ({}^{VI}Al + Cr^{tot})$. Representative mineral data are presented in Tabs. G.1.1-G.1.4.

Garnet

Garnets in granulite types A, B, C-coarse, D and E (Fig. 4.7a and Tab. G.1.1) are almost pure pyrope-almandine solid solutions with small grossular and spessartine components (Xgrs < 0.05, Xsps < 0.03). Garnets in types A, B, C-coarse and D granulites are relatively richer in magnesium (X_{pyr}: 0.45-0.57) than garnets of type E (X_{pyr}: 0.38-0.41). Garnets in type C-fine and F granulites are generally richer in iron (X_{pyr}: 0.35-0.48) than granulites type A, B and C-coarse and show variable grossular content (X_{grs}: 0.03-0.13). Garnets of charnockites are considerably richer in iron (X_{pyr}: 0.21-0.27) than garnets in granulites and display low grossular (X_{grs}: 0.04-0.05) and spessartine (X_{sps}: 0.05-0.07) contents.

Different zoning patterns exist. Most garnet porphyroblasts are characterised by decreasing Mg content and slightly increasing Fe^{2+}, Ca and Mn towards the rim. Some garnet porphyroblasts in granulites of types A, B and C-fine exhibit more complex 4-phase zoning features. Two major patterns are recognized in type A and B granulites (see also Droop and Bucher-Nurminen, 1984; Schefer, 2005):

    (i) a large homogeneous core, an inner zone of rimwards decreasing Mg and increasing Ca, an outer zone of increasing Mg and decreasing Ca and Fe^{2+}, and a rim with decreasing Mg, and slightly increasing Ca and Mn;
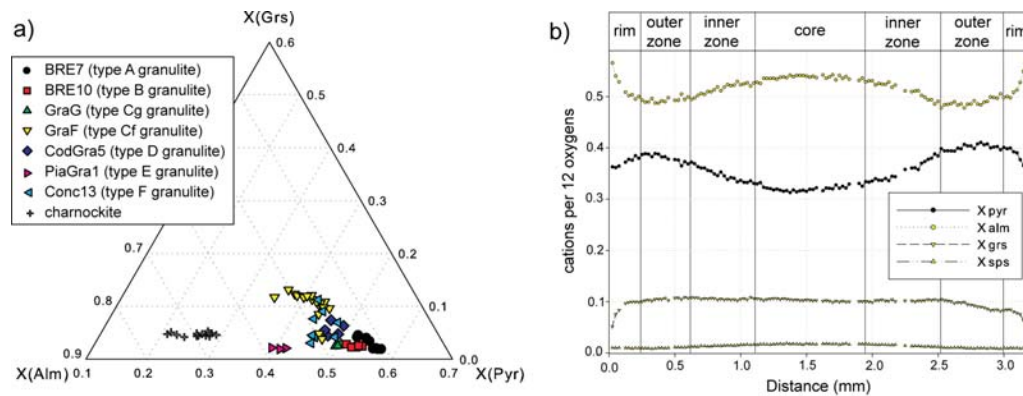
Figure 4.7: *((a) Compositions of garnet porphyroblast cores; (b) chemical zoning pattern of garnet porphyroblast in sample GraF (type C-fine granulite).*

(ii) a homogeneous core, an inner zone of rimwards sharply increasing Mg and decreasing Fe^{2+}, Ca and Mn, an outer zone of gently decreasing Mg and increasing Fe^{2+}, and a rim of abrupt decrease of Mg and increase of Fe^{2+}. Garnets in type C-fine granulites display a homogeneous core, an inner zone of rimwards increasing Mg and decreasing Fe^{2+}, an outer zone of homogeneous Mg and Fe^{2+} but gently decreasing Ca, and a rim of abruptly increasing Fe^{2+} and strongly decreasing Mg and Ca (Fig. 4.7b).

These complex zoning patterns suggest that the rocks underwent multiple stages of equilibrium. Zoning pattern i) in type A and B granulites probably formed as a consequence of (re)-heating after a period of homogenisation of the garnet core. In contrast, zoning pattern ii) in type A and B granulites and zoning in type C-fine granulite may reflect prograde garnet growth during heating and progressive extraction of melt, leading to the observed increase of X_{pyr} from the core rimwards (Fig. 4.7b).

Orthopyroxene

The composition of orthopyroxene varies with its texture (Fig. 4.8a and Tab. G.1.2). In type A, B and C-coarse granulites, the highest Al_2O_3 contents are preserved in the core of large opx_1 (7.6-9.8 wt% Al_2O_3 in types A and B; 8.7-9.3 wt% Al_2O_3 in type C-coarse), steeply decreasing rimwards probably due to decreasing metamorphic conditions (5.7-6.7 wt% Al_2O_3 in types A; 4.7-5.5 wt% Al_2O_3 in type B; 5.8-6.4 wt% Al_2O_3 in type C-coarse). In type C-fine and D granulites, opx_1 show an increase in Al_2O_3 from a broad core relatively poor in alumina (3.5-4.8 wt% Al_2O_3 in type C-fine; 4.7-5.5 wt% Al_2O_3 in type D) to narrow rims rich in alumina (8.0-8.8 wt% Al_2O_3 in type C-fine; 7.0-7.9 wt% Al_2O_3 in type D), while X_{Mg} decreases more regularly rimwards (Fig. 4.8b). This zoning probably reflects heating and prograde orthopyroxene growth occured during progressive melt extraction. Small opx blasts from type E granulites are unzoned and show a low Al_2O_3-content of 5.7-6.6 wt% and X_{Mg} values of about 0.64. Opx porphyroblasts of type F granulites has high Al_2O_3-content of 8.13-10.15 wt% but low X_{Mg} values of 0.58-0.60. Opx in

charnockites exhibits low Al_2O_3-content of 4.3-4.7 wt% and X_{Mg} of 0.51-0.53.
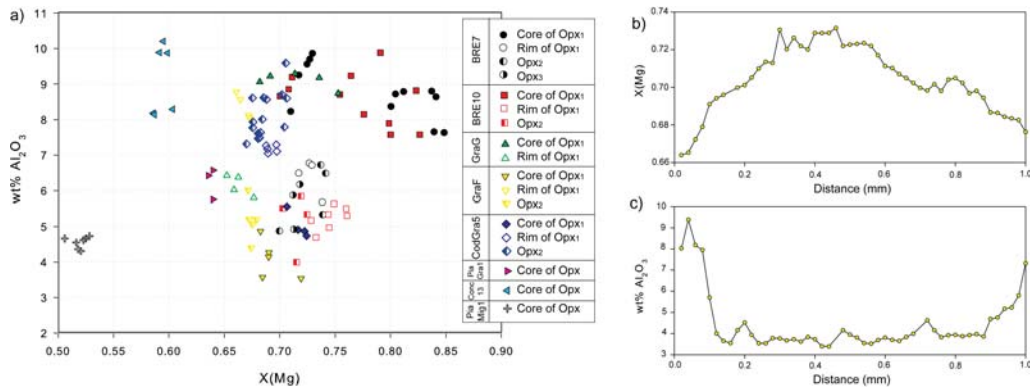
Figure 4.8: *(a) Composition of different textural types of orthopyroxene in Al_2O_3 vs. X_{Mg} space; (b) X_{Mg} zoning in orthopyroxene porphyroblast in sample GraF (type C-fine granulite); c) Al_2O_3 zoning in orthopyroxene porphyroblast in sample GraF (type C-fine granulite)*

Symplectitic opx_2 and opx_3 in types A and B granulites display similar X_{Mg} and slightly lower Al_2O_3 contents (4.9-6.7 wt% Al_2O_3 in type A; 4.9-5.8 wt% Al_2O_3 in type B) than porphyroblast rims. Opx_2 symplectites in type C-fine granulites have an intermediate composition between porphyroblast core and rim (4.4-5.9 wt% Al_2O_3), whilst opx_2 of type D granulites are richer in alumina than opx_1 rims (7.9-8.6 wt% Al_2O_3). In general, Fe^{3+} represents less than 13% of Fe^{tot}, except for type C-coarse and type D granulites which have $Fe^{3+} \sim$ 17-20%. No systematic zoning of Fe^{3+} has been noticed.

Sapphirine

Sapphirine in type A granulite display an intermediate (Fe^{tot} + Mg):Al_2:Si composition between 2:2:1 and 7:9:3 (Fig. 4.9a and Tab. G.1.3) and a X_{Mg} value gently decreasing towards the rim from 0.81-0.86 in the core to 0.76-0.81 at the rim. Symplectitic sapphirine shows a wider compositional range. Lamellar sapphirine symplectites in type B and E granulites are relatively rich in alumina and poor in silica respect to sapphirine porphyroblasts and have a $X_{Mg} \sim$ 0.73-0.82 and $X_{Mg} \sim$ 0.67-0.68, respectively. Symplectitic sapphirine grains in type C-coarse granulites display a similar Si-content as symplectitic sapphirine in type B and E granulites but are poorer in alumina, with a $X_{Mg} \sim$ 0.70-0.75. Symplectitic sapphirines in type D and F granulites exhibit a strong compositional variation and have $X_{Mg} \sim$ 0.71-0.73 and 0.67-0.69 respectively. All textural types of analysed sapphirine lie off the ideal line of Tschermak's substitution ($Al_2Si_{-1}Mg_{-1}$), suggesting a considerable incorporation of Fe^{3+} in the structure. Similarly to opx, sapphirine in type C-coarse and type D granulites show the highest Fe^{3+} content. Estimates of ferric iron content after Higgins *et al.* (1979) yield for all analysed samples Fe^{3+}/Fe^{tot} values of $\sim$ 0.15-0.30.
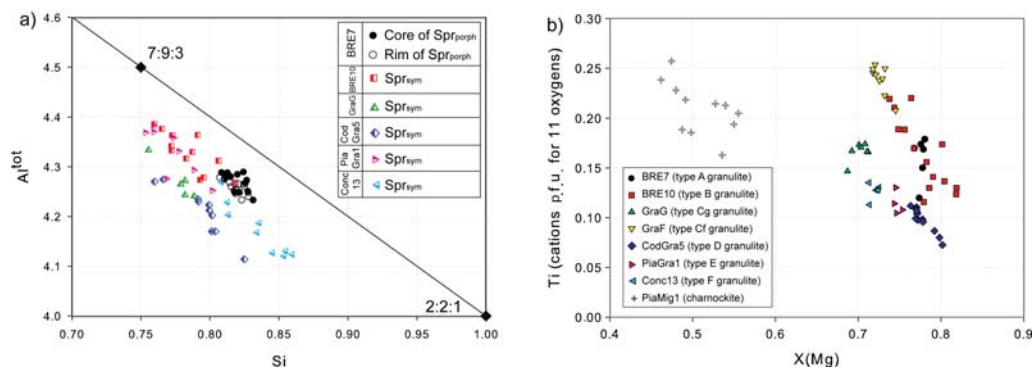
Figure 4.9: *(a) Composition of different textural types of sapphirine in the Al vs. Si diagram (a.p.f.u. for 10 oxygens). 7:9:3 and 2:2:1 in the figure imply representative compositions of $Mg_{1.75}Al_{0.45}Si_{0.75}O_{10}$ and $Mg_2Al_4SiO_{10}$, respectively; (b) composition of biotite in Ti vs. X_{Mg} space.*

Biotite

Biotite from all different types of granulites is highly magnesian with $X_{Mg} = 0.69\text{-}0.82$ and is rich in titanium (0.07-0.25 Ti p.f.u. calculated for 11 oxygens). Biotite in type A, B and D granulites displays the highest X_{Mg} values of 0.76-0.82, reflecting the highest bulk-rock X_{Mg}, whereas biotite in charnockites is considerably less magnesian with $X_{Mg} \sim 0.45\text{-}0.64$ (Tab. G.1.4). In general, biotite in granulites, particularly in types C-fine, D and E, shows a negative correlation between X_{Mg} and Ti (Fig. 4.9b).

Cordierite

Cordierite has a homogeneous, highly magnesian composition in all analysed samples (Tab. G.1.4) with X_{Mg} values comprised between 0.81 and 0.90. No relevant compositional variations between different textural types have been observed. The total sum of oxides is much lower than 100%, suggesting the presence of $H_2O + CO_2$ in the structure.

Spinel

Spinel is a hercynite - spinel solid solution (Tab. G.1.3) with very low Cr_2O_3 contents (< 0.10 wt%). Spinel inclusions in garnet and prismatic sapphirine in type A granulites yield high X_{Mg} values of 0.45-0.53. Symplectitic spinel mantling sillimanite or spinels forming lobate symplectites are generally less magnesian with X_{Mg} values from 0.26 to 0.45. Spinel inclusions are richer in Fe^{3+} ($Fe^{3+}/Fe^{tot} \sim 11\text{-}25$ %) than symplectitic spinels ($Fe^{3+}/Fe^{tot} \sim 5\text{-}14$ %).

Plagioclase

Plagioclase compositions vary strongly with granulite type (Tab. G.1.4). Matrix plagioclase of type C-fine granulites has the highest X_{An} of 0.57-0.76. Plagioclase in the matrix of type F granulites has $X_{An} = 0.44\text{-}0.57$, matrix plagioclase of type D granulites have $X_{An} = 0.38\text{-}0.44$,

whereas matrix plagioclase of type E granulites and charnockites have X_{An} = 0.12-0.30. Within individual samples, plagioclase grains in symplectites with sapphirine $\pm$ spinel in type D and E granulites are slightly more anorthitic than matrix plagioclase, displaying a X_{An} = 0.41-0.55 and X_{An} = 0.25-0.34, respectively.

4.1.6 Textural evolution

Mg-Al-rich granulites preserve reaction textures such as coronae and symplectites that allow deciphering their metamorphic history. Textures achieved during the prograde evolution are rare and usually overprinted by metamorphic peak or post-peak assemblages. More frequently, high-grade rocks display reaction textures developed at lower grade conditions. This may help to constrain part of their metamorphic evolution, for example allowing post-peak isothermal decompression to be distinguished from isobaric cooling (Harley, 1989), so that a high-grade terrain can be assigned to a specific tectonic framework (Ellis, 1987; Bohlen, 1991; Platt *et al.*, 1998).

Prograde evolution

Earliest recognizable mineral assemblage

Information on the early metamorphic history of the Gruf granulites is essentially provided only by inclusions in the cores of porphyroblasts in type A and C-coarse granulites. Staurolite inclusions in garnet cores of both types of granulite, together with quartz, plagioclase, biotite and alumosilicate inclusions, represent parts of the earliest preserved mineral assemblage. The reaction

$$St = Grt + Spl + Ky/Sil + H_2O \qquad (4.1)$$

was experimentally calibrated by Richardson (1968) and may explain the widespread occurrence of spinel and composite staurolite-spinel inclusions in garnet porphyroblasts, probably formed during granulite metamorphism of earlier amphibolite facies staurolite-quartz assemblages.

Prismatic sillimanite in type B and type C-coarse granulites (Fig. 4.4e and Fig. 4.5c) resembles in both shape and internal structure the sillimanite pseudomorphs after kyanite described by Lal *et al.* (1984), Raith *et al.* (1997) and Tong and Wilson (2006). We thus propose that kyanite was the stable Al_2SiO_5 polymorph during the earlier metamorphic history.

Heating and partial melting

We suggest that during prograde heating the early mineral assemblage was involved in a series of fluid-absent biotite melting reactions affecting all investigated types of granulite. Melting most likely persisted until the thermal peak was attained. Melting is held responsible for the partial or complete consumption of quartz and/or biotite from the rock matrix and for the production of

garnet and orthopyroxene porphyroblasts. The macroscopically observable segregation of melt led to the development of orthopyroxene-bearing leucosome (charnockite, although we note that this almost certainly does not record any single pristine extracted melt composition) and residual melanosome (granulite) domains. Experimentally calibrated melting reactions in the meta-aluminous system are:

$$Qtz + Bt = Opx + Kfs + melt \qquad (4.2)$$

$$Qtz + Bt = Grt + Kfs + melt \qquad (4.3)$$

$$Qtz + Bt = Grt + Opx + Kfs + melt \qquad (4.4)$$

$$Qtz + Bt + Pl = Grt + Opx + Kfs + melt \qquad (4.5)$$
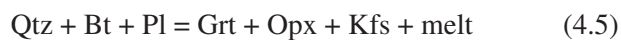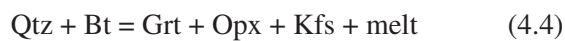
(Vielzeuf and Holloway, 1988; Vielzeuf and Montel, 1994; Clemens *et al.*, 1997), whereas possible melting reactions in more aluminous systems are:

$$Bt + Sil + Qtz = Spr + Ksp + melt \qquad (4.6)$$

$$Bt + Sil + Spl = Opx + Spr + Ksp + melt \qquad (4.7)$$
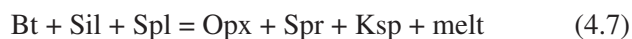
(Hensen and Harley, 1990). Reactions (4.2) to (4.5) explain the common occurrence of biotite and quartz inclusions in orthopyroxene and garnet in type C-fine, E, and F granulites and charnockite, as well as the orthopyroxene coronae separating quartz from biotite in type C-fine granulites (Fig. 4.5e). Reactions (4.6) and (4.7) led to the formation of sapphirine porphyroblasts in the rock matrix of type A, D and F granulites, and explain the occurrence of spinel (in type A granulite) and rare sillimanite (in type A and F granulites) inclusions in prismatic sapphirine porphyroblasts (Fig. 4.4c). Reaction (4.6) would also account for the rare occurrence of composite sapphirine-quartz inclusions in the rims of garnet porphyroblasts in type A and C-coarse granulites. During the melting event, early spinel was consumed from the matrix of type A granulites and is pre-

served exclusively as inclusions in prismatic sapphirine (Fig. 4.4c) and in garnet porphyroblasts. Composite inclusions of spinel-corundum and spinel-sapphirine-corundum in garnets from type A granulites result from the completed reaction

$$Spl + Sil = Grt + Crn \qquad (4.8)$$
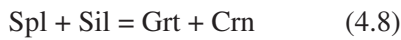
(which exhausted sillimanite), and from the equilibrium

$$Grt + Spl + Crn = Spr \qquad (4.9)$$
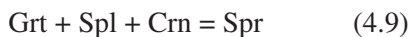
Reaction (4.9) also explains the prograde consumption of corundum from the matrix of type E granulites, where resorption of corundum and garnet by sapphirine, which is typically attributed to heating (Kelsey *et al.*, 2005), led to the formation of the observed corundum-sapphirine-spinel symplectites (Fig. 4.6c).

Post-peak evolution

The post-peak evolution is characterised by the development of complex symplectitic textures. As proposed by Fyfe (1973), Powell (1983), Waters (1988), Powell and Downes (1990) and White and Powell (2002), we suggest that substantial melt and H_2O loss may have precluded the completion of retrograde reactions, preserving parts of the peak mineral assemblages.

Textures involving garnet

In type A - D granulites, garnet porphyroblasts generally display polymineralic symplectitic coronae (Figs. 4.4a and b, Figs. 4.5e and 6 and Fig. 4.6a). As proposed by Droop and Bucher-Nurminen (1984), the reaction

$$Grt + Kfs + H_2O = Opx + Crd + Bt \qquad (4.10)$$
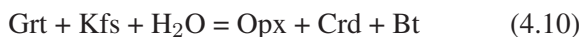
accounts for both the observed opx-cordierite symplectites between garnet and orthopyroxene (e.g. Fig. 4.4b) and the biotite coronae around garnet. In the quartz-bearing type C-fine granulites (Figs. 4.5e and f) the same texture could also be formed by the reaction

$$Grt + Qtz = Opx_{sym} + Crd \qquad (4.11)$$
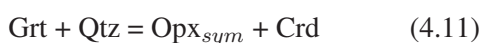
(experimentally calibrated by Hensen (1970) and Schreyer and Abraham (1978)). However, it is unlikely that reaction (4.11) accounts for the formation of opx-cordierite symplectites in type A,

B and D granulites, where quartz was probably exhausted during partial melting. We interpret the formation of composite symplectites of orthopyroxene, cordierite, sapphirine and spinel in type B and D granulites (Fig. 4.6a) as the result of reactions

$$Grt = Opx + Spr + Crd\ (\pm\ Pl) \qquad (4.12)$$

$$Grt = Opx + Spl + Crd\ (\pm\ Pl) \qquad (4.13)$$

(Hensen, 1971). Reaction (4.12) also explains the opx-sapphirine intergrowth pseudomorph after garnet, as observed in type D granulites (Fig. 4.6b). The same intergrowth is commonly substituted by spinel and cordierite, probably via the reaction

$$Spr + Opx = Crd + Spl \qquad (4.14)$$
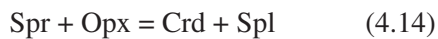
which is rendered possible through the involvement of significant Fe^{3+}.

Textures involving sillimanite

In type B and C-coarse granulites, prismatic sillimanite is typically mantled by composite symplectitic coronae and moats of sapphirine-cordierite $\pm$ spinel, biotite (Fig. 4.4e and Fig. 4.5c). The reactions

$$Sil + Opx = Spr + Crd \qquad (4.15)$$

$$Sil + Grt = Spr + Crd \qquad (4.16)$$
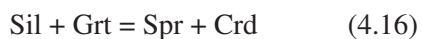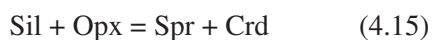
(Schreyer, 1970; Hensen, 1971) account for the formation of sapphirine-cordierite coronae, whereas the reaction

$$Spr = Spl + Crd \qquad (4.17)$$

explains the growth of fine-grained spinel at the expenses of symplectitic sapphirine (Fig. 4.5c).

4.1.7   P-T estimates

Prograde conditions

The quantitative reconstruction of the prograde segment of a PT path for granulite facies rocks is generally problematic because of i) overprinting of the earliest mineral assemblages by peak and/or post-peak mineral assemblages; ii) resetting of original phase compositions during the metamorphic evolution; and iii) modification of the original bulk composition through melt loss.

Nevertheless, we reconstruct the early metamorphic history of the Gruf granulites and charnockites by combining available experimental data for pelitic and semi-pelitic compositions (Fig. 4.10). Metamorphic evolution probably began in the stability field of kyanite, with increasing temperature leading to the formation of sillimanite pseudomorphs after kyanite (Fig. 4.4e). At approximately 840 °C and 9-10 kbar, reactions (4.8) and (4.9) occurred in granulite types A and C-coarse, producing corundum and sapphirine grains now preserved as corundum and sapphirine-corundum-spinel inclusions in garnet porphyroblasts. At approximately 875 °C, the upper stability limit of staurolite was overstepped, consuming staurolite from the matrix via reaction (4.1) (Richardson, 1968). However, rare staurolite grains have been trapped as "relict" inclusions in garnet porphyroblasts of type A and C-coarse granulites. Fluid-absent biotite melting experiments on magnesian pelites and metagreywackes topologically analysed in the system KFMASH (Vielzeuf and Holloway, 1988; Hensen and Harley, 1990; Vielzeuf and Montel, 1994; Clemens *et al.*, 1997) show that further heating would progressively lead to reactions (4.2), (4.4) and (4.7) in all granulite types at temperatures to 900 °C, producing coarse-grained opx, garnet and sapphirine porphyroblasts. However, experiments in the system KFMASNaCaTi (Stevens *et al.*, 1997) indicate that Ti will stabilize biotite to approximately 40-50 °C higher temperature. In accordance with the high-Ti character of the biotite observed in all of our granulite types (Fig. 4.9b), reactions (4.2), (4.4) and (4.7) may thus have been completed to temperatures of 930-940 °C.

Metamorphic peak conditions

Three approaches have been applied and compared in order to calculate metamorphic peak conditions:

   (i) conventional geothermobarometry,

  (ii) P-T pseudosections,

 (iii) contouring of P-T pseudosection for Al-in-orthopyroxene.

Conventional thermobarometry

The most robust available mineral composition thermobarometers consider the Al content of orthopyroxene coexisting with garnet, because of the relative immobility of Al with respect to Fe-Mg (Harley and Green, 1982; Aranovich and Berman, 1997). Resetting of mineral chemistry during
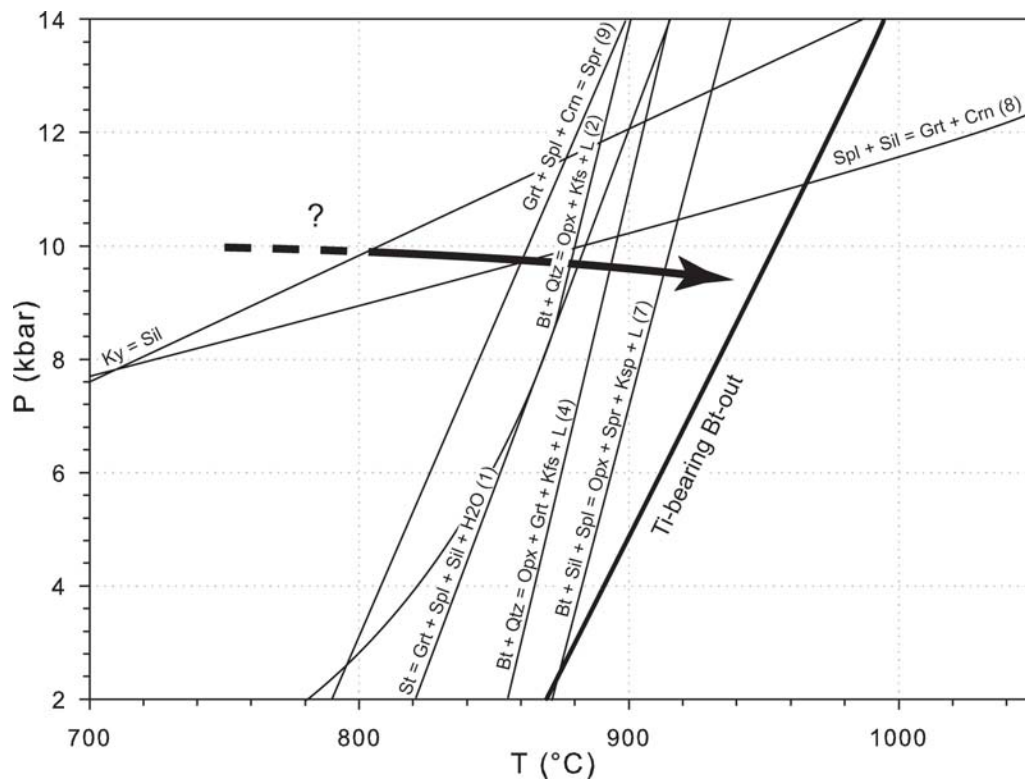
Figure 4.10: *P-T diagram showing the locations of experimentally determined reactions occurred during prograde metamorphism. References for reactions in the text. Upper stability of Ti-bearing biotite after Stevens* et al. *(1997).*

cooling and/or retrograde metamorphism is a major source of uncertainty when applying conventional thermobarometry particularly for those based on Fe-Mg exchange to high-grade rocks (Frost and Chacko, 1989). This has partly been overcome by employing retrieval techniques (Fitzsimons and Harley, 1994; Pattison and Begin, 1994; Pattison *et al.*, 2003) in which measured Fe-Mg mineral compositions are corrected such that calculated temperatures converge in PT space with those derived from the Al content.

We estimated metamorphic peak-conditions for granulites and charnockites using the orthopyroxene -garnet thermobarometers of both Harley and Green (1982) and Aranovich and Berman (1997), and we performed correction for Fe-Mg diffusion with the program RCLC-P (Pattison *et al.*, 2003). For granulite types A, B, C-coarse and E, and for charnockites, average core compositions of garnet and orthopyroxene porphyroblasts were chosen for the calculation. Based on increasing alumina contents towards the rim of orthopyroxene porphyroblasts of type D granulites, we paired average garnet core composition with average orthopyroxene rim composition for this rock type, inferred to represent equilibrated mineral compositions at the peak of metamorphism. Due to the complex zoning displayed by garnet and opx porphyroblasts in type C-fine granulite (Figs. 4.7b and 4.8b and c) and because of the wide compositional range displayed by porphyroblasts in type F granulite (Figs. 4.7 and 4.8a), we did not investigate these rock types, for which it was impossible to pair mineral compositions representative of equilibrium at the peak of meta-

morphism. The content of Al on the M1 site of opx was calculated as $y(Al) = Al^{M1} = Al^{total}$ /2. In this estimate we did not consider ferric iron, following the approach of Harley and Green (1982), Fitzsimons and Harley (1994) and Aranovich and Berman (1997). This approach provides a maximum estimate for $y(Al)$ and may lead to overestimated peak temperature (Harley, 1989; Nandakumar and Harley, 2000; Pattison *et al.*, 2003). Typically, calculated temperatures will decrease by approximately 20-50 °C when the effect of ferric iron on the M1 site in orthopyroxene is taken into account (Harley, 2008). Peak-temperatures were calculated for pressures of 8, 9 and 10 kbar. This pressure range has been inferred from peak assemblage stabilities as deduced from pseudosections. Mineral compositions and results are presented in Tab. 4.1.7 and Fig. 4.11

Table 7
Tpeak estimates for granulites Types A – E and charnockites at P = 8, 9, 10 kbar.

Sample	Garnet		Orthopyroxene		HaG-(1982)	AaB-(1997)	RCLC-P
	X_{pyr}	X_{grs}	X_{en}	y(Al)	8 / 9 / 10 kbar	8 / 9 / 10 kbar	8 / 9 / 10 kbar
BRE7	0.544	0.03	0.807	0.183	917 / 950 / 982 °C	813 / 860 / 906 °C	908 / 936 / 963 °C
BRE10	0.521	0.024	0.788	0.183	920 / 952 / 984 °C	819 / 866 / 912 °C	924 / 951 / 963 °C
GraG	0.448	0.033	0.75	0.195	954 / 987 / 1020 °C	818 / 864 / 911 °C	976 / 1002 / 1028 °C
CodGra5	0.526	0.049	0.735	0.153	916 / 947 / 978 °C	899 / 946 / 992 °C	918 / 944 / 970 °C
PiaGra1	0.405	0.021	0.676	0.136	898 / 927 / 956 °C	858 / 902 / 947 °C	910 / 935 / 959 °C
PiaMig1	0.305	0.047	0.544	0.103	906 / 933 / 961 °C	862 / 904 / 946 °C	951 / 972 / 993 °C

Abbreviations: HaG-(1982) – Harley and Green (1982); AaB-(1997) – Aranovich and Berman (1997). Uncertainties are ± 40 °C.

The investigated samples of type A, B, D and E granulites and the charnockite yield similar temperatures of 900-920 °C at 8 kbar, 930-950 °C at 9 kbar and 960-980 °C at 10 kbar, using the Al-in-opx thermobarometer of Harley and Green (1982). Estimated temperatures for coarse-grained type C are approximately 30 °C higher at all considered pressures. The Aranovich and Berman (1997) calibration yielded considerably lower temperatures than the Harley and Green (1982) calibration for all the investigated samples (Fig. 4.11). The former calibration is strongly susceptible to Fe-Mg diffusion on cooling, generally yielding lower temperatures than the Aranovich and Berman expression (see discussion in Harley, 2008). Correction of the Aranovich and Berman (1997) thermometer with RCLC-P (Pattison et al., 2003) yielded results similar to those from the Harley and Green (1982) thermobarometer. Estimates for type A, B, D and E granulites corrected for Fe-Mg diffusion consistently yielded temperatures of 910-925 °C at 8 kbar, 935-950 °C at 9 kbar and 960-970 °C at 10 kbar. With the diffusion correction, the calculated temperatures for charnockite and coarse-grained type C granulites are about 20-30 °C and 50-60 °C higher than for the other granulites, respectively (Fig. 4.11).

P-T pseudosections and Al-in-orthopyroxene contours

Pseudosections were constructed to represent the stability fields of coexisting minerals in PT space for a specific bulk-rock composition employing an internally-consistent thermodynamic dataset (here the 2004 update of (Holland and Powell, 1998)), and mineral solution models as listed in the caption to Fig. 4.12. Key advantages of this approach include the ability to repre-
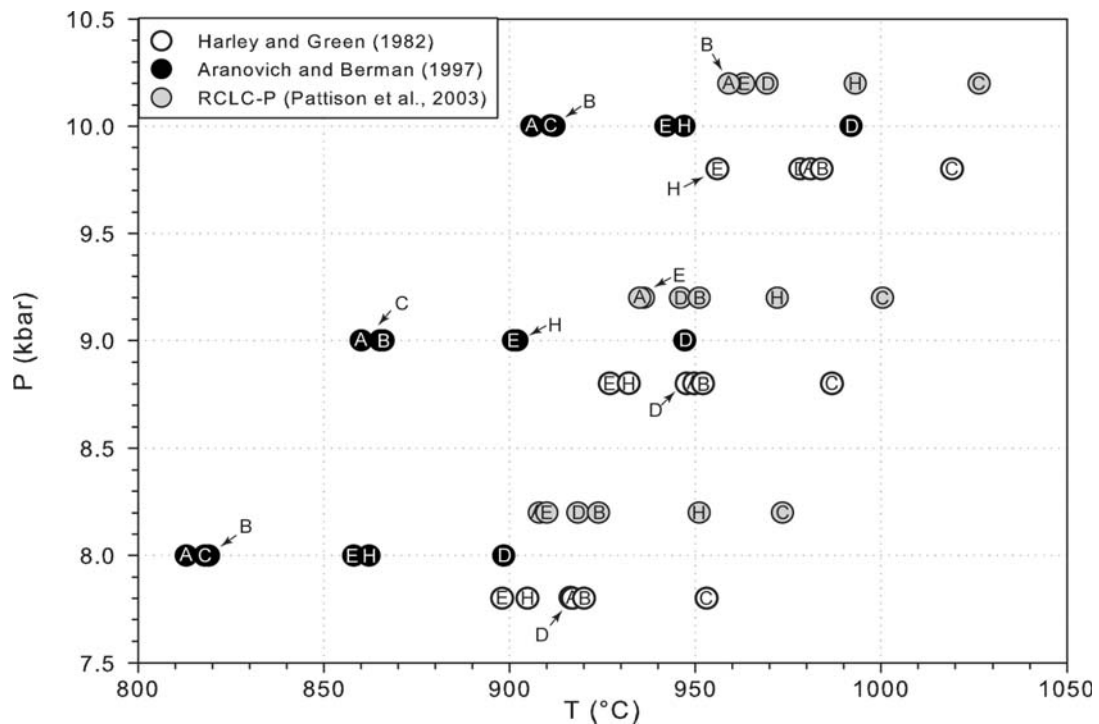
Figure 4.11: *Summary of conventional thermobarometric calculation at 8, 9 and 10 kbar with the Harley and Green (1982) and Aranovich and Berman (1997) thermobarometers and correction for Fe-Mg back exchange with the program RCLC-P (Pattison* et al., *2003). Letters refer to type of granulite (A: type A, sample BRE7; B: type B, sample BRE10; C: type C-coarse, sample GraG; D: type D, sample CodGra5; E: type E, sample PiaGra1; F: type F, sample Conc13; H: charnockite, sample PiaMig1). For clarity, the calculated Harley and Green (1982) and RCLC-P (Pattison* et al., *2003) data were plotted at slightly lower and higher pressures, respectively.*

sent more complex chemical systems than FMAS (Hensen, 1971, 1973, 1987; Kelly and Harley, 2004) or KFMASH (Hensen and Harley, 1990; Srogi *et al.*, 1993; Sengupta *et al.*, 1999; McDade and Harley, 2001), not having to rely directly on measured mineral compositions that may have re-equilibrated during cooling, and the ability to contour for mineral proportions and mineral chemistry. In particular, combining calculated contours of Al-in-opx with the observed mineral composition and/or zoning trends can allow the metamorphic history of a specific rock to be unravelled in more detail (Harley, 1998b; Kelsey *et al.*, 2003; Baldwin *et al.*, 2005).

Nevertheless, several important limitations for the use of pseudosections for high-grade rocks have to be considered. Major problems arise from uncertainties in the thermodynamic properties of sapphirine (review in Harley, 2008), and particularly the lack of data available to quantify the role of ferric iron on the stability of crucial high-temperature phases such as sapphirine, spinel and orthopyroxene (Annersten and Seifert, 1981; Hensen, 1986; Sandiford *et al.*, 1987; Powell and Sandiford, 1988; Das *et al.*, 2001; White *et al.*, 2002). A further problem is the choice of an appropriate "reactive" bulk-composition for the problem to be treated (Stüwe, 1997). Despite these limitations, pseudosections offer a complementary approach to traditional thermobarometry when investigating metamorphic processes in high-grade rocks.

For the bulk compositions of granulite types A (sample BRE7), B (BRE10), C-fine (GraF) and F (Conc13), we calculated PT pseudosections in Na_2O-CaO-K_2O-FeO-MgO-Al_2O_3-SiO_2-H_2O-TiO_2-MnO (NCKFMASHTiMn), employing the 2007 version of Perplex (Connolly, 2005). The inclusion of MnO was not strictly required for these calculations and can sometimes be detrimental (see discussion of White et al., 2007), but was justified by the garnet-zoning modelling that follows and probably has limited negative consequences for samples as garnet-rich as those examined here. Pseudosections were contoured for Al-content in orthopyroxene (using the Powell and Holland (1999) pyroxene model, contoured in wt% Al_2O_3 in Figs. 4.12 a-d). We note here that because of the lack of appropriate solution models accounting for Fe^{3+}, we do not include ferric iron in these calculations. However, Fe^{3+} will enhance the stability of all phases that readily incorporate it (i.e. sapphirine, orthopyroxene and spinel), moving the Al-in-opx isopleths. Therefore, these results are likely to slightly overestimate peak PT conditions.

In the pseudosection calculated for sample BRE7 (type A granulites, Fig. 4.12a), the Bt-Melt-Spr-Ksp-Opx-Grt field corresponds to the observed peak assemblage. The appearance of sapphirine and the simultaneous disappearance of sillimanite are predicted to occur at T > 915 °C, while the disappearance of orthopyroxene with increasing pressure limits the peak pressure to 9.5-12 kbar depending on T. The observed peak assemblage is predicted for a wide PT range. Contouring the pseudosection for Al in orthopyroxene (measured average: 8.8 wt% Al_2O_3) allows us to restrict our PT estimate to the lower-T domain of this field (about 915-950 °C and 8-9.5 kbar). These conditions are in good agreement with conventional thermobarometric estimates corrected for Fe-Mg back-exchange, which yield $\sim$ 936 °C at 9 kbar (Tab. 4.1.7).

The high sensitivity of silica undersaturated rocks to bulk silica content (Kelsey *et al.*, 2005), is illustrated by comparing pseudosections of type A and B granulites. A pseudosection for the SiO_2-richer and FeO-MgO-poorer type B granulite (sample BRE10) predicts a substantial increase in quartz and sillimanite stabilities, and a retreat of the sapphirine field towards higher temperatures (Fig. 4.12b). The stability field corresponding to the observed peak-assemblage (Bt-Melt-Ksp-Pl-Sil-Opx-Grt) is limited to a narrow PT range between 900-945 °C and 8-10 kbar. This is supported by the Al content in opx (measured average 8.7 wt% Al_2O_3) and is in broad agreement with conventional thermobarometric estimates (Fe^{3+}-absent calculations giving 951 °C at 9 kbar, Tab. 4.1.7).

A pseudosection calculated for sample GraF (type C-fine granulite, Fig. 4.12c) predicts that the observed peak assemblage (Grt-Opx-Bt-Ksp-Pl-Qtz) is stable at 900-930 °C (depending on pressure). At higher temperatures, quartz and subsequently biotite would be completely consumed by fluid-absent biotite melting reactions (see reactions (4.2) to (4.5)). The Al-in-opx isopleth corresponding to the measured peak composition ($\sim$ 8.4 wt% Al_2O_3) is located at slightly higher temperature than the stability of quartz and biotite, predicting peak conditions of 930-1020 °C at 8-10 kbar. This discrepancy could be resolved by expansion of the biotite stability field with addition of components such as F, Cl or Fe^{3+}, which are not considered here (Peterson *et al.*, 1991; Hensen and Osanai, 1994; Mouri *et al.*, 1996), or with use of a newer biotite model which permits M2 site Ti and is shown to enhance high-T biotite stability (Tajcmanová *et al.*, 2009).
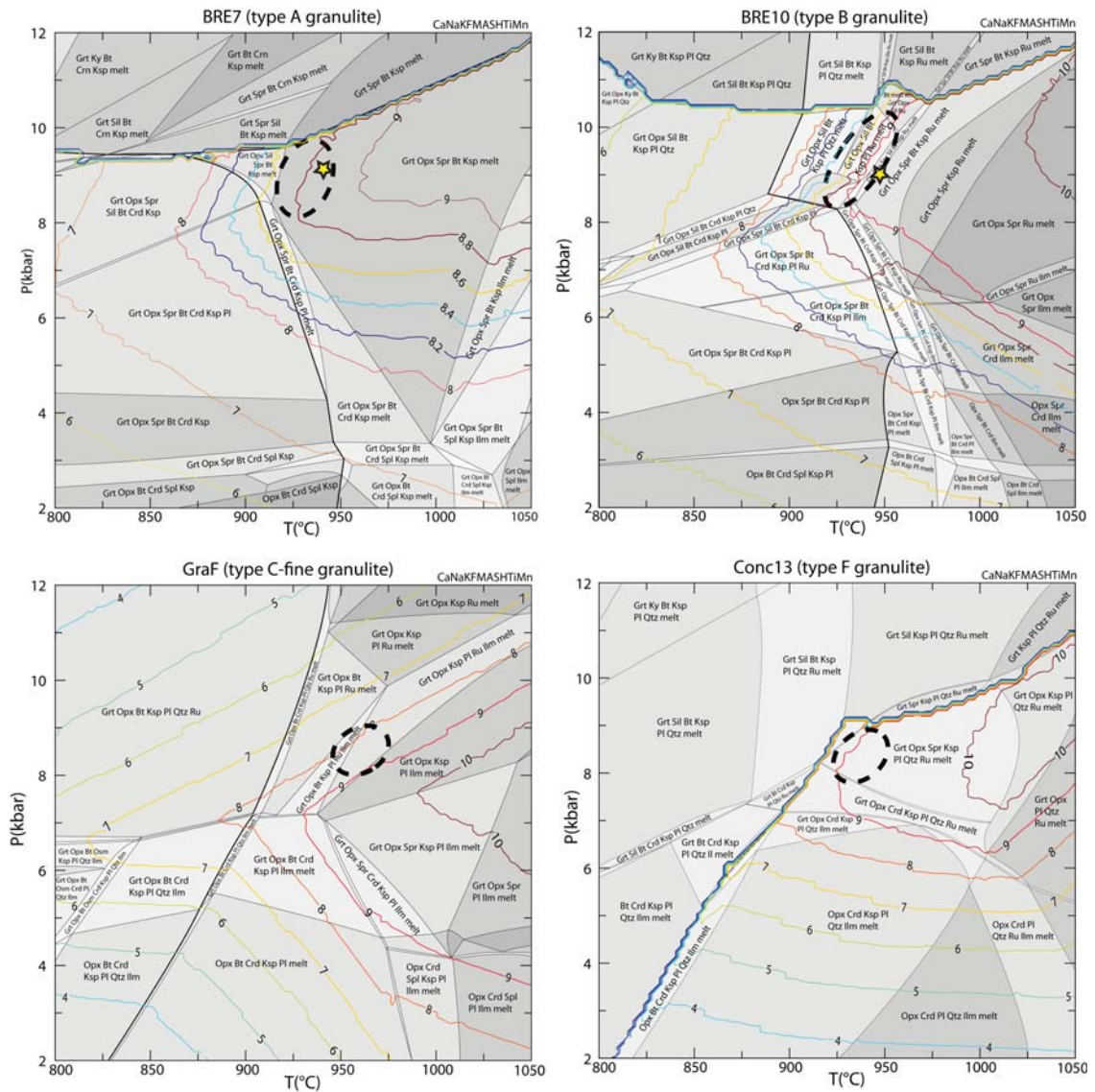
Figure 4.12: *(a - d) P-T pseudosections for type A (BRE7), B (BRE10), C-fine (GraF) and F (Conc13) granulites calculated in the system NaCaMnTiKFMASH and contoured for wt% Al$_2$O$_3$ in orthopyroxene. Solution-phase models used in the calculations are: garnet - Gt(WPH): White* et al. *(2007); biotite - TiBio(WPH): White* et al. *(2007); orthopyroxene - Opx(HP): Powell and Holland (1999); sapphirine - Sapp(KWP): Kelsey* et al. *(2004); cordierite - hCrd: Holland and Powell (1998); feldspars - feldspar: Fuhrman and Lindsley (1988); spinel - Sp(HP): Holland and Powell (1998); osumilite - Osm(HP): Holland* et al. *(1996); ilmenite - IlGkPy: Andersen and Lindsley (1988); melt - melt(HP): White* et al. *(2007), names as defined in solute.dat of Perplex; stars represent conventional thermobarometric estimates corrected for Fe-Mg back exchange at 9 kbar; dotted ellipses represents estimates of granulitic peak conditions.*

Conversely, the Al-in-opx isopleth is likely to move towards slightly lower T and P if Fe^{3+} is included. Due to the low Fe^{3+} content estimated in opx ($\sim 5\%$ of Fe^{total}), however, we favour the former explanation and suggest that type C-fine granulite formed at approximately 950 °C and 8-9 kbar. This is in accordance with conventional thermobarometry estimates for the coarser-grained type C-coarse granulites, which yield T > 950 °C (Tab. 4.1.7).

For type-F granulites, the occurrence of the peak assemblage (Melt-Spr-Ksp-Pl-Grt-Opx-Qtz-Ru) in the appropriate pseudosection (Fig. 4.12d) limits the minimum peak temperature to 915 °C at pressures between 7 and 10 kbar. Again, Al-in-opx isopleths (measured average 9.0 wt% Al_2O_3) help to refine the estimated conditions to T $\sim$ 915-940 °C and P $\sim$ 8-9 kbar.

Post-peak conditions

During the post-peak history, the Gruf granulites developed a series of symplectitc assemblages (secction 4.1.6). Decreased cation diffusion rates at lower temperatures and/or loss of melt (White and Powell, 2002) lead to the development of micro-scale volumes of equilibration in these rocks. Estimating the effective bulk composition involved in any specific reaction corona/symplectite is problematic and in this case, identification of a single reaction using the pseudosection approach may be seriously misleading (Stüwe, 1997).

Effectively, pseudosections for type A, B, C-fine and F compositions predict that the post-peak reactions forming cordierite at the expense of sillimanite and garnet should occur at $\sim$ 900 °C and $\sim$ 7-8 kbar. However, this is inconsistent with the measured Al-content of orthopyroxene porphyroblast rims (5-6 wt%) and symplectitic opx (5-5.5 wt%) in all of the considered samples (Tab. G.1.2). Al-in-opx contours in pseudosections (Fig. 4.12) suggest that the observed Al_2O_3 decrease (3-3.5 wt% relative to porphyroblast cores) corresponds to a temperature decrease of approximately 150 °C, compatible with isopleth spacing estimates of $\sim$ 40-50 °C per 1 wt% Al_2O_3 (Aranovich and Berman, 1996; Harley and Motoyoshi, 2000).

As an alternative to the pseudosection approach, we calculated the PT conditions of the most relevant reactions leading to formation of cordierite-bearing post-peak coronae and symplectites in samples BRE10 (type B granulite), GraG (type C-coarse), GraF (type C-fine) and CodGra5 (type D), using the measured compositions of the participating phases. Post-peak mineral assemblages occurring in each sample and phase activities used in the calculations are given in Tab. 4.1.7.

Table 4.1.7
Calculation of metamorphic post-peak conditions for samples BRE10 (type B granulite), GraG (type C-coarse granulite), GraF (type C-fine granulite) and CodGra5 (type D granulite) using the P-T average approach of Powell and Holland (1994).

Sample	Post-peak assemblage	Garnet		Opx			Spr		Spl	Crd		Bt			Pl		PT-estimate			
		x(g)	z(g)	x(opx)	y(opx)	Q(opx)	x(sa)	y(sa)	x(sp)	x(cd)	h(cd)	x(bi)	y(bi)	Q(bi)	ca(pl)	k(pl)	T(°C)	P(kbar)	cor	fit
BRE10	Grt, Opx, Spr, Spl, Crd, Bt, Sil	0.5	0.03	0.27	0.12	0.15	0.17	0.22	0.53	0.13	0.1	0.25	0.52	0.15	-	-	721 ± 59	7.3 ± 0.5	0.61	3.48
GraG	Grt, Opx, Spr, Spl, Crd, Bt, Sil	0.55	0.04	0.3	0.13	0.15	0.2	0.22	0.55	0.15	0.1	0.28	0.55	0.15	-	-	731 ± 59	7.1 ± 0.5	0.63	3.55
GraF	Grt, Opx, Crd, Bt, Qtz	0.57	0.07	0.32	0.11	0.15	-	-	-	0.14	0.1	0.27	0.51	0.15	-	-	745 ± 51	7.7 ± 0.5	0.16	2.33
CodGra5	Grt, Opx, Spr, Spl, Crd, Bt, Pl	0.5	0.05	0.28	0.17	0.15	0.2	0.22	0.6	0.13	0.1	0.24	0.47	0.15	0.5	0.01	684 ± 68	8.1 ± 1.1	0.19	5.27

Co - core of porphyroblast; R - rim of porphyroblast. Fe3+ calculated after charge balance based on 8 cations. XMg = Mg / (Mg + Fetot); XMg* = Mg / (Mg + Fe2+); Xpyr = Mg / (Mg + Fe2+ + Ca + Mn); Xalm = Fe2+ / (Fe2+ + Mg + Ca + Mn); Xgrs = Ca / (Ca + Fe2+ + Mg + Mn); Xsps = Mn / (Mn + Fe2+ + Mg + Ca).

Sample BRE10 displays the widest range of post-peak reaction textures, involving the desta-bilisation of both sillimanite and garnet. For this sample, the intersection of the slightly T-sensitive cordierite producing reactions (4.12), (4.13), (4.15) and (4.16) with the Grt-Opx thermobarometer corrected for Fe-Mg back diffusion (calculated by pairing Opx_{sym} with garnet rim compositions, using RCLC-P, Pattison et al., 2003) yields 720-750 °C and 6-7.5 kbar for symplectite formation (Fig. 4.13). The location of the spinel-cordierite forming reaction (4.17), although having a large uncertainty, is in agreement with this result. The location of reactions (4.11), (4.12) and (4.15), calculated respectively for samples GraF, CodGra5 and GraG, also agree well with these post-peak conditions (Fig. 4.13). PT conditions for texturally-equilibrated post-peak assemblages of samples BRE10, GraG and GraF were also calculated with the PT average approach of Powell and Holland (1994). Results coincide with the estimates from single reactions, yielding consis-tent conditions of 720-740 °C and 6.5-7.5 kbar (Tab. 4.1.7). A PT average calculation on sample CodGra5, although yielding lower temperatures of 684 ± 68 °C and higher pressures of 8.1 ± 1.1 kbar (Tab. 4.1.7), is in error of this range. We note that decreased Al-contents in opx rims and symplectites (Tab. G.1.2) fit well with Al-in-opx compositions predicted by the pseudosections at these inferred conditions.
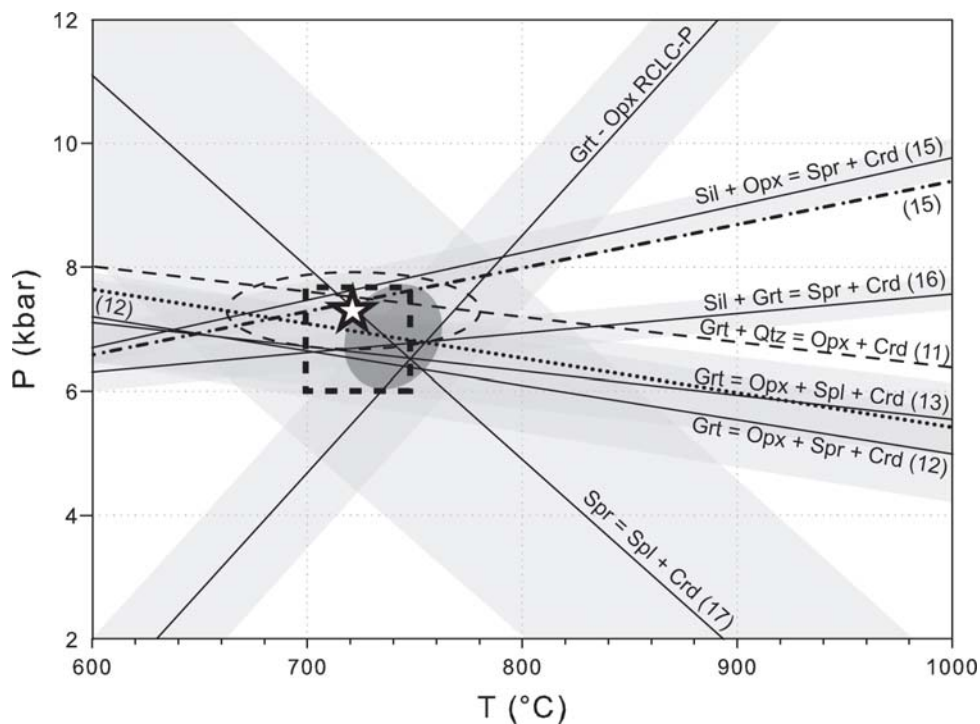
Figure 4.13: *P-T diagram showing the locations of reactions in coronae and symplectites of Gruf granulites (black lines - BRE10; dotted line - CodGra5; dotted-dashed line - GraG; dashed line - GraF). The star and the dashed ellipse represent P-T average estimate for sample BRE10 and corresponding uncertainty. The grey ellipse corresponds to the best estimate post-peak conditions consistent with the central Alpine Lepontine metamorphism (dashed box, after Heitzmann, 1975, Schmidt, 1989, Engi et al., 1995, Stucki, 2001, Nagel, 2002 and Burri et al., 2005). Reactions are written with the high-T assemblage to the right of the "=" sign. Numbers refer to reaction numbers in the text.*

4.2   Metamorphic conditions during migmatization

The occurrence of sillimanite + alkali feldspar and the scarcity or lack of syn-kinematic muscovite observed in most of the migmatitic micaschists of the Gruf Complex suggest that partial melting was induced by the breakdown of muscovite according to:

$$Ms + Qtz = Sill + Ksp + melt \qquad (4.18)$$

or

$$Ms + Pl = Sill + Ksp + melt \qquad (4.19)$$
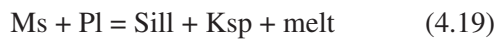
(Chatterjee and Johannes, 1974; Vielzeuf and Holloway, 1988). Rare, but still present, muscovite flakes parallel to the main foliation in migmatitic metasediments indicate that temperatures approached conditions of muscovite dehydration melting at about 700-750 °C (Fig. 4.14). The occurrence of sillimanite as stable alumosilicate limits the maximal pressure to 8 kbar at these temperatures (Fig. 4.14). The reaction

$$Bt + Sill + Qtz = Ksp + Crd + melt \qquad (4.20)$$

(Vielzeuf and Holloway, 1988) may have produced the observed low amount of cordierite at the expense of biotite and sillimanite, at metamorphic conditions of 700-750 °C and 6-7 kbar (Fig. 4.14). Nevertheless, the lack of orthopyroxene in migmatitic metagranitoids and metasediments shows that temperatures did not reach the orthopyroxene-forming biotite dehydration melting reactions

$$Bt + Qtz = Opx + Ksp + melt \qquad (4.21)$$

or

$$Bt + Qtz = Opx + Grt + Ksp + melt \qquad (4.22)$$

(Vielzeuf and Holloway, 1988; Vielzeuf and Montel, 1994), constraining the maximal temperature to < 800 °C (Fig. 4.14). Metamorphic temperatures deduced from the mineral assemblage chlorite-spinel-orthopyroxene-olivine in the metaperidotites yield 700-770 °C (Fig. 4.14), coherent with the above temperatures.

The occurrence of rare, relictic corundum grains within strongly migmatitic sillimanite-alkali

feldspar-garnet-cordierite-biotite schists (Fig. 2.11d) at the direct contact to the Bergell tonalite (Fig. J.1) suggests metamorphic temperatures to the upper end of the above range. The reaction

$$Ms = Ksp + Cor + melt \qquad (4.23)$$
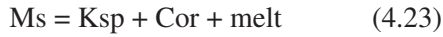
(Chatterjee and Johannes, 1974) may account for the production of corundum and the complete consumption of muscovite from the rock, indicating temperatures of 750-775 °C at the contact between the Bergell Intrusion and the Gruf Complex (Fig. 4.14). Slightly higher temperatures at the contact are coherent with the local increase in leucosome in the migmatitic metasediments east of Bivacco Vaninetti (2 in Fig. 2.29).
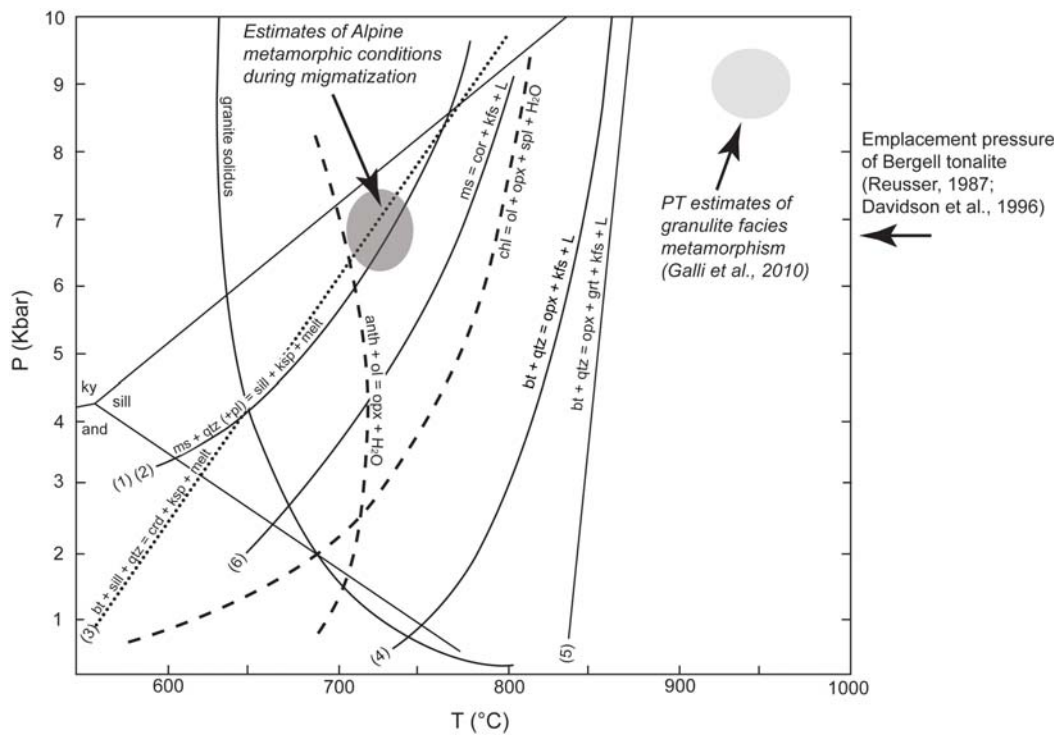
Figure 4.14: *Metamorphic conditions during migmatization. Solid lines: experimentally determined reactions for the metapelitic system (references for reactions as in the text); dashed lines: reaction curves for natural ultramafic bulk composition (Jenkins and J.V., 1986; Evans and Guggenheim, 1988); dotted line: reaction calculated using the version 3.33 of THERMOCALC (Powell and Holland, 2009; activities used in the calculation: biotite: x(bt) = 0.59; y(bi) = 0.54; Q(bi) = 0.15; cordierite: x(cd) = 0.39, h(cd) = 0.1; alkali feldspar: na(ksp) = 0.68; ca(ksp) = 0.11); dark grey ellipse: estimated metamorphic peak conditions during migmatization; light grey ellipse: metamorphic peak conditions of granulites and charnockite (section 4.1).*

4.3 Discussion

4.3.1 Ultra-high temperature (UHT): age and significance

Our thermobarometry on charnockites and six granulite types distributed over the entire Gruf Complex shows that these rocks formed at temperatures in excess of 900 °C and pressures of 8.5-9.5 kbar. The high temperature attained by the Gruf charnockites and granulites is unique evidence for UHT metamorphism in the Gruf Complex and, more generally, in the Central Alps. Such high-grade conditions within a growing orogen are uncommon and very difficult to integrate within the framework of the Alpine metamorphism as previously inferred by Droop and Bucher-Nurminen (1984), Liati and Gebauer (2003) and Schmitz *et al.* (2009). It is likely that such conditions can only be attained if mantle diapirism (coeval with or independent of slab breakoff) advects the necessary heat, but such an event should influence a region far larger than just the Gruf Complex (Schubert *et al.*, 2001). An alternative explanation sees the Gruf charnockites and granulites as lower crustal relics of a pre-Alpine high-grade metamorphism. In this case, a UHT Alpine event is unnecessary and the most likely candidate for such high temperatures is the post-Variscan Permian event responsible for both the widespread formation of granulites and charnockites in the European crust (Lorenz and Nicholls, 1976, 1984; Schuster and Stüwe, 2008) and the vast southern European rhyolitic province (Lorenz and Nicholls, 1984).

Granulites related to the extensive rifting that occurred in the Permian are exposed in several parts of the Alps and record similar PT conditions to the Gruf granulites. Metapelitic granulites formed at ∼ 850 °C and ∼ 8 kbar are present in the Malenco Unit, 15 km east of the Gruf Complex (Müntener *et al.*, 2000). Granulites of pelitic composition that occur in the Sondalo Complex (Braga *et al.*, 2001), 50 km to the east-south-east of the Gruf Complex, yield a temperature of approximately 900 °C and pressure of 8 kbar (Braga *et al.*, 2003). Permian granulites recording T > 850 °C are also exposed in the Ivrea and Sesia Zones (Barboza and Bergantz, 2000; Lardeaux, 1991; Rebay and Spalla, 2001) approximately 60 and 100 km west-south-west of the Gruf, respectively (although these two distances are reduced by 30 km after reintegration of post-Oligocene dextral displacement along the Periadriatic Fault System; Müller *et al.* (2000)).

Several arguments indicate a pre-Alpine age for the granulite facies metamorphism studied here:

(i) ultramafic, mafic and carbonate rocks occurring in the Gruf Complex and regarded as equivalent to the Mesozoic Chiavenna Unit (Diethelm, 1989; Davidson *et al.*, 1996; Schmid *et al.*, 1996a) show no sign of UHT-metamorphism;

(ii) intense fluid-absent biotite melting as observed for these granulites is absent from the mid-Tertiary upper amphibolite-facies migmatites which volumetrically dominate the Gruf Complex (section 4.2). These rather developed by fluid-saturated and also fluid-absent muscovite melting reactions which formed widespread migmatites throughout the Central Alps (Burri *et al.*, 2005);

(iii) the 32-30 Ma granodioritic-tonalitic Bergell Intrusion (Von Blanckenburg, 1992) in-

duced a local increase in partial melting of proximal metapelitic rocks, which is inconsistent with host-rocks that were already at UHT conditions;

(iv) SHRIMP ages of zircons from the charnockites consistently yield a Permian intrusion age of 266-280 Ma (section 5). Textural evidence and inclusions within these crystals strongly imply granulite-facies mineralogy at this time.

We propose that a single, well defined population of 272.0 ± 4.1 Ma ages from zircon cores from the type A and B Gruf granulites (Liati and Gebauer, 2003) corresponds to the age of the UHT event. This disagrees with the interpretation of Liati and Gebauer (2003), who attribute the 272 Ma age to crystallisation of a supposed granite precursor, the magmatic character being inferred from oscillatory zoning of the inner portions of the zircons. However, the high Mg-Al character of the granulites, the widespread occurrence of prismatic sillimanite (type B), and staurolite inclusions in garnet (types A and C-coarse) indicate a Mg-Al-rich metapelitic precursor protolith. This interpretation is supported by mass balance calculations showing that the required amount of granitic melt extracted from Mg-rich pelites in order to reach a residual composition corresponding to type A or B granulites would be 40-50 %, in accordance with the amount of melt formed by first fluid-absent muscoviyte and then fluid-absent biotite melting of Mg-rich metapelites at 920-940 °C and 9 kbar (Stevens *et al.*, 1997). In the case of a granitic protolith, extraction of > 90 % melt would be required to generate a somewhat similar but strongly peraluminous residual composition. If this melting was related to post nappe stacking Lepontine metamorphism, then it should have been widespread throughout the Gruf (and possibly other units), which is not the case.

In our interpretation, Permian oscillatory zoning in zircon formed during extensive partial melting related to peak granulite metamorphism, and Oligocene homogeneous zircon rims recrystallised during the Alpine, upper-amphibolite-facies Lepontine metamorphism. This interpretation is also in agreement with granulites constituting schlieren and enclaves within the charnockites (Fig. 4.2b), suggesting that pelitic rocks underwent intense partial melting (during the Permian UHT event), leading to the formation of the orthopyroxene-bearing charnockitic melts and granulitic residuals.

4.3.2   Post-peak evolution

Commonly, reaction textures such as the observed symplectites and coronae which partly or completely replace garnet and sillimanite have been used to infer rapid isothermal decompression (Hensen, 1987; Harley, 1989, 1998b). In fact, the Gruf Complex has been considered a classical high-grade terrain that experienced a strong (Alpine) isothermal decompression (ITD) along a steep retrograde PT path (Droop and Bucher-Nurminen, 1984; Harley, 1989). This interpretation arose due to estimated PT conditions of 830 °C, 10 kbar for peak conditions and 750 °C, 5 kbar for symplectite formation (Droop and Bucher-Nurminen, 1984), implying a decompressional cooling path with a dP/dT gradient of 60 bar/°C (Fig. 4.15).
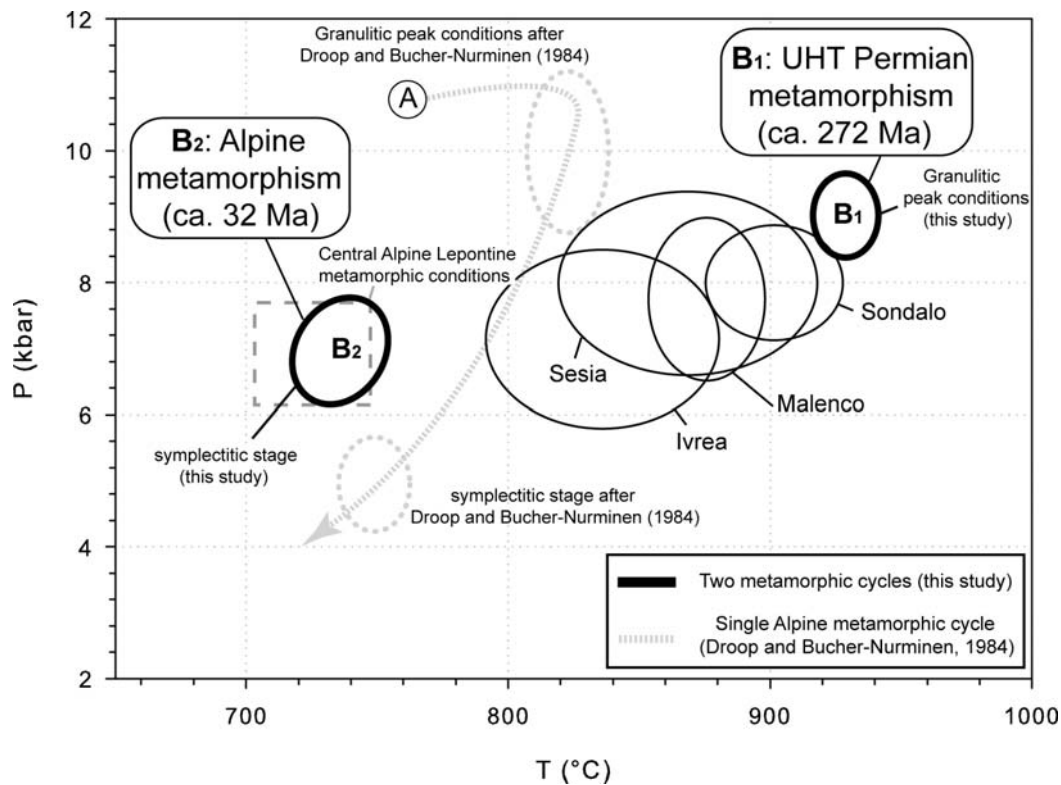
Figure 4.15: *Comparison between single metamorphic cycle model (Droop and Bucher-Nurminen, 1984) and two metamorphic cycles model for the Gruf granulites. Leight greysh ellipses: estimates of peak and post-peak conditions after Droop and Bucher-Nurminen (1984); leight greysh dotted line (A): isothermal decompression (ITD) path during a single Alpine metamorphic cycle (Droop and Bucher-Nurminen, 1984); black bold ellipses: estimates of peak and post-peak conditions from this study; B1 - Permian metamorphic evolution for the Gruf granulites at 272 Ma, B2 - estimated metamorphic path for the Alpine regional metamorphism at 32 Ma; black ellipses: Permian metamorphic conditions estimates for Malenco, Sondalo, Ivrea and Sesia granulites (Müntener et al., 2000; Braga et al., 2003; Barboza and Bergantz, 2000; Lardeaux and Spalla, 1991; Rebay and Spalla, 2001); dashed square: estimates of the central Alpine metamorphic conditions (Heitzmann, 1975, Schmidt, 1989, Engi et al., 1995, Stucki, 2001, Nagel, 2002 and Burri et al, 2005).*

Our thermobarometric calculations, however, suggest that these rocks may have formed at temperatures in excess of 900 °C and pressures of 8.5-9.5 kbar (approximately 100 °C hotter than previously thought). Calculations also suggest that the peak assemblage subsequently partly re-equilibrated at 720-740 °C and 7-7.5 kbar (deeper than previous estimates). Thus, the inferred post-peak dP/dT gradient is ∼ 10 bar/°C, much less than previously suggested. This considerably lower dP/dT forces a reinterpretation of the tectono-metamorphic evolution and significance of the Gruf granulites in an Alpine context. Whereas granulite and charnockite peak-conditions are incompatible with any other metamorphic conditions determined for Lepontine metamorphism, post-peak conditions correspond to the generally accepted mid-Tertiary regional metamorphic conditions for this part of the Lepontine Dome (section 4.2 and Bucher-Nurminen and Droop (1983), Burri *et al.* (2005)) and to intrusion pressures of the adjacent Bergell tonalite (Reusser,

1987a). This suggests three possible tectonic scenarios:

(i) granulites and charnockites formed at ultra-high temperature conditions during the Permian event and cooled slowly over the following 250 Ma to 720-740 °C (< 1 °C Myr^{-1});

(ii) granulites and charnockites were formed by Permian UHT metamorphism, were rapidly exhumed and cooled, and were not affected by the subsequent Lepontine metamorphism;

(iii) granulites and charnockites experienced UHT metamorphic conditions during the Permian and were subsequently overprinted by the Alpine Lepontine event. Thus, peak- and post-peak conditions may not represent progressive stages of the same Alpine metamorphic cycle, reflecting instead two different and tectonically unrelated metamorphic events (Fig. 4.15).

4.3.3 Duration of UHT metamorphism and subsequent cooling: insight from garnet zoning

In order to approximately constrain the duration of the thermal event and test whether any of the three scenarios outlined above can be excluded, we investigated major element zoning in garnet porphyroblasts, using techniques similar to several recent works (Ague and Baxter, 2007; Dachs and Proyer, 2002; Lasaga and Jiang, 1995; Storm and Spear, 2005).

Calculation methods

Garnet crystals from the Gruf Complex typically record prograde zoning patterns (Droop and Bucher-Nurminen, 1984) but do not contain the distinct steps in zoning patterns which have been used to infer pre-diffusion compositional zoning (Ague and Baxter, 2007). Because this information is required to forward model the intra-crystalline diffusive history, we use an alternative technique, described in more detail in Caddick *et al.* (2010) and Caddick and Thompson (2008). Briefly, this approach follows suggestions (Konrad-Schmolke *et al.*, 2005, 2007; Spear, 1988; Spear *et al.*, 1991) that equilibrium thermodynamic calculations can provide an initial growth zoning for any given P-T path, which then can be used to assess the extent of diffusive resetting experienced.

Preserved garnet zoning (e.g. Fig. 4.7b) and the inferred prograde P-T history of Gruf Complex samples (Figs. 4.10 and 4.12) suggest that garnet growth began significantly before peak temperature, requiring both assumption of the early prograde P-T path and sensitive treatment of bulk-rock composition. We assume here a simple path involving heating during burial to 11 kbar, then decompression to 8.5 kbar during further heating to 950 °C (path a-b, Fig. 4.16). Following peak-T (point b of Fig. 4.16a), two types of path continuation were tested; either cooling directly through 720 °C to 400 °C (dashed black curve b-c-d, Fig. 4.16a) or cooling first to some lower temperature (represented by e on Fig. 4.16a although various temperatures were tested) then heating

again to inferred Alpine conditions (solid blue curve b-e-c-d, Fig. 4.16a). Garnet composition and modal proportion were calculated at approximately 200 points along each P-T path with Perple-X (dataset and mineral solution models as described in section 4.1). Calculations used a starting bulk-rock composition calculated by mixing the compositions of samples GraF and PiaMig1 (Tab. E) in the ratio 60 % to 40 %, respectively, to simulate an estimated pre-melt-loss composition. The composition of any melt formed along the P-T path was progressively removed from the residual bulk-rock composition, which provides an additional check of calculation consistency; the calculated residual bulk-rock composition tending to that of sample GraF as the calculation progresses and melt is extracted. The final model composition agrees relatively well with that of sample GraF, albeit with higher MgO and FeO contents (Tab. E). All of the melt produced at each PT step was removed from the residual composition, so the final restite composition is almost completely devoid of Na_2O.

Garnet modal proportion along the P-T path was converted to crystal radius assuming a spherical geometry. A final crystal diameter of 3 mm was prescribed and it was assumed that crystals nucleated at the garnet-in reaction (i.e. without reaction overstepping). Garnet compositions were recorded along retrograde paths (to indicate the orientation of late-stage resetting), but crystal resorption was not permitted because detailed simulation of symplectite formation is outside the scope of the simple 1-dimensional approach applied here. This undoubtedly results in uncertainty in modelled crystal rim compositions, but as shown below permits extraction of the approximate timescale of the UHT event. A model time was assigned to each of the P-T points at which phase abundance and composition were calculated, yielding a series of time-steps. In each time-step the model crystal was allowed to instantaneously grow or change its rim composition (as predicted by the Perple-X calculations), and diffusive re-equilibration of the zoning profile established by previous steps was calculated. Composition-dependent Fe, Mg, Ca and Mn diffusivities of Carlson (2006) were used with the Lasaga (1979) formulation for multi-component diffusion in ionic lattices. Diffusivity was calculated at each time-step (i.e. for each P-T condition) and at each of the 100 recorded model positions (i.e. at each crystal composition).

Results

In the absence of intra-crystalline diffusion, P-T path a-b-c-d Fig. 4.16a results in a garnet zoning profile showing decreasing X_{Mn} and X_{Ca}, and increasing X_{Mg} from core to rim (Fig. 4.16b). X_{Fe} initially increases rimwards, then decreases and finally flattens towards the crystal rim. Permitting intra-crystalline diffusion throughout the same P-T history allows us to model the effects of a single long period of cooling from UHT to Lepontine conditions (e.g. Fig. 4.16c). Here we re-model path a-b-c-d, setting the duration of b-c to 250 Myrs (an initial cooling rate of ca. 1 °C $Myrs^{-1}$) and the duration of c-d to 20 Myrs (consistent with Alpine exhumation rates of Rubatto *et al.* (2009)). The duration of prograde phase a-b is not known, but multiple tested possibilities yield effectively the same result because the subsequent long period of cooling from UHT conditions removes all evidence of earlier zoning (e.g. Fig. 4.16c). In particular, increases in X_{Mg} and decreases in X_{Fe} and X_{Mn} measured from core to near-rim in natural crystals (Fig. 4.7b) are
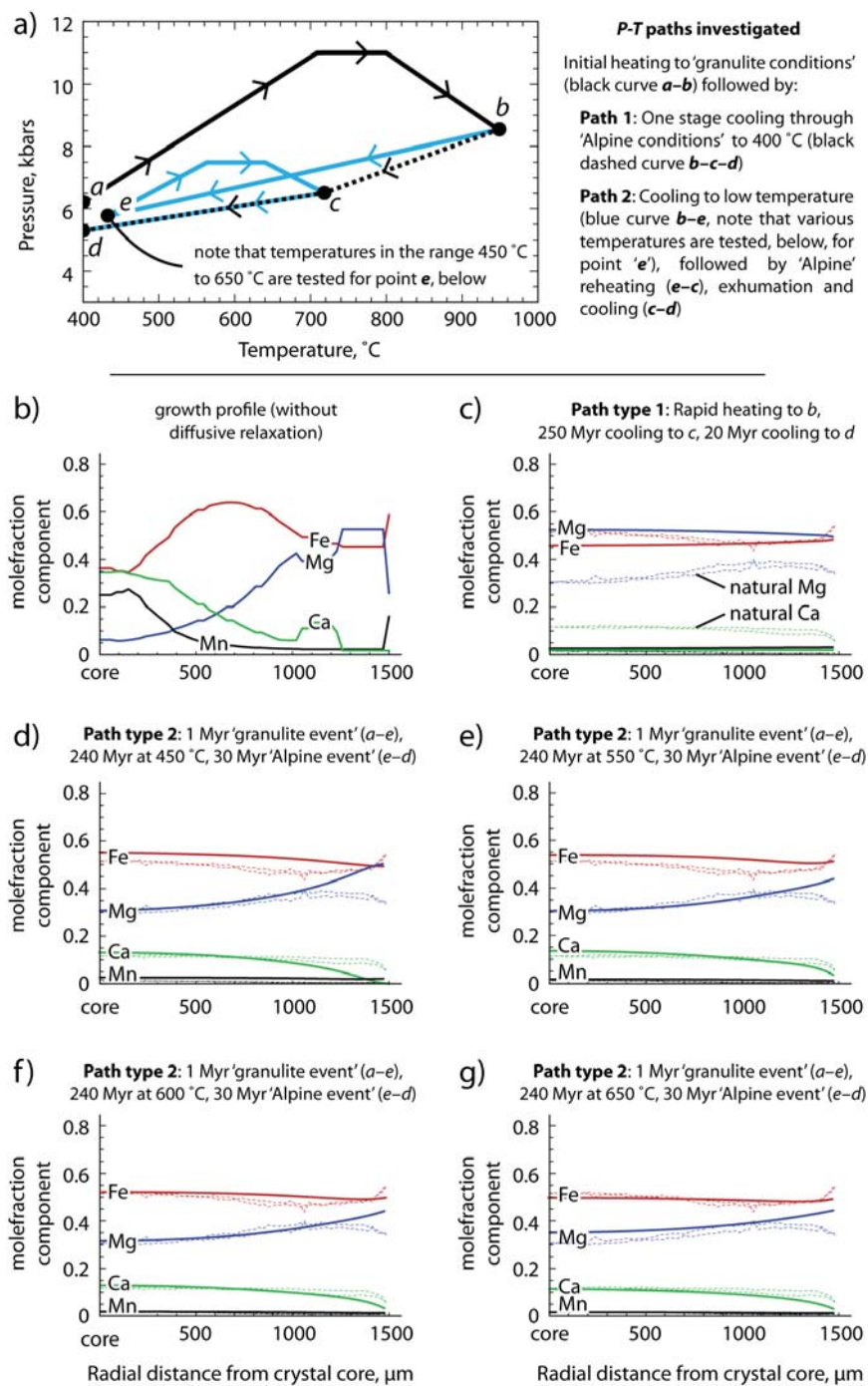
Figure 4.16: *Modelled garnet zoning profiles formed during various P-T-t histories. (a) P-T path types modelled, with a common prograde history (black curve a-b) then either a one stage cooling path (dashed black curve b-c-d) or cooling followed by later reheating then exhumation (blue curve b-e-c-d); (b) Core to rim zoning profile established in a 3 mm diameter spherical crystal along P-T path a-b-c-d, without considering intra-crystalline diffusion; (c) Profile established by a one-stage heating-cooling path (as panel a), but considering diffusion and with 250 Myrs cooling from UHT to Lepontine conditions and 20 Myrs cooling from Lepontine conditions. Bold cuves are model outputs, fine dashed lines represent microprobe traverses through natural crystals (see also Fig. 4.7b); (d-g) Profiles established by two-phase P-T paths, with rapid early UHT metamorphism followed by 240 Myrs at either 450 °C, 550 °C, 600 °C or 650 °C, and then a 30 Myr Lepontine event. Bold cuves are model outputs, fine dashed lines represent microprobe traverses through natural crystals.*

97

poorly represented (and indeed reversed) by the model result (Fig. 4.16c). The model result also has very high X_{Mg} and low X_{Ca} in the crystal core because of the long duration spent at high-T, where equilibrium (i.e. crystal rim) compositions differ significantly from those experienced earlier in the growth history and intra-crystalline diffusivities are sufficiently high to modify the crystal core composition. We emphasise here that sluggish post high-T interaction between the crystal of interest and the matrix (due to slow inter-granular diffusivity or physical shielding by growth of a new rim) will reduce this significant modification of modelled crystal bulk composition. For example, complete closed-system behaviour following peak-T would result in fixed total Fe, Mg, Ca and Mn contents in each crystal, but additional calculations (not shown) suggest that a 250 Myr cooling phase (b-c) would simply yield entirely unzoned crystals, preserving none of the prograde zoning seen in natural crystals (Fig. 4.7b) and Droop and Bucher-Nurminen (1984).

An alternative P-T history involves rapid cooling from peak-T, followed by Alpine reheating and subsequent exhumation (path a-b-e-c-d, Fig. 4.16a). Intra-crystalline diffusion was modelled along this path, for post-UHT residence temperatures of 450 °C, 550 °C, 600 °C and 650 °C (Figs. 4.16d-g). In all cases, the fit to measured crystal zoning profiles is relatively good if the UHT event is sufficiently fast. It is beyond the scope of this modelling to more accurately estimate the duration of this event, but total timescales of less than 20 Myrs for path segment a-b-e are required to maintain prograde zoning if the heating and cooling rates are constant throughout the model. This duration can be extended if the proportion of the total path time that is spent near peak-T is reduced.

For the purpose of illustration, Fig. 4.16d-g represents a very rapid UHT event (1 Myrs) followed by 240 Myrs residence at either 450 °C, 550 °C, 600 °C or 650 °C, then reheating to inferred peak Lepontine conditions and subsequent exhumation (using the cooling curves of (Rubatto *et al.*, 2009)). Results for residence at each temperature are similar, highlighting the huge difference in diffusivities between UHT (where 1 Myr of diffusion significantly modifies zoning profiles) and low-grade conditions (where 240 Myrs of diffusion has relatively little effect on the preserved profile of 3 mm diameter crystals). Permian to Alpine residence temperatures between 550 and 600 °C fit observations best (Fig. 4.16e-f), with hotter models flattening profiles in all components (particularly Mg and Fe). We emphasise, however, that it is not possible to particularly accurately resolve the lower bound on the residence temperature because results from all models are similar and because of the likely uncertainties arising from (i) the model assumptions described above, (ii) the activity models used to predict growth compositions, and (iii) the diffusivity data employed. Despite this, it is clear that all models involving rapid post-UHT cooling and subsequent heating (Fig. 4.16d-g) preserve garnet zoning trends broadly consistent with natural crystals, unlike the 1-stage model (Fig. 4.16c). All models poorly fit the outermost parts of the observed garnet profile. This is presumably partly due to a combination of the assumptions listed above, although longer durations spent just before peak-T and during parts of the exhumation path would result in slightly better fits.

4.3.4   Granulite: Alpine overprint

It is not possible with the current garnet zoning model to easily distinguish whether the post-peak symplecitite assemblages grew during cooling from the UHT event, or re-heating during the Oligocene. However, various lines of evidence lead us to attribute the formation of symplectitic, mostly cordierite-bearing, post-peak assemblages to the Central Alpine Lepontine metamorphism. The intense loss of melt during the pre-Alpine granulitic event lead to a subsequent absence or scarcity of melt or intergranular fluid, such that reaction kinetics may have been too slow to completely recrystallize the peak-assemblages, leading to symplectite and coronae formation (Fyfe, 1973; Powell, 1983; Waters, 1988; Powell and Downes, 1990; White and Powell, 2002). Hence, we propose that owing to their extremely refractory bulk-rock composition, the Gruf granulites only partially re-equilibrated during the Central Alpine upper-amphibolite facies metamorphism (at 720-740 °C and 7-7.5 kbar). This event was responsible for the development of 32 Ma metamorphic rims on zircons separated from the Gruf granulites (Liati and Gebauer, 2003). Monazite ages of 33 Ma (Schmitz *et al.*, 2009) are also consistent with this, although we acknowledge Schmitz et al.'s interpretation that this records granulite-facies rather than amphibolite-grade metamorphism. The possibility that this may record Pb loss due to diffusion in pre-existing (Permian) grains is controversial (see for example Cherniak *et al.* (2004); Smith and Giletti (1997); Spear and Parrish (1996) as monazite resetting temperatures are in the vicinity of the Lepontine metamorphic temperatures. Without further textural study, it is difficult to assess whether partial re-crystallisation of earlier grains may have occurred.

Chapter 5

Geochronology

5.1   Introduction

Reconstructing the geodynamic evolution of complex orogenic systems cannot prescind from reliable geochronological data. U-Pb dating of zircons has proved to be an accurate record of multiple, high temperature geological events (Watson and Harrison, 1983; Watson, 1996; Cherniak and Watson, 2003; Hoskin and Schaltegger, 2003). The method has gained even more trust from geologists after analytical progresses such as the Sensitive High Resolution Ion MicroProbe (SHRIMP), which allows measuring isotopic ratios of compositional domains imaged previously with backscattered electrons and cathodoluminescence in single mineral grains (Compston *et al.*, 1992; Hanchar and Miller, 1993; De Laeter and Kennedy, 1998). Knowing the value of the technique, we carried out SHRIMP isotopic determinations on zircons separated from charnockites and their migmatitic country rocks in the Gruf Complex, Central Alps.

This complex is unique and preeminent in the Central Alps for these ultra-high temperature (UHT) charnockites and related residual sapphirine-orthopyroxene granulites (Cornelius, 1916; Wenk *et al.*, 1974). The comprehension of this lower crustal rock association is fundamental to decipher the tectono-metamorphic evolution of the Central Alps and, from a more general point of view, to understand the significance of ultrahigh temperature metamorphism in modern orogenesis. The charnockites and granulites occur in the Gruf Complex as lenses embedded within regional dominant, upper amphibolite facies migmatitic orthogneisses. Ultra-high temperature peak mineral assemblages formed at temperatures in excess of 900 °C and pressures of 8-9.5 kbar and were overprinted and partly re-equilibrated at conditions of 720-740 °C and 7-7.5 kbar (chapter 4.1). Whereas peak conditions are extreme at crustal levels and do not fit any known metamorphic event in the Central Alps, post-peak conditions match the generally accepted mid-Tertiary regional metamorphic conditions for this part of the Lepontine (Bucher-Nurminen and Droop, 1983; Burri *et al.*, 2005). This duality renders the UHT metamorphism a questionable Alpine event. Furthermore, zircon cores in a strongly residual granulite yield U-Pb ages of 272 ± 4 Ma (Liati and Gebauer, 2003), an age that corroborates petrographical similarity with granulites of the European lower crust (Downes *et al.*, 1990; Costa and Rey, 1995) related to post-Variscan extension and also fitting with granulite ages from the Southern Alps. Nevertheless, an Alpine age for the UHT metamorphism has been postulated by Liati and Gebauer (2003) on the basis of Oligocene U-Pb zircon rim ages (32.7 ± 0.5 Ma) and by Schmitz *et al.* (2009) on the basis of chemical U-Th-Pb dating of monazite (33 ± 4.4 Ma) from the same residual granulites. These granulites are composed of > 80 % mafic minerals (saphirine, orthopyroxene, garnet, Ti-rich biotite; Wenk et al. 1974) and represent refractory residuals formed after extraction of considerable amounts of charnockitic melt from a Mg-Al-rich metapelitic precursor. They have suffered multiple stages of equilibration and zircon zones and monazite ages cannot be unambiguously related to distinct metamorphic or magmatic events. We thus decided to investigate zircons from the recently discovered charnockites because they explicitly represent melt formed during the ultra-high temperature granulite event.

The major aims of this work are:

(i) to determine the age of the charnockitic magmatism and consequently clarify the tim-
ing of the granulitic event;

(ii) to establish the age of the regionally widespread partial melting;

(iii) to assess the protolith age of the migmatitic granitoids and thus establish the timing of
crustal growth;

(iv) to integrate the dated events of the Gruf Complex in the frame of the tectonic and
metamorphic history of the Central Alps.

5.2   Sample description and location

Fifteen samples representative of the entire spectrum of metagranitoid rocks in the Gruf Complex
were selected for dating. They cover the whole complex at different structural levels (Fig. 5.1).
The geological relationships, the petrography, the thermobarometry and the bulk rock analyses
of these metagranitoids are described in chapter 2 and 4.1. A summary of field features, mineral
assemblages and the exact sample locations are presented in table 5.2 and Fig. 5.1. The main
features and genetic interpretation of each dated rock are given in the following.
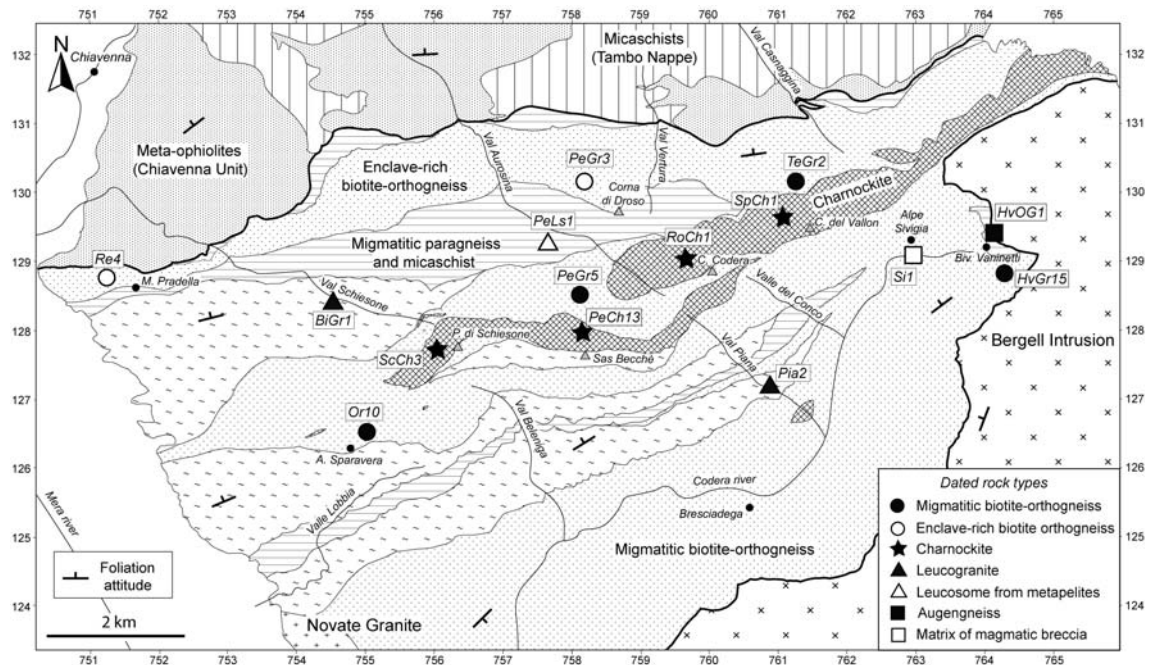
Figure 5.1: *Locations of investigated samples in simplified geological map of the Gruf Complex. Swiss co-
ordinates are given with units in kilometres.*

Charnockite (ScCh3, PeCh13, RoCh1, SpCh1)

Charnockites constitute sheet-like bodies within migmatitic biotite-orthogneiss. Anastomosing shear zones surround lense-shaped domains with preserved magmatic fabrics, sapphirine-orthopyroxene-bearing schlieren and disordered networks of crosscutting leucocratic veins. All samples were collected from homogeneous cores of charnockitic lenses (Fig. 5.2a), where the rock is medium- to coarse-grained, massive and mostly composed of quartz, plagioclase, alkali feldspar, orthopyroxene, garnet, biotite and ilmenite. Thermobarometric calculations showed that they crystallized at > 900 °C and 8-9.5 kbar (chapter 4.1). Their geochemistry is coherent with an origin through fluid-absent biotite melting at these conditions (chapter 3).

Migmatitic biotite-orthogneiss (PeGr5, HvGr15, Or10, TeGr2)

This orthogneiss constitute the largest part of the Gruf Complex. All investigated samples are homogeneous, coarse-grained and mostly constituted of quartz, plagioclase, alkali feldspar and biotite. Sample PeGr5 is almost equigranular (Fig. 5.2b), samples Or10, TeGr2 and HvGr15 are foliated (Fig. 5.2c).

Enclave-rich biotite-orthogneiss (PeGr3, Re4)

This orthogneiss is a 100-1500 m thick sheet along the northern border of the Gruf Complex. The rock is coarse-grained, weakly foliated, mainly composed of quartz, plagioclase, alkali feldspar and coarse-grained biotite, and characterised by centimetric to decimetric, internally undeformed, rounded enclaves of mafic composition (Fig. 5.2d). These enclaves, originally mainly composed of plagioclase + amphibole, are heavily overgrown by biotite and are commonly intruded by veinlets of granitic composition. The migmatitic and enclave-rich orthogneisses have slightly peraluminous granodioritic compositions (chapter 3).

Leucogranite (BiGr1, Pia2)

Leucogranites are spatially associated to migmatitic micaschists and paragneisses. They typically contain m-sized enclaves of metasediments. Sample BiGr1 is fine-grained, weakly foliated and composed of quartz, plagioclase, alkali feldspar, biotite, sillimanite, spinel and millimetric garnet porphyroblasts (Fig. 5.2e). Sample Pia2 is sub-equigranular, coarse-grained and constituted of quartz, plagioclase, alkali feldspar, biotite, muscovite and garnet. These leucogranites are peraluminous (chapter 3).

Leucosome within metapelites (PeLs1)

This sample was taken from a leucocratic, 40 - 50 cm large melt pocket within sillimanite-garnet-alkali feldspar-biotite migmatitic schists (Fig. 5.2f). It is interpreted as in-situ melts generated during regional partial melting. The rock is fine- to medium-grained, almost unfoliated and composed of quartz, plagioclase, alkali feldspar, biotite, muscovite and millimetric, rounded garnet
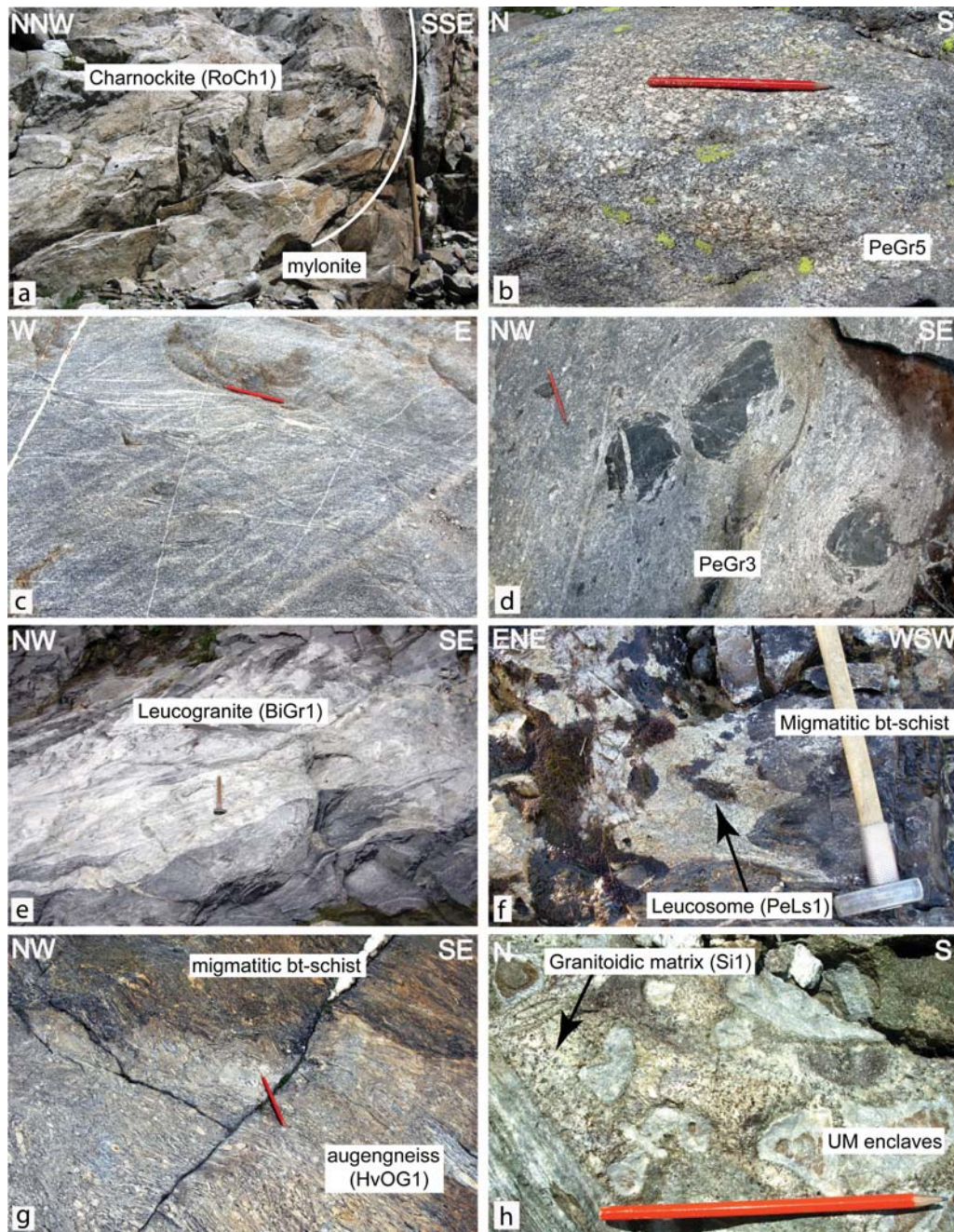
Figure 5.2: *Field aspect of investigated rock types. (a) homogeneous, coarse-grained and massive lense-shaped domain in charnockite, bounded by centimetric thick, anastomosing shear zone (sample RoCh1, Val Vertura, 759'652/129'116); (b) massive and coarse-grained biotite orthogneiss (sample PeGr5, Val Aurosina, 758'306/128557); (c) foliated biotite orthogneiss marked by NNE dipping ductile shear zones (sample HvGr15, Bivacco Vaninetti, 764'135/129'063); (d) Slightly foliated and coarse-grained enclave-rich biotite orthogneiss marked by up to 25 cm large, almost undeformed, mafic enclaves (sample PeGr3, Val Aurosina, 758'153/129'875); (e) slightly foliated leucogranite (sample BiGr1, Val Schiesone, 754'574/128'454); (f) leucosome collection in a melt pocket discordant to the main foliation of migmatitic biotite-schists (sample PeLs1, Val Aurosina, 757'796/129'158); (g) Slightly foliated and coarse-grained augengneiss (bottom) intrusive into migmatitic biotite-schists (top) (sample HvOG1, Bivacco Vaninetti, 763'960/129'377); (h) magmatic breccia formed by massive, leucocratic matrix of granitoidic composition and rounded components of ultramafic compositions. The components display greyish reaction rims of talc and chlorite (sample Si1, Alpe Sivigia, 763'089/128'940).*

porphyroblasts. The occurrence of sillimanite + alkali feldspar and the lack of syn-kinematic muscovite in the host migmatite suggest that melting was induced by the breakdown of muscovite at about 700 - 750 °C (chapter 4.1).

Augengneiss (HvOG1)

This sample was collected in an up to 20 m thick sheet within migmatitic metasediments. It is slightly foliated, coarse-grained, mainly composed of quartz, plagioclase, alkali feldspar, biotite and muscovite, characterized by centimetric augen of quartz and feldspar. The sheet displays sharp intrusive contacts with the country rocks (Fig. 5.2g). Its geochemistry is, like the migmatitic orthogneisses, slightly peraluminous (chapter 3).

Matrix of magmatic breccia (Si1)

This sample represents the granitic matrix of a breccia (Fig. 5.2h) characterised by 5-50 % rounded, mostly ultramafic but also mafic enclaves (the "Sivigia-Zug" of Wenk and Cornelius, 1977). It is medium- to coarse-grained, almost unfoliated and constituted of quartz, plagioclase, alkali feldspar, biotite and rare, millimetric garnet. Field observations suggest that this breccia (and similar occurences nearby) formed by injection of leucosomes from the migmatitic biotite-orthogneiss into ultramafic lenses and associated metabasic rocks.

5.3 SHRIMP U-Pb geochronology

5.3.1 Analytical technique and data evaluation

More than 1 kg fresh and homogeneous material was processed for each sample. Zircons were separated at ETH Zurich by standard grinding, Wilfley table, heavy liquids and magnetic separation procedures. The zircons have been cast with Buehler Epokwick resiny along with standard zircons 91500 (Wiedenbeck *et al.*, 1995) and Temora (Black *et al.*, 2003). After epoxy cured (ca. 4-5 days) the puck was polished till zircon grains were half-sectioned. Both transmitted and reflected light images as well as BSE and CL microphotographs were taken in order to distinguish between different zircon domains and choose the positions of analytical spots. In-situ U-Pb analyses were performed using SHRIMP-II in the Center of Isotopic Research (CIR) at VSEGEI, applying a secondary electron multiplier in peak-jumping mode following the procedure described by Williams (1998) and Larionov *et al.* (2004). The primary O_2-c. 27x20 μm in size beam had corresponding current 4.5-5.0 nA. The mass-resolution M/ΔM > 5000 (1% valley) allowed resolution of possible isobaric interferences.

Four cycles through the following ion species were measured: ^{196}(Zr2O)-^{204}Pb-background (c. 204 AMU)-^{206}Pb-^{207}Pb-^{208}Pb-^{238}U-^{248}ThO-^{254}UO. Each fifth measurement was carried out on the Temora standard. The collected results have been processed with the SQUID v1.12 (Ludwig, 2005a) and ISOPLOT/Ex 3.22 (Ludwig, 2005b) software, with decay constants of Steiger and Jäger (1977) and common lead corrected using measured ^{204}Pb/^{206}Pb (Stacey and Kramers,

Table 5.2
Main field characteristics, observed mineral assemblage and provenance of the investigated samples

Sample	Formation	Field characteristics	Mineral assemblage	Swiss coordinates	Altitude
Charnockite					
ScCh3	Opx–Grt-bearing melt formed	8 x 0.5 km large sheet-like bodies within the migmatitic bt-OG	qtz, pl, ksp, bt, opx, grt, amp, zrc, rut, ilm, op	756'056 / 127'803	2200 m
PeCh13	by biotite-dehydration melting	marked by lense-shaped domains with flow structures, granulitic	qtz, pl, ksp, bt, opx, grt, amp, chl, spl, zrc, rut, ilm, op	758'057 / 128'116	2400 m
RoCh1	of a sedimentary precursor	schlieren, networks of crosscutting melts and dykes separated by	qtz, pl, ksp, bt, opx, grt, chl, amp, zrc, rut, ilm, op	759'652 / 129'116	2350 m
SpCh1	at UHT granulitic conditions	anastomosing shear zones. Mylonitic contacts to the country rock	qtz, pl, ksp, bt, opx, grt, amp, zrc, rut, ilm, op	760'869 / 129592	2220 m
Migmatitic biotite-orthogneiss					
Or10	Granitoid intrusion	Coarse-grained, slightly foliated	qtz, pl, ksp, bt, ± ms, chl, ep, ap, zrc, rut/sph, ilm, op	755'073 / 126'380	1890 m
PeGr5		Coarse-grained, massive	qtz, pl, ksp, bt, chl, amp, ap, zrc, rut/sph, ilm, op	758'306 / 128557	2200 m
TeGr2		Coarse-grained, slightly foliated	qtz, pl, ksp, bt, chl, ep, ap, zrc, rut/sph, ilm, op	761'400 / 130'037	2240 m
HvGr15		Coarse-grained, slightly foliated, with cm shear zones	qtz, pl, ksp, bt, chl, ep, ap, zrc, rut/sph, ilm, op	764'135 / 129'063	2540 m
Enclave-rich biotite-orthogneiss					
PeGr3	Granitoid intrusion	Coarse-grained, undeformed with up to 30 cm large,	qtz, pl, ksp, bt, chl, ep, ap, zrc, rut/sph, ilm, op	758'153 / 129'875	2015 m
Re4		rounded, massive enclaves of mafic composition	qtz, pl, ksp, bt, ep, ap, zrc, rut/sph, ilm, op	751'502 / 128'762	880 m
Leucogranite					
BiGr1	Melt derived by the melting	Fine-grained and slightly foliated	qtz, pl, ksp, bt, ms, grt, sil, spl, zrc, rut/sph, op	754'574 / 128'454	1315 m
Pia2	of a peltic precursor	Coarse-grained and massive	qtz, pl, ksp, bt, grt, sil, ms (rare), zrc, op	761'011 / 127'131	1750 m
Leucosome					
PeLs1	Melt formed by muscovite-dehydration melting of pelites	Up to 50 cm large, leucocratic, massive melt pocket discordant to the host migmatitic metapelites	qtz, pl, ksp, bt, ms, grt, sil, spl, zrc, rut/sph, op	757'796 / 129'158	1890 m
Augengneiss					
HvOG1	Granitoid intrusion into sedimentary sequence	Coarse-grained, slightly foliated, up to 20 m thick granitic sheet discordant into migmatitic sediments	qtz, pl, ksp, bt, ms, ep, ap, zrc, rut/sph, op	763'960 / 129'377	2600 m
Matrix of magmatic breccia					
Si1	Melt originated by partial melting of a granitoid precursor	Up to 10 cm thick, leucocratic, massive granitic dykes forming the matrix of a ultramafic breccia	qtz, pl, ksp, bt, grt, ap, zrc, rut/sph, op	763'089 / 128'940	2080 m

Mineral abbreviations: qtz – quartz; pl – plagioclase; ksp – alkali feldspar; bt – biotite; ms – muscovite; chl – chlorite; grt – garnet; sil – sillimanite; opx – orthopyroxene; amp – amphibole; spl – spinel; ep – epidote; ap – apatite; zrc – zircon; rut – rutile; sph – sphene; ilm – ilmenite.

1975). The data are presented on concordia (Wetherill, 1956) or Tera-Wasserburg diagrams (Tera and Wasserburg 1972).

5.3.2   CL-pattern and zircon characteristics

Charnockite

CL-imaging shows homogeneous and similar zircon populations in the four charnockite samples. Crystals are commonly elongate, prismatic, euhedral to subhedral with rounded outlines (Fig. 5.3a and Figs. H.7-H.10). They are 180-450 μm long and 70-200 μm wide. They display low to highly luminescent, both oscillatory and planar zoned cores, typical for zircons precipitated during granite crystallization (Corfu *et al.*, 2003). A few zircon cores of samples RoCh1 and SpCh1 exhibit broad planar banding (Fig. 5.3a). In ScCh3 and PeCh13, rare xenocrystic cores are mantled by magmatic zircon domains with oscillatory zoning.

Rims around the magmatic zircon domains and commonly truncating zoning patterns are characterised by homogeneous and moderate luminescence. These rims are normally interpreted as metamorphic growth that may or may not have involved melts of migmatitic origin. Zircons from samples ScCh3 and RoCh1 display well developed, 20-30 μm wide rims; zircon rims of samples PeCh13 and SpCh1 are < 15 μm wide. In general, rims are slightly thicker at grain terminations (Fig. 5.3a).

Migmatitic biotite-orthogneiss

All samples exhibit homogeneous zircon populations characterised by elongate, prismatic grains. Zircons from samples Or10, PeGr5 and HvGr15 are euhedral to subhedral with slightly rounded outlines, while zircons from sample TeGr2 are euhedral with straight edges and sharp angles (Fig. 5.3b and Figs. H.1-H.4). Grain size varies between 250 600 μm in length and 100-200 μm in width. Cores are dominated by well developed oscillatory zoning with variable luminescence, interpreted as magmatic in origin. A few crystal cores in samples Or10 and PeGr5 display sector and broad planar zoning. Regular zoning is commonly truncated or resorbed and subsequently overgrown by growth-zoned domains. Rare xenocrystic inner cores were observed in PeGr5 and HvGr15.

The volumetrically dominant oscillatory zoned cores are surrounded and truncated by homogeneous, moderately luminescent rims of variable thickness, strongly luminescent for their outermost part (< 5 μm). Zircons from sample Or10 show < 5 μm thin rims; rims are are 15-20 μm wide in PeGr5 and HvGr15. Rims in TeGr2 are well developed and show weak oscillatory and sector zoning. In some grains the rims almost replace the oscillatory cores (Fig. 5.3b).

Enclaves-rich biotite granite

Zircon populations from both samples are homogeneous and comprise elongate, prismatic, euhedral crystals with straight edges and sharp angles (Fig. 5.3c and Figs. H.5-H.6), typically 250-600
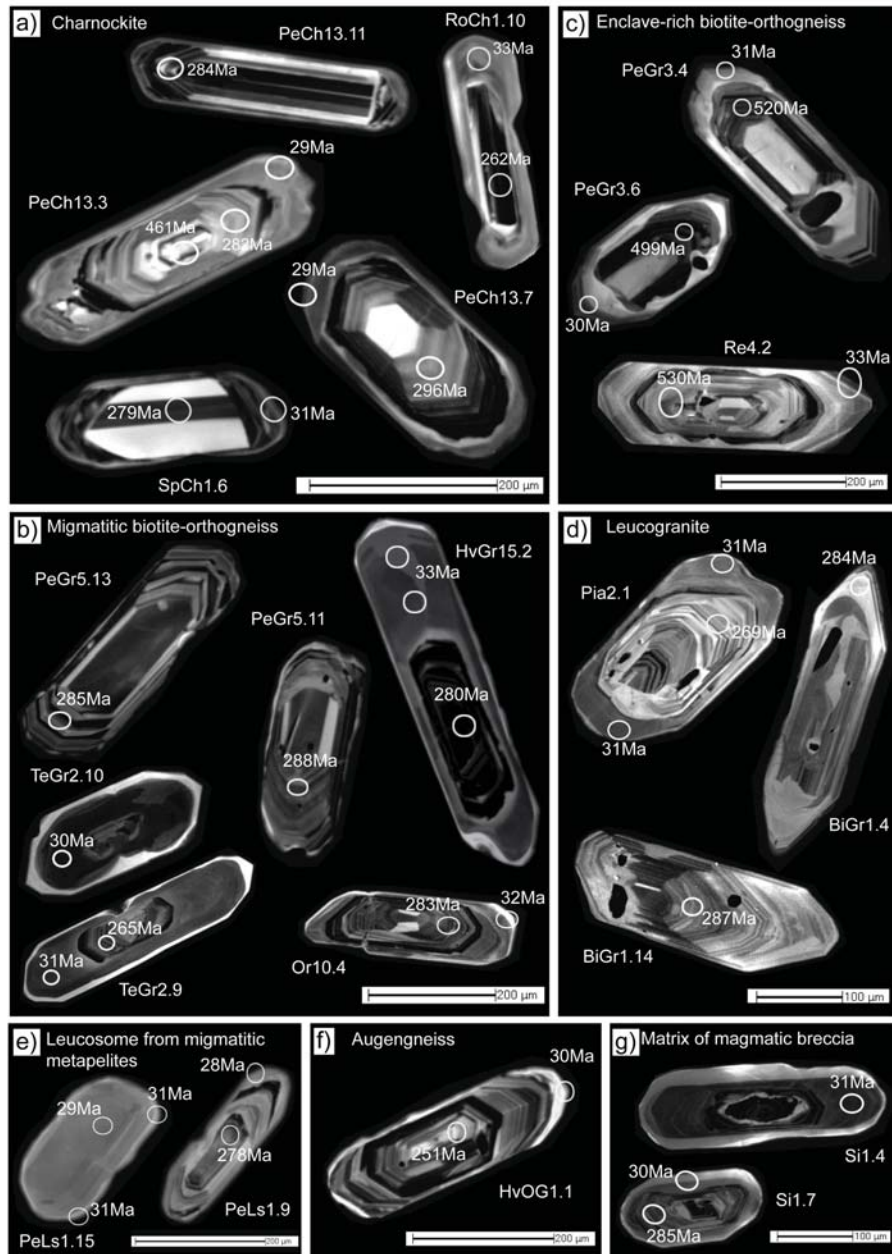
Figure 5.3: *Cathodoluminescence (CL) pictures of representative zircons crystals from metagranitoids of the Gruf Complex. (a) Zircon from charnockites are characterised by Permian oscillatory, sector or planar zoned cores and homogeneous outer rims of Alpine age; (b) zircon from migmatitic biotite orthogneisses display oscillatory zoned Permian cores and Alpine metamorphic rims. Rim development strongly depends on sample. Generally, rims are homogeneous. In sample TeGr2, rims display sector and oscillatory zoning; (c) zircons from the enclave-rich biotite-orthogneiss display both Cambrian and Ordovician oscillatory zoned cores. The grains are characterised by thick, oscillatory zoned metamorphic rims, suggesting that rim re-crystallised during partial melting; (d) sector and oscillatory zoned cores and thin metamorphic rims of Alpine age constitute zircon crystals of leucogranites; (e) zircons from leucosome of metapelites display oscillatory zoned cores and thick metamorphic rims. The left grain is completely recrystallised during the Lepontine metamorphism at ca. 30 Ma; (f) zircon from the augengneiss present a well developed oscillatory zoning formed in Permian. Alpine metamorphic rims are almost absent; (g) zircon from the leucocratic matrix of magmatic breccia are generally small and constituted by Permian oscillatory zoned cores and thick outer rims. Rims present slightly developed oscillatory or sector zoning.*

μm long and 100-170 μm wide. Crystal cores are low to highly luminescent and exhibit oscillatory zoning or, in rarer cases, sector zoning, typical of zircons of granitic origin. Inherited xenocrystic cores were not found. The oscillatory zoned cores are truncated by 25-30 μm thick rims, thickest at grain terminations (< 80 μm). Rims are heterogeneous and usually marked by oscillatory, concentric or broad planar zoning, often discordant on the inner zoning of grain cores. Some zircon rims have homogeneous, moderately luminescent inner parts surrounded by a thin (< 5-0 μm) highly luminescent outermost domain, similar to the rims exhibited by zircons of sample TeGr2.

Leucogranite

Zircons from both samples are elongate to equant, prismatic and euhedral to subhedral with slightly rounded outlines (Fig. 5.3d and Figs. H.11-H.12). Grains are 150-550 μm long and 75-150 μm wide. In both samples, zircon cores display two different types of zoning. Some crystals exhibit a regular oscillatory zoning while others show large, highly luminescent sector-zoned domains surrounded by a thinner, less luminescent oscillatory zoning. No inherited xenocrystic zircons were observed. Zircons in sample BiGr1 have thin (< 3-4 μm) or no rims. Zircons in sample Pia2 display moderately luminescent, 20-25 μm wide rims that are thicker (up to 70 μm) at grain terminations.

Leucosome within metapelites

Zircon crystals are elongate, prismatic, euhedral to subhedral with slightly rounded outlines (Fig. 5.3e and Fig. H.13). They are 200-300 μm long and 75-100 μm wide. Crystal cores are usually moderate to highly luminescent and display oscillatory, sector or broad planar zoning. Rare xenocrystic inner cores were observed. The oscillatory cores are surrounded by homogeneous, bright rims with a thickness ranging from several to 25 μm. One zircon is characterised by a bright, homogeneous CL intensity (Fig. 5.3e). We interpret this single crystal pattern as due to complete re-homogenisation during metamorphism/anatexis.

Augengneiss

CL-imaging shows a homogeneous zircon population, characterised by elongate, prismatic, euhedral grains with slightly rounded outlines (Fig. 5.3f and Fig. H.15). Crystal sizes are 250-500 μm in length and 100-150 μm in width. Zircons present moderate to highly luminescent oscillatory zoned cores representing granite crystallization.Grain cores rarely display sector zoning. Xenocrystic inheritance was not observed. Magmatic inner domains are surrounded by thin (< 5 μm), homogeneous and highly luminescent rims, which truncate the internal zoning.

Matrix of magmatic breccia

Zircons are elongate to equant, euhedral to subhedral with slightly rounded outlines (Fig. 5.3g and Fig. H.14). Their length varies from 200 to 600 μm and their width from 75 to 150 μm.

CL-imaging revealed cores with moderate luminescence and magmatic oscillatory or, in rarer cases, sector zoning. A few grains display inherited xenocrystic inner cores. The oscillatory cores are surrounded by wide discordant rims. These rims are moderately luminescent but highly luminescent in the outermost part. Some rim domains show the same oscillatory pattern as the cores, preserved as ghost oscillatory zoning (Fig. 5.3g). Rim thicknesses vary strongly from grain to grain.

Summary

In summary, zircons have rare xenocrystic inner cores and wide, volumetrically dominant outer cores made up by oscillatory and sector zoning; these are attributed to zircon growth during the crystallization of the granitic host rocks. Outer zircon rims are attributed to metamorphic recrystallization. Nevertheless, the migmatitic biotite-orthogneisses (TeGr2), the enclave-rich biotite-orthogneiss sheet and the granitic matrix of the magmatic breccia developed rims with oscillatory zoning. These rims point to significant partial melting of the hosting granites during regional anatexis.

5.3.3 U-Pb results

After the SHRIMP measurements the exact locations of the single spots were checked by CL imaging and mixed analyses of different zircon domains excluded. Results are summarized in Tab. 5.3.3, SHRIMP data are available in appendix H.

Charnockite

ScCh3. Seven data points were obtained from the oscillatory zoned cores of seven zircon grains. Th/U ratios vary between 0.34 and 0.65. One spot yielded an Ordovician age of 478 Ma and six analyses yielded Permo-Triassic ages of 298-245 Ma. On a Concordia diagram, 3 spots yielded concordant ages of 260 ± 3 Ma (Fig. 5.4a). Ten spots from the homogeneous rims of ten zircon crystals were measured, but post-SHRIMP CL-imaging revealed that four spots touched the oscillatory zoned cores yielding mixed ages. The remaining six have Th/U ratios between 0.02 and 0.44. On a Tera-Wasserburg diagram, they plot on a mixing line between common Pb and calibrated total ^{238}U/^{206}Pb, intersecting the concordia at a weighted mean age of 30.63 ± 0.92 Ma (Fig. 5.4b).

PeCh13. Twelve data points were obtained from the oscillatory zoned cores of twelve zircon grains. For these, Th/U ratios vary from 0.14 to 0.96. One spot yielded a Carboniferous age of 305 Ma, nine analyses Permo-Triassic ages between 296 Ma and 247 Ma, while two data spots yielded 193 and 131 Ma, respectively. On a Concordia diagram, a cluster of four analyses gives a concordant age of 282 ± 2 Ma (Fig. 5.4c). Seven spots from homogeneous rims of seven grains yield Th/U ratios of 0.01-0.04. On the Tera-Wasserburg diagram, they plot on a mixing line between common Pb and calibrated ^{238}U/^{206}Pb (Fig. 6d) giving a weighted mean age of 29.17 ± 0.25 Ma (Fig. 5.4d).

RoCh1. Eleven oscillatory zoned cores of eleven grains were analysed. Their Th/U ratios vary between 0.15 and 1.25. All points yield Carboniferous to Triassic ages, between 310 and 212 Ma. On a Concordia diagram, a cluster of four measurements gives a concordant age of 260.8 ± 2.1 Ma (Fig. 5.4e). Two out of ten homogeneous rim analyses from ten grains were mixed. The remainders gave Th/U ratios of 0.02-0.35. On a Tera-Wasserburg diagram, seven of them plot on a mixing line between common Pb and calibrated total ^{238}U/^{206}Pb (Fig. 5.4f), yielding a weighted mean age of 34.29 ± 0.77 Ma.

SpCh1. Nine oscillatory zoned cores were measured, yielding Th/U ratios between 0.16 and 0.78. Six spots gave concordant ages of 279.5 ± 2.6 Ma (Fig. 5.4g), one analysis yielded an older age of 314.7 ± 3.3 Ma. Post analysis CL-imaging revealed that this latter spot spans a crack, where accumulation of radiogenic Pb may have led to the slightly higher age. Two analyses yielded younger ages, probably due to partial Pb-loss after crystallization. Ten spots were measured in outer rims of nine grains, but post analysis CL-imaging revealed three mixed analyses. The other seven give Th/U ratios of 0.01-0.05, and on the Tera-Wasserburg diagram lie on a mixing line between common Pb and calibrated total ^{238}U/^{206}Pb, intersecting the Concordia at a weighted

mean age of 30.6 ± 1.2 Ma (Fig. 5.4h).

Migmatitic biotite-orthogneiss

Or10. Nine spot analyses of oscillatory zoned cores from nine zircon crystals yield Th/U ratios of 0.19-0.62 and Permo-Triassic ages between 291.3 and 245.6 Ma (Fig. 5.5a). Five are concordant and give an age of 287.0 ± 6.1 Ma. Ten homogeneous rims were analysed but two were mixed. The Th/U ratios range between 0.01 and 0.07 and the eight spots yielded a concordant age of 32.20 ± 0.82 Ma (Fig. 5.5b).

HvGr15. Twelve spot analyses of oscillatory zoned cores display Th/U ratios of 0.10-0.63 and yield Carboniferous to Triassic ages comprised between 320 and 245 Ma. Six of them give a concordant age of 280 ± 3 Ma (Fig. 5.5c). Two analyses of xenocryst cores yielded Ordovician age of 482 Ma and Devon age of 389 Ma, respectively. Thirteen homogeneous outer rims were analysed but eight of them were mixed. The other five display Th/U ratios of 0.01-0.16 and yield a metamorphic age of 32.3 ± 1.8 Ma (Fig. 5.5d).

TeGr2. Eight oscillatory zoned cores from eight zircon grains display Th/U ratios of 0.18-0.44. Five of them give a concordant age of 266.4 ± 1.9 Ma (Fig. 5.5e). One spot analysis yielded a higher age of ∼ 290 Ma. This analysis was not taken into account for calculation because of its high U content of 2343 ppm, which may lead to erroneously high ages (Mc Laren *et al.*, 1994; Williams *et al.*, 1996). Two other analyses yielded slightly younger ages probably due to post-crystallization Pb-loss. Twelve analyses of the thick outer rims were obtained, eleven of them yielding a low Th/U ratio of 0.01-0.04 and a concordant age of 30.46 ± 0.28 Ma (Fig. 5.5f). One analysis gave a slightly higher age of ∼ 36 Ma. CL-imaging of this spot revealed that it covers ghost textures of the oscillatory zoning, which may induce mixed isotopic ages.

PeGr5. Twelve oscillatory zoned cores of twelve different grains with Th/U ratios of 0.02-0.47 were analysed. Ten of them yield a concordant age of 287 ± 3 Ma (Fig. 5.5g). One analysis gave a slightly older age of 305 Ma but was not taken into account for calculation because of its high U content of 2577 ppm. One spot analysis yielded a slightly younger Triassic age probably due to post-crystallization Pb-loss. Metamorphic outer rims were too thin to obtain an age.

Enclaves-rich biotite granite

PeGr3. Ten data points were obtained from oscillatory zoned cores of nine zircons with Th/U ratios between 0.12 and 0.18. Two sets of ages have been identified. Five spots yield a concordant Cambrian age of 513.3 ± 7.5 Ma, and four yield a concordant Ordovician age of 453.0 ± 8.4 Ma (Fig. 5.6a). Thirteen spot analyses were carried out on the wide oscillatory zoned rims of nine crystals yielding variable Th/U ratios of 0.01-0.18. All of them plot on a mixing line between common Pb and calibrated total ^{238}U/^{206}Pb, intersecting the Concordia at a weighted mean age of
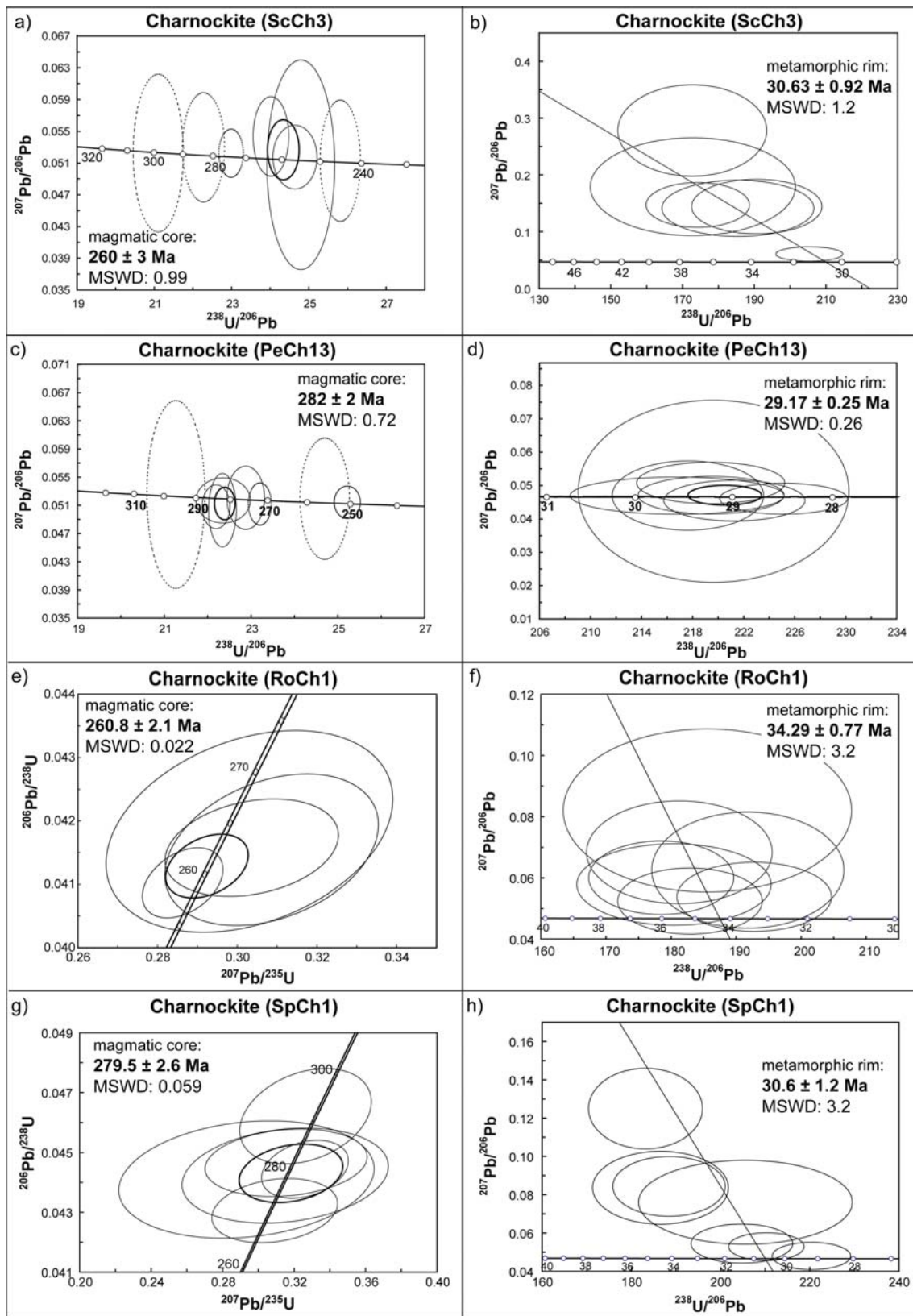
Figure 5.4: *Concordia and Tera-Wasserburg diagrams with data of zircons separated from the Gruf charnockites. The ages are calculated as weighted mean and the errors on the ages are at the 95% c.l. The ellipses are plotted with a 2σ-error*
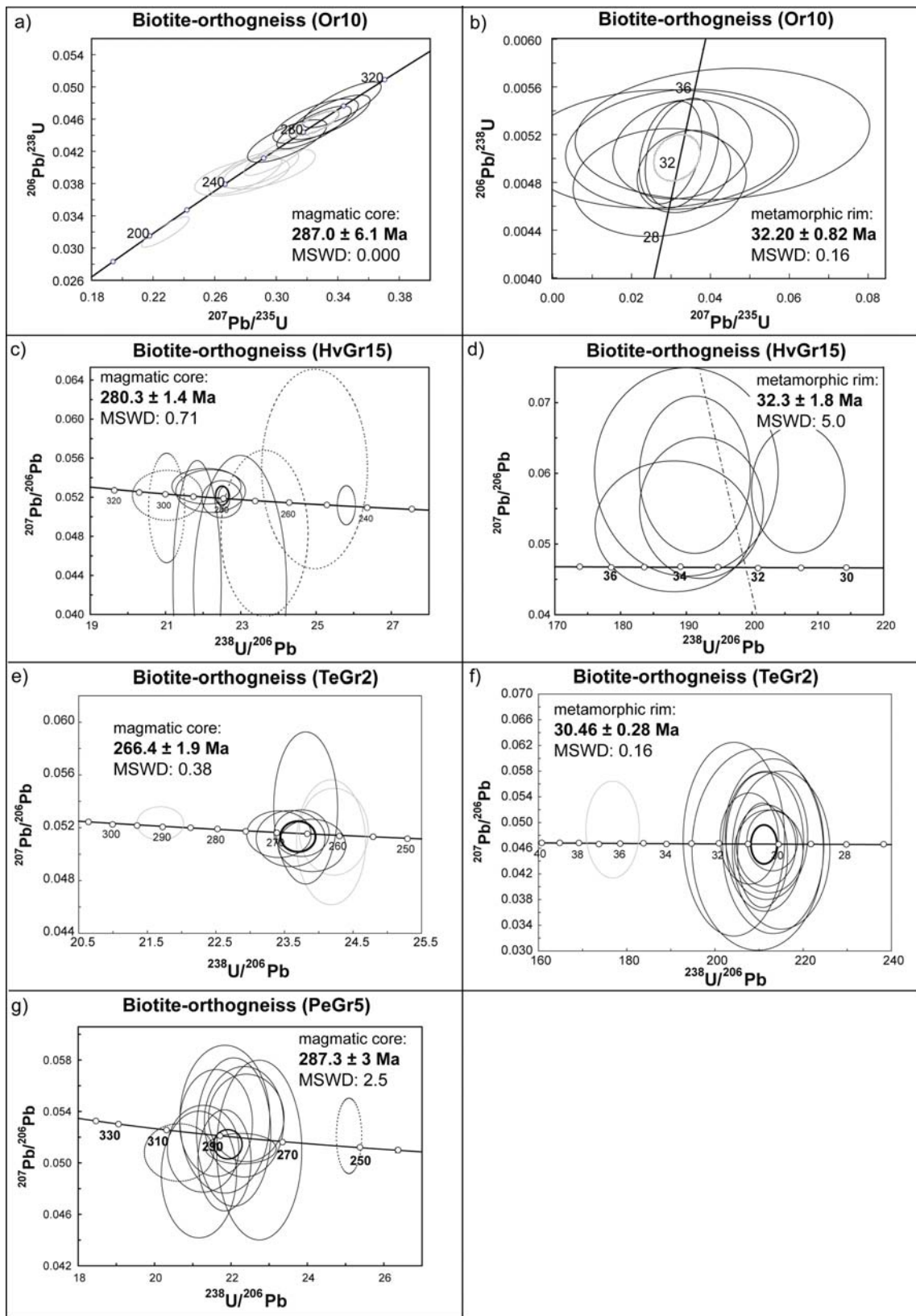
Figure 5.5: *Concordia and Tera-Wasserburg diagrams with data of zircons separated from the Gruf migmatitic biotite-orthogneisses. The ages are calculated as weighted mean and the errors on the ages are at the 95% c.l. The ellipses are plotted with a 2σ-error*

115

30.92 ± 0.67 Ma (Fig. 5.6b).

Re4. Nine oscillatory zoned cores from nine zircon grains give Th/U ratios of 0.04-0.79. One data point yielded a Cambrian age of 530 ± 20 Ma, two points yielded Ordovician ages of 464 and 473 Ma, while six points yielded Permian ages between 224 and 300 Ma (Fig. 5.6c). A cluster of three spots yielded a concordant age of 290.4 ± 8.1 Ma. Twelve points in the oscillatory zoned rims of eleven zircon crystals, with Th/U ratio of 0.01-0.20, give a concordant age of 32.19 ± 0.53 Ma (Fig. 5.6d).
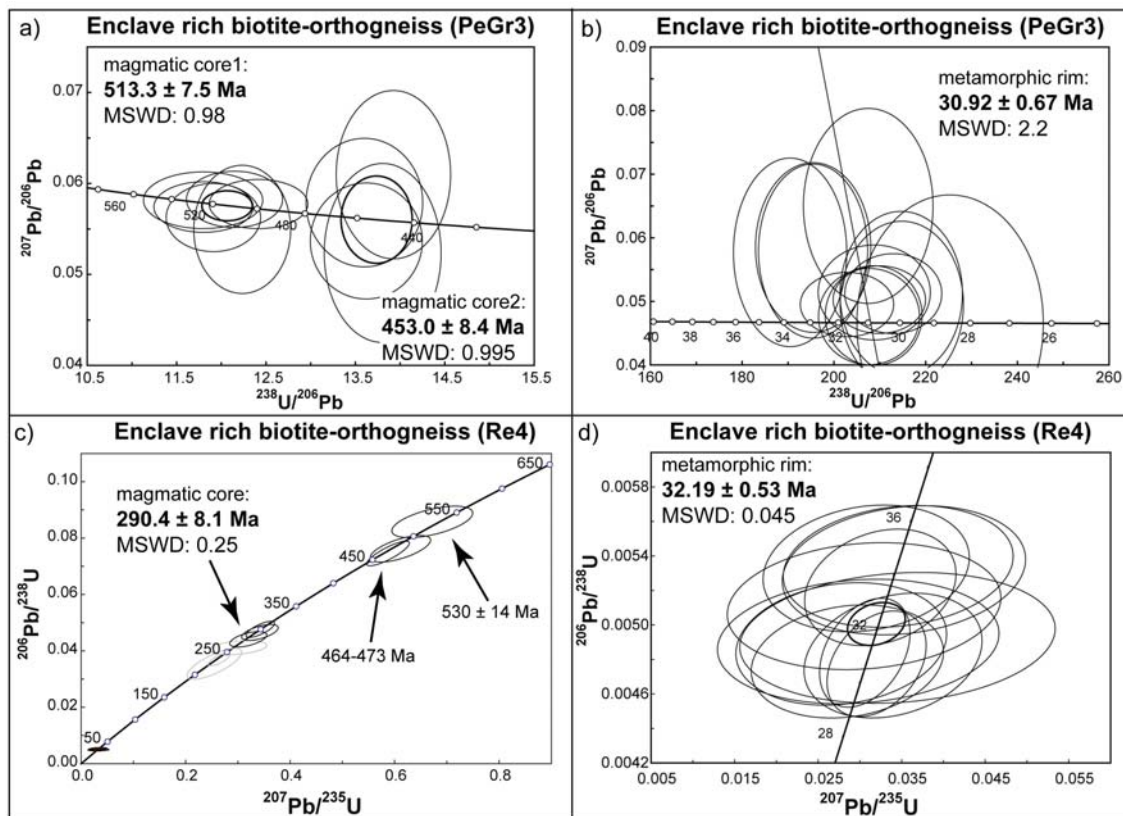
Figure 5.6: *Concordia and Tera-Wasserburg diagrams with data of zircons separated from the Gruf enclave-rich biotite-orthogneisses. The ages are calculated as weighted mean and the errors on the ages are at the 95% c.l. The ellipses are plotted with a 2σ-error*

Leucogranite

Pia2. Ten analyses of oscillatory and sector zoned cores from nine zircon grains give variable Th/U ratios of 0.01-0.45 and Permo-Triassic ages of 153 to 298 Ma (Fig. 5.7a). No systematic difference between oscillatory and sector zoning was observed. Three spots yield a concordant age of $293.9 \pm 0.3.8$ Ma. The broad scattering of the other data likely results from extensive post-crystallization Pb loss. Eight homogeneous rims were analysed giving Th/U ratios < 0.01. Six data points yield a concordant age of 30.86 ± 0.31 Ma (Fig. 5.7b). The other two were identified

as mixed analyses during post-SHRIMP CL-imaging.

BiGr1. Twenty data points were obtained from oscillatory and sector zoned cores of fifteen grains. Th/U ratios vary between 0.01 and 0.67 and ages are scattered between 300 and 146 Ma (Fig. 5.7c). A cluster of seven ages yield a concordant age of 288 ± 2 Ma. Rims were too thin ($<$ 3-4 μm) to obtain an age.
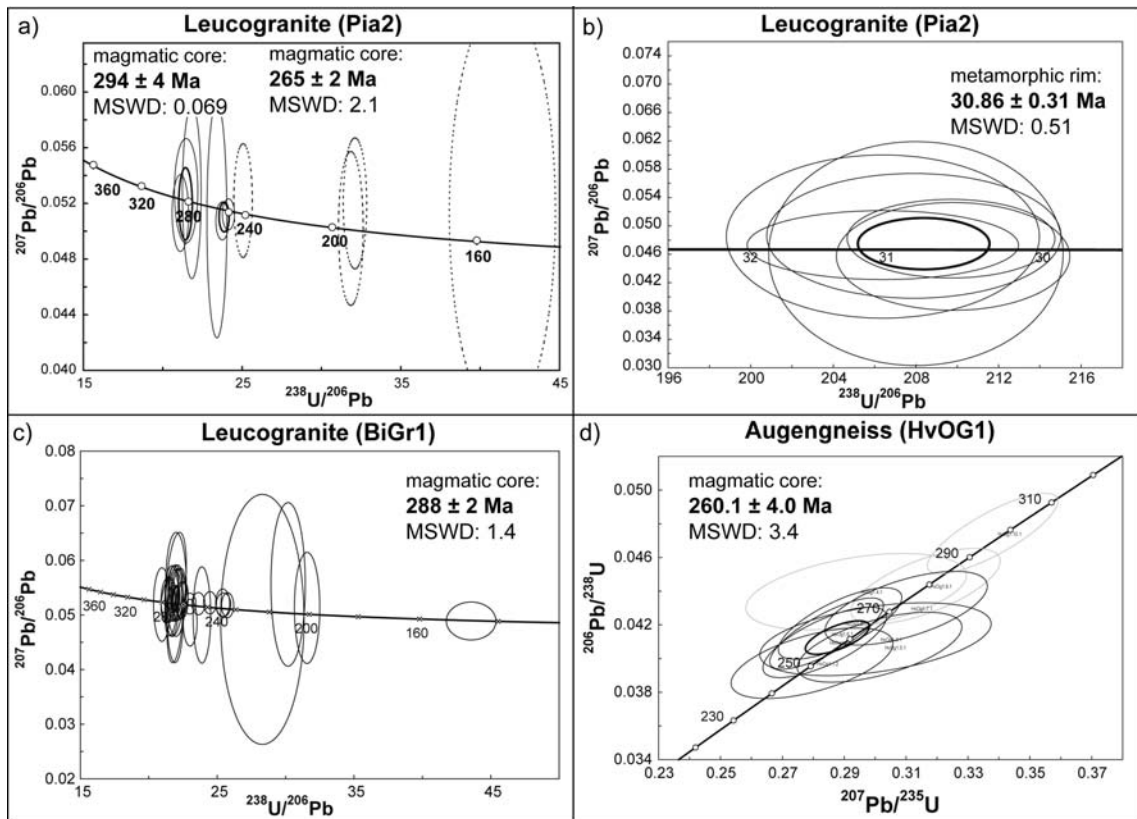
Figure 5.7: *Concordia and Tera-Wasserburg diagrams with data of zircons separated from the Gruf leucogranites. The ages are calculated as weighted mean and the errors on the ages are at the 95% c.l. The ellipses are plotted with a 2σ-error*

Leucosome within metapelites

PeLs1. Twelve oscillatory and sector zoned core spots with Th/U ratios of 0.01-0.83 yield ages between 538 Ma and 172 Ma (Fig. 5.8a). No preferred age is obtained for the oscillatory zoned cores of presumably magmatic origin, in agreement with a detrital zircon component in the protolith sediment. Three rim data points out of fifteen were mixed. Twelve yield Th/U ratios of 0.01-0.19 and plot on a mixing line between common Pb and calibrated total ^{238}U/^{206}Pb, intersecting the Concordia at a weighted mean age of 30.06 ± 0.93 Ma (Fig. 5.8b). The same age was calculated from the completely re-homogenised grain (Fig. 5.3e), suggesting that 30.06 ± 0.93 Ma dates partial melting.
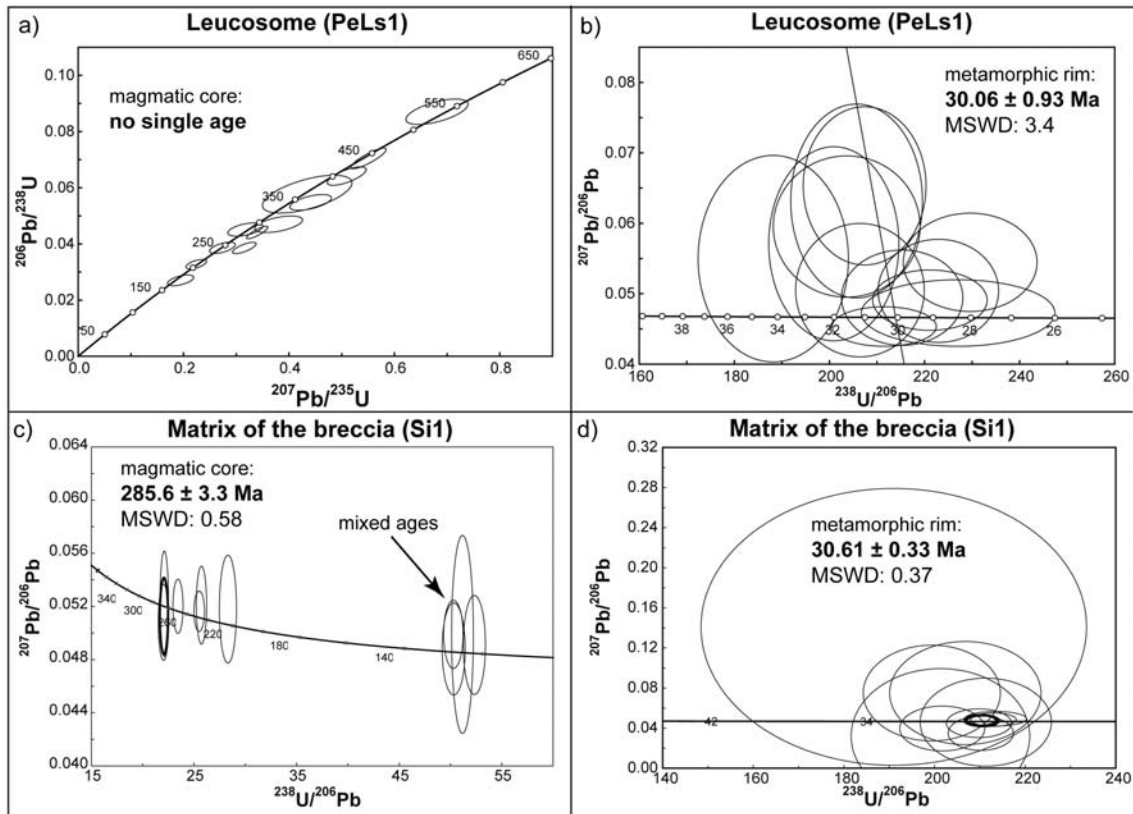
Figure 5.8: *Concordia and Tera-Wasserburg diagrams with data of zircons separated from the Gruf leucogranites. The ages are calculated as weighted mean and the errors on the ages are at the 95% c.l. The ellipses are plotted with a 2σ-error*

Augengneiss

HvOG1. Ten spots were investigated from the oscillatory zoned cores of ten crystals. The measured Th/U ratios range between 0.05 and 0.28. On a Concordia diagram, seven measurements yield a concordant age of 260.1 ± 4 Ma (Fig. 5.7d). No age could be obtained from the < 5 μm wide rims.

Matrix of magmatic breccia

Si1. Six oscillatory zoned inner cores of six zircon grains have Th/U ratios of 0.21-0.55 and ages scattering between 286 and 220 Ma. Two data points yield a concordant age of 285.6 ± 3.3 Ma (Fig. 5.8c). Fourteen spots were measured in rims, but four were sampling both oscillatory zoned domains and metamorphic outer rims. The remainder yields Th/U ratios of 0.01-0.51 and concordant ages of 30.61 ± 0.33 Ma (Fig. 5.8d).

Table 5.3.3

Summary of SHRIMP ages for the metagranitoid rocks of the Gruf Complex

Sample	Core age (Ma)[*]			Rim age (Ma)[**]
ScCh3	260 ± 3			30.63 ± 0.92 Ma
PeCh13	282 ± 2			29.17 ± 0.25
RoCh1	260.8 ± 2.1			34.29 ± 0.77
SpCh1	279.5 ± 2.6			30.6 ± 1.2
Or10	287 ± 6.1			32.2 ± 0.82
PeGr5	289.4 ± 4.9			no measurable rim
TeGr2	266 ± 1.9			30.61 ± 0.47[***]
HvGr15	286.7 ± 9.2			36.1 ± 1.6
PeGr3	513.3 ± 7.5;	453.0 ± 8.4		30.92 ± 0.67[***]
Re4	530 ± 14;	~ 470;	290.4 ± 8.1	32.19 ± 0.53[***]
BiGr1	288 ± 2			no measurable rim
Pia2	293 ± 3.8			30.86 ± 0.31
PeLs1	no single age but scattering between 538 Ma and 172 Ma			30.06 ± 0.93
HvOG1	260.1 ± 4			no measurable rim
Si1	285.6 ± 3.3			30.61 ± 0.33[***]

Ages are given as weighted mean ages and the error is at the 95% c.l. [*] Magmatic age of oscillatory zoned zircon cores; [**] metamorphic age of homogeneous outer zircon rims; [***] rims display also oscillatory zoning.

5.4 Discussion - Formation conditions of zircon domains

5.4.1 Mineral inclusions in charnockite zircons

In order to relate the measured zircon ages in the charnockite with the stable mineral assemblage during zircon formation, we investigated mineral inclusions within their Permian, oscillatory zoned cores. All minerals of the rock matrix, i.e. quartz, plagioclase, alkali feldspar, Ti-rich biotite, garnet, orthopyroxene and apatite, were also found included within the Permian zircon cores. Inclusions have similar compositions as the same minerals in the rock matrix (Tab. 5.4.1). Most relevant, Permian zircon cores of samples SpCh1(Figs. 5.9a and b), RoCh1 (Figs. 5.9c and d) and ScCh3 (Figs. 5.9e and f) contain tiny, 10-30 μm long orthopyroxene grains.

5.4.2 Zircon dissolution during migmatization: age of the granulite facies metamorphism

Investigation of the crystal morphology coupled with U-Pb analyses revealed the composite nature of the studied zircon grains. They all have inherited, oscillatory and/or sector zoned cores and homogeneous rims. Due to its low solubility in crustal melts (Watson, 1979; Watson and Harrison, 1983; Tole, 1985), zircons from anatectic migmatites in amphibolite facies migmatitic rocks are expected to retain some degree of isotopic inheritance (Paterson *et al.*, 1992; Watson, 1996; Oliver *et al.*, 1999). The major factors controlling Zr-solubility in a melt are bulk-rock composition and temperature, according to the equation
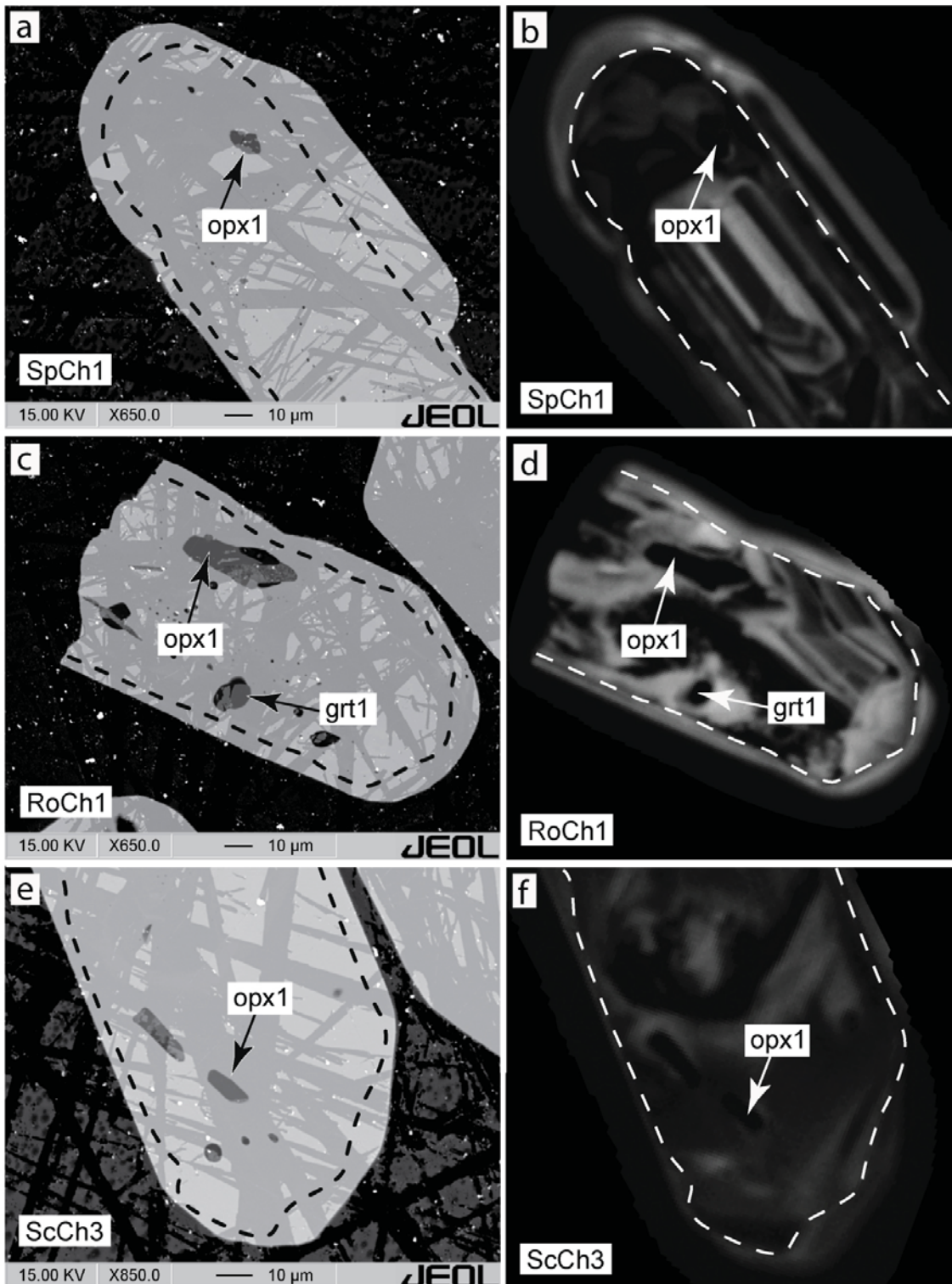
Figure 5.9: *Back scatter (a, c, e) and cathodoluminescence (b, d f) pictures of zircon grains separated from charnockites of the Gruf Complex (samples SpCh1, RoCh1 and ScCh3). Orthopyroxene and garnet grains included within the zircon cores of Permian age indicate that the charnockitic mineral assemblage formed in Permian time. Dotted lines show the boundary between Permian cores and metamorphic Alpine rims.*

Table 5.4.1
Representative chemical compositions of phases included in the oscillatory zoned Permian cores of zircon grains sepa-
rated from charnockites (samples RoCh1, SpCh1 and ScCh3) and comparison with mineral composition displayed by
the same phases in the rock matrix

Mineral	**Opx**					**Grt**		**Ksp**	**Pl**		**Bt**
Sample	RoCh1	RoCh1	SpCh1	ScCh3	RoCh1	RoCh1	RoCh1	ScCh3	RoCh1	RoCh1	ScCh3
Grain	opx_1	opx_2	opx_1	opx_1	opx_M	grt_1	grt_M	ksp_1	pl_1	pl_M	bt_1
Texture	In	In	In	In	M	In	M	In	In	M	In
SiO_2	50.66	50.95	49.71	46.25	49.4	39.47	38.22	64.25	62.98	59.1	34.92
TiO_2	0.039	0.023	0.069	0.098	0.169	0.009	0.06	0.033	0.015	0.018	4.82
Cr_2O_3	0	0	0.04	0.089	0.005	0.047	0.013	0	0.01	0.008	0.029
Al_2O_3	3.62	3.35	4.9	8.24	2.99	21.88	22.19	18.64	21.2	23.93	15.4
FeO	29.27	29.36	24.59	31.66	29.66	31.33	31.79	0	0.007	0.075	20.03
MnO	0.369	0.36	0.269	0.274	0.386	1.274	1.197	0.014	0	0	0.035
MgO	15.76	15.67	19.11	12.52	17.42	5.55	6.03	0	0	0	8.94
CaO	0.184	0.223	0.085	0.194	0.197	1.62	2.19	0.007	6.92	6.81	0.018
Na_2O	0	0	0	0	0	0	0	0.694	5.09	6.75	0.276
K_2O	0.011	0.003	0.003	0.005	0.005	0	0.004	14.98	0.282	0.371	8.91
Tot	99.9	99.9	98.8	99.3	100.2	101.2	101.7	98.6	96.5	97.1	93.4
O	6	6	6	6	6	12	12	8	8	8	11
Si	1.959	1.972	1.895	1.819	1.893	3.078	2.958	3.01	2.981	2.73	2.487
Ti	0.001	0.001	0.002	0.003	0.005	0.001	0.003	0.001	0.001	0.001	0.258
Cr	0	0	0.001	0.003	0	0.003	0.001	0	0	0	0.002
Al	0.165	0.153	0.22	0.382	0.135	2.011	2.024	1.029	1.183	1.303	1.293
Fe^{tot}	0.946	0.95	0.784	1.041	0.951	2.043	2.057	0	0	0.003	1.193
Mn	0.012	0.012	0.009	0.009	0.013	0.084	0.078	0.001	0	0	0.002
Mg	0.908	0.904	1.086	0.734	0.995	0.645	0.696	0	0	0	0.949
Ca	0.008	0.009	0.003	0.008	0.008	0.135	0.182	0	0.351	0.337	0.001
Na	0	0	0	0	0	0	0	0.063	0.467	0.604	0.038
K	0.001	0	0	0	0	0	0	0.895	0.017	0.022	0.809
Sum	4	4	4	4	4	8	8	5	5	5	7.032

Abbreviations: Opx – orthopyroxene; Grt – garnet; Ksp – alkali feldspar; Pl – plagioclase; Bt – biotite; In – inclusion;
M – matrix.

$$\text{Zr in melt (ppm)} = 5 \times 10^5 \times \exp[3.80 + 0.85 \times (M - 1) - (12900 / T)] \qquad (5.1)$$

where T is the absolute temperature and M the cation ratio $M = (Na + K + 2*Ca) / (Al \times Si)$,
relating these to Zr-solubility (Watson and Harrison, 1983). Using this expression, we calculated
the temperature at which complete zircon dissolution would occur at equilibrium and the concen-
trations of Zr required for zircon-saturation of our samples at 700, 750, 800 and 900 °C. By simple
3-dimensional modelling, we then estimated the ratio $V_{zircon}^{rim} / V_{zircon}^{total}$ to calculate the amount of
Zr hosted in zircon rims. XRF bulk-rock data, Zr concentrations, M values and the results of our
calculations are given in Tab. 5.4.2.

These calculations show that, for the granitic melt compositions of investigated samples, zir-
con could completely dissolve between 750 and 840 °C, the leucosome excepted, for which zircon
could completely dissolve at 700 °C (Tab. 5.4.2).

Table 5.4.2
Bulk rock composition and saturation level for the Gruf metagranitoids

Rock type	Charnockite				Migmatitic bt-OG				Enclave-rich bt-OG		Leucogranite		Leucosome	Augengneiss	Matrix
Sample	SpCh1	RoCh1	PeCh13	ScCh3	HvGr15	PeGr5	Or10	TeGr2	PeGr3	Re4	Pia2	BiGr1	PeLs1	HvOG1	Si1
SiO_2	65.748	66.349	70.373	61.489	66.315	68.752	63.659	66.986	67.172	70.593	73.173	73.063	74.347	69.405	71.233
TiO_2	0.612	0.548	0.329	0.719	0.64	0.454	0.724	0.446	0.504	0.325	0.246	0.262	0.062	0.605	0.263
Al_2O_3	16.045	16.207	14.983	18.382	16.196	15.306	17.277	15.817	16.274	15.081	14.182	14.839	14.027	14.795	14.521
FeO^*	5.416	4.814	3.124	5.745	4.567	3.496	5.056	3.936	3.699	2.273	1.932	1.943	0.941	3.581	3.416
MnO	0.107	0.09	0.091	0.068	0.088	0.076	0.069	0.074	0.059	0.046	0.044	0.035	0.032	0.038	0.134
MgO	2.219	1.563	0.92	1.676	1.892	1.001	1.329	1.437	1.497	0.905	0.447	0.442	0.146	1.022	1.251
CaO	3.272	3.483	2.68	4.777	3.253	2.833	3.725	3.187	3.489	2.221	1.463	1.604	1.029	1.637	2.491
Na_2O	3.175	3.443	4.009	4.083	4.247	3.723	4.338	3.805	4.777	3.785	3.238	3.666	3.58	2.681	3.445
K_2O	2.338	2.701	1.76	1.98	2.11	3.616	2.31	2.915	1.626	3.753	4.459	3.564	5.035	5.209	2.162
P_2O_5	0.176	0.187	0.107	0.342	0.169	0.158	0.262	0.184	0.169	0.054	0.202	0.14	0.069	0.123	0.081
Tot	99.11	99.39	98.38	99.26	99.48	99.42	98.75	98.79	99.26	99.04	99.39	99.56	99.27	99.10	99.00
Measured Zr (ppm)	150.28	190.61	95.17	321.73	186.11	184.55	299.78	130.61	158.52	188.1	93.2	132.48	43.71	247.84	138.39
M value	1.119	1.187	1.039	1.394	1.18	1.161	1.266	1.191	1.226	1.036	0.896	0.871	0.869	0.936	0.991
% V_{rim} vs. V_{zircon}	20-25%	20-25%	20-25%	25-30%	15-20%	< 10%	10-15%	35-40%	25-30%	15-20%	15-20%	< 10%	50-55%	10-15%	10-15%
Concentration of zircon (ppm) saturating melt at indicating temperature															
700 °C	53.569	58.325	51.861	68.096	60.35	61.6	64.108	60.77	63.08	56.333	50.696	48.554	52.456	51.987	49.445
800 °C	184.299	200.662	178.425	234.279	207.63	211.931	220.561	209.076	217.023	193.809	174.416	167.049	180.471	178.857	170.113
900 °C	513.621	559.221	497.251	652.909	578.642	590.629	614.677	582.67	604.818	540.122	486.077	465.545	502.953	498.453	474.086
F(%) - Degree of melting (as indicated temperature) necessary to dissolve zircon rims in a granitic melt															
700 °C	56-70	65-82	37-46	118-142	46-62	15-30	47-70	75-86	63-75	50-67	28-37	14-27	42-46	48-72	28-42
750 °C	29-37	34-43	19-24	62-74	24-32	8-16	24-37	39-45	40-48	30-40	12-15	6-12	23-25	27-40	14-21
800 °C	16-20	19-24	11-13	34-41	13-18	4-9	14-20	22-25	18-22	15-19	8-11	4-8	12-13	14-21	8-12
900 °C	6-7	7-9	4-5	12-15	5-6	2-3	5-7	8-9	7-8	5-7	3-4	1-3	4-5	5-7	3-4
T of dissolution (°C)	790	799	756	835	795	791	837	773	778	801	755	789	696	837	796

* Total iron as FeO; M = (Na + K + 2*Ca) / (Al * Si) after Watson and Harrison (1983).
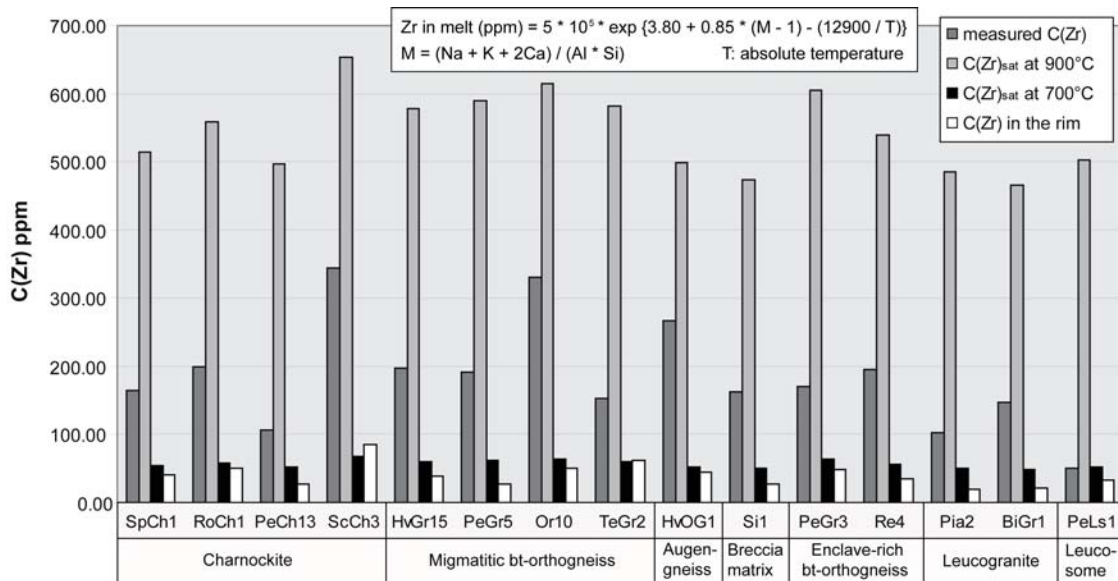
Figure 5.10: *Summary results of zircon dissolution calculation for the Gruf metagranitoids using the equation of Watson and Harrison (1983). The diagram displays the relationships between measured Zr concentration, predicted Zr content saturating the melt at 700 °C and 900 °C and estimated Zr content hosted in the metamorphic zircon outer rims. At ultra-high temperatures of 900 °C as estimated for the formation of the Gruf charnockites and granulites, all the investigated melt compositions would be largely oversaturated in Zr. If such high grade conditions were achieved during the Alpine metamorphism, the inheritance of Permian (or older) zircon cores is not expected. Instead, estimated Zr content in zircon rim fit well the calculated Zr content saturating the melt at 700 °C, suggesting that Alpine rim recrystallisation occurred at upper amphibolote facies conditions of about 700°C, in accordance with thermobarometric P-T estimates for the Alpine Lepontine metamorphism in the Gruf Complex.*

Zircon dissolution during prograde melting is not an equilibrium process. However, the solubility data and relative volumes of cores and rims corroborate several conclusions. In particular, charnokites formed at > 900 °C and thus all of their Zr could have been dissolved in the parental melt. Accordingly, zircons could all have crystallized during the charnokite formation. In support to this conclusion, xenocrystic cores are rare in the studied samples. They correspond to the very few ages older than 280-260 Ma, and we take this latter age, obtained from the oscillatory cores that make up 70-80 vol% of the zircon grains, as that of the charnokite formation.

5.4.3   Zircon dissolution during Alpine remelting: age of migmatites

The homogeneity of volumetrically large rims (50-55 vol%) in the leucosome sample and one of the migmatitic biotite-orthogneisses (35-40 vol% rim, sample TeGr2) indicates that in-situ melting did not lead to oscillatory rims. Therefore, it cannot be shown whether rim formation is only fluid-assisted or associated with partial melting. The degree of melting necessary to form such rims through crystallisation from a granitic melt of close to eutectic composition would be 10-20 vol%, which is consistent with the degree of melting expected during metamorphism at 700-750 °C. Rims are oscillatory zoned in the enclave-rich biotite-orthogneiss and the magmatic breccia. The

amount of Zr contained in these rims requires at least 20-30 vol% of melting at 700 °C and the field occurence of these two lithologies suggests major movements of a granitic magma or crystal mushes (see discussion below) at the age indicated by these rims (31 and 32 Ma, respectively).

In conclusion, the Gruf Complex is composed of gneisses with Alpine migmatites that contain Permian sheets of charnokites, which in turn contain most of the granulites.

5.4.4 Significance of the Gruf ages in the Alpine context

Three main groups of ages have been recognised within the zircons separated from the metagranitoids of the Gruf Complex: Cambro - Ordovician $\sim$ 510-530 Ma and $\sim$ 455-470 Ma; Permian $\sim$ 290-260 Ma, and Oligocene $\sim$ 34-29 Ma (Tab. 5.3.3 and Fig. 5.11).
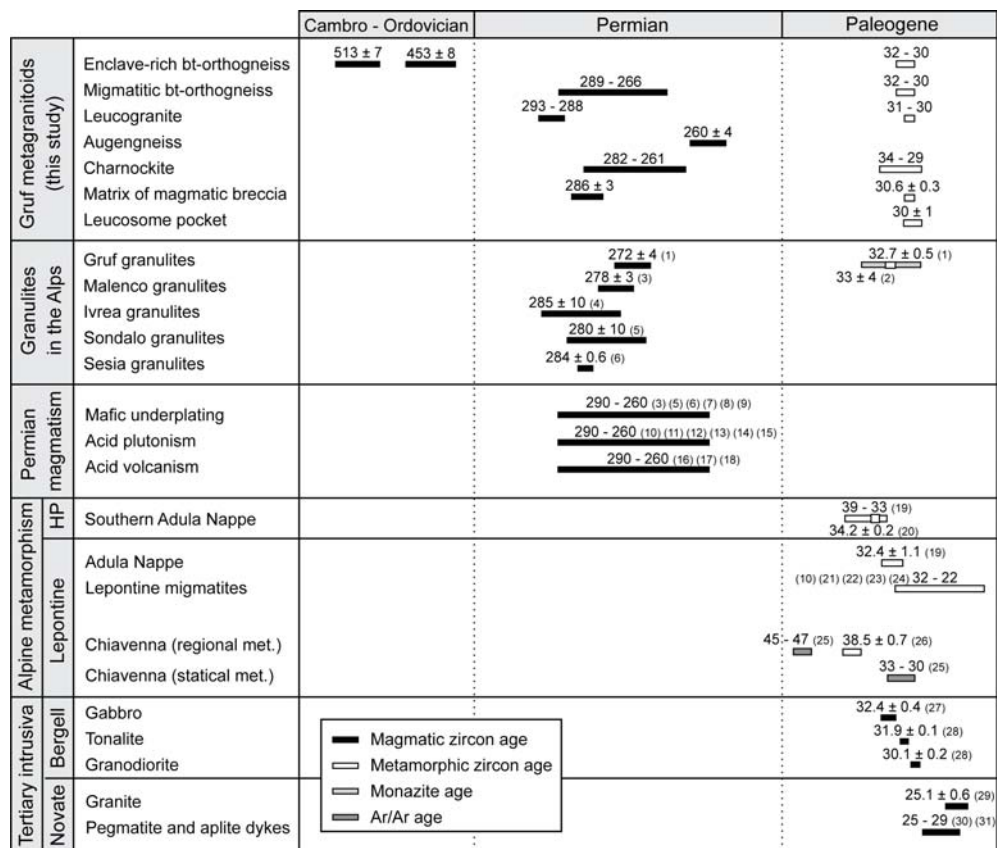
Figure 5.11: *Summary of magmatic and metamorphic ages for the Gruf metagranitoids and comparison with geochronological data available for Permian granulites, Permian magmatism, Alpine metamorphism in the south- and south-eastern part of the Lepontine Dome and Tertiary intrusiva. References: (1) Liati and Gebauer (2003); (2) Schmitz et al. (2009); (3) Hansmann et al. (2001); (4) Henk et al. (1997); (5) Tribuzio et al. (1999); (6) Monjoie and Bussy (2007); (7) Pin (1986); (8) Quick et al. (2003); (9) Peressini et al. (2007); (10) Hänny et al. (1975); (11) Hunziker and Zingg (1980); (12) Pinarelli et al. (1988); (13) Boriani et al. (1990); (14) Bussy et al. (1998); (15) Marquer et al. (1998); (16) Barth et al. (1994); (17) De Capitani et al. (1994); (18) Schaltegger and Brack (2007); (19) Gebauer (1994); (20) Hermann et al. (2006); (21) Rubatto et al. (2009); (22) Berger et al. (2009); (23) Köppel et al. (1981); (24) Vance and O'Nions (1992); (25) Talerico (2000); (26) Liati et al. (2003); (27) Gregory et al. (2009); (28) Von Blanckenburg (1992); (29) Liati et al. (2000); (30) Romer et al. (1996); (31) Schärer et al. (1996).*

Cambro - Ordovician xenocrysts

Concordant Cambrian ($\sim$ 513 Ma) and Ordovician ($\sim$ 453 Ma) ages have been measured in cores of zircons from the enclave-rich biotite-orthogneisses (sample PeGr3). Similar ages have been reported from all over Western Europe, from Iberia (Lancelot and Allegret, 1982; Sánchez-García *et al.*, 2003) to the Bohemian Massif (Dostal *et al.*, 2001; Friedl *et al.*, 2004) through the Pyrenees (Delaperrière *et al.*, 1994; Castiñeira *et al.*, 2008), French Massif Central (Pin and Lancelot, 1978; Melleton *et al.*, 2010), Sardinia (Helbing and Tiepolo, 2005; Oggiano *et al.*, 2010), and the Alps (Sergeev and Steiger, 1993, 1995; Bertrand and Leterrier, 1997; Poller *et al.*, 1997). These ages reflect magmatism at the end of the Cadomian orogeny and herald continental break-up of Gondwana (Pin and Marini, 1993; Von Raumer *et al.*, 2002). The two ages from the same orthogneiss suggest a Cambrian precursor subsequently involved in granitoid reworking during Ordovician plutonism, a well documented process (Alexandre, 2007). The ca. 290 Ma zircon cores of sample Re4, the same orthogneiss as PeGr3, indicate additional reworking in Permian times.

Permian magmatic cores

Oscillatory and/or sector zoned cores of zircons separated from charnockites, biotite-orthogneisses, leucogranites, and the augengneiss yielded concordant Permian ages between 290 and 260 Ma. We interpret this age as the time of emplacement of charnockitic and granitic magmas in the crust, consistent with worldwide magmatism at that time (Lorenz and Nicholls, 1984; Veevers and Tewari, 1995; Wilson *et al.*, 2004). In Europe, this widespread magmatism is associated with lithospheric thinning and trantensional collapse of the Variscan collisional orogen (Burg *et al.*, 1994; McCann and Kiersnowski, 2008; Timmerman, 2008; Schuster and Stüwe, 2008).

In the Alps, Late Carboniferous-Permian intrusions are recognized in several places from the Ivrea Zone (Peressini *et al.*, 2007) to the Eastern Alps (Eichhorn *et al.*, 2000). This widespread mafic underplating and lower crustal magmatism is contemporaneous with, and may partly derive from the granulitic lower crust of Europe (Downes *et al.*, 1990; Costa and Rey, 1995), whose seismic reflectivity is compatible with post-orogenic lithospheric extension (Rey, 1993; Holliger and Levander, 1994). The early Permian charnockites, orthogneisses and leucogranites dated in this work fit well into this picture, suggesting that the Gruf Complex includes a part of the European lower crust (Fig. 5.12a).

The analyzed zircon cores display a wide scattering of partly discordant Permo-Triassic ages as late as ca. 200 Ma (Figs. 5.4, 5.5, 5.6, 5.7, 5.8). This feature is common in Variscan granitoids of the Central and Western Alps (Schaltegger, 1990; Vavra *et al.*, 1996; Gebauer *et al.*, 1997; Vavra and Schaltegger, 1999). It is generally attributed to post-crystallization thermal events during renewed extension and magmatism in the late-Permian early-Triassic (Schaltegger and Gebauer, 1999), which signals opening of the Neo-Tethys Ocean (Ziegler, 1993).
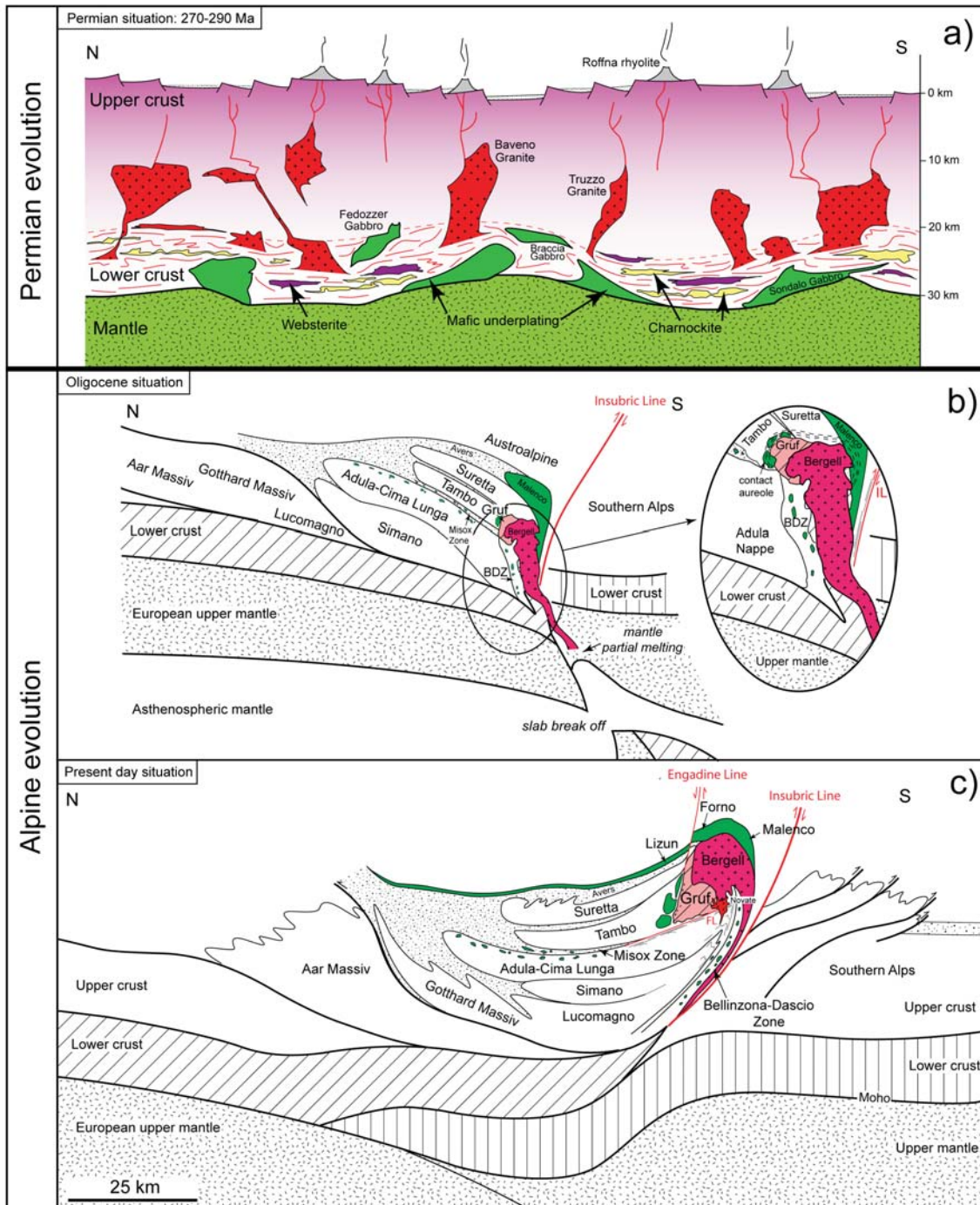
Figure 5.12: *(a) Permian situation: mafic underplating and lower crustal magmatism during post-orogenic litho-spheric extension; (b-c) Alpine evolution: intrusion of the Bergell Pluton after slab breakoff and contemporaneous exhumation of the Gruf Complex as pluton-related migmatitic dome. The uprising magmas helped the exhumation of lower crustal pieces.*

Early Oligocene metamorphic rims

Most analyzed zircons have Early Oligocene rims, dated between 34 and 29 Ma. These rims are coeval with the Alpine regional metamorphism (32 to 22 Ma in the southern and southeastern Lepontine Dome; Hänny et al., 1975; Köppel et al., 1981; Vance and O'Nions, 1992; Gebauer, 1996; Berger et al., 2009; Rubatto et al., 2009) and the emplacement of the adjacent Bergell Pluton (33 to 30 Ma; Von Blanckenburg, 1992; Oberli et al., 2004; Gregory et al., 2009). Field observations supportively show that migmatization in the Gruf was contemporaneous with pluton emplacement (section 2.3.3; Davidson et al., 1996; Berger et al., 1996).

The strongly variable degree of rim development from sample to sample and between grains of the same sample suggests a heterogeneous availability of metamorphic fluids and anatectic melt. Mostly homogeneous rims may have formed at sub-solidus conditions or during melting. In contrast, the oscillatory zoned rims demonstrate significant anatexis. Partial melting of granitic rocks produced leucocratic melts that locally intruded older rocks. Partial melting during Lepontine metamorphism is further inferred from zircons extracted from the PeLs1 leucosome sample. These zircons partly (completely for one grain) re-equilibrated in presence of melt at ca. 30 Ma.

Oscillatory zoned rims are prominent in the enclave-rich biotite-orthogneiss and the magmatic breccia. The amount of Zr contained in these rims requires but does not delimit melting to about 20-30 vol% (at 700 °C). The viscosity of rocks molten to the extent of the rheological critical melt fraction is almost that of the granitic melt (Arzi, 1978). The magmatic breccia containing 5-50 vol% ultramafic enclaves is intrusive into the biotite-orthogneisses and the oscillatory zircon rims suggest that it formed at 30.6 ± 0.3 Ma. Similarly, the oscillatory zircon rims of the enclave-rich orthogneiss at the contact Gruf-Chiavenna, suggest a fluidal state of this granite sheet at 31-32 Ma. This corraborates the interpretation that this sheet has accommodated most of the strain related to the ascent of the Gruf Complex along its northern boundary while the Bergell Intrusion (30-32 Ma) was active at the southern and eastern limits of the Gruf (Fig. 5.12 b,c and section 2.4.1).

Chapter 6

Conclusions: tectono-metamorphic evolution

Most of the previous interpretations considered the Gruf Complex as a migmatitic unit that suffered granulite-facies metamorphism during Alpine metamorphism (Droop and Bucher-Nurminen, 1984; Liati and Gebauer, 2003; Schmitz *et al.*, 2009). The Gruf Complex was regarded as either the eastern continuation of the Adula Nappe (Schmid *et al.*, 1996b; Davidson *et al.*, 1996; Frey and Ferreiro Mählmann, 1999; Liati and Gebauer, 2003; Berger *et al.*, 2005) or the equivalent of the Bellinzona-Dascio Zone (Wenk, 1973; Wenk and Cornelius, 1977; Milnes and Pfiffner, 1980). Nevertheless, previous authors separated the evolution of the Gruf Complex from the Bergell Intrusion. This study introduces new structural, petrological and geochronological arguments that necessarily lead to a re-interpretation of the history of the eastern end of the Lepontine Dome.

6.1   Charnockites and granulites vs. migmatization: evidence for polymetamorphism in the Gruf Complex

Internally boudinaged, sheet-likes charnockite bodies show a deformation pattern and mineral associations different from those of the Gruf metasediments and orthogneisses (Figs. 2.23 and 4.14). The occurrence of orthopyroxene-bearing assemblages and orthopyroxene-sapphirine-bearing granulitic schlieren in the core of charnockite boudins, implies that these high-grade rocks were produced by intense biotite-dehydration melting of pelitic rocks at ultra-high temperatures (UHT) of 920-940 °C and pressures of 8-9.5 kbar (section 4.1.7). Generally, charnockites and granulites display post-peak reaction textures, such as polymineralic coronae and composite symplectites (section 4.1.6, see also Droop and Bucher-Nurminen, 1984). These testify for an incomplete re-equilibration of the UHT peak assemblages at metamorphic conditions of 720-740 °C at 6.5-7.5 kbar (section 4.1.7). Whilst peak metamorphic conditions of charnockites and granulites largely exceed metamorphic conditions determined for the Lepontine metamorphism in the Central Alps (Figs. 4.14 and 4.15), estimated pressures and temperatures for the cordierite-bearing coronae and symplectites fit well with the migmatization conditions of the Gruf Complex and the generally accepted mid-Tertiary regional metamorphism in the southern and south-eastern parts of the Lepontine Dome of 700-750 °C at 6-7.5 kbar (Todd and Engi, 1997; Stucki, 2001; Nagel *et al.*, 2002; Burri *et al.*, 2005). Therefore, we suggest that a polymetamorphic history is preserved in the charnockite bodies. Granulitic peak mineral assemblages would represent partially preserved relicts of a pre- Lepontine UHT event, while post-peak reaction textures would be produced by the incomplete overprint of the UHT peak assemblage during the upper amphibolite-facies Lepontine metamorphism.

6.2   Polymetamorphism - geodynamical interpretation

Like other granulites rocks in the Alps (e.g. Ivrea zone, Barboza and Bergantz, 2000; Malenco Unit, Müntener et al., 2000; Sesia zone, Lardeaux and Spalla, 1991; Rebay and Spalla, 2001; Sondalo Complex, Braga et al., 2001; Braga et al., 2003), UHT metamorphic conditions experienced by the Gruf charnockites and granulites may have been achieved during the post-Variscan Permian

extension. Intense partial melting of pelitic rocks at deep crustal levels during a rifting-related thermal climax may have produced orthopyroxene-bearing charnockitic melts and strongly refractory, sapphirine-bearing granulitic residuals. Therefore, we propose that the charnockites and granulites, together with the tholeitic websterites to gabbronorites, are relics of a Permian event that characterised much of the European crust (Fig. 5.12) (Lorenz and Nicholls, 1976, 1984; Vielzeuf and Pin, 1991; Rey, 1993; Schuster and Stüwe, 2008). In particular, the association of charnockites + granulites with websterites + gabbronorites, the latter of cumulative origin, has been described in many locations documenting a post-Variscan high temperature event. In the Gruf Complex, these lower crustal relics have been subsequently exhumed and partially overprinted during the Alpine orogenesis. The incomplete re-equilibration of the granulitic peak-assemblage during the Lepontine event may be partially imputed to the severe loss of melt and near to complete dehydration during the UHT event (session 4.3.4).

The increased migmatization and the occurrence of corundum-cordierite-bearing micaschists in the contact zone between the Gruf Complex and the Bergell Intrusion (Figs. 2.11d and 2.29), together with back-veining of leucosomes from metasediments into the Bergell Pluton (1 on Fig. 2.29), collaborate the picture of an already high grade metamorphic crust before Alpine metamorphism. We interpret the increase of leucosome and the back-veining as reflecting contact metamorphism in the vicinity of the Bergell Intrusion at about 750-775 °C (Fig. 4.14), mainly facilitated by magmatic fluids released during final solidification of the Bergell Pluton. This < 50 m thick contact aureole would indicate that during Bergell emplacement, between 32 and 30 Ma (Von Blanckenburg, 1992), the Gruf Complex already was at upper amphibolite facies metamorphic conditions, a further argument against an Oligocene age of the granulitic facies metamorphism previously inferred (Droop and Bucher-Nurminen, 1984; Liati and Gebauer, 2003; Schmitz *et al.*, 2009).

Our interpretation fits also well with geochronological data on zircons from Gruf granulites, charnockites and metagranitoids. These zircons display oscillatory cores, typical for crystallisation from granitic melts, formed in Permian times and have thin homogeneous Oligocene rims of 30-32 Ma (Liati and Gebauer, 2003; chapter 5).

6.3   A common exhumation and emplacement history for the Gruf Complex and the Bergell Pluton?

The emplacement of the Bergell Intrusion contemporaneous with migmatization and deformation of the Gruf Complex suggests that these two units shared, at least since the Early Oligocene, the same history. The calc-alkaline magmas of the Bergell Pluton derived from a primitive mantle melt (Von Blanckenburg *et al.*, 1992). The magmas of the Bergell and the numerous smaller plutons along the Insubric Line, were channelled from the base of the continental crust into the Periadriatic Fault system (Rosenberg, 2004). We propose that during its ascent, the dynamics of the uprising Bergell Pluton helped the exhumation of the Gruf Complex as a pluton-related migmatitic dome (Fig. 5.12b), which, possibly together with the migmatite-rich Bellinzona-Dascio Zone, may have

acted as partially molten "lubricant" on the northern side of the intrusion. We tentatively infer that brecciation at the basis of the chlorite-spinel-enstatite- olivine fels and websteritic lenses (e.g. Fig. 2.8a and 4 and 5 in Fig. 2.29), as well as leucosome veins from migmatitic metasediments into the base of the Bergell Pluton (1 in Fig. 2.29) are way-up criteria pointing to the vertical dynamics of the Gruf - Bergell system.

As a corollary, the Gruf Complex has to be treated independently from the other Penninic units. From the tectonic and geodynamic points of view, the Bergell Pluton and Gruf Complex are likely to have a common uplift and emplacement history. In fact, migmatitic domes related to calc-alkaline plutonism are common features of collisional orogenic belts (Soula, 1982; Faure *et al.*, 1999; Lin *et al.*, 2007; Charles *et al.*, 2009; Corsini and Rolland, 2009). The ascending Bergell Pluton may have entrained lower crustal rocks, such as charnockites, granulites and websterite to gabbronorite (Fig. 5.12b), a well documented process (Best and Christiansen, 2001) also produced in numerical models of magma emplacement (Gerya and Burg, 2007).

As already proposed previously (Bucher-Nurminen and Droop, 1983; Talerico, 2000), the joint exhumation of the Bergell with the hot Gruf Complex may also explain the increase of metamorphic temperatures from ca. 450 °C to ca. 700 °C within 3 km across the Chiavenna Unit and the Tambo Nappe towards the contact with the Gruf Complex (Schmutz, 1976; Talerico, 2000). Ar-Ar ages on statically recrystallised amphibole grains of the Chiavenna amphibolites show that this anomalously high thermal gradient of $\sim$ 80 °C/km formed between 33 and 30 Ma (Talerico, 2000), coeval with the emplacement of the Bergell Pluton (Von Blanckenburg, 1992) and with the metamorphic peak in the Gruf Complex (Liati and Gebauer, 2003). In contrast to previous studies, we infer that the differential movement of the Gruf Complex did not occur along a well defined Gruf Line but was accommodated in a at least several 100 m wider zone within the enclave-rich biotite-orthogneiss. We propose that the juxtaposition of the hot Gruf Complex against the Chiavenna ophiolites triggered the dehydration of the former Chiavenna serpentinites in the southern part of the unit, leading to a release of fluids that locally increased the degree of partial melting in the adjacent biotite-orthogneiss leading to weakening and strain localization. The partly molten enclave-rich biotite-orthogneiss acted in a crystal-mush-like manner accommodated the movement related to the exhumation of the Gruf Complex. We also tentatively suggest that the enclaves embedded within the orthogneiss, which are mostly of basic and, rarely, pelitic, ultramafic and calcareous compositions, might be relics of the Chiavenna ophiolites sheared into the orthogneiss during its syn-kinematic partial melting.

6.4 Metaperidotites and associated metabasic: remnants of a Meso-zoic ocean?

Metaperidotites and associated amphibolites that occur as lenses within the Gruf migmatites bear many similarities with Mesozoic ophiolites exposed in the southern part of the Central Alps. The occurrence of metamorphosed rodingite and ferro-gabbro dykes within ultramafic lenses mostly near the Bergell Intrusion and the geochemical affinity to MORB basalts displayed by the Gruf

amphibolites (Diethelm, 1989) indicate that these rocks underwent an oceanic stage during their early history.

In the adjacent Adula-Cima Lunga Nappe Complex (Evans *et al.*, 1979; Pfiffner and Trommsdorf, 1998), Chiavenna Unit (Schmutz, 1976; Talerico, 2000) and Bellinzona-Dascio Zone (Crespi, 1965; Hansmann, 1981; Stucki *et al.*, 2003), ophiolitic rock associations undisputedly belong to the Mesozoic Tethys. In the Bellinzona-Dascio Zone, zircons from two plagiogranite dykes yielded SHRIMP ages of ca. 145 Ma (Stucki *et al.*, 2003), interpreted as the late stage of magmatic activity in the Piemont-Ligurian ocean. Zircons separated from the Chiavenna amphibolites yielded younger formation ages of ca. 93 Ma (Liati *et al.*, 2003), leading the authors to assign the Chiavenna ophiolites to the Valais realm.

Similarly to the Gruf Complex, ophiolitic relics in the other units comprise metaperidotites with metamorphic rodingite dykes, amphibolites and calcsilicates, preserved as lenses embedded within migmatitic orthogneisses and metasediments (Schmidt, 1989; Pfiffner and Trommsdorf, 1998; Stucki *et al.*, 2003). Due to the petrological and geochemical similarity and to the same mode of occurrence, we therefore suggest that the Gruf ultramafic-mafic rock associations are remnants of the Mesozoic ocean, as already proposed by Diethelm (1989). Nevertheless, their paleogeographic assignment to the Piemont-Ligurian Ocean, as the ophiolites of the Bellinzona-Dascio Zone, or to the Valais Through, as the Chiavenna ophiolites remains open.

From a metamorphic point of view, the Gruf metaperidotites display the same peak mineral assemblage chlorite-olivine-enstatite-spinel as the ultramafic boudins within the Bellinzona-Dascio Zone (Stucki, 2001), suggesting that both were metamorphosed at temperatures slightly in excess of 700 °C (Fig. 4.14). Both these units are contrasting the ultramafic-mafic association of the Adula-Cima Lunga Nappe Complex which underwent eclogite facies metamorphism reaching 3-6 GPa (Heinrich, 1983, 1986; Pfiffner and Trommsdorf, 1998; Nimis and Trommsdorff, 2001; Dale and Holland, 2003; Brouwer *et al.*, 2005). No evidence of such an early stage of high pressure metamorphism occured either in the metaperidotites nor in the amphibolites of the Gruf. This suggests that these rocks have never been deeply subducted but rather that they remained near the surface attached to the Adriatic continent in the accretionary wedge.

6.5   The Gruf Complex in the framework of regional geology

The distinct style and orientation of deformation structures and the petrological differences support the interpretation of an evolution of the Gruf Complex independent from other Central Alpine units. The ENE-WSW trending, heterogeneously developed main foliation and strain concentration in ductile shear zones are different from deformation features in both the Adula Nappe and Bellinzona-Dascio Zone (Wenk, 1973; Meyre *et al.*, 1998) characterised by distinguishable sets (phases) of structures (Hafner, 1993; Berger *et al.*, 1996; Davidson *et al.*, 1996; Schmid *et al.*, 1996b; Meyre *et al.*, 1998; Stucki, 2001). Thus, the correlation of the Gruf Complex with the Adula Nappe on the basis of structural arguments (Berger *et al.*, 1996; Davidson *et al.*, 1996; Schmid *et al.*, 1996a) is a disputable attribution. Whereas on both sides of the southernmost part

of Valle della Mera the main foliation in the Adula Nappe and Gruf Complex seem to be coherent and the axial plane of the so-called Cressim antiform could be prolonged from Monte Peschiera in the Adula Nappe ($\sim$ 1 km W of the Valle della Mera) into Val Revelaso ($\sim$ 2.5 km south of Bresciadega) within the Gruf Complex (Hänny *et al.*, 1975; Hafner, 1993; Davidson *et al.*, 1996), the deformation features in the Adula Nappe, on the west side of Valle della Mera north of No-vate are fundamentally different from those in the Gruf Complex exposed on the opposite side of the valley (compare Hänny (1972); Meyre *et al.* (1998). The disorganised structures, the lack of regularly developed and systematic parasitic folds whose S/Z asymmetry would change from one limb to the other, as observed in the Adula Nappe, along with the lack of a clearly defined hinge zone (with M folds) question the reality of a large antiform within the Gruf Complex as previously proposed (Moticska, 1970; Wenk, 1973; Wenk and Cornelius, 1977; Davidson *et al.*, 1996; Schmid *et al.*, 1996a). This has major implications on the tectono-paleogeographical interpretation of the area. In fact, large-scale folds were invoked to connect the ophiolites of the Chiavenna Unit with meta-ultramafic, -mafic and -sedimentary rocks occurring at the contact between the Gruf Complex and the Bergell Pluton and, finally, with the ophiolites of the Bellinzona-Dascio Zone (Diethelm, 1989; Davidson *et al.*, 1996; Schmid *et al.*, 1996a). However, the same lithological association is also exposed within the Gruf Complex and not exclusively at its eastern margin towards the Bergell Intrusion (see geological map of the Gruf Complex). This suggests that these rocks are questionable markers to infer large-scale.
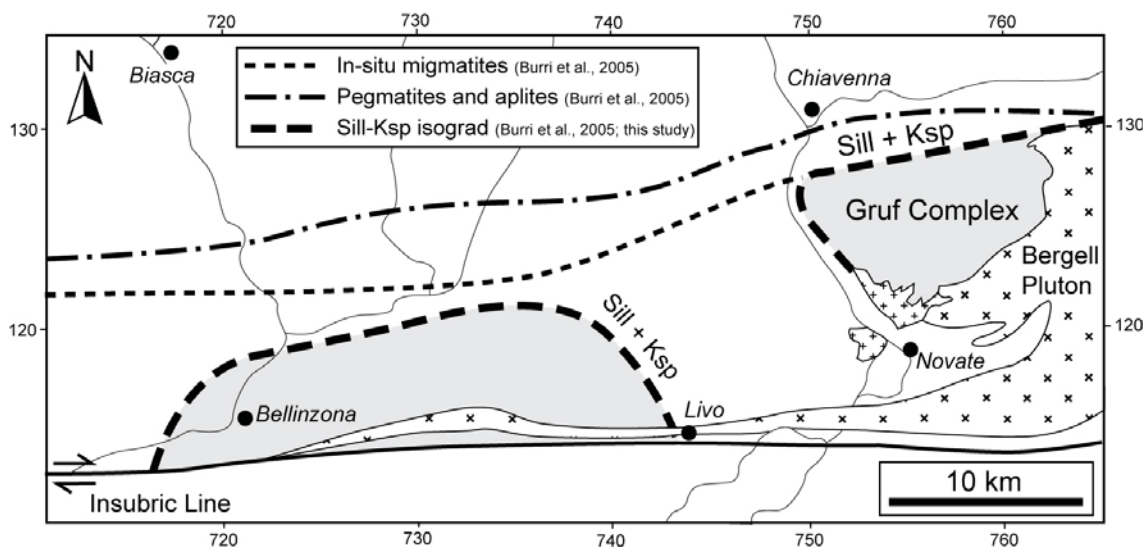
Figure 6.1: *Delimitation of migmatites, pegmatitic and aplitic dykes and location of the Sill-Ksp isograd, corresponding to the limit of fluid-absent muscovite melting in the Central Alps (modified after Burri et al., 2005). Swiss co-ordinates are given with units in kilometres.*

The occurrence of UHT relics (charnockites and granulites), the contemporaneous lack of high pressure rocks, widespread in the Adula Nappe, and the simultaneous occurrence of sillimanite + alkali feldspar within partly migmatitic metasediments render the Gruf Complex petrographically distinct from the adjacent Penninic units, as already recognized by Hänny *et al.* (1975). The oc-

currence of sillimanite + alkali feldspar observed within the partly migmatitic micaschists leads to a modification of the location of the Sill-Ksp isograd (Burri *et al.*, 2005) within the Lepontine Dome. This area between Bellinzona and Livo was considered to be the hottest sector of the Lepontine dome, where partial melting was in part triggered by muscovite-dehydration melting rather than only by fluid-assisted melting as in the rest of the Lepontine migmatites. The identification of this mineral association also in the Gruf Complex leads to a second Sill-Ksp isograd around the Gruf Complex (Fig. 6.1). The strikt coincidence of this isograd with the Gruf Complex supports the idea of the Gruf as migmatitic dome independent from other Penninic units, its uplift and emplacement related to the Bergell Pluton rather than to the Alpine nappe stacking.

An independent Bergell-Gruf association may be part of the remnants of a tectonic accretion channel (TAC) along the boundary of the European plate during subduction (Engi *et al.*, 2001). Alternatively, the Bergell and Gruf may be treated as a dome-shaped sub-unit of a larger hot channel formed in Oligocene time during the continental collision that followed subduction of the European slab (Gerya *et al.*, 2008). The dynamics of such hot channels would be characterised by the convolute flow pattern responsible for the differential exhumation of crustal blocks in a dome-shaped manner as proposed for the Bergell-Gruf association.

6.6 The Gruf Complex in the framework of Alpine tectonics

Since the charnockites represent melts formed at granulite facies conditions their early Permian intrusion age dates the granulite event. Most of the granulites found in outcrops are indeed within the charnockites. All studied rocks also record Early Oligocene migmatisation. The UHT granulitic relicts found in the Gruf Complex are therefore polymetamorphic, polyorogenic rocks. Garnet diffusion modelling within the granulites demonstrates that they have been cooled down to < 550-600 °C within < 20 Ma after their crystallization (section 4.3.3). Garnet rim compositions, symplectites and coronae agree well with a migmatitic event of 10 Ma duration, as has been proposed for the Alpine amphibolite facies migmatisation (Rubatto *et al.*, 2009). The Gruf granulites were therefore part of the lower crust formed and thermally re-equilibrated after the Variscan orogeny as identified in Europe, i.e. the northern realm of Pangea (Fig. 6.2a). It remains to bring the charnockites and granulites, formed at = 900°C, into contact with the volumetrically dominant migmatic gneisses and metasediments of the Gruf which have not suffered through more than 700-750 °C. Two possibilities are envisaged.

One considers the charnockites as intrusions originating in the deepest lower crust and emplaced in paragneiss almost at the same time as post-Variscan granites intruded shallower crustal levels. Schlieren and boudins of granulites are enclaves of the lower crust in the charnockites. Not all granulites found in outcrops are contained in charnockites, even if all charnockites are not necessarily preserved. In some places, migmatisation may have completely destroyed orthopyroxene. In that case, the charnockites, granites, and metasediments of the Gruf Complex would be involved in Alpine migmatisation as a mostly coherent block.

Alternatively, our preferred interpretation, the Permian charnockites and granulites remained

in the lowermost crust until they were introduced in the migmatites during the Alpine orogeny. We follow previous tectonic models involving asymmetric extension of the European margin (Manatschal *et al.*, 2006) before opening (Figs. 6.2b and c) and closure (Figs. 6.2d and e) of the Tethys Ocean by south-dipping subduction below the northern margin of Adria (Schmid *et al.*, 1996a). Subduction produced the pull down forces necessary to occasionally open marginal basins such as the Valais Trough (Fig. 6.2d) and drag down minor continental fragments isolated within Tethys after separation from the European margin (the Briançonnais terranes, now forming the Tambo and Suretta, amphibolite facies nappes, Figs. 6.2c-e). Since such fragments were thin, the resulting collisional system could not involve major crustal thickening at that stage and during early subduction of the thinned continental front of Europe (Fig. 6.2e). We also follow previous models (Schmid *et al.*, 1996a; Froitzheim *et al.*, 2003) in subducting the European crust deep enough to produce eclogites that characterise the Adula nappe (Fig. 6.2f). From that stage we use results from analogue (Chemenda *et al.*, 2001) and numerical modelling (Gerya *et al.*, 2008). Once the continental crust is deeply buried, buoyancy forces overwhelm crustal strength and allow vertical extrusion of crustal segments; this explains emplacement of the eclogitic Adula below previous nappes with normal senses of shear in between (Fig. 6.3g). Upward extrusion has important consequences: it thickens the orogenic system by return and addition of crustal slabs, and it weakens the subducted lithosphere by removing crustal material delaminated from its lower crust and upper mantle. These two phenomena favour slab breakoff and the subsequent roll back of the orogenic system freed from slab pull and therefore rapidly uplifting for obvious isostatic reasons (Fig. 6.3g). This major event is consistent with ascent of the Bergell Pluton at 32 Ma (Von Blanckenburg, 1992) and the contemporaneous climax of erosion processes as documented by Oligocene deposits in the Molasse basin (Hay *et al.*, 1992). Roll-back opens space in the Alpine crust for magma emplacement, hence the Bergell Pluton. In this scenario, the Bergell Intrusion plays an important role in exhuming the granulites, charnockites and the host migmatitic gneisses. We contend that the mantle-derived Bergell magmas have dragged some of the lower crustal rocks that they pierced, brecciated and partly assimilated (Fig. 6.3h). Some of the volumetrically small granulitic chunks were mixed with migmatitic ortho- and paragneisses generated in higher crustal levels, perhaps as ductile inner part of the Bergell contact aureole. The buoyant, partially molten Gruf Complex was ascended towards upper levels with the Bergell Pluton (Figs. 6.3h and i). Exhumation of lower crustal blocks and migmatites next to buoyant plutons is a documented, multiple process reproduced in numerical models of magma intrusion (Best and Christiansen, 2001; Gerya and Burg, 2007). Models tuned for the Bergell case should clarify this thermo-mechanical history.
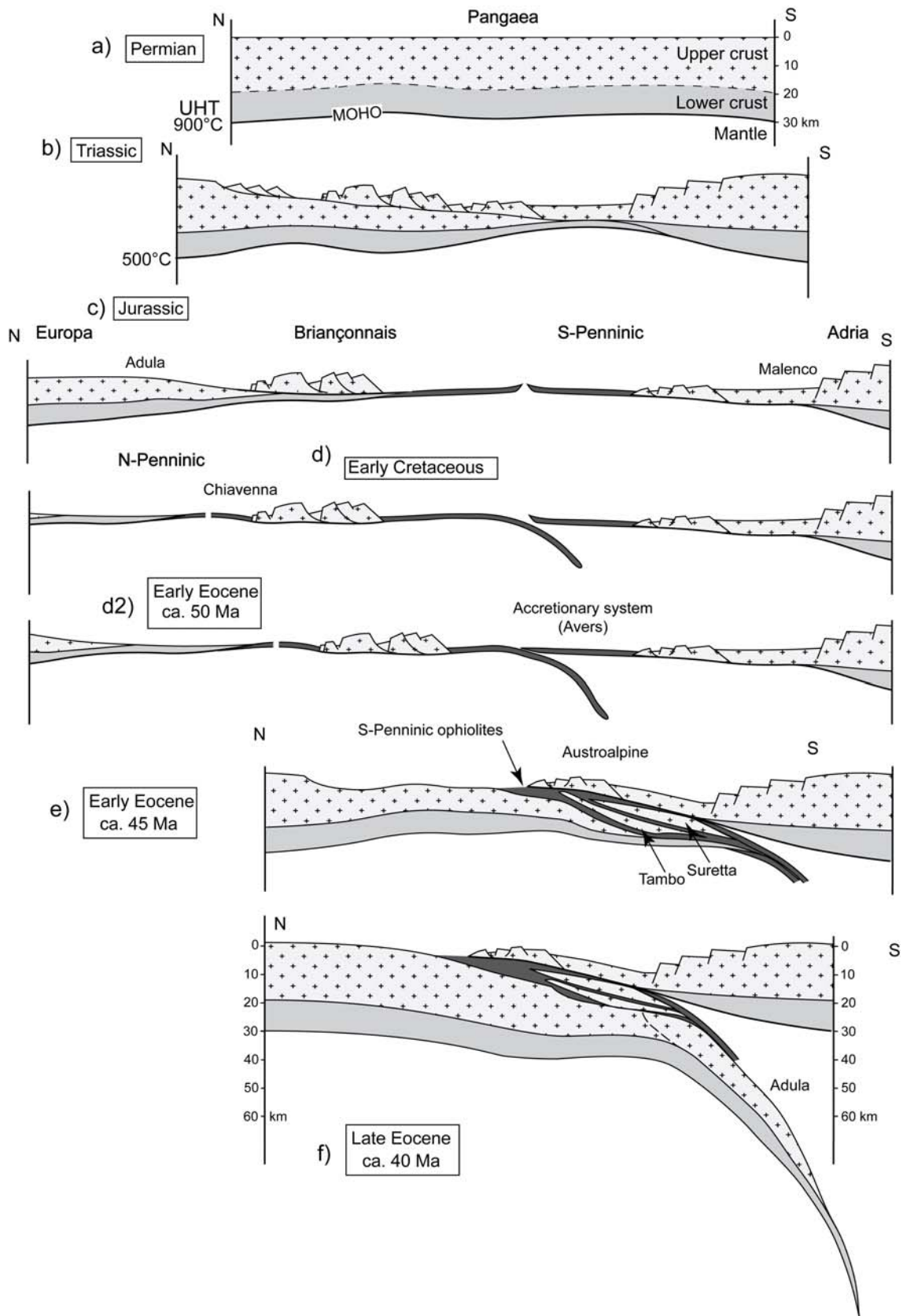
Figure 6.2: *Sketches of the tectonic evolution of the eastern Central Alps part I. Explanation in the text.*
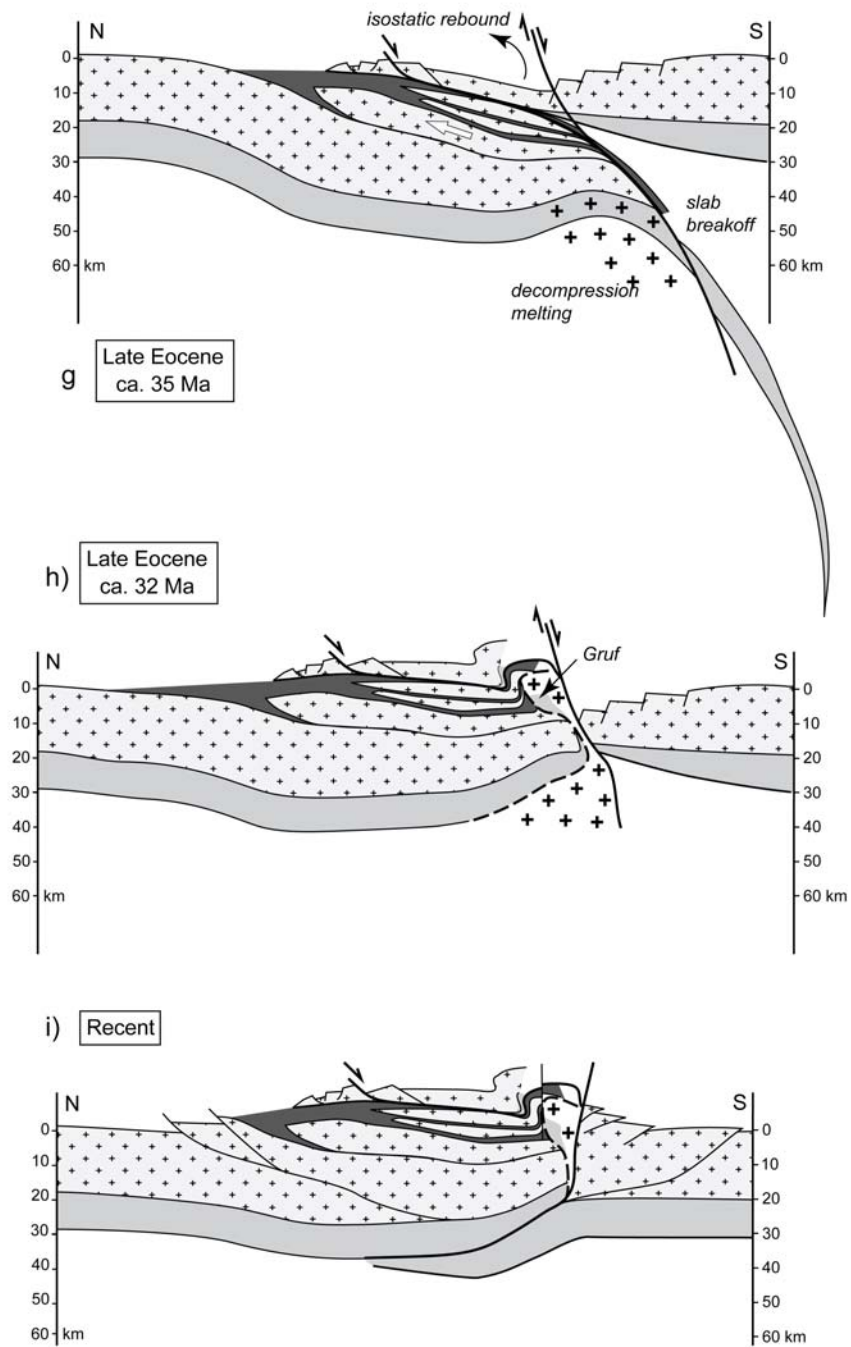
Figure 6.3: *Sketches of the tectonic evolution of the eastern Central Alps part II.*

Bibliography

Ackermand, D. and Seifert, F. (1969). Druck- und Temperaturbedingungen bei der Bildung der sapphirinführenden Gesteine von Val Codera. *Fortschritte der Mineralogie*, **47**, p. 1 (abstract).

Ague, J. and Baxter, E. (2007). Brief thermal pulses during mountain building recorded by Sr diffusion in apatite and multicomponent diffusion in garnet. *Earth and Planetary Science Letters*, **261**, 500–516.

Alexandre, P. (2007). U-Pb SIMS ages from the French Massif Central and implication for the pre-Variscan tectonic evolution in Western Europe. *Comptes Rendus Geosciences*, **339**, 613–621.

Andersen, D. and Lindsley, D. (1988). Internally Consistent Solution Models for Fe-Mg-Mn-Ti Oxides - Fe-Ti Oxides. *American Mineralogist*, **73**, 714–726.

Annersten, H. and Seifert, F. (1981). Stability of the assemblage orthopyroxene-sillimanite-quartz in the system $MgO-FeO-Fe_2O_3-Al_2O_3-SiO_2-H_2O$. *Contributions to Mineralogy and Petrology*, **77**, 158–165.

Aranovich, L. and Berman, R. (1996). Optimized standard state and solution properties of minerals II. Comparisons, predictions, and applications. *Contributions to Mineralogy and Petrology*, **126**, 25–37.

Aranovich, L. and Berman, R. (1997). A new garnet-orthopyroxene thermometer based on reversed Al_2O_3 solubility in $FeO-Al_2O_3-SiO_2$ orthopyroxene. *American Mineralogist*, **82**, 345–353.

Artus, F. (1959). Über metamorphe Breccien basischer Gesteine im Granit des Bergeller Massivs. *Hamburger Beiträge zur Mineralogie Kristallphysik und Petrogenese*, **2**, 1–39.

Arzi, A. (1978). Critical phenomena in the rheology of partially melted rocks. *Tectonophysics*, **44**, 173–184.

Baldwin, J., Powell, R., Brown, M., Moraes, R., and Fuck, R. (2005). Mineral equilibria modeling of ultrahigh-temperature metamorphism: an example from the Anápolis-Itauçu Complex, central Brazil. *Journal of Metamorphic Geology*, **23**, 511–531.

Barbosa, J., Nicollet, C., Leite, C., Kienast, J.-R., Fuck, R., and Macedo, E. (2006). Hercynite-quartz-bearing granulites from Brejões Dome area, Jequié Block, Bahia, Brazil: Influence of charnockite intrusion on granulite facies metamorphism. *Lithos*, **92**, 537–556.

Barboza, S. and Bergantz, G. (2000). Metamorphism and Anatexis in the Mafic Complex Contact Aureole, Ivrea Zone, Northern Italy. *Journal of Petrology*, **41**, 1307–1327.

Barker, F. (1964). Sapphirine-bearing rock, Val Codera, Italy. *American Mineralogist*, **49**, 146–152.

Barth, S., Oberli, F., and Meier, M. (1994). Th-Pb versus U-Pb isotope systematics in allanite from cogenetic rhyolite and granodiorite: implications for geochronology. *Earth and Planetary Sciences Letters*, **124**, 149–159.

Baudin, T. and Marquer, D. (1993). Metamorphism and deformation in the Tambo nappe (Swiss Central Alps): evolution of the phengite substitution during Alpine deformation. *Schweizerische Mineralogische und Petrographische Mitteilungen*, **73**, 285–299.

Berger, A., Rosenberg, C., and Schmid, S. (1996). Ascent, emplacement and exhumation of the Bergell pluton within the Southern Steep Belt of the Central Alps. *Schweizerische Mineralogische und Petrographische Mitteilungen*, **76**, 357–382.

Berger, A., Mercolli, I., and Engi, M. (2005). The central Lepontine Alps: Notes accompanying the tectonic and petrographic map sheet Sopra Ceneri (1:100'000). *Schweizerische Mineralogische und Petrographische Mitteilungen*, **85**, 109–146.

Berger, A., Burri, T., Alt-Epping, P., and Engi, M. (2008). Tectonically controlled fluid flow and water-assisted melting in the middle crust: An example from the Central Alps. *Lithos*, **102**, 598–615.

Berger, A., Rosenberg, C., and Schaltegger, U. (2009). Stability and isotopic dating of monazite and allanite in partially molten rocks: examples from the Central Alps. *Swiss Journal of Geosciences*, **102**, 15–29.

Berman, R. and Aranovich, L. (1996). Optimized standard state and solution properties of minerals I. Model calibration for olivine, orthopyroxene, cordierite, garnet, and ilmenite in the system FeO-MgO-CaO-Al$_2$O$_3$-TiO$_2$-SiO$_2$. *Contributions to Mineralogy and Petrology*, **126**, 1–24.

Bernotat, W. and Bambauer, H. (1982). The microcline/sanidine transformation isograd in metamorphic regions. II. The region of Lepontine metamorphism, central Swiss Alps. *Schweizerische Mineralogische und Petrographische Mitteilungen*, **62**, 231–244.

Bertrand, J. and Leterrier, J. (1997). Granïtoides d'âge Paléozoïque inférieur dans le socle de Vanoise méridionale: géochronologie U-Pb du métagranite del'Arpont (Alpes de Savoie, France). *Comptes Rendus de l'Académie des Sciences Paris, Sciences Terre Planet*, **325**, 839–844.

Best, M. and Christiansen, E. (2001). Igneous Petrology. *Blackwell Science Inc., Malden, p. 458.*

Black, L., Kamo, S., Allen, C., Aleinikoff, J., Davis, D., Korsch, R., and Foudoulis, C. (2003). TEMORA 1: a new zircon standard for Phanerozoic U-Pb geochronology. *Chemical Geology*, **200**, 155–170.

Bohlen, S. (1991). On the formation of granulites. *Journal of Metamorphic Geology*, **9**, 223–229.

Boriani, A., Burlini, L., and Sacchi, R. (1990). The Cossato-Mergozzo-Brissago Line and the Pogallo Line (Southern Alps, Northern Italy) and their relationships with the late-Hercynian magmatic and metamorphic events. *Tectonophysics*, **182**, 92–102.

Bousquet, R., Goffé, B., Vidal, O., Oberhänsli, R., and Patriat, M. (2002). The tectono-metamorphic history of the Valaisan domain from the Western to the Central Alps: New constraints on the evolution of the Alps. *Geological Society of America Bulletin*, **114**, 207–225.

Braga, R., Giacomini, F., Messiga, B., and Tribuzio, R. (2001). The Sondalo gabbroic complex (Central Alps, orthern Italy): evidence for emplacement of mantle-derived melts into amphibolite-facies metapelites. *Physics and Chemistry of the Earth, Part A: Solid Earth and Geodesy*, **26**, 333–342.

Braga, R., Callegari, A., Messiga, B., Ottolini, L., Renna, M., and Tribuzio, R. (2003). Origin of prismatine from the Sondalo granulites (Central Alps, northern Italy). *European Journal of Mineralogy*, **15**, 393–400.

Brandt, S., Will, T., and Klemd, R. (2007). Magmatic loading in the Proterozoic Epupa Complex, NW Namibia, as evidenced by ultrahigh-temperature sapphirine-bearing orthopyroxene-sillimanite-quartz granulites. *Precambrian Research*, **153**, 143–178.

Brouwer, F., Burri, T., Engi, M., and Berger, A. (2005). Eclogite relics in the Central Alps: PT-evolution, Lu-Hf ages and implications for formation of tectonic mélange zones. *Schweizerische Mineralogische und Petrographische Mitteilungen*, **85**, 147–174.

Brown, M. (2006). Duality of thermal regimes is the distinctive characteristic of plate tectonics since the Neoarchaean. *Geology*, **34**, 961–964.

Brown, M. (2007). Metamorphic conditions in orogenic belts: a record of secular change. *International Geology Review*, **49**, 193–234.

Bucher-Nurminen, K. and Droop, G. (1983). The metamorphic evolution of garnet-cordierite-sillimanite-gneisses of the Gruf-Complex, Eastern Pennine Alps. *Contributions to Mineralogy and Petrology*, **84**, 215–227.

Buob, A. (1997). Considerazioni petrografiche e strutturali nella regione del Corno di Gesero (TI/GR), parte II. Unpublished Diploma Thesis, ETH Zürich.

141

Burg, J., Van den Driescsche, J., and Brun, J. (1994). Syn- to post-thickening extension in the Variscan Belt of Western Europe: Modes and structural consequences . *Géologie de la France*, **3**, 33–51.

Burri, T., Berger, A., and Engi, M. (2005). Tertiary migmatites in the Central Alps: Regional distribution, field relationship, conditions of formation, and tectonic implications. *Schweizerische Mineralogische und Petrographische Mitteilungen*, **85**, 215–232.

Bussy, F., Venturini, G., Hunziker, J., and Martinotti, G. (1998). U-Pb ages of magmatic rocks of the western Austroalpine Dent-Blanche-Sesia Unit. *Schweizerische Mineralogische und Petrographische Mitteilungen*, **78**, 163–168.

Caddick, M. and Thompson, A. (2008). Zoned garnets and the duration of metamorphic events. *Geochimica et Cosmochimica Acta*, **72**, 127.

Caddick, M., Konopásek, J., and Thompson, A. (2010). Preservation of garnet growth zoning and the duration of prograde metamorphism. *Journal of Petrology*, page in review.

Callegari, E. and Monese, A. (1961). Studio petrogenetico dei bordi di reazione metamorfico-metasomatici attorno a lenti ultrafemici incluse nel granito di San Fedelino (Sondrio). *Rend. Società Mineralogica Italiana*, **17**, 147–192.

Carlson, W. (2006). Rates of Fe, Mg, Mn and Ca diffusion in garnet. *American Mineralogist*, **91**, 1–11.

Castiñeira, P., Navidad, M., Liesa, M., Carreras, J., and Casas, J. (2008). U-Pb zircon ages (SHRIMP) for Cadomian and Early Ordovician magmatism in the Eastern Pyrenees: new insights inte the pre-Variscan evolution of the northern Gondwana margin. *Tectonophysics*, **461**, 228–239.

Charles, N., Faure, M., and Chen, Y. (2009). The Montagne Noire migmatitic dome emplacement (French Massiv Central): new insights from petrofabric and AMS studies. *Journal of Structural Geology*, **31**, 1423–1440.

Chatterjee, N. and Johannes, W. (1974). Thermal Stability and Standard Thermodynamic Properties of Synthetic $2M_1$-Muscovite, $KAl_2[AlSi_3O_{10}(OH)_2]$. *Contributions to Mineralogy and Petrology*, **48**, 89–114.

Chemenda, A., Hurpin, D., Tang, J., Stephan, J., and Buffet, G. (2001). Impact of arc-continent collision on the conditions of burial and exhumation of UHP/LT rocks: experimental and numerical modelling. *Tectonophysics*, **341**, 137–161.

Cherniak, D. and Watson, E. (2003). Diffusion in zircon. *In: Hanchar, J.M. and Hoskin P.W.O. (eds.): Reviews in mineralogy and geochemistry, 53, Zircon. Mineralogical Society of America, Washington*, pages 113–143.

Cherniak, D., Watson, E., Grove, M., and Harrison, T. (2004). Pb diffusion in monazite: A combined RBS/SIMS study. *Geochimica et Cosmochimica Acta*, **68**, 829–840.

Ciancaleoni, L. and Marquer, D. (2006). Syn-extension leucogranite deformation during convergence in the Eastern Central Alps: example of the Novate intrusion. *Terra Nova*, **18**, 170–180.

Clemens, J., Droop, G., and Stevens, G. (1997). High-grade metamorphism, dehydration and crustal melting: a reinvestigation based on new experiments in the silica-saturated portion of the system $KAlO_2$-MgO-SiO_2-H_2O-CO_2 at P = 1.5 GPa. *Contributions to Mineralogy and Petrology*, **129**, 308–325.

Compston, W., Williams, I., Kirschvink, J., Zichao, Z., and Guogan, M. (1992). Zircon ages for the Early Cambrian time-scale. *Journal of the Geological Society of London*, **149**, 171–184.

Connolly, J. (2005). Computation of phase equilibria by linear programming: A tool for geodynamic modelling and its application to subduction zone decarbonation. *Earth and Planetary Sciences Letters*, **236**, 524–541.

Corfu, F., Hanchar, J., Hoskin, P., and Kinny, P. (2003). Atlas of Zircon Textures. *In: Hanchar, J.M. and Hoskin, P.W.O. (eds.): Reviews in mineralogy and geochemistry, 53, Zircon. Mineralogical Society of America, Washington*, pages 469–500.

Cornelius, S. (1916). Ein alpines Vorkommen von Sapphirin. *Centralblatt für Mineralogie, Geologie und Paläontologie*, pages 265–269.

Corsini, M. and Rolland, Y. (2009). Late evolution of the southern European Variscan belt: Exhumation of the lower crust in a context of oblique convergence. *Comptes Rendus Geosciences*, **341**, 214–223.

Costa, S. and Rey, P. (1995). Lower crustal rejuvenation and growth during post-thickening collapse: Insights from a crustal cross section through a Variscan metamorphic core complex. *Geology*, **23**, 905–908.

Crespi, R. (1965). Migmatiti e rocce verdi di Bagni di Masino del Masino. *Istituto Lombardo Accademico Scienze e Lettere*, **99**.

Dachs, E. and Proyer, A. (2002). Constraints on the duration of high-pressure metamorphism in the Tauern Window from diffusion modelling of discontinuous growth zones in eclogite garnet. *Journal of Metamorphic Geology*, **20**, 769–780.

Dale, J. and Holland, T. (2003). Geothermobarometry, P-T paths and metamorphic field gradients of high-pressure rocks from the Adula Nappe, Central Alps. *Journal of Metamorphic Geology*, **21**, 813–829.

Das, K., Dasgupta, S., and Miura, H. (2001). Stability of osumilite coexisting with spinel solid solution in metapelitic granulites at high oxygen fugacity. *American Mineralogist*, **86**, 1423–1434.

Davidson, C., Rosenberg, C., and Schmid, S. (1996). Synmagmatic folding of the base of the Bergell pluton, Central Alps. *Tectonophysics*, **265**, 213–238.

Davies, J. and von Blanckenburg, F. (1995). Slab breakoff: A model of lithosphere detachment and its test in the magmatism and deformation of collisional orogens. *Earth and Planetary Letters*, **129**, 85–102.

De Capitani, L., Delitalia, M., Liborio, G., Mottana, A., Rodeghiero, F., and Thöni, M. (1994). The granitoid rocks of Val Navazze, Val Torgola and Val di Rango (Val Trompia, Lombardy, Italy). *Mem. Sci. Geol. (Padova)*, **46**, 329–343.

De Laeter, J. and Kennedy, A. (1998). A double focusing mass spectrometer for geochronology. *Internetional Journal for Mass Spectrometry*, **178**, 43–50.

Delaperrière, E., Saint-Blanquat, M., Brunel, M., and Lancelot, J. (1994). Géochronologie U-Pb sur zircons et monazites dans le massif du Saint-Barthélémy (Pyrénées, France): discussion des âges des événements varisques et prévarisques. *Bullétin de la Société Géologique de France*, **165**, 101–112.

Diethelm, K. (1985). Hornblendite und Gabbros im östlichen Bergell (Val Sissone, Provinz Sondrio, Italien). *Schweizerische Mineralogische und Petrographische Mitteilungen*, **65**, 223–246.

Diethelm, K. (1989). *Petrographische und geochemische Untersuchungen an basischen Gesteinen der Bergeller Intrusion (Graubünden, Schweiz/Provinz Sondrio, Norditalien*. Ph.D. thesis, ETH, Zürich.

Dostal, J., Patocka, F., and Pin, C. (2001). Middle/Late Cambrian intracontinental rifting in the central West Sudetes, NE Bohemian Massif (Czech Republic): geochemistry and petrogenesis of the bimodal metavolcanic rocks. *Journal of Geology*, **36**, 1–17.

Downes, H., Dupuy, C., and Leyreloup, A. (1990). Crustal evolution of the Hercynian belt of Western Europe: Evidence from lower-crustal granulitic xenoliths (French Massif Central). *Chemical Geology*, **83**, 209–231.

Drescher-Kaden, F. (1940). Beiträge zur Kenntnis der Migmatit- und Assimilationsbildungen sowie der synanatektischen Reaktionsformen. 1. Über Schollenassimilation und Kristallisationsverlauf im Bergeller Granit. *Chemie der Erde*, **12**, 304–417.

Droop, G. and Bucher-Nurminen, K. (1984). Reaction Textures and Metamorphic Evolution of Sapphirine-bearing Granulites from the Gruf Complex, Italian Central Alps. *Journal of Petrology*, **25**, 766–803.

Dürr, S., Ring, U., and Frisch, W. (1993). Geochemistry and geodynamic significance of North Penninic ophiolites from the Central Alps. *Schweizerische Mineralogische und Petrographische Mitteilungen*, **73**, 407–419.

Eichhorn, R., Loth, G., Höll, R., Finger, F., Schermaier, A., and Kennedy, A. (2000). Multistage Variscan magmatism in the central Tauern Window (Austria) unveiled by U/Pb SHRIMP zircon data. *Contributions to Mineralogy and Petrology*, **139**, 418–435.

Ellis, D. (1987). Origin and evolution of granulites in normal and thickened crust. *Geology*, **15**, 167–170.

Engi, M., Berger, A., and Roselle, G. (2001). The role of the tectonic accretion channel in collisional orogeny. *Geology*, **29**, 1143–1146.

Evans, B. and Guggenheim, S. (1988). Talc, Pyrophyllite and related Minerals. *Reviews in Mineralogy*, **19**, 225–294.

Evans, B., Trommsdorff, V., and Richter, W. (1979). Petrology of an eclogite-metarodingite suite at Cima di Gagnone, Ticino. *American Mineralogist*, **64**, 15–31.

Faure, M., Lin, W., Shu, L., and Sun, Y. (1999). Tectonics of the Dabieshan (eastern China) and possible exhumation mechanism of ultra high-pressure rocks. *Terra Nova*, **11**, 251–258.

Fitzsimons, I. and Harley, S. (1994). The influence of retrograde cation-exchange on granulite P-T estimates and a convergence technique for the recovery of peak metamorphic conditions. *Journal of Petrology*, **35**, 543–576.

Frey, M. and Ferreiro Mählmann, R. (1999). Alpine metamorphism of the Central Alps. *Schweizerische Mineralogische und Petrographische Mitteilungen*, **79**, 135–154.

Friedl, G., Finger, F., Paquette, J., Von Quadt, A., McNaughton, N., and Fletcher, I. (2004). Pre-Variscan geological events in the Austrian part of the Bohemian Massif deduced from U-Pb zircon ages. *International Journal of Earth Sciences*, **93**, 802–823.

Froitzheim, N., Schmid, S., and Conti, P. (1994). Repeated change from crustal shortening to orogen-parallel extension in the Austroalpine units of Graubünden. *Eclogae Geologicae Helvetiae*, **87**, 559–612.

Froitzheim, N., Pleuger, J., Roller, S., and Nagel, T. (2003). Exhumation of high- and ultrahigh-pressure metamorphic rocks by slab extraction. *Geology*, **31**, 925–928.

Frost, B. and Chacko, T. (1989). The granulite uncertainty principle: limitations on thermometry in granulites. *Journal of Geology*, **18**, 441–454.

Fuhrman, M. and Lindsley, D. (1988). Ternary-feldspar modelling and thermometry. *American Mineralogist*, **73**, 201–215.

Fumasoli, M. (1974). *Geologie des Gebietes nördlich und südlich der Iorio-Tonale-Linie im Westen von Gravedona (Como, Italia)*. Ph.D. thesis, ETH, Zürich.

Fyfe, W. (1973). The granulite facies, partial melting and the Archaean crust. *Philosophical Transactions of the Royal Society of London, Series A. Mathematical and Physical Sciences*, **247**, 457–461.

Gebauer, D. (1994). A P-T-t path for some high-pressure ultramafic/mafic rock associations and their felsic country rocks based on SHRIMP-dating of magmatic and metamorphic zircons domains. Example: Central Swiss Alps. *Abstract of the ICOG 8, Berkeley, USA. US Geological Survey Circular*, **1107**, 109.

Gebauer, D. (1996). A P-T-t path for a (ultra?) high-pressure ultramafic/mafic rock associations and their felsic country rock based on SHRIMP-dating of magmatic and metamorphic zircon domains. Example: Alpe Arami (Central Swiss Alps). *In: Basu, A. and Hart, S. (eds.) Earth Processes: Reading the Isotopic Code. Geophysical Monograph, American Geophysical Union*, **95**, 307–329.

Gebauer, D., Schertl, H., Brix, M., and Schreyer, W. (1997). 35 Ma old ultrahigh-pressure metamorphism and evidence fro very rapid exhumation in the Dora Maira Massif, Western Alps. *Lithos*, **41**, 5–24.

Gerya, T. and Burg, J.-P. (2007). Intrusion of ultramafic magmatic bodies into the continental crust: Numerical simulation. *Physics of the Earth and Planetary Interiors*, **160**, 124–142.

Gerya, T., Perchuk, L., and Burg, J.-P. (2008). Transient hot channels: Perpetrating and regurgitating ultrahigh-pressure, high-temperature crust-mantle associations in collisional belts. *Lithos*, **103**, 236–256.

Ghizzoni, S. and Mazzoleni, G. (2005). Itinerari mineralogici in Val Codera. Geologia Insubrica - Rivista di Scienze della Terra (Milano - Morbio Inferiore), 316 pp.

Gianettoni, T. (1997). Considerazioni petrografiche e strutturali nella regione del Corno di Gesero (TI/GR), parte I. Unpublished Diploma Thesis, ETH Zürich.

Gregory, C., McFarlane, C., Hermann, J., and Rubatto, D. (2009). Tracing the evolution of calc-alkaline magmas: In-situ Sm-Nd isotope studies of accessory minerals in the Bergell Igneous Complex, Italy. *Chemical Geology*, **260**, 73–86.

Gulson, B. (1973). Age relations in the Bergell region of the Southern Swiss Alps: with some geochemical comparisons. *Eclogae Geologicae Helvetiae*, **66**, 293–323.

Hafner, M. (1993). Strukturgeologische und geochemische Untersuchungen von leukokraten Granit-Gängen und Migmatiten der südlichen Adula am Monte Peschiera (It). Unpublished Diploma Thesis, Univ. Basel.

Hanchar, J. and Miller, C. (1993). Zircon zonation patterns as revealed by cathodoluminescence and backscattered electron images: implications for interpretation of complex crustal histories. *Chemical Geology*, **110**, 1–13.

Handy, M., Herwegh, M., and Regli, C. (1993). Tektonische Entwicklung der westlichen Zone von Samedan (Oberhalbstein, Graubünden, Schweiz). *Eclogae Geologicae Helvetiae*, **86**, 785–817.

Hansmann, W. (1981). Geologisch-petrographische Untersuchungen im südlichen Bergell; 2. Val Ligoncio. Unpublished Diploma Thesis, ETH Zurich.

Hansmann, W. (1996). Age determinations on the Tertiary Masino-Bregaglia (Bergell) intrusives (Italy, Switzerland): a review. *Schweizerische Mineralogische und Petrographische Mitteilungen*, **76**, 421–451.

Hansmann, W., Müntener, O., and Hermann, J. (2001). U-Pb zircon geochronology of a tholeiitic intrusion and associated migmatites at a continental crust-mantle transition, Val Malenco, Italy. *Schweizerische Mineralogische und Petrographische Mitteilungen*, **81**, 239–255.

Harley, S. (1989). The origins of granulites: a metamorphic perspective. *Geological Magazine*, **126**, 215–247.

Harley, S. (1998a). An appraisal of peak temperatures and thermal histories in ultrahigh-temperature (UHT) crustal metamorphism: the significance of aluminous orthopyroxene. *In: Motoyoshi, Y., Shiraishi, K. (Eds.), Origin and Evolution of Continents. Memoir National Institute of Polar Research, Tokyo, Special Issue*, **53**, 49–73.

Harley, S. (1998b). On the occurrence and characterisation of ultrahigh-temperature crustal metamorphism. *In: Treloar, P.J., O'Brien, P.J. (Eds.), What Drives Metamorphism and Metamorphic Reactions?, Geological Society of London Special Publications, London*, **138**, 215–247.

Harley, S. (2004). Extending our understanding of ultrahigh temperature crustal metamorphism. *Journal of Mineralogical and Petrological Sciences*, **99**, 140–158.

Harley, S. (2008). Refining the P-T records of UHT crustal metamorphism. *Journal of Metamorphic Geology*, **26**, 125–154.

Harley, S. and Green, D. (1982). Garnet-orthopyroxene barometry for granulites and peridotites. *Nature*, **300**, 697–701.

Harley, S. and Motoyoshi, Y. (2000). Al zoning in orthopyroxene in a sapphirine quartzite: evidence for ¿ 1120 °C UHT metamorphism in the Napier Complex, Antarctica, and implications for the entropy of sapphirine. *Contributions to Mineralogy and Petrology*, **138**, 293–307.

Harley, S., Hensen, B., and Sheraton, J. (1990). Two-stage decompression in orthopyroxene-sillimanite granulites from Forefinger Point, Enderby Land, Antarctica: implications for the evolution of the Archean Napier Complex. *Journal of Metamorphic Geology*, **8**, 591–613.

Hay, W., Wold, C., and Hezog, J. (1992). Preliminary mass-balanced 3-D reconstructions of the Alps and surrounding areas during the miocene. *Lecture Notes in Earth Sciences*, **41**, 99–110.

Heinrich, C. (1983). *Die regionale Hochdruckmetamorphose der Aduladecke, Zentralalpen, Schweiz.* Ph.D. thesis, ETH, Zürich.

Heinrich, C. (1986). Eclogite facies regional metamorphism of hydrous mafic rocks in the Central Alpine Adula nappe. *Journal of Petrology*, **27**, 123–154.

Heitzmann, P. (1975). Zur Metamorphose und Tektonik im südöstlichen Teil der Lepontinischen Alpen (Provincia di Como, Italia). *Schweizerische Mineralogische und Petrographische Mitteilungen*, **55**, 467–522.

Helbing, H. and Tiepolo, M. (2005). Age determination of Ordovician magmatism in NE Sardinia and its bearing on Variscan basement evolution. *Journal of the Geological Society of London*, **162**, 689–700.

Henk, A., Franz, L., Teufel, S., and Oncken, O. (1997). Magmatic Underplating, Extension, and Crustal Reequilibration: Insights from a Cross-Section through the Ivrea Zone and Strona-Ceneri Zone, Northern Italy. *Journal of Geology*, **105**, 367–377.

Hensen, B. (1971). Theoretical phase relations involving cordierite and garnet in the system MgO-FeO-Al$_2$O$_3$-SiO$_2$. *Contributions to Mineralogy and Petrology*, **33**, 191–214.

Hensen, B. (1986). Theoretical phase relations involving cordierite and garnet revisited: the influence of oxygen fugacity on the stability of sapphirine and spinel in the system Mg-Fe-Al-Si-O. *Contributions to Mineralogy and Petrology*, **92**, 362–367.

Hensen, B. (1987). P-T grids for silica-undersaturated granulites in the system MAS (n + 4) and FMAS (n + 3) - tools for the derivations of P-T paths of metamorphism. *Journal of Metamorphic Geology*, **5**, 255–271.

Hensen, B. and Harley, S.L., . (1990). Graphical analysis of P-T-X relations in granulite facies metapelites. *In: High-temperature Metamorphism and Crustal Anatexis (eds. Ashworth, J.R. and Brown, M.), Series 2, The Mineralogical Society of Great Britain, Unwin-Hyman, London*, pages 19–56.

Hensen, B. and Osanai, Y. (1994). Experimental study of dehydration melting of F-bearing biotite in model pelitic compositions. *Mineralogical Magazine*, **58A**, 410–411.

Hensen, B.J., G. D. (1970). Experimental data on coexisting cordierite and garnet under high grade metamorphic conditions. *Physics of the Earth and Planetary Interiors*, **3**, 431–440.

Hensen, B.J., G. D. (1973). Experimental Study of the Stability of Cordierite and Garnet in Pelitic Compositions at High Pressures and Temperatures. III. Synthesis of Experimental Data and Geological Applications. *Contributions to Mineralogy and Petrology*, **38**, 151–166.

Hermann, J., Rubatto, D., and Trommsdorff, V. (2006). Sub-solidus Oligocene zircon formation in garnet peridotite during fast decompression and fluid infiltration (Duria, Central Alps. *Mineralogy and Petrology*, **88**, 181–206.

Higgins, J., Ribbe, P., and Herd, R. (1979). Sapphirine I. Crystal Chemical Contributions. *Contributions to Mineralogy and Petrology*, **68**, 349–356.

Hänny, R. (1972). Das Migmatitgebiet der Valle Bodengo (östl. Lepontin). Beiträge zur Geologischen Karte der Schweiz, (N.F.) 145, 109 pp.

Hänny, R., Grauert, B., and Soptrajanova, G. (1975). Paleozoic migmatites affected by high grade Tertiary metamorphism in the central Alps (Valle Bodengo, Italy). A geochronological study. *Contributions to Mineralogy and Petrology*, **51**, 173–196.

Holland, T. and Powell, R. (1990). An enlarged and updated internally consistent data-set with uncertainties and correlations: the system K_2O-Na_2O-CaO-MgO-MnO-FeO-Fe_2O_3-Al_2O_3-TiO_2-SiO_2-C-H_2-O_2. *Journal of Metamorphic Geology*, **8**, 89–124.

Holland, T. and Powell, R. (1998). An internally consistent thermodynamic dataset for phases of petrological interest. *Journal of Metamorphic Geology*, **16**, 309–343.

Holland, T., Babu, E., and Waters, D. (1996). Phase relations of Osumilite and dehydration melting in pelitic rocks: a simple thermodynamic model for the KFMASH system. *Contributions to Mineralogy and Petrology*, **124**, 383–394.

Holliger, K. and Levander, A. (1994). Lower crustal reflectivity modeled by rheological controls on mafic intrusions. *Geology*, **22**, 367–370.

Hoskin, P. and Schaltegger, U. (2003). The composition of zircon and igneous and metamorphic petrogenesis. *In: Hanchar, J.M. and Hoskin, P.W.O. (eds.): Reviews in mineralogy and geochemistry, 53, Zircon. Mineralogical Society of America, Washington*, pages 27–62.

Huber, R. (1999). *Tectonometamorphic evolution of the Eastern Pennine Alps during Tertiary continental collision: Structural and petrological relationships between Suretta, Tambo, Chiavenna and Gruf units (Switzerland/Italy*. Ph.D. thesis, Univ. Neuchâtel.

Huber, R. and Marquer, D. (1998). The tectonometamorphic history of the peridotitic Chiavenna unit from Mesozoic to Tertiary tectonics: a restoration controlled by melt polarity indicators (Eastern Swiss Alps). *Tectonophysics*, **296**, 205–223.

Huber, R., Challandes, N., and Marquer, D. (1999). Subduction and exhumation rates during Tertiary collisional tectonics in the eastern Pennine units for the Suretta, Tambo, Chiavenna and Gruf units (Val Bregaglia, Switzerland/Italy. *EUG 10, Journal of Conference Abstracts*, **4**, 434.

Hunziker, J. and Zingg, A. (1980). Lower Paleozoic amphibolite to granulite facies metamorphism in the Ivrea-Zone (Southern Alps-Northern Italy). *Schweizerische Mineralogische und Petrographische Mitteilungen*, **60**, 181–213.

Hutton, D. H. W. (1988). Granite emplacement mechanisms and tectonic controls: Inferences from deformation studies. *Trans. Royal Society Edinburgh*, **79**, 245–255.

Jenkins, D. and J.V., C. (1986). Phase-equilibria and crystallochemical properties of Mg-Chlorite. *American Mineralogist*, **71**, 924–936.

Jäger, E., Niggli, E., and Wenk, E. (1967). Rb-Sr Alterbestimmung an Glimmern der Zentralalpen. Beiträge zur Geologischen Karte der Schweiz, 134.

Kelly, N. and Harley, S. (2004). Orthopyroxene-corundum in Mg-Al-rich granulites from the Oygarden Islands, east Antarctica. *Journal of Petrology*, **45**, 1481–1512.

Kelsey, D. (2008). On ultrahigh-temperature metamorphism. *Gondwana Research*, **13**, 1–29.

Kelsey, D., White, R., and Powell, R. (2003). Orthopyroxene-sillimanite-quartz assemblages: distribution, petrology, quantitative P-T-X constraints and P-T paths. *Journal of Metamorphic Geology*, **21**, 439–453.

Kelsey, D., White, R., Holland, T., and R., P. (2004). Calculated phase equilibria in K_2O-FeO-MgO-Al_2O_3-SiO_2-H_2O for sapphirine-quartz-bearing mineral assemblages. *Journal of Metamorphic Geology*, **22**, 559–578.

Kelsey, D., White, R., and R., P. (2005). Calculated phase equilibria in K_2O-FeO-MgO-Al_2O_3-SiO_2-H_2O for silica-undersaturated sapphirine-bearing mineral assemblages. *Journal of Metamorphic Geology*, **23**, 217–239.

Knoblauch, P. (1939). Geologischer Atlas der Schweiz, 1:25'000, Blatt Nr. 516, Iorio. Publikationen der Schweizerischen Geologischen Kommission.

Konrad-Schmolke, M., Handy, M., Babist, J., and O'Brien, P. (2005). Thermodynamic modelling of diffusion-controlled garnet growth. *Contributions to Mineralogy and Petrology*, **149**, 181–195.

Konrad-Schmolke, M., O'Brien, P., De Capitani, C., and Carswell, D. (2007). Garnet growth at high- and ultra-high pressure conditions and the effect of element fractionation on mineral modes and composition. *Lithos*, **103**, 309–332.

Köppel, V., Günthert, A., and Grünenfelder, M. (1981). Patterns of U-Pb zircon and monazite ages in polymetamorphic units of the Swiss Alps. *Schweizerische Mineralogische und Petrographische Mitteilungen*, **61**, 97–119.

Lal, R., Ackermand, D., Raith, M., Raase, P., and Seifert, F. (1984). Sapphirine-bearing assemblages from Kiranur, Southern India: a study of chemographic relationships in the Na_2O-FeO-MgO-Al_2O_3-SiO_2-H_2O system. *Neues Jahrbuch für Mineralogische Abhandlungen*, **150**, 121–152.

Lancelot, J. and Allegret, A. (1982). Radiochronologie U/Pb de l'Ortogneiss de Alter Pedroso (Alto lentejo) et évolution anteé-hercynienne de l'Europe occidentale. *Neues Jahrberichten der Mineralogie*, **9**, 305–394.

Lardeaux, J.M., S. M. (1991). From granulites to eclogites in the Sesia zone (Italian Western Alps): a record of the opening and closure of the Piedmont ocean. *Journal of Metamorphic Geology*, **9**, 35–59.

Larionov, A., Andreichev, V., and Gee, D. (2004). The Vendian alkaline igneous suite of northern Timan: ion microprobe U-Pb zircon ages of gabbros and syenite. *In: Gee, D.G. and Pease, V.L. (eds): The Neoproterozoic Timanide Orogen of Eastern Baltica. Geological Society of London Memoires*, **30**, 69–74.

Lasaga, A. (1979). Multicomponent exchange and diffusion in silicates. *Geochimica et Cosmochimica Acta*, **43**, 455–469.

Lasaga, A. and Jiang, J. (1995). Thermal history of rocks: P-T-t paths from geospeedometry, petrologic data, and inverse theory techniques. *American Journal of Science*, **295**, 697–741.

Leite, C. d. M., Barbosa, J., Goncalves, P., Nicollet, C., and Sabaté, P. (2009). Petrological evolution of silica-undersaturated sapphirine-bearing granulite in the Paleoproterozoic Salvador-Curaçá Belt, Bahia, Brazil. *Gondwana Research*, **15**, 49–70.

Liati, A. and Gebauer, D. (2001). U–Pb SHRIMP-dating of zircon domains from eclogites of Antrona (Western Alps): evidence for a Valais Ocean origin. *EUG 11. Journal of Conference Abstract*, **6**, 600.

Liati, A. and Gebauer, D. (2003). Geochronological constraints for the time of metamorphism in the Gruf Complex (Central Alps) and implications for the Adula-Cima Lunga nappe system. *Schweizerische Mineralogische und Petrographische Mitteilungen*, **83**, 159–172.

Liati, A., Gebauer, D., and Fanning, C. (2000). U-Pb SHRIMP-dating of zircon from the Novate granite (Bergell, Central Alps): evidence for Oligocene-Miocene magmatism, Jurassic-Cretaceous continental rifting and opening of the Valais trough. *Schweizerische Mineralogische und Petrographische Mitteilungen*, **80**, 305–316.

Liati, A., Gebauer, D., and Fanning, C. (2003). The youngest basic oceanic magmatism in the Alps (Late Cretaceous; Chiavenna unit, Central Alps): geochronological constraints and geodynamic significance. *Contributions to Mineralogy and Petrology*, **146**, 144–158.

Liati, A., Gebauer, D., and Fanning, C. (2009). Geochronological evolution of HP metamorphic rocks of the Adula nappe, Central Alps, in pre-Alpine and Alpine subduction cycles. *Journal of the Geological Society of London*, **166**, 797–810.

Lin, W., Ebami, M., Faure, M., Schärer, U., and Arnaud, N. (2007). Survival of eclogite xenolith in a Cretaceous granite intruding the Central Dabieshan migmatite gneiss dome (Eastern China) and its tectonic implications. *International Journal of Earth Sciences*, **96**, 707–724.

Lorenz, V. and Nicholls, I. (1976). The Permocarboniferous Basin and Range Province of Europe. An application of plate tectonics. In: The Continental Permian in Central, West, and South Europe (eds. Falke, H.), Dordrecht, Holland, D. Reidel Publishing Company, 313-342.

Lorenz, V. and Nicholls, I. (1984). Plate and intraplate processes of Hercynian Europe during the Late Paleozoic. *Tectonophysics*, **107**, 25–56.

Löw, S. (1987). Die tektono-metamorphe Entwicklung der Adula-Decke (Zentralalpen, Schweiz). Beiträge zur Geologischen Karte der Schweiz, (N.F.) 161.

Manatschal, G., Engström, A., Desmurs, L., Schaltegger, U., Cosca, M., Müntener, O., and Bernoulli, D. (2006). What is the tectono-metamorphic evolution of continental break-up: The example of the Tasna Oceane-Continent Transition. *Journal of Structural Geology*, **28**, 1849–1869.

Marquer, D., Challandes, N., and Schaltegger, U. (1998). Early Permian magmatism in Briançonnais terranes: Truzzo granite and Roffna rhyolite (eastern Penninic nappes, Swiss and Italian Alps. *Schweizerische Mineralogische und Petrographische Mitteilungen*, **78**, 397–414.

Mc Laren, A., Fitzgerald, J., and Williams, I. (1994). The microstructure of zircon and its influence on the age determination from Pb/U isotopic ratios measured by ion microprobe. *Geochimica Cosmochimica Acta*, **58**, 607–610.

McCann, T. and Kiersnowski, H. (2008). Permian. *In: McCann, T. (eds): The Geology of Central Europe, Volume 1: Precambrian and Paleozoic. Geological Society of London*, pages 531–597.

McDade, P. and Harley, S. (2001). A petrogenetic grid for aluminous granulite facies metapelites in the KFMASH system. *Journal of Metamorphic Geology*, **19**, 45–59.

Melleton, J., Cocherie, A., Faure, M., and Rossi, P. (2010). Precambrian protoliths and Early Paleozoic magmatism in the French Massif Central: U-Pb data and the North Gondwana connection in the west European Variscan belt. *Gondwana Research*, **17**, 13–25.

Meyre, C., De Capitani, C., and Partzsch, J. (1997). A ternary solid solution model for omphacite and its application to geothermobarometry of eclogites from the Middle Adula nappe (Central Alps, Switzerland). *Journal of Metamorphic Geology*, **15**, 687–700.

Meyre, C., Marquer, D., Schmid, S., and Ciancaleoni, L. (1998). Syn-orogenic extension along the Forcola fault: Correlation of Alpine deformations in the Tambo and Adula nappes (Eastern Penninic Alps). *Eclogae Geologicae Helvetiae*, **91**, 409–420.

Meyre, C., De Capitani, C., Zack, T., and Frey, M. (1999). Petrology of High-Pressure Metapelites from the Adula Nappe (Central Alps, Switzerland). *Journal of Petrology*, **40**, 199–213.

Milnes, A. and Pfiffner, O. (1980). Tectonic evolution of the Central Alps in the cross section St. Gallen-Como. *Eclogae Geologicae Helvetiae*, **71**, 619–633.

Müller, W., Prosser, G., Mancktelow, N., Villa, I., Kelley, S., Viola, G., and Oberli, F. (2000). Geochronological constraints on the evolution of the Periadriatic Fault System (Alps). *Internetional Journal of Earth Sciences*, **90**, 623–653.

Müntener, O., Hermann, J., and Trommsdorff, V. (2000). Cooling history and exhumation of lower crustal granulite and Upper Mantle (Malenco, Eastern Central Alps). *Journal of Petrology*, **41**, 175–200.

Monjoie, P. and Bussy, F., S. U. M. A. L. H. P. H. (2007). Contrasting magma types and timing of intrusion in the Permian layered mafic complex of Mont Collon (Western Alps, Valais, Switzerland): evidence from U/Pb zircon and ^{40}Ar/^{39}Ar amphibole dating. *Swiss Journal of Geosciences*, **100**, 125–135.

Moraes, R., Brown, M., Fuck, R., Camargo, M., and Lima, T. (2002). Characterization and P-T Evolution of Melt-bearing Ultrahigh-temperature Granulites: an Example from the Anápolis-Itauçu Complex of the Brasília Fold Belt, Brazil. *Journal of Petrology*, **43**, 1673–1705.

Moticska, P. (1970). Petrographie und Strukturanalyse des westlichen Bergeller Massivs und seines Rahmens. *Schweizerische Mineralogische und Petrographische Mitteilungen*, **50**, 355–443.

Mottana, A., Morten, L., and Brunfelt, A. (1978). Distribuzione delle terre rare nel Massiccio Val Masino - Val Bregaglia (Alpi Centrali). *Rend. Società Mineralogica Italiana*, **34**, 485–497.

Mouri, H., Guiraud, M., and Hensen, B. (1996). Petrology of phlogopite-sapphirine-bearing Al-Mg granulites from Ihouhaouene, In Ouzzal, Hoggar, Algeria: an example of phlogopite stability at high temperature. *Journal of Metamorphic Geology*, **14**, 725–738.

Muralt, R. (1986). Mineralogisch-geologische Untersuchungen in der Adula-Decke am Nordhang des San Bernardino-Passes (Graubünden, Schweiz). Unpublished Diploma Thesis, Univ. Bern.

Nagel, T., De Capitani, C., and Frey, M. (2002). Isograds and P-T evolution in the eastern Lepontine Alps (Graubünden, Switzerland). *Journal of Metamorphic Geology*, **20**, 309–324.

Nandakumar, V. and Harley, S. (2000). A reappraisal of the pressure-temperature path of granulites from the Kerala Khondalite Belt, southern India. *Journal of Geology*, **108**, 687–703.

Niggli, E. and Niggli, C. (1965). Karten der Verbreitung einiger Mineralien der alpidischen Metamorphose in den Schweizer Alpen (Stilpnomelan, Alkali-Amphibol, Chloritoid, Staurolith, Disthen, Sillimanit). *Eclogae Geologicae Helvetiae*, **58**, 335–368.

Nimis, P. and Trommsdorff, V. (2001). Revised thermobarometry of Alpe Arami and other garnet peridotites from the Central Alps. *Journal of petrology*, **42**, 103–115.

Nussbaum, C., Marquer, D., and Biino, G. (1998). Two subduction events in a polyciclic basement: example of Alpine and pre-Alpine high pressure in the Alps (Suretta nappe, Swiss Eastern Alps. *Journal of Metamorphic Geology*, **16**, 591–605.

Oberli, F., Meier, M., Berger, A., Rosenberg, C., and Gieré, R. (2004). U-Th-Pb and 230Th/238U disequilibrium isotope systematics: Precise accessory mineral chronology and melt evolution tracing in the Alpine Bergell intrusion. *Geochimica et Cosmochimica Acta*, **68**, 2543–2560.

Oggiano, G., Gaggero, L., Funedda, A., Buzzi, L., and Tiepolo, M. (2010). Multiple early Paleozoic volcanic events at the northern Gondwana margin: U-Pb age evidence from the Southern Variscan branch (Sardinia, Italy). *Gondwana Research*, **17**, 44–58.

Oliver, N., Bodorkos, S., Nemchin, A., Kinny, P., and Watt, G. (1999). Relationships between Zircon U-Pb SHRIMP Ages and Leucosome Type in Migmatites of the Halls Creek Orogen, Western Australia. *Journal of Petrology*, **40**, 1553–1575.

Oschidari, H. and Ziegler, U. (1992). Vergleichende Sm-Nd und Rb-Sr Untersuchungen an Bergeller Geröllen aus der Gonfiolite Lombarda (”Südalpine Molasse”) und an Bergeller und Novate-Granitoiden des Ursprungsgebietes. *Eclogae Geologicae Helvetiae*, **85**, 375–384.

Oterdoom, W. (1980). *Scapoliote in metamorphic calcsilicate rocks: crystallographic and phase relations*. Ph.D. thesis, ETH, Zürich.

Partzsch, J. (1998). *The tectono-metamorphic evolution of the middle Adula nappe, Central Alps, Switzerland*. Ph.D. thesis, Univ. Basel.

Paterson, B., Stephens, W., Rogers, G., Williams, I., Hinton, R., and Herd, D. (1992). The nature of zircon inheritance in two granite plutons. *Earth Sciences*, **83**, 459–471.

Paterson, S., Vernon, R., and Tobisch, O. (1989). A review of criteria for the identification of magmatic and tectonic foliations in granitoids. *Journal of Structural Geology*, **11**, 349–363.

Pattison, D. and Begin, N. (1994). Zoning patterns in orthopyroxene and garnet in granulites: implications for geothermometry. *Journal of Metamorphic Geology*, **12**, 387–410.

Pattison, D., Chacko, T., Farquhar, J., and McFarlane, C. (2003). Temperatures of granulite-facies metamorphism: constraints from experimental phase equilibria and thermobarometry corrected for retrograde exchange. *Journal of Petrology*, **44**, 867–900.

Peressini, G., Quick, J., Sinigoi, S., Hofmann, A., and Fanning, M. (2007). Duration of a Large Mafic Intrusion and Heat Transfer in the Lower Crust: a SHRIMP U-Pb Zircon Study in the Ivrea-Verbano Zone (Western Alps, Italy). *Journal of Petrology*, **48**, 1185–1218.

Peterson, J., Chacko, T., and Kühner, S. (1991). The effect of fluorine on the vapour-absent melting of phlogopite + quartz: implication for deep-crustal processes. *American Mineralogist*, **76**, 470–476.

Pfiffner, M. and Trommsdorf, V. (1998). The high-pressure ultramafic-mafic-carbonate suite of Cima Lunga-Adula, Central Alps: Excursions to Cima di Gagnoneand Alpe Arami. *Schweizerische Mineralogische und Petrographische Mitteilungen*, **78**, 337–354.

Piccoli, G. (1961). Metasomatismo e migmatiti nelle rocce verdi di Novate Mezzola (Sondrio, Alpi Lombarde). *Rend. Società Mineralogica Italiana*, **17**, 427–454.

Pin, C. (1986). Datation U-Pb sur zircons à 285 M.a. du complexe gabbro-dioritique du Val Sesia-Val Mastallone et âge tardi-hercynien du métamorphisme granulitique de la zone Ivrea-Verbano (Italie). *Comptes Rendus de l'Académie de Sciences*, **303**, 827–830.

Pin, C. and Lancelot, J. (1978). Un exemple de magmatisme cambrien dans le Massif Central: les métadiorites quartziques intrusives dans la série de Lot. *Bullétin de la Société Géologique de France*, **20**, 203–208.

Pin, C. and Marini, F. (1993). Early Ordovician continental brwak-up in Variscan Europe: Nd-Sr isotope and trace element evidence from bimodal igneous associations of the Southern Massif Central, France. *Lithos*, **29**, 177–196.

Pinarelli, L., Del Moro, A., and Boriani, A. (1988). Rb-Sr geochronology of Lower Permian plutonism in Massiccio dei Laghi, Southern Alps (NW Italy). *Rendiconti della Società Italiana di Mineralogia e Petrografia*, **43**, 411–428.

Platt, J., Soto, J.-I., Whitehouse, M., Hurford, A., and Kelly, S. (1998). Thermal evolution, rate of exhumation, and tectonic significance of metamorphic rocks from the floor of the Alboran extensional basin, western Mediterranean. *Tectonics*, **17**, 671–689.

Poller, U., Liebetrau, V., and Todt, W. (1997). U-Pb single-zircon dating under cathodoluminescence control (CLC-method): application to polymetamorphic orthogneisses. *Chemical Geology*, **139**, 287–297.

Powell, R. (1983). Processes in Granulite-facies Metamorphism. *In: Migmatites, Melting and Metamorphism (eds. Atherton, M.P. and Gribble, C.D.), Shiva Publishing, Nantwich, Cheshire*, pages 127–139.

Powell, R. and Downes, J. (1990). Garnet porphyroblast-bearing leucosomes in metapelites: mechanisms, phase diagrams, and an example from Broken Hill, Australia. *In: High-Temperature Metamorphism and Crustal Anatexis, The Mineralogical Society of Great Britain, Series 2. (eds. Ashworth, J.R. and Brown, M.), Unwin-Hyman, London*, pages 105–123.

Powell, R. and Holland, T. (1988). An internally consistent thermodynamic dataset with uncertainties and correlations. 3. Applications, methods, worked examples and a computer program. *Journal of Metamorphic Geology*, **6**, 173–204.

Powell, R. and Holland, T. (1994). Optimal geothermometry and geobarometry. *American Mineralogist*, **79**, 120–133.

Powell, R. and Holland, T. (1999). Relating formulations of the thermodynamics of mineral solid solutions: activity modelling of pyroxenes, amphiboles and micas. *American Mineralogist*, **84**, 1–14.

Powell, R. and Sandiford, M. (1988). Sapphirine and spinel phase relationships in the system FeO-MgO-Al$_2$O$_3$-TiO$_2$-O$_2$ in the presence of quartz and hypersthene. *Contributions to Mineralogy and Petrology*, **98**, 64–71.

Quick, J., Sinigoi, S., Snoke, A., Kalakay, T., Mayer, A., and Peressini, G. (2003). Geologic map of the southern Ivrea-Verbano Zone, Northwestern Italy. *Geologic Investigations Series map I-2776 USGS, map + pamphlet*, page pp. 22.

Raith, M., Karmakar, S., and Brown, M. (1997). Ultra-high temperature metamorphism and multistage decompressional evolution of sapphirine granulites from the Palni Hill Ranges, southern India. *Journal of Metamorphic Geology*, **15**, 379–399.

Rebay, G. and Spalla, M. (2001). Emplacement at granulite facies conditions of the Sesia-Lanzo metagabbros: an early record of Permian rifting? *Lithos*, **58**, 85–104.

Repossi, E. (1915). La bassa Valle della Mera. Studi petrografici e geologici II. Memorie della Società Italiana di Scienze Naturali Milano 8, 186 pp.

Reusser, E. (1980). Radiometrische Untersuchungen am Bergeller Granodiorit. Unpubl. Diplome Thesis. Unpublished Diploma Thesis, ETH Zurich.

Reusser, E. (1987a). Phasenbeziehungen im Tonalit der Bergeller Intrusion. *Bericht über die 62. Hauptversammlung in Luzern, Schweizerische Moneralogische und Petrographische Mitteilungen*, **67**, 377–378.

Reusser, E. (1987b). *Phasenbeziehungen im Tonalit der Bergeller Intrusion (Graubünden, Schweiz/Provinz Sondrio, Italien)*. Ph.D. thesis, ETH, Zürich.

Rey, P. (1993). Seismic and tectonometamorphic characters of the Lower continental crust in Phanerozoic areas: a consequence of post-thickening extension. *Tectonics*, **12**, 580–590.

Richardson, S. (1968). Staurolite stability in a part of the system Fe-Al-Si-O-H. *Petrology*, **9**, 757–768.

Ring, U. (1992). The Alpine geodynamic evolution of Penninic nappes in the eastern Central Alps: geothermobarometric and kinematic data. *Journal of Metamorphic Geology*, **10**, 33–53.

Romer, R., Schärer, U., and Steck, A. (1996). Alpine and pre-Alpine magmatism in the root-zone of the western Central Alps. *Contributions to Mineralogy and Petrology*, **123**, 138–158.

Rosenberg, C. (2004). Shear zones and magma ascent: A model based on a review of the Tertiary magmatism in the Alps. *Tectonics*, **23**.

Rosenberg, C., Berger, A., and Schmid, S. (1995). Observations from the floor of a granitoid pluton: Inferences on the driving force of final emplacement. *Geology*, **23**, 443–446.

Rubatto, D., Berger, A., Gregory, C., Hermann, J., and Engi, M. (2007). Migmatisation in the Central Alps lasting 10 m.y. *Geochim. Cosmochim. Acta*, **71**, A857.

Rubatto, D., Hermann, J., Berger, A., and Engi, M. (2009). Protracted fluid-present melting during Barrovian metamorphism in the Central Alps. *Contributions to Mineralogy and Petrology*, pages DOI 10.1007/s00410–009–0406–5.

Ruzicka, R. (1997). Der Nordrand des Gruf-Komplexes und seine Beziehung zur Engadiner Linie. Unpublished Diploma Thesis, Univ. Basel.

Sajeev, K. and Osanai, Y. (2004). Ultrahigh-temperature Metamorphism (1150°C, 12 kbar) and Multistage Evolution of Mg-, Al-rich Granulites from the Central Highland Complex, Sri Lanka. *Journal of Petrology*, **45**, 1821–1844.

Sandiford, M., Neale, F., and Powell, R. (1987). Metamorphic evolution of aluminous granulites from Labwor Hills, Uganda. *Contributions to Mineralogy and Petrology*, **95**, 217–225.

Santini, L. (1992). *Geochemistry and geochronology of the basic rocks of the Penninic Nappes of East–Central Alps (Switzerland)*. Ph.D. thesis, Univ. Lausanne.

Santosh, M. and Sajeev, K. (2006). Anticlockwise evolution of ultrahigh-temperature granulites within continental collision zone in southern India. *Lithos*, **92**, 447–464.

Schaltegger, U. (1990). Post-magmatic resetting of Rb-Sr whole rock ages - a study in the Central Aar Granite (Central Alps, Switzerland). *Geologisches Rundschau*, **79**, 709–724.

Schaltegger, U. and Brack, P. (2007). Crustal-scale magmatic system during intracontinental strike-slip tectonics: U, Pb and Hf isotopic constraints from Permian magmatic rocks of the Siuthern Alps. *International Journal of Earth Sciences*, **96**, 1131–1151.

Schaltegger, U. and Gebauer, D. (1999). Pre-Alpine geochronology of the Central, Western and Southern Alps. *Schweizerische Mineralogische und Petrographische Mitteilungen*, **79**, 79–88.

Schefer, S. (2005). Deformation und Metamorphose im Gruf-Komplex (1), Val Codera, Italien. Unpublished Diploma Thesis, Univ. Basel.

Schmid, S., Zingg, A., and Handy, M. (1987). The kinematics of movements along the Insubric Line and the emplacement of the Ivrea zone. *Tectonophysics*, **135**, 47–66.

Schmid, S., Aebli, H., Heller, F., and Zingg, A. (1989). The role of the Periadriatic line in the tectonic evolution of the Alps. *In: Coward, M.P., Dietrich, D. and Park, R.G. (eds): Alpine Tectonics. Geol. Soc. Spec. Publ.*, **45**, 153–171.

Schmid, S., Rück, P., and Schreurs, G. (1990). The significance of the Schams nappes for the reconstruction of the paleotectonic and orogenic evolution of the Penninic zone along the NFP 20 East Traverse (Grisons, eastern Switzerland). *Mémoire de la Société géologique de France*, **156**, 263–287.

Schmid, S., Pfiffner, O., Froitzheim, N., Schönborn, G., and Kissling, E. (1996a). Geophysical-geological transect and tectonic evolution of the Swiss-Italian Alps. *Tectonics*, **15**, 1036–1064.

Schmid, S., Berger, A., Davidson, C., Gieré, R., Hermann, J., Nievergelt, P., Puschnig, A., and Rosenberg, C. (1996b). The Bergell pluton (Southern Switzerland, Northern Italy): overview accompanying a geological-tectonic map of the intrusion and surrounding country rocks. *Schweizerische Mineralogische und Petrographische Mitteilungen*, **76**, 329–355.

Schmidt, M. (1989). Petrography and structural evolution of ophiolitic remnants in the Bellinzona Zone, Southern Steep Belt, Central Alps (CH, I). *Schweizerische Mineralogische und Petrographische Mitteilungen*, **69**, 393–405.

Schmitz, S., Möller, A., Wilke, M., Malzer, W., Kanngiesser, B., Bousquet, R., Berger, A., and Schefer, S. (2009). Chemical U-Th-Pb dating of monazite by 3D-Micro X-ray fluorescence analysis with synchrotron radiation. *European Journal of Mineralogy*, **21**, 927–945.

Schmutz, H. (1976). Der Mafitit-Ultramafitit-Komplex zwischen Chiavenna und Val Bondasca (Provinz Sondrio, Italien; Kt. Graubünden, Schweiz). Beiträge zur Geologischen Karte der Schweiz, (N.F.) 149, 73 pp.

Schärer, U., Cosca, M., Steck, A., and Hunziker, J. (1996). Termination of major ductile strike-slip shear and differential cooling along the Insubric line (Central Alps): U-Pb, Rb-Sr and ^{40}Ar/^{39}Ar ages of cross-cutting pegmatites. *Earth and Planetary Sciences Letters*, **142**, 331–351.

Schreyer, W. (1970). pelitischer Gesteine im Modellsystem MgO-Al$_2$O$_3$-SiO$_2$-H$_2$O. *Fortschritte der Mineralogie*, **47**, 124–165.

Schreyer, W. and Abraham, K. (1978). Symplectitic cordierite-orthopyroxene-garnet assemblages as products of contact metamorphism of pre-existing basement granulites in the Vredefort structure, South Africa and their relation to pseudotachylite. *Contributions to Mineralogy and Petrology*, **68**, 53–62.

Schubert, G., Turcotte, D., and Olson, P. (2001). Mantle convection in the earth and planets. *Cambridge University Press, Cambridge, 941 pp*, **36**.

Schuster, R. and Stüwe, K. (2008). Permian metamorphic event in the Alps. *Geology*, **36**, 603–606.

Sengupta, P., Sen, J., Dasgupta, S., Raith, M., Bhui, U., and Ehl, J. (1999). Ultra-high temperature metamorphism of metapelitic granulites from Kondapalle, Eastern Ghats Belt: Implications for the Indo-Antarctic correlation. *Journal of Petrology*, **40**, 1065–1087.

Sergeev, S. and Steiger, R. (1993). High-precision U-Pb single zircon dating of Variscan and Caledonian magmatic cycles in the Gotthard massif, Central Swiss Alps. *Terra Nova Abstracts*, **5**, 394–395.

Sergeev, S. and Steiger, R. (1995). New estimate of emplacement and source ages of the acid gneisses constituting the pre-Alpine basement: single-zircon and zircon fragment U/Pb dating. *Schweizerische Mineralogische und Petrographische Mitteilungen*, **76**, 121–122.

Smith, H. and Giletti, B. (1997). Lead diffusion in monazite. *Geochimica et Cosmochimica Acta*, **61**, 1047–1055.

Sánchez-García, T., Bellido, F., and Quesada, C. (2003). Geodynamic setting and geochemical signatures of Cambrian-Ordovician rift-related igneous rocks (Ossa-Morena Zone, SW Iberia). *Tectonophysics*, **365**, 233–255.

Soula, J.-C. (1982). Characteristics and mode of emplacement of gneiss domes and plutonic domes in central-eastern Pyrenees. *Journal of Structural Geology*, **4**, 313–342.

Spear, F. (1988). Metamorphic fractional crystallization and internal metasomatism by diffusional homogenization of zoned garnets. *Contributions to Mineralogy and Petrology*, **99**, 507–517.

Spear, F. and Parrish, R. (1996). Petrology and cooling rates of the Valhalla Complex, British Columbia, Canada. *Journal of Petrology*, **37**, 733–765.

Spear, F., Kohn, M., Florence, F., and Menard, T. (1991). A model for garnet and plagioclase growth in pelitic schists: Implications for thermobarometry and P-T path determinations. *Journal of Metamorphic Geology*, **8**, 683–696.

Srogi, L., Wagner, M. E., and Lutz, T. M. (1993). Dehydration partial melting and disequilibrium in the granulite-facies Wilmington Complex, Pennsylvania-Delaware Piedmont. *American Journal of Science*, **293**, 405–462.

Staub, R. (1918). Geologische Beobachtungen am Bergeller Massiv. *Vierteljahrssch. Naturforsch.ellschaft Zürich*, **63**, 1–18.

Staub, R. (1946). Geologische Karte der Berninagruppe und ihrer Umgebung im Oberengadin, Bergell, Val Malenco, Puschlav und Livigno, 1:50'000. Geologische Spezialkarte 118, Schweiz. Geol. Kommission.

Steck, A. and Hunziker, J. (1994). The Tertiary structural and thermal evolution of the Central Alps - Compressional and extensional structures in an orogenic belt. *Tectonophysics*, **238**, 229–254.

Steinmann, M. and Stille, P. (1999). Geochemical evidence for the nature of the crust beneath the eastern North Penninic basin of the Mesozoic Tethys ocean. *Geologische Rundschau*, **87**, 633–643.

Stevens, G., Clemens, J., and Droop, G. (1997). Melt production during granulite-facies anatexis: experimental data from "primitive" metasedimentary protoliths. *Contributions to Mineralogy and Petrology*, **128**, 352–370.

Storm, L. and Spear, F. (2005). Pressure, temperature and cooling rates of granulite facies migmatitic pelites from the southern Adirondack Highlands, New York. *Journal of Metamorphic Geology*, **23**, 107–130.

Stucki, A. (2001). *High grade Mesozoic ophiolites of the Southern Steep Belt, Central Alps*. Ph.D. thesis, ETH, Zürich.

Stucki, A., Rubatto, D., and Trommsdorff, V. (2003). Mesozoic ophiolite relics in the Southern Steep Belt of the Central Alps. *Schweizerische Mineralogische und Petrographische Mitteilungen*, **83**, 285–299.

Stüwe, K. (1997). Effective bulk composition changes due to cooling: a model predicting complexities in retrograde reaction textures. *Contributions to Mineralogy and Petrology*, **129**, 43–52.

Sun, S.-S. and McDonough, W. (1989). Chemical and isotopic systematics of oceanic basalts: implications for mantle composition and processes. *Geological Society Special Publication*, **42**, 313–345.

Tajcmanová, L., Connolly, J., and Cesare, B. (2009). A thermodynamic model for titanium and ferric iron solution in biotite. *Journal of Metamorphic Geology*, **27**, 153–165.

Talerico, C. (2000). *Petrological and chemical investigation of a metamorphosed oceanic crust-mantle section (Chiavenna, Bergell Alps)*. Ph.D. thesis, ETH, Zürich.

Timmerman, M. (2008). Paleozoic magmatism. *In: McCann, T. (eds.): The Geology of Central Europe, Volume 1: Precambrian and Paleozoic, Geological Society London*, pages 665–748.

Todd, C. and Engi, M. (1997). Metamorphic field gradients in the Central Alps. *Journal of Metamorphic Geology*, **15**, 513–530.

Tole, M. (1985). The kinetics of dissolution of zircon ($ZrSiO_4$). *Geochimica Cosmochimica Acta*, **49**, 453–458.

Tong, L. and Wilson, C. (2006). Tectonothermal evolution of the ultrahigh temperature metapelites in the Rauer Group, east Antarctica. *Precambrian Research*, **149**, 1–20.

Tribuzio, R., Thirlwall, M., and Messiga, B. (1999). Petrology, mineral and isotope geochemistry of the Sondalo gabbroic complex (Central Alps, Northern Italy): implications for the origin of post-Variscan magmatism. *Contributions to Mineralogy and Petrology*, **136**, 48–62.

Trümpy, R. (1960). Paleotectonic Evolution of the Central and Western Alps. *Bulletin of the Geological Society of America*, **71**, 1–104.

Trommsdorff, V. (1966). Progressive Metamorphose kieseliger Karbonatgesteine in den Zentralalpen zwischen Bernina und Simplon. *Schweizerische Mineralogische und Petrographische Mitteilungen*, **46**, 431–460.

Trommsdorff, V. (1990). Metamorphism and tectonics in the Central Alps: The Alpine lithospheric mélange of Cima Lunga and Adula. *Memorie della Società Geologica Italiana*, **45**, 39–49.

Trommsdorff, V. and Connolly, J. (1996). The ultramafic contact aureole about the Bregaglia (Bergell) tonalite: isotherms and a thermal model. *Schweizerische Mineralogische und Petrographische Mitteilungen*, **76**, 537–547.

Trommsdorff, V. and Evans, B. (1972). Progressive metamorphism of antigorite schist in the Bergell tonalite aureole. *American Journal of Sciences*, **272**, 423–437.

Trommsdorff, V. and Evans, B. (1977). Antigorite-ophicarbonates: contact metamorphism in Valmalenco, Italy. *Contributions to Mineralogy and Petrology*, **62**, 301–312.

Trommsdorff, V. and Nievergelt, P. (1983). The Bregaglia (Bergell) Iorio intrusive and its field relations. *Memorie della Società Geologica Italiana*, **26**, 55–68.

Vance, D. and O'Nions, R. (1992). Prograde and retrograde thermal histories from the Central Swiss Alps. *Earth and Planetary Sciences Letters*, **114**, 113–129.

Vavra, G. and Schaltegger, U. (1999). Post-granulite facies monazite growth and rejuvenation during Permian to Lower Jurassic thermal and fluid events in the Ivrea Zone (Southern Alps). *Contributions to Mineralogy and Petrology*, **134**, 405–414.

Vavra, G., Gebauer, D., Schmid, R., and Compston, W. (1996). Multiple growth and recrystallization during polyphase Late Carboniferous to Triassic metamorphism in granulites of the Ivrea Zone (Southern Alps): an ion microprobe (SHRIMP) study. *Contributions to Mineralogy and Petrology*, **122**, 337–358.

Veevers, J. and Tewari, R. (1995). Permian-Carboniferous and Permian-Triassic magmatism in the rift zone bordering the Tethyan margin of southern Pangea. *Geology*, **23**, 467–470.

Vernon, R. H. (2000). Review of microstructural evidence of magmatic and solid-state flow. *Electron. Geosciences*, **5**, 1–23.

Vielzeuf, D. and Holloway, J. (1988). Experimental determination of the fluid-absent melting relations in the pelitic system. Consequences for crustal differentiation. *Contributions to Mineralogy and Petrology*, **98**, 257–276.

Vielzeuf, D. and Montel, J. (1994). Partial melting of metagreywackes. Part I. Fluid-absent experiments and phase relationships. *Contributions to Mineralogy and Petrology*, **117**, 375–393.

Vielzeuf, D. and Pin, C. (1991). Late-Hercynian granulites of igneous origin - Example of the Treilles Norite, Corbieres (Aude, France). *Bulletin de la Société Géologique de France*, **162**, 1057–1066.

Von Blanckenburg, F. (1992). Combined high-precision chronometry and geochemical tracing using accessory minerals: applied to the Central-Alpine Bergell intrusion. *Chemische Geologie*, **100**, 19–40.

Von Blanckenburg, F. and Davies, J. (1995). Slab breakoff: A model for syncollisional magmatism and tectonics in the Alps. *Tectonics*, **14**, 120–131.

Von Blanckenburg, F., Früh-Green, G., Diethelm, K., and Stille, P. (1992). Nd-, Sr-, O-isotopic and chemical evidence for a two-stage contamination history of mantle magma in the Central-Alpine Bergell intrusion. *Contributions to Mineralogy and Petrology*, **110**, 33–45.

Von Blanckenburg, F., Kagami, H., Deutsch, A., Oberli, F., Meier, M., Wiedenbeck, M., Barth, S., and Fischer, H. (1998). The origin of Alpine plutons along the Periadriatic Lineament. *Schweizerische Mineralogische und Petrographische Mitteilungen*, **78**, 55–66.

Von Raumer, J., Stampfli, G., Borel, G., and Bussy, F. (2002). Organization of pre-Variscan basement areas at the north-Gondwanan margin. *International Journal of Earth Sciences*, **91**, 35–52.

Waters, D. J. (1988). Partial melting and the formation of granulite facies assemblages in Namaqualand, South Africa. *Journal of Metamorphic Geology*, **6**, 387–404.

Watson, E. (1979). Zircon saturation in felsic liquids: experimental results and applications to trace element geochemistry. *Contributions to Mineralogy and Petrology*, **70**, 407–419.

Watson, E. (1996). Dissolution, growth and survival of zircons during crustal fusion: kinetic principles, geological models and implications for isotopic inheritance. *Transactions of the Royal Society of Edinburgh*, **87**, 43–56.

Watson, E. and Harrison, T. (1983). Zircon saturation revisited: temperature and composition effects in a variety of crustal magma types. *Earth and Planetary Science Letters*, **64**, 295–304.

Wenk, E. (1955). Eine Strukturkarte der Tessiner Alpen. *Schweizerische Mineralogische und Petrographische Mitteilungen*, **35**, 139–152.

Wenk, H. (1973). The structures of the Bergell Alps. *Eclogae Geologicae Helvetiae*, **66**, 255–291.

Wenk, H. (1982). A geological history of the Bergell granite and related rocks. *In: Transformists petrology. Theophrastus publications Athens*, pages 113–148.

Wenk, H. (1986). Introduction to the geology of the Bergell Alps with Guide for Excursions. *Jber. Natf. Ges. Graubünden*, **103**, 29–90.

Wenk, H. (1992). Note esplicative. Foglio 70: Sciora. Servizio idrologico e geologico nazionale, 61pp.

Wenk, H. and Cornelius, S. (1977). Geologischer Atlas der Schweiz, 1:25'000, Blatt Sciora. Publ. Schweiz. Geol. Kommission.

Wenk, H., Wenk, E., and Wallace, J. (1974). Metamorphic mineral assemblages in pelitic rocks of the Bergell Alps. *Schweizerische Mineralogische und Petrographische Mitteilungen*, **54**, 507–554.

Wenk, H., Hsiau, J., Flowers, G., Weibel, M., Ayranci, B., and Fejér, Z. (1977). A geochemical survey of granitic rocks in the Bergell Alps. *Schweizerische Mineralogische und Petrographische Mitteilungen*, **57**, 233–265.

Wenk, H.-R. (1970). Zur Regionalmetamorphose und Ultrametamorphose der Zentralalpen. *Fortschritte der Mineralogie*, **47**, 34–51.

White, R. and Powell, R. (2002). Melt loss and the preservation of granulitie facies mineral assemblages. *Journal of Metamorphic Geology*, **20**, 621–632.

White, R., Powell, R., and Clarke, G. (2002). The interpretation of reaction textures in Fe-rich metapelitic granulites of the Musgrave Block, central Australia: constraints from mineral equilibria calculations in the system K_2O-FeO-MgO-Al_2O_3-SiO_2-H_2O-TiO_2-Fe_2O_3. *Journal of Metamorphic Geology*, **20**, 41–55.

White, R., Powell, R., and Holland, T. (2007). Progress relating to calculation of partial melting equilibria for metapelites. *Journal of Metamorphic Geology*, **25**, 511–527.

Wiedenbeck, M., Alle, P., Corfu, F., Griffin, W., Meier, M., Oberli, F., Von Quadt, A., Roddick, J., and Spiegel, W. (1995). Three natural zircon standards for U-Th-Pb, Lu-Hf, trace element and REE analyses. *Geostandards Newsletter*, **19**, 1–23.

Williams, I. (1998). U-Th-Pb geochronology by ion microprobe. *In: McKibben, M.A., Shanks, W.C. and Ridley, W.I. (Eds.): Applications of microanalytical techniques to understanding mineralizing processes. Reviews Economic Geology, 7*, pages 1–35.

Williams, I., Buick, S., and Cartwright, I. (1996). An extended episode of early Mesoproterozoic metamorphic fluid flow in the Reynolds Range, central Australia. *Journal of Metamorphic Geology*, **14**, 29–47.

Wilson, M., Neumann, E., Davies, G., Timmerman, M., Heeremans, M., and Larsen, B. (2004). Permo-Carboniferous magmatism and rifting in Europe. *Geological Society Special Publications*, **223**, 1–10.

Ziegler, P. (1993). Late Palaeozoic-Early Mesozoic plate reorganization: evolution and demise of the Variscan fold belt. *In: Von Raumer, J.F. and Neubauer, F. (eds): Pre-Mesozoic geology in the Alps. Springer, Berlin*, pages 203–216.

Zulbati, F. (2008). Structural and metamorphic evolution of the phengite-bearing schists of the northern Adula Nappe (Central Alps, Switzerland). *Geological Journal*, **43**, 33–57.

Appendix A

List of abbreviations

Mineral abbreviations

Abbr.	Mineral	Abbr.	Mineral	Abbr.	Mineral	Abbr.	Mineral
Ksp	Alkali feldspar	Cpx	Clinopyroxene	Opx	Orthopyroxene	Sph	Sphene
Amp	Amphibol	Crd	Cordierite	Pl	Plagioclase	Spl	Spinel
An	Anorthite	Crn	Corundum	Qtz	Quartz	Tc	Talc
Ap	Apatite	Ep	Epidote	Rut	Rutile	Tr	Tremolite
Bt	Biotite	Grt	Garnet	Spr	Sapphirine	Zrc	Zircon
Cc	Calcite	Ms	Muscovite	Serp	Serpentine		
Chl	Chlorite	Ol	Olivine	Sil	Sillimanite		

Other abbreviations used in the text

Structures

S	main foliation
L	lineation

Structures

S_{SZ}	plane of shearing
L_{SZ}	lineation on the plane of shearing

i

Appendix B

List of samples

Locality/sample	Swiss coordinates	Rocktype	Mineral assemblage
Bivacco Vaninetti			
HvGr1	763783 / 129783	Bt-orthogneiss	Qtz, Pl, Ksp, Bt, Chl, Zr, Ap, Ep, Tit, Ms (rare), opaques
HvGr2	763802 / 129731	2 mica granite	Qtz, Pl, Ksp, Bt, Ms, Chl, Ap, opaques
HvGr3	763833 / 129688	Bt-orthogneiss	Qtz, Pl, Ksp, Bt, Ms (rare), Chl, Grt (rare), Zr, Ap, opaques
HvGr4	764060 / 129425	leucogranite	Qtz, Pl, Ksp, Bt, Ms, Sil, Chl , opaques
HvGr5	764060 / 129425	Bt-orthogneiss	Qtz, Pl, Ksp, Bt, Ep, Ap, Zr, opaques
HvGr6	764060 / 129425	Bt-orthogneiss	Qtz, Pl, Ksp, Bt, Chl, Ms (rare)
HvGr7	764135 / 129063	retrogressed granite	Qtz, Pl, Ksp, Ms, Bt (rare), Chl, Sil (?), Ep, Zr, opaques
HvGr8	763742 / 129971	leucogranite	Qtz, Pl, Ksp, Bt, Sil, Ms, Chl
HvGr9	763952 / 129833	Bt-orthogneiss	Qtz, Pl, Ksp, Bt, Chl, Ap, Ep, Ms (rare), Zr
HvGr10	764001 / 129785	2 mica granite	Qtz, Pl, Ksp, Bt, Ms, Chl
HvGr11	763958 / 129395	Bt-orthogneiss	Qtz, Pl, Ksp, Bt, Ms (rare), Chl
HvGr12	763753 / 129330	2 mica granite	Qtz, Pl,Ksp, Bt, Ms, Chl, Ep, Zr
HvGr13	763790 / 129508	Bt-orthogneiss	Qtz, Pl, Ksp, Bt, Zr, Chl, Ep, Tit, opaques
HvGr14	763809 / 129350	Bt-orthogneiss	Qtz, Pl, Ksp, Bt, Ep, Chl , opaques
HvGr15	764135 / 129063	Bt-orthogneiss	Qtz, Pl, Ksp, Bt, Ep, Chl, Ap, Zrc, Rut/Tit, opaques
HvOG1	763960 / 129377	Bt-orthogneiss	Qtz, Pl, Ksp, Bt, Ep, Ap, Ms, Chl, Rut/Tit, Zrc, opaques
HvOG2	763979 / 129389	2 mica OG	Qtz, Pl, Ksp, Bt, Ms, Rut, Chl, Zr, opaques
HvOG3	763982 / 129357	leucogranite	Qtz, Pl, Ksp, Grt, Ms, Bt, Chl
HvOG5	764035 / 129375	leucogranite	Qtz, Pl, Ksp, Ms, Bt, Crd, Rut, Chl, Zr
HvPe1	763960 / 129377	metapelite	Qtz, Pl, Ksp, Bt, Ms, Chl, Sil, Ep, Ap, Rut, Zrc, Crd, opaques
HvPe2	763960 / 129377	metapelite	Qtz, Pl, Bt, Sil, Grt, Crd, Ms, opaques
HvPe3	764060 / 129425	metapelite	Qtz, Pl, Bt, Sil, Crd, Zrc, opaques
HvPe4	764060 / 129425	metapelite	Qtz, Pl, Ksp, Bt, Cor, Sil, Crd, Tit, Chl, Zrc, opaques
HvPe5	764079 / 129392	metapelite	Qtz, Pl, Bt, Grt, Sil, Crd, opaques
HvBa1	764021 / 129383	amphibolite	Amp, Pl, Qtz, Chl, Rut/Tit, opaques
HvBa2	764060 / 129370	migmatitic amphibolite	Amp: Amp, Pl, Qtz, Bt, opaques; melt: Qtz, Pl, Ksp, Bt, Amp, Ap, Zrc, opaques
HvBa3	764060 / 129370	amphibolite	Amp, Bt, Pl, Qtz, Zrc, opaques
HvBa4	763964 / 129419	amphibolite	Amp, Bt, Pl, Qtz, Chl, Rut, opaques
HvBa5	763964 / 129419	amphibolite	Amp, Bt, Chl, Ms (rare), Pl, Qtz, opaques
HvRo1	763946 / 129433	metarodingite	Grt, Ep, Di, Pl, Tit, Rut, Qtz
HvRo2	763940 / 129339	metarodingite	Grt, Ep, Di, Pl, Tit, Rut, Qtz
HvUM1	763915 / 129362	Ol-Tc-Tr fels	Ol, Tc, Tr (rare), Chl, opaques
HvUM2	763936 / 129367	Ol-Tc-Tr fels	Ol, Tr, Tc, Chl, opaques
HvSi1	763952 / 129833	Porphyric granite	Qtz, Pl, Ksp, Bt, Ms (rare), Ep, Chl, Zrc, opaques
HvSi2	763755 / 129356	Migmatitic paragneiss	Pl, Bt, Amp, Crd, Spl, Rut, Opx (?), Zr, opaques
HvBr1	763756 / 129728	Migmatitic paragneiss	Qtz, Pl, Ksp, Bt, Chl, Ms (rare), Crd, Ap, Zrc, opaques
HvBr2	763979 / 129389	Migmatitic paragneiss	Qtz, Pl, Bt, Chl, Grt, Amp, Ep, Ap, Rut, Zrc, opaques
HvBr3	764021 / 129383	Migmatitic paragneiss	Qtz, Pl, Ksp, Bt, Chl, Grt, Ep, Ap, Crd, Zrc, opaques
HvBr4	763935 / 129483	Migmatitic paragneiss	Qtz, Pl, Ksp, Bt, Chl, Grt, Ep, Ap, Spl, Crd, opaques
HvBr5	763935 / 129483	Migmatitic metapelite	Qtz, Pl, Ksp, Bt, Chl, Ms (rare), Grt, Sil, Crd, Zrc, opaques
Hv1	764441 / 129153	Bt-orthogneiss	Qtz, Pl, Ksp, Bt, Ep, Chl, Ap, opaques
Hv2	764282 / 129183	Paragneiss	Qtz, Pl, Grt, Bt, Chl, Zr, Rut
Hv3	764282 / 129183	?	Qtz, Pl, Bt, Ms, Chl, Sil, Crd, Zrc, rut/tit, opaques
Hv4	764259 / 129204	2 mica granite	Qtz, Pl, Ksp, Bt, Ms, Chl, Ep, opaques
Hv5	763964 / 129419	Bt-orthogneiss	Qtz, Pl, Ksp (?), Bt, Chl, Ep, Rut/Tit, opaques
Hv6	763964 / 129419	2 mica granite	Qtz, Pl, Ksp, Bt, Ms, Chl, Ep, Zr, opaques
Hv7	763821 / 129346	metapelite	Qtz, Pl, Grt, Bt, Sil, Crd, Tit/Rut, opaques
Hv8	763623 / 129084	Sivigia (?)	Qtz, Pl, Bt, Amp
Valle dei Vanni			
VaWh1	762869 / 130060	Websterite	Opx, Cpx, Amp, Bt, Tc (late), opaques
VaMa1	763024 / 130193	Retrosgrssed Websterite	Cpx, Amp, Pl, Bt, Tit, Cc
VaUM1	763283 / 130461	Retrogressed Websterite	
VaUM2	763374 / 130448	Websterite	Opx, Cpx, Bt, Amp, Tc, Chl, Pl, opaques
VaCh1	763283 / 130461	?	Qtz, Pl, Bt, Chl, Amp, Cc, Ap,opaques
Val Bondasca			
BoGr1	765561 / 131978	opx-granitoid	Qtz, Pl, Ksp, Opx, Bt, Amp, Chl, Ep, Zr, opaques
BoGr2	766369 / 132032	Bt-orthogneiss	Qtz, Pl, Ksp, Bt, Ms (rare), Grt (rare), Ep, Ap, Zr, opaQtzue
BoUM1	765457 / 131741	Websterite	Cpx, Amp, Tc, Bt, Opx, opaques
Bo1	763941 / 132225	Leucogranite	Qtz, Pl, Ksp, Bt, Ms, Chl, Sil (?), Ap
Bo2	763941 / 132225	Leucogranite	Qtz, Pl, Ksp, Bt, Ms, Sil, Rut, Ap, opaques
Bo3	763941 / 132225	UM	Serp, Ol, Spl, Tc, Tr, yellow mineral (?), opaques
Bo4	763941 / 132225	UM	Ol, Tr, Tc, Chl, Spl, opaques
Bo5	763941 / 132225	Migmatiti metapelite	Qtz, Pl, Ksp, Bt, Ms, Sil, Grt (rare), Chl (rare), Ap, Rut, Zrc, opaques
Bo6	763958 / 132136	Bt-orthogneiss	Qtz, Pl, Ksp, Bt, Ms, Chl, Ap, Zrc, opaques
Bo7	764219 / 131117	opx-granitoid	Qtz, Pl, Ksp, Bt, Opx, Amp, Chl, opaques
Bo8	764133 / 131043	Retrogressed Websterite	Opx, Cpx, Bt, Tc, Amp, opaques

List of samples

Locality/sample	Swiss coordinates	Rocktype	Mineral assemblage
Val Bondasca			
BoGr1	765561 / 131978	opx-granitoid	Qtz, Pl, Ksp, Opx, Bt, Amp, Chl, Ep, Zr, opaques
BoGr2	766369 / 132032	Bt-orthogneiss	Qtz, Pl, Ksp, Bt, Ms (rare), Grt (rare), Ep, Ap, Zr, opaQtzue
BoUM1	765457 / 131741	Websterite	Cpx, Amp, Tc, Bt, Opx, opaques
Bo1	763941 / 132225	Leucogranite	Qtz, Pl, Ksp, Bt, Ms, Chl, Sil (?), Ap
Bo2	763941 / 132225	Leucogranite	Qtz, Pl, Ksp, Bt, Ms, Sil, Rut, Ap, opaques
Bo3	763941 / 132225	UM	Serp, Ol, Spl, Tc, Tr, yellow mineral (?), opaques
Bo4	763941 / 132225	UM	Ol, Tr, Tc, Chl, Spl, opaques
Bo5	763941 / 132225	Migmatiti metapelite	Qtz, Pl, Ksp, Bt, Ms, Sil, Grt (rare), Chl (rare), Ap, Rut, Zrc, opaques
Bo6	763958 / 132136	Bt-orthogneiss	Qtz, Pl, Ksp, Bt, Ms, Chl, Ap, Zrc, opaques
Bo7	764219 / 131117	opx-granitoid	Qtz, Pl, Ksp, Bt, Opx, Amp, Chl, opaques
Bo8	764133 / 131043	Retrogressed Websterite	Opx, Cpx, Bt, Tc, Amp, opaques
Denc dal Luf			
DLOG1	762750 / 131148	Bt-orthogneiss	Qtz, Pl, Ksp, Bt, Chl, Ep, Zrc
DLUM1	762718 / 131403	Ol-Tc-Tr fels	Ol, Tc, Tr, Chl, opaques
DL1	762718 / 131403	Bt-orthogneiss	Qtz, Pl, Ksp, Bt, Ep, Zrc
DL2	762782 / 131614	metapelite	Qtz, Pl, Bt, Sil, Crd (?), Ms, Tit, Chl
DL3	762782 / 131614	Amp-bearing gneiss	Qtz, Pl, Amp, Bt, Tit, Ep
DL4	762782 / 131614	submylonitic gneiss	Qtz, Pl, Bt, Ms, Chl
DL5	763640 / 131901	Bt-orthogneiss	Qtz, Pl, Ksp, Bt, Ms, Chl, Ep, Zrc, opaques
DL6	763597 / 131578	Basica	Amp, Pl, Bt, Rut, Ap, Crd (???), opaques
DL7	763382 / 130917	Migmatitic metasediment	Qtz, Pl, Ksp, Bt, Grt, Chl, Ap, Zrc, opaques
DL8	763382 / 130917	Migmatitic metasediment	Qtz, Pl, Ksp, Bt, Ms (rare), Grt, Ep
DL9	763382 / 130917	Migmatitic metasediment	Qtz, Pl, Ksp, Bt, Grt, Ep
DL10	762296 / 131232	Leucogranite	Qtz, Pl, Ksp, Bt, Ms, Sil, Ap, Chl (rare), Zrc
DL11	762296 / 131232	amphibolite	Amp, Pl, Qtz, Bt, Tit, Ep, opaques
DL12	762195 / 131174	Leucogranite	Qtz, Pl, Ksp, Bt, Ms, Grt, Sil (rare), Ap, Zrc
DL13	762106 / 131208	Migmatitic metapelite	Qtz, Pl, Ksp, Bt, Ms (rare), Sil, Crd (?), Chl (rare), Ap, opaques
DL14	761618 / 131417	Migmatitic metapelite	Qtz, Pl, Ksp, Bt, Ms (rare), Sil, Crd, Ap, Chl, opaques
Upper Val Casnaggina			
Te1	761872 / 130368	Amp-bearing granitoid	Qtz, Pl, Ksp, Bt, Amp, Chl, Ep, Ap, Zr, opaques
Te2	761883 / 130356	Grt-bearing granitoid (?)	Qtz, Pl, Ksp, Bt, Grt, Ms, Zrc, Ap, opaques
TeGr1	761298 / 130315	Amp-bearing granitoid	Qtz, Pl, Ksp, Bt, Chl, Amp, Tit, Ep, Ap, Zrc, opaques
TeGr2	761400 / 130037	Bt-orthogneiss	Qtz, Pl, Ksp, Bt, Ep, Ap, Rut, opaques
TeGr3	762604 / 130650	2 mica granite	Qtz, Pl, Ksp, Bt, Ms, Chl, Ap, Zrc
TeGr4	762536 / 130692	Bt-orthogneiss	Qtz, Pl, Ksp, Ep, Bt, Chl, Zrc, opaques
TeGr5	761871 / 131108	liQtzuides from metapelites	Qtz, Pl, Ksp, Bt, Ms, prismatic Sil, Grt
TeCh1	761500 / 129887	retrogressed opx-granitoid	Qtz, Pl, Ksp, Bt, Chl, Grt, opaques
TeCh2	761438 / 129979	retrogressed opx-granitoid	Qtz, Pl, Ksp, Grt, Bt, Chl, Ms (rare), Ap, Ep, Zrc, opaques
TeCh3	762095 / 130197	2 mica granite	Qtz, Pl, Ksp, Bt, Ms, Grt (rare), Chl, Ep, Ap, Zrc, opaques
TeCh4	762237 / 130240	opx-granitoid	Qtz, Pl, Ksp, Grt, Opx, Bt, Ap, Zrc, opaques
TeCh5	762628 / 130613	opx-granitoid	Qtz, Pl, Ksp, Grt, Opx, Rut, Bt, Zrc, Chl, opaques
Alpe Spluga			
SpUM1	760858 / 129691	Tr-Tc-Ol Fels	Ol, Tr, Tc, Chl, Serp, Spl, opaques
SpCh1	760869 / 129592	opx-granitoid	Qtz, Pl, Ksp, Bt, Grt, Opx, Chl, opaques
SpCh2	760869 / 129592	retrogressed opx-granitoid	Qtz, Pl, Ksp, Grt, Bt, Chl, Amp, opaques
SpMa1	760460 / 129798	amphibolite	Amp, Pl, Cpx, Rut, Tit, Hm, opaques
SpPe1	760472 / 129788	Migmatitic paragneiss	Qtz, Pl, Ksp, Bt, Chl, Grt, Sil, Crd, Rut, opaques
Alpe Rosaccio			
RoBa1	759444 / 129655	amphibolite	Amp, Pl, Qtz, Bt, Chl, Ap, opaques
RoBa2	759444 / 129655	amphibolite	Amp, Qtz, Pl, Bt, opaques
RoLe1	759490 / 129603	leucogranite	Qtz, Pl, Ksp, Grt, Sil, Bt, Crd, Tit, Zrc, opaques
RoPe1	759490 / 129603	migmatitic metapelite	Qtz, Pl, Ksp, Bt, Grt, Sil, Crd, Ep, Zr, opaques
RoPe2	758827 / 129964	migmatitic metapelite	Qtz, Pl, Ksp (?), Bt, Sil, Ms, Crd
RoPe3	758954 / 129432	migmatitic metapelite	Qtz, Pl, Ksp (?), Bt, Grt, Sil, Crd (?), Tit, Zrc, opaques
RoPe4	759031 / 129360	migmatitic metapelite	Qtz, Pl, Ksp (?), Bt, Grt, Sil, Crd (?), Tit, Zrc, opaques
RoCh1	?	opx-granitoid	Qtz, Pl, Ksp, Bt, Opx, Grt, Chl, Zrc, opaques
RoCh2	759843 / 129466	Migmatitic Paragneis	Qtz, Pl, Ksp, Bt, Grt (rare), Zrc, Chl, Ap, opaques
RoCh3	759888 / 129536	Bt-orthogneiss	Qtz, Pl, Ksp, Bt, Chl, Ep, Zrc, Ap, opaques
RoCh4	759052 / 129299	opx-granitoid	Qtz, Pl, Ksp, Bt, Grt, Opx, Amp, Rut, Ap, Zrc, Chl, opaques
RoCh5	759173 / 129319	Bt-orthogneiss	Qtz, Pl, Ksp, Bt, Chl, Ms, Zr, Rut/Tit, opaques
RoCh6	759173 / 129319	Migmatitic metapelite	Qtz, Pl, Ksp, Bt, Ms, Grt, Sil, opaques
RoGr1	758872 / 129928	2 mica gneiss	Qtz, Pl, Ksp, Bt, Ms, Chl, Zrc, opaques
RoGr2	758823 / 129870	Leucogranite	Qtz, Pl, Ksp, Bt, Ms, Sil, Zrc
RoGr3	759833 / 129617	Leucogranite	Qtz, Pl, Ksp, Bt, Ms, Grt, Sil, Chl, Ap, Zrc,

Locality/sample	Swiss coordinates	Rocktype	Mineral assemblage
Alpe Rosaccio			
Ro1	758823 / 129870		
Ro2	758930 / 129504	Migmatitic metapelite	Qtz, Pl, Ksp (?), Bt, Grt, Sil, Crd (?), Chl, Zrc, opaques
Ro3	758930 / 129504	Paragneiss	Qtz, Pl, Grt, Bt, Chl (rare), Turm, Ap, opaques
Ro4	759805 / 129629	Leucogranite	Qtz, Pl, Ksp, Bt, Grt, Chl, opaques
Ro5	759031 / 129360	Leucogranite	Qtz, Pl, Ksp, Bt, Ms, Grt, Sil (?), Chl, Rut, Zrc, opaques
Cima di Droso			
DrGr1	758599 / 129757	2 mica granite	Qtz, Pl, Ksp, Bt, Ms, Chl, Zr, opaques
DrGr2	758410 / 130088	Bt-orthogneiss	Qtz, Pl, Ksp, Bt, Chl, Ap
DrGr3	758023 / 131009	2 mica granite (OG)	Qtz, Pl, Ksp, Bt, Ms, Chl, Grt, Ep
DrPe1	758467 / 129729	metapelite	Qtz, Pl, Ksp, Bt, Grt, Sil, Crd (?), Chl, Rut/Tit, Ap
Val Aurosina			
PeGr1	758873 / 129353	Bt-orthogneiss	Qtz, Pl, Ksp, Bt, Rut/Tit, Ap, opaques
PeGr2	756569 / 128664	Leucogranite	Qtz, Pl, Ksp, Bt, Ms (rare), Chl, Grt, Ap, Zrc
PeGr3	758153 / 129875	Bt-orthogneiss	Qtz, Pl, Ksp, Bt, Chl, Ap, Ep, Rut/Tit
PeGr4	758152 / 129848	Bt-orthogneiss	Qtz, Pl, Ksp, Bt, Chl, Ap, Rut, Zrc, opaques
PeGr5	758306 / 128557	Amp-bearing granitoid	Qtz, Pl, Ksp, Bt, Amp, Ap, Zrc, opaques
PeGr6	757959 / 128235	Leucogranite	Qtz, Pl, Ksp, Bt, Grt, Zrc, opaques
PeGr7	756317 / 128791	Leucogranite	Qtz, Pl, Ksp, Bt, Grt, Sil, Spl
PeOG1	757787 / 129162	Granite	Qtz, Pl, Ksp, Bt, Ms, Ap, Zrc
PeOG2	758741 / 128288	Granite	Qtz, Pl, Ksp, Bt, Chl, Ep, Ap, Zrc, opaques
PeOG3	758222 / 129546	Granite	Qtz, Pl, Ksp, Bt, Ms, Chl, Ep, Ap, Rut, opaques
PeOG4	756703 / 129925	Paragneiss	Qtz, Pl, Ksp, Bt, Grt, Ms (rare), opaques
PeOG5	757200 / 128426	Migmatitic paragneis	Qtz, Pl, Ksp, Bt, Grt, Chl, Ap, Zrc, opaques
PeCh1	758535 / 128617	opx-granitoid	Qtz, Pl, Ksp, Bt, Grt, Opx, Amp, Ap, Rut/Tit, opaques
PeCh2	758741 / 128288	Bt-orthogneiss	Qtz, Pl, Ksp, Bt, Amp, Rut, Ap, Zrc, opaques
PeCh3	758741 / 128288	Amp-bearing Bt-orthogneiss	Qtz, Pl, Ksp, Bt, Amp, Rut, Ap, Zrc, opaques
PeCh4	758741 / 128288	?	Qtz, Pl, Ksp (?), Pyx, Amp, Tit, Ep, opaques
PeCh5	758741 / 128288	Bt-orthogneiss	Qtz, Pl, Ksp, Bt, Chl, Tit, Ap, Zrc, opaques
PeCh6	758873 / 129353	opx-granitoid	Qtz, Pl, Ksp, Bt, Grt, Opx, Chl, Zrc, opaques
PeCh7	757365 / 128111	Migmatitic paragneis	Qtz, Pl, Ksp, Bt, Grt, Chl, Ap, Tit, Ms (rare), opaques
PeCh8	757436 / 128533	Retrogressed opx-granitoid	Qtz, Pl, Ksp, Bt, Grt, Amp, Chl, Zrc, opaques
PeCh9	756450 / 128822	Migmatitic paragneis	Qtz, Pl, Ksp, Bt, Grt, Ap, opaques
PeCh10	756444 / 128880	Migmatitic paragneis	Qtz, Pl, Ksp (?), Bt, Grt, Chl, Ms, Amp, opaques
PeCh11	756444 / 128880	Migmatitic paragneis	Qtz, Pl, Ksp, Bt, Grt, Ms, opaques
PeCh12	758018 / 128178	Migmatitic paragneis	Qtz, Pl, Ksp, Bt, Grt, Chl, Ap, opaques
PeCh13	758057 / 128116	Migmatitic paragneis	Qtz, Pl, Ksp, Bt, Grt, Chl, Ms, Spl, opaques
PeCh14	758057 / 128116	Migmatitic pelite	Qtz, Pl, Ksp, Grt, Bt, Sil, Chl, Rut, opaques
PeCh15	757664 / 129211	Migmatitic paragneis	Qtz, Pl, Ksp, Bt, Grt, Ms, Chl, Zr, opaques
PeAm1	757697 / 129390	Bt-amphibolite	Amp, Bt, Pl, Ap, Ep (rare), opaques
PeBa2	758741 / 128288	Gabbro (?)	Amp, Pl, Bt, Cpx, Chl, opaques
PeBa3	756569 / 128664	Paramphibolites	Qtz, Pl, Bt, Amp, Grt, Ep, Rut, Chl, opaques
PeLs1	757796 / 129158	Leucosome from metapelites	Qtz, Pl, Ksp, Bt, Ms, Grt
PeLs2	756569 / 128664	opx-granitoid	Qtz, Pl, Ksp, Bt, Opx, opaques
PeLs3	756003 / 129069	Leucosome from metapelites	Qtz, Pl, Ksp, Bt, Grt, Sil, Ms
PePel1	758079 / 129725	Migmatitic metapelites	Qtz, Pl, Grt, Bt, Sil, Crd, Ms (rare), Rut, Zrc, opaques
PeMig1	758458 / 129444	Migmatitic metapelites	Qtz, Pl, Grt, Bt, Sil, Ms, Chl, Crd, Ep, Ap, Tur, opaques
PeGra1	758177 / 128547	Amp-bearing granitoid	Qtz, Pl, Bt, Amp (green),
PeGra2	758177 / 128547	Amp-bearing granitoid	Qtz, Pl, Bt, Amp (green),
PeGra3	758057 / 128116	Spr-bearing granulite	Qtz, Pl, Grt, Bt, Sil, Spl, Spr
PeGra4	758057 / 128116	Spr-bearing granulite	Qtz, Pl, Ksp (?), Bt, Grt, Sil, Spl, opaques
PeGra5	758057 / 128116		Qtz, Pl, Ksp, Bt, Grt, Sil, Spl, opaques
Pe1	755962 / 129361	Migmatitic metapelites	Qtz, Pl, Grt, Bt, Crd, Zr, Sil, opaques
Pe2	755962 / 129361	Grt - amphibolites	Amp, Qtz, Grt, Bt, Pl, Chl, Ru
Pe3	758471 / 129656	Bt-granitoid	Qtz, Bt, Pl, Tit, Zr, Ap, Ep, opaques
Pe5	758518 / 129627	Granulites	Bt, Amp, Opx, Spl, Crd, Spr
Pe6	758560 / 129606	amphibolite	Qtz, Pl, Ksp, Amp, Bt, Chl, opaques
Pe7	758560 / 129606	amphibolite	Qtz, Pl, Amp, Bt, opaques
Pe8	758609 / 129569	LiQtzuid? Diorite?	Qtz, Pl, Ksp, Amp(uncolored), Bt, Chl
Pe9	758609 / 129569	amphibolite	Qtz, Pl, Amp, Bt, opaques
Pe10	758120 / 129856	Grt-paragneiss	Qtz, Pl, Bt, Grt, Chl
Pe11	758232 / 128340	Granulites	Bt, Grt, Amp, Opx, Crd, Spl, Cor, Spr
Pe12	757906 / 128302	Grt-bearing liQtzuide	Qtz, Pl, Ksp, Bt, Grt, Chl , Tit
Pe13	757664 / 129211	migmatitic paragneiss	Qtz, Pl, Ksp, Bt, Ms, Grt, Tit, Rut, Chl
Pe14	756324 / 128812	Migmatitic paragneiss	Qtz, Pl, Ksp,Bt, Grt, Chl, Zr
Pe15	756324 / 128812	amphibolite	Amp, Tit, Bt, Pl
Pe16	756324 / 128812	amphibolite	Amp, Tit, Bt, Pl
Pe17	756317 / 128791	migmatitic paragneiss	Qtz, Pl, Ksp, Bt, Grt, Spl
Pe18	756317 / 128791	Bt-orthogneiss	Qtz, Pl, Ksp, Bt, Grt, Ap, opaques

Locality/sample	Swiss coordinates	Rocktype	Mineral assemblage
Val Aurosina			
Pe19	756258 / 128796	Paragneiss	Qtz, Pl, Bt, Amp, Grt (rare), Ap, Zrc, opaques
Pe20	756258 / 128796	amphibolites	Pl, Amp, Tit, Bt
Pe21	756258 / 128796	Amphibolite	Amp, Bt, Pl, Ep, Ap, Tit, opaques
Pe22	756258 / 128796	Amphibolite	Amp, Bt, Pl, Ep, Ap, Tit, opaques
Pe23	756215 / 128555	Leucogranite	Qtz, Pl, Ksp, Bt, Ms, Grt, Chl
Pe24	756135 / 128390	Paragneiss	Qtz, Pl, Ksp, Bt, Grt
Pe25	756035 / 128425	Paragneiss	Qtz, Pl, Ksp, Bt, Grt, Sil
Pe26	756035 / 128425	Paragneiss	Qtz, Pl, Ksp, Bt, Ms, Grt
Pe29	759138 / 128988	Aplit	Qtz, Pl, Ksp, Bt, Ms (rare), Grt (rare), Chl, Ap, opaques
Pe32	758983 / 129294	Diorit	Amp, Pl, Bt, Ep, Ap, opaques
Pe34	758877 / 129340	migmatitic paragneiss	Qtz, Pl, Ksp, Bt, Grt, Ms (rare), Crd (?), Zrc
Val Schiesone			
ScCh1	756056 / 127803	Charnokite	Qtz, Pl, Ksp, Bt, Grt, Opx, opaques
ScCh2	756056 / 127803	charnokitic melt and Grt-Bt rich restites	Qtz, Pl, Ksp, Bt, Grt, Opx, Zr, opaques
ScCh3	756056 / 127803	Charnockite	Qtz, Ksp, Pl, Bt, Px, Grt, Zr, opaques
ScCh4	756056 / 127803	Grt-bearing liQtzuid (charnockite ?)	Qtz, Pl, Ksp, Bt, Grt, opaques
ScCh5	756056 / 127803	Grt-Bt-Sil rich restite	Qtz, Pl, Bt, Grt, Sil, Spl, Ms (rare), Rut/Tit, opaques
ScCh6	755547 / 128828	Leucogranite	Qtz, Pl, Ksp, Grt, Bt, Opx, Zrc, Tit, opaques
ScPe1	755351 / 129034	migmatitic metapelite	Qtz, Pl, Ksp, Bt, Grt, Sil, Crd (?), Ms (rare), Rut/Tit, opaques
ScPe2	755537 / 128867	migmatitic metapelite	Qtz, Pl, Ksp, Grt, Bt, Sil, Crd, Tit, Zrc
Sc1	755788 / 128563	Sil-bearing leucogranite	Qtz, Pl, Ksp, Grt, Bt, Sil, Chl, Zrc
Sc13		Bt-orthogneiss	Qtz, Pl, Ksp, Bt, Ms (rare), Chl, Ap, Zr, opaques
Sc14		leucogranite	Qtz, Pl, Ksp, Bt, Ms (rare), Sil (rare), Grt, Ap, Zr, opaques
ScGr 1	755989 / 128257	Bt-orthogneiss	Qtz, Pl, Ksp, Bt, Ep, Ap, Chl, Zrc, opaques
BiGr1	754574 / 128454	leucogranite	Qtz, Pl, Ksp, Bt, Grt, Sil, Spl, Zrc, opaques
BiGr2	754574 / 128454	2 mica gneiss	Qtz, Pl, Ksp, Bt, Ms, Rut, opaques
ScUM1	755788 / 128563	Retrogressed Websterite	Pl, Bt, Cpx, Opx, Amp, Chl, opaques
ScUM2		Anth-Ol Fels	Ol, Chl, Tc, Cc, Anth, Serp, opaques
ScUM3		Tc-Ol Fels	Ol, Chl, Tc, Cc, Ti-KHum, Serp, opaques
ScUM4		Tc-Tr-Ol Fels	Ol, Chl, Tc, Tr, Ms, opaques
ScUM5		Tc-Tr-Ol Fels	Ol, Chl, Tc, Tr, Cc, opaques
ScUM6		Tc-Tr-Ol Fels	Ol, Chl, Tc, Tr, Ms, opaques
ScUM7		Tc-Tr-Ol Fels	Ol, Chl, Tr, Serp, Tc, Bt, Spl, opaques
Alpe Sivigia			
Si1	763089 / 128940	Magmatic breccia	Qtz, Pl, Ksp, Bt, Grt
Si2	763089 / 128940	Magmatic breccia	Qtz, Pl, Ksp, Bt, Grt
Si3	763089 / 128940	Magmatic breccia	Qtz, Pl, Ksp, Bt, Grt
Val Averta			
Av1	763511 / 126369	Bt-orthogneiss	Qtz, Pl, Ksp, Bt, Chl, Rut, Ms, Ep, Zrc, opaques
Av2	763511 / 126369	Gabbro	Amp, Pl, Qtz, Bt, Chl, opaques
Av3	763511 / 126369	Bt-orthogneiss	Qtz, Pl, Ksp, Bt, Chl, Tit, Ap, Zrc
Av4	763602 / 126649	Paragneiss	Qtz, Pl, Ksp, Bt, Chl, Grt, Ap, opaques
Av5	763273 / 126923	Bt-orthogneiss	Qtz, Pl, Ksp, Bt, Chl, Aln, Ep, Ap, Zrc, opaques
Av6	763207 / 126951	Bt-orthogneiss	Qtz, Pl, Ksp, Bt, Amp, Ap, Chl, Zrc, opaques
Av7	762987 / 126926	Bt-orthogneiss	Qtz, Pl, Ksp, Bt, Ap, Chl, Zrc, opaques
Av8	762921 / 126872	Bt-orthogneiss	
AvCh1	763575 / 126675	Paragneiss	Qtz, Pl, Ksp, Bt, Grt, Chl, Rut, Zrc, opaques
Lower Val Codera			
Co1	762636 / 128538	Bt-orthogneiss	Qtz, Pl, Ksp, Bt, Ms, Chl, Rut, Ap, Zrc, opaques
Val Scarrione			
Or1	752017 / 127008	Leucogranite	Qtz, Pl, Ksp, Grt, Sil, Ms (rare)
Or2	752410 / 126845	Migmatitic Paragneiss	Qtz, Pl, Ksp, Bt, Grt, Rut/Tit
Or3	752609 / 126762	Migmatitic Paragneiss	Qtz, Pl, Ksp, Bt, Ms, Grt
Or4	753174 / 126620	Retrogressed websterite	Amp, Bt, Hm, Tit, Opx (?), Cpx (?), Cc (?), opaques
Or5	753068 / 126616	Hbl-bearing bt-granitoid	Qtz, Pl, Ksp, Bt, Amp, Chl, Zrc, opaques
Or6	753514 / 126739	Hbl-bearing bt-granitoid	Qtz, Pl, Ksp, Bt, Amp, Ep, Rut/Tit, opaques
Or7	753632 / 126828	Leucogranite	Qtz, Pl, Ksp, Bt, Grt, Sil, Rut/Tit, opaques
Or8	754290 / 126524	Charnockite	Qtz, Pl, Ksp, Bt, Opx, Amp, Zrc, opaques

Locality/sample	Swiss coordinates	Rocktype	Mineral assemblage
Val Scarrione			
Or9	755071 / 126366	Leucogranite	Qtz, Pl, Ksp, Bt, Ms, Grt, Sil
Or10	755073 / 126380	Bt-granitoid	Qtz, Pl, Ksp, Bt, Ms (rare), Chl, Ep, Ap, Zrc, Rut/Tit, opaques
Or11	754690 / 126356	Bt-granitoid	Qtz, Pl, Ksp, Bt, Ms (very rare), Chl, Ep, Rut/Tit
Or12	753121 / 126588	Bt-granitoid	Qtz, Pl, Ksp, Bt, Ms (rare), Chl, Ep
Or13	752945 / 126428	Bt-granitoid Qtz, Pl, Ksp, Bt, Chl, Amp (?), Ap	
Or14	752546 / 126443	Migmatitic metasediment	Qtz, Pl, Ksp, Bt, Sil, Ep, Chl (rare), Rut/Tit
Valle del Conco			
Conc1	761142 / 128402	Retrogressed websterite	Pl, Amp, Bt, Chl, Rut, Ap, Tit, Tc, opaques
Conc2	760816 / 128634	Retrogressed websterite	Pl, Amp, Bt, Chl, Rut, opaques
Conc3	760944 / 128726	Meta-dunite	Ol, Serp, Opx (rare), opaques
Conc4	760927 / 128752	Hornblendite	Amp, Bt, Tit
Conc5	760579 / 128940	Charnockite	Qtz, Pl, Ksp, Bt, Opx, Cpx or Amp (?), Rut, opaques
Conc6	760560 / 128972	Charnockite	Qtz, Pl, Ksp; Bt, Opx; Grt
Conc7	760536 / 128998	Charnockite	Qtz, Pl, Ksp, Bt, Opx, Amp, Chl, opaques
Conc8	760317 / 129019	Migmatitic Paragneiss	Qtz, Pl, Ksp, Bt, Chl, Zrc
Conc9	760254 / 128946	Migmatitic Paragneiss	Qtz, Pl, Ksp, Bt, Chl, Zrc
Conc9B	760075 / 128585	Leucogranite	Qtz, Pl, Ksp, Bt, Grt, Chl, Zrc, opaques
Conc10	760173 / 128560	Websterite	Opx, Cpx, Bt, Pl, Amp, Rut/Tit, opaques
Conc11	760173 / 128560	Granulite	Qtz, Pl, Ksp, Bt, Opx, Grt, Spr, Sil, Crd, Spl, Zrc, opaques
Conc12	760173 / 128560	Granulite	Qtz, Pl, Ksp, Bt, Opx, Grt, Spr, Sil, Crd, Spl, Chl, Zrc, opaques
Conc13	760173 / 128560	Granulite	Qtz, Pl, Ksp, Bt, Opx, Grt, Spr, Sil, Crd, Spl, Ms (rare), opaques
Conc14	760173 / 128560	Charnockite	Qtz, Pl, Ksp, Bt, Opx, Grt, Spl, Sil, Chl, opaques
Conc15	760173 / 128560	Websterite	Opx, Cpx, Bt, Pl, Rut, opaques
Conc16	760861 / 128108	amphibolite + melt	Amp, Bt, Pl, Tit, Rut, opaques
Conc17	760813 / 127709	Tc-Tr-Ol-Fels	Ol, Tc, Tr, Chl, Serp, opaques
Conc18	760955 / 127797	Metapelite	Qtz, Pl, Ksp, Bt, Grt, Spl, Sil, Crd, Rut/Tit, opaques
Val Piana			
Pia1	760785 / 127212	Leucogranite	Qtz, Pl, Ksp, Bt, Grt, Spl, Sil, Chl (rare), Ms (rare)
Pia2	761011 / 127131	Leucogranite	Qtz, Pl, Ksp, Bt, Grt, Sil, Ms (rare), opaques
Pia3	761079 / 127081	Migmatite	Qtz, Pl, Ksp, Bt, Grt, Grt, Chl, Rut/Tit, Zrc
Pia4	761079 / 127081	Migmatite	Qtz, Pl, Ksp, Bt, Grt (rare), Chl, Ms, opaques
Pia5	761079 / 127081	Leucogranite	Qtz, Pl, Ksp, Bt, Grt, Ms, Sil (?), Chl, opaques
Pia6	761288 / 126933	Charnockite (?)	Qtz, Pl, Ksp, Bt, Chl, Grt (rare), opaques
Pia7	761288 / 126933	Charnockite (?)	Qtz, Pl, Ksp, Bt, Chl, opaques
Pia8	761377 / 126878	Charnockite	Qtz, Pl, Ksp, Bt, Grt, Opx, Sil, Spl, opaques
Pia9	760423 / 127917	Migmatitic paragneis	Qtz, Pl, Ksp, Bt, Ms, Chl, Grt, Sil (?), Rut, opaques
Pia10	760260 / 128039	Migmatitic metapelite	Qtz, Pl, Ksp, Bt, Ms, Chl, Grt, Sil, Crd, Rut, Ap, Zrc, opaques
Pia11	760138 / 128212	?	Qtz, Pl,Ksp, Bt, Chl, Ap, Ep, Zrc, opaques
Pia12	760138 / 128212	Charnockite	Qtz, Pl, Ksp, Bt, Chl, Opx, Ap, Zrc, opaques
Pia13	759652 / 128352	?	Qtz, Pl, Ksp, Bt, Grt, Chl, Ap, Rut, Zrc, opaques
Pia14	759772 / 128290	Charnockite	Qtz, Pl, Ksp, Bt, Grt, Opx, Chl, Ap, Zrc, opaques
Pia15	760004 / 128077	Retrogressed websteritte	
Pia16	760219 / 127726		
Pizzal			
Piz1	760124 / 127325	Migmatitic metapelite	Qtz, Pl, Ksp, Bt, Sil, Crd, Rut/Tit, Ms, Zrc
Piz2	760155 / 127255	Bt-orthogneiss	Qtz, Pl, Ksp, Bt, Rut/Tit, Ap, Zrc, opaques
Piz3	760173 / 127210	Retrogressed websterite	Amp, Opx, Tc, Pl, Rut, opaques
Piz4	760440 / 127036	Leucogranite (?)	Qtz, Pl, Ksp, Bt, Grt (rare), Chl, Ap, opaques
Rebbia			
Re1	751110 / 128518	Leucogranite	Qtz, Pl, Ksp, Bt, Ms, Sil (?)
Re2	751110 / 128518	Migmatitic metapelite	Qtz, Pl, Ksp, Bt, Grt, Sil, Crd, Rut/Tit, Zrc
Re3	751417 / 128321	Leucogranite	Qtz, Pl, Ksp, Bt, Grt, Sil, Ms (rare), Zrc
Re4	751502 / 128762		
Val Deserta			
De1	759357 / 126442	Leucogranite	Qtz, Pl, Ksp, Bt, Ms, Grt, Sil (rare), Chl (rare), opaques
De2	759086 / 126754	Migmatitic metapelite	Qtz, Pl, Ksp, Bt, Ms, Sil, Chl (rare), Zrc
De3	759147 / 127067	Retrogressed Websterite	Amp, Pl, Rut, Bt, Opx, Cpx, opaques
De4	759170 / 127104	Bt-orthogneiss	Qtz, Pl, Ksp, Bt, Chl, Zrc, opaques
De5	758643 / 127405	Hornblendite (?)	Amp, Tit, Ep
De6	758493 / 127487	Migmatitic paragneis	Qtz, Pl, Ksp, Bt, Grt, Crd (?), Chl (rare), Ep, Ap, Rut, opaques
De7	758808 / 127699	Charnockite (?)	Qtz, Pl, Ksp, Bt, Chl, Grt, Opx (?), Crd, Ep, Zrc, opaques

List of samples

Locality/sample	Swiss coordinates	Rocktype	Mineral assemblage
Val Salubiasca			
Sa1	759758 / 124843	Leucogranite	Qtz, Pl, Ksp, Bt, Ms, Chl (rare), Zrc, opaques
Sa2	758708 / 123655	Leucogranite	Qtz, Pl, Ksp, Bt, Ms, Ep, Zrc
Uschione			
US1	752768 / 131348	amphibolite	Amp, Pl, Tit, Ep (?), Rut, opaques
US2	754169 / 130199	Migmatitic metasediment	Qtz, Pl, Ksp, Bt, Ms (rare), Sil, Chl (rare), Rut/Tit
US3	754169 / 130199	amphibolite	Amp, Pl, Rut, opaques
US4	754169 / 130199	Leucogranite	Qtz, Pl, Ksp, Bt, Sil, Tit, Rut, Crd (?), Chl (rare), Zrc, opaques
US5	755172 / 129433	Leucogranite	Qtz, Pl, Ksp, Bt, Ms (rare), Sil, Rut
US6	755172 / 129433	Leucogranite	Qtz, Pl, Ksp, Bt, Ms, Grt, Sil, Crd (?), Ep
US7	755182 / 129439	Migmatitic paragneis	Qtz, Pl, Ksp, Bt, Grt, Chl (rare), Ms (rare), Rut/Tit
US8	755182 / 129439	Migmatitic metapelite	Qtz, Pl, Ksp, Bt, Grt, Sil, Crd (?), Ap, Zrc
US9	755182 / 129439	Migmatitic metapelite	Qtz, Pl, Ksp, Bt, Grt, Sil, Tit
US10	755127 / 129271	Migmatitic metapelite	Qtz, Pl, Ksp, Bt, Grt, Crd, Rut, Zrc, opaques
US11	755080 / 129359	Migmatitic metapelite	Qtz, Pl, Ksp, Bt, Sil, Ms (rare), Crd, Rut/Tit, Zrc
US12	754072 / 129897	amphibolite	Amp, Pl, Tit, Rut, Bt (rare), opaques
Lower Valle della Mera			
Max1	750513 / 128501	Leucogranite	Qtz, Pl, Ksp, Bt, Ms, Grt, Sil, Zrc
Max2	750513 / 128501	Bt-granitoid	Qtz, Pl, Ksp, Bt, Chl, Rut, Zrc, opaques
Max3	750590 / 128420	Migmatitic paragneis	Qtz, Pl, Ksp, Bt, Grt, Ms (rare), Chl (rare), Crd (?), Ap, Zrc, opaques
Max4	750625 / 128402	Migmatitic paragneis	Qtz, Pl, Ksp, Bt, Ms, Crd, Sil, Rut/Tit, Ap, Zrc, opaques
Max5	750625 / 128402	Migmatitic paragneis	Qtz, Pl, Ksp, Bt, Ms (rare), Grt (rare), Sil, Crd (?), Ap, Zrc, opaques
Max6	750649 / 128388	Leucogranite	Qtz, Pl, Ksp, Bt, Ms, Sil, Grt, Ap, Zrc

Samples location
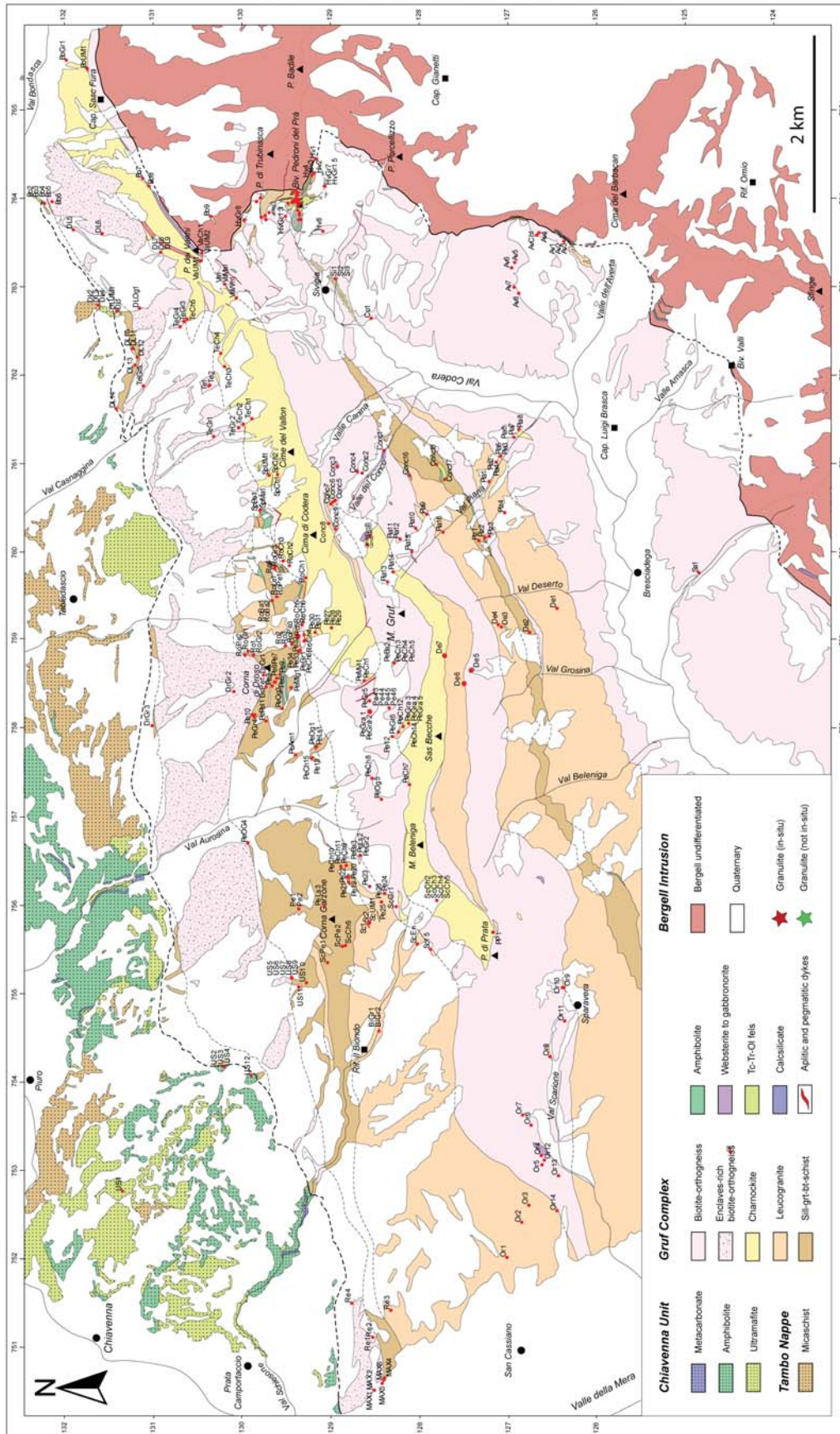
Samples location around Bivacco Vaninetti
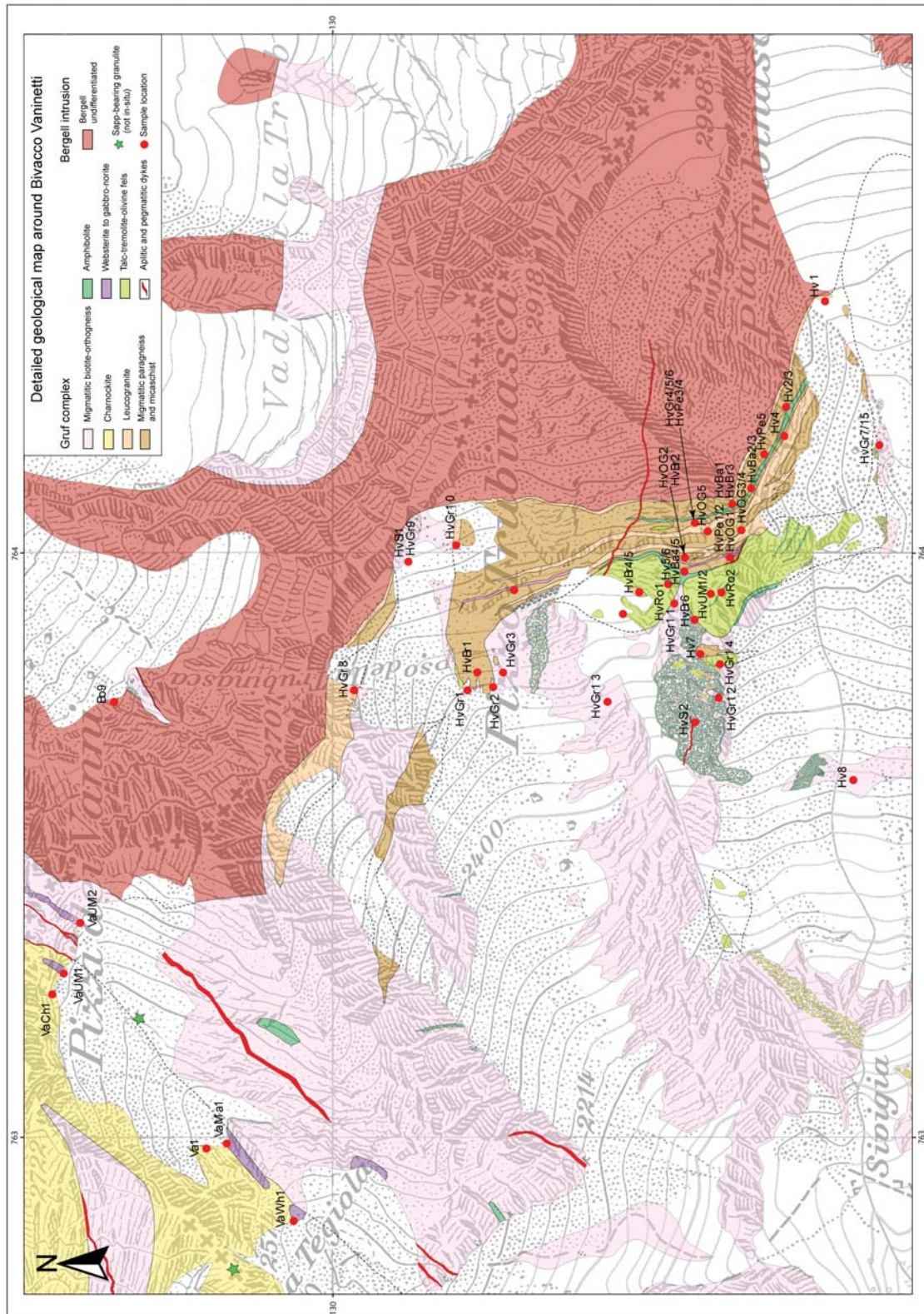
Appendix C

Mapping

The field work was performed during three summer field seasons (2006-2008), spring 2008 and several weekends during 2007 and 2008. Summer 2006 (ca. 2 months field work) was an explorative field season, focused on the identification of different types of granulites and comprehension of their local extension and geological context. Summer 2007 and 2008 (more than 5 month in total), were the main mapping seasons and consisted in the mapping of the middle and upper parts of the Gruf Complex. Both summer mapping were done together with Benjamin Le Bayon. His help, field experience and friendship have been fundamental to carry on day after day gaining the hostile Gruf. During spring 2008 and many weekends on 2007 and 2008, I mapped the lower part of the Gruf, profiting of the temporaneous partial lack of vegetation.

During field work, we sampled about 1 ton material. The most of the samples have been collected using a "Petrohammer" and a normal 1 kg hammer coupled with chisels. More tricky samples have been extracted using a motor saw. Mr. Rochin, Mr. Cotola, Mr. Ranzoni and Mr. Biavaschi are greatly thanks for their assistance during hard sampling. Mr. Rochin is also thanks for legendary sample transport by "Vespa" through Val Codera. Samples have been numbered according to their location and main lithological belonging. More than an half of the samples have been brought down by walking. The rest have been transported by helicopter.

All data points (e.g. field observations, sample description, structural data) have been positioned by satellite coordinates (Swiss grid CH-1903) and subsequently georeferenced on Arc-Gis software. Georeferenced data have been imported in Illustrator CS3 and, combined with field observations, satellite immages, field pictures and panoramas, used to draw the geological and structural maps. Structural data have been processed with the program "Spheristat 2.1c" (Pangaea Scientific) that allows the constructions of stereographic projections and averaged structural maps.

Appendix D

Analytical methods

D.1 Geochemical investigation: XRF and LA-ICP MS

110 fresh samples representing all rock types occurring in the Gruf complex have been analysed for major elements and 29 of them also for trace elements. First, a saw was used to reduce samples in size and to remove weathering and organic parts. Subsequently, samples were reduced using a hydraulic press in a stainless-steel braker and grinded to powder with an agate mill. Major and trace elements analysis were performed on fused glass-beads prepared from rock powder mixed with Lithium-Tetraborate (1:5 in proportion) with a Claisse M4® fluxer. About 1.5 g rock powder were mixed together with 7.5 g Lithium-Tetraborate.

Major elements were analysed uisng a Panalytical Axios wavelength dispersive XRF spectrometer (WDXRF, 2.4 KV). Samples were analysed for SiO_2, TiO_2, Al_2O_3, Fe_2O_3, MnO, MgO, CaO, Na_2O, K_2O, P_2O_5, Cr_2O_3 and NiO. H_2O content was estimated from loss of ignition (LOI) occurred during glass-bead preparation. Analysis were calibrated on the basis of ca. 40 certified internetional standards. Minor and trace elements in whole rocks were analysed with a Elan 6000 laser-ablation microsampler coupled to an inductively plasma mass spectrometer on glass-beads. Samples were analysed for Li, S, Sc, V, Co, Ni, Cu, Zn, As, Rb, Sr, Y, Zr, Nb, Ag, Sb, Cs, Ba, La, Ce, Pr, Nd, Sm, Eu, Gd, Tb, Dy, Ho, Er, Tm, Yb, Lu, Hf, Ta, Pb, Th, U.

Sincere thanks are given to Pierre Bouilhol for his helpfull explanations during crushing process and to Lidya Zhender and Peter Ulmer for rapid XRF measurements.

D.2 Mineral chemistry investigation: EMS

Mineral chemical compositions were obtained using a "JEOL-8200 WDS/EDS microanalyser" microprobe. Operating conditions for spot analyses were 15 kV accelerating voltage, 20 nA sample current, 40 s counting time and beam size ≤ 5 μm. Natural and synthetic standards were used for calibration. Minerals were analysed for SiO_2, TiO_2, Cr_2O_3, Al_2O_3, FeO, MnO, MgO, CaO, Na_2O, K_2O. Fe^{3+} was calculated from charge balance. Ferric iron in sapphirine was estimated using the approach of Higgins *et al.* (1979): $^{VI}Fe^{3+} = {}^{IV}Al^{3+} - ({}^{VI}Al + Cr^{tot})$.

D.3   Geochronological investigation: SHRIMP

Zircon grains separated from 15 samples representing the most important granitoidic rock types of the Gruf Complex were analysed. Zircon separation thecniques and analytical procedures are largely explained in section 5.3.1.

Appendix E

XRF Analysis

Table E1: Bulk rock XRF data of migmatitic biotite-orthogneiss; major elements in wt-%, trace elements in ppm.

	Migmatitic biotite-orthogneiss												
Sample	ScGr1	PeGr1	PeGr5	Pe46	HvGr1	HvGr 3	HvGr5	HvGr6	HvGr9	HvGr11	HvGr12	HvGr13	HvGr14
SiO_2	66.09	65.58	68.75	68.88	51.96	70.73	59.00	67.51	68.24	72.15	69.32	68.36	52.43
TiO_2	0.59	0.66	0.45	0.51	0.99	0.38	0.94	0.43	0.45	0.24	0.49	0.45	0.99
Al_2O_3	16.12	15.26	15.31	15.2	22.95	14.77	17.31	16.57	15.93	14.83	15.43	15.85	22.31
Fe_2O_3[1]	4.47	4.74	3.5	3.63	5.31	2.92	6.68	3.06	3.52	1.48	3.57	3.48	6.15
MnO	0.07	0.08	0.08	0.08	0.04	0.05	0.09	0.05	0.08	0.02	0.05	0.06	0.05
MgO	1.07	2.44	1	1.57	3.23	0.8	3.39	1.17	1.38	0.8	1.26	0.85	3.11
CaO	3.01	2.84	2.83	2.55	5.88	1.99	4.68	3.1	3	2.73	3.18	3.07	6.05
Na_2O	3.78	3.23	3.72	3.71	4.94	3.29	3.46	5.29	4.89	4.29	4.29	3.62	4.75
K_2O	3.72	2.74	3.62	2.68	2.93	4.18	2.68	1.51	1.53	1.89	1.53	3.52	2.55
P_2O_5	0.24	0.27	0.16	0.13	0.56	0.12	0.61	0.12	0.15	0.04	0.12	0.15	0.42
Cr_2O_3	0	0.01	0	0.01	0.01	0	0.01	0	0	0	0	0	0.01
LOI[2]	0.47	0.83	0.37	0.67	0.86	0.73	0.79	0.35	0.5	0.51	0.47	0.39	0.66
Total	99.63	98.68	99.79	99.62	99.66	99.96	99.64	99.17	99.67	98.99	99.73	99.79	99.49
Rb	108	142	102	103	135	87	123	78	59	59	50	99	135
Ba	1031	422	777	466	1086	1171	1007	222	472	618	473	1157	925
Sr	300	169	267	198	832	257	418	247	350	336	321	276	530
Nb	15	15	12	14	10	7	15	12	9	6	12	13	14
Zr	295	188	191	161	353	218	231	209	121	156	160	250	398
Hf	6	5	5	5	8	5	5	5	4	4	4	6	8
Y	20	29	28	45	23	22	26	19	13	7	39	23	21
Ga	23	22	18	20	34	20	25	22	19	17	21	20	31
Zn	74	73	73	60	101	48	91	57	61	30	56	61	119
Cu	8	19	8	12	18	4	30	8	10	6	3	7	25
Ni	9	44	5	22	22	6	24	8	11	16	10	5	26
Co	7	11	8	7	15	2	19	7	6	6	6	4	19
Cr	4	79	8	42	41	5	40	10	18	10	13	4	53
V	49	83	50	63	102	33	151	34	48	19	45	44	107
Sc	11	12	9	12	11	8	15	8	6	5	9	9	13
La	38	29	29	36	24	34	25	61	11	22	27	52	48
Ce	58	58	39	67	40	34	40	130	11	9	44	61	94
Nd	24	24	18	28	18	16	18	50	8	7	20	26	37
Pb	13	19	18	18	27	15	18	24	11	33	170	15	18
Th	7	9	1	14	2	3	3	31	4	8	7	8	13
U	0	0	0	3	0	0	0	0	2	0	0	0	0

[1] Fe_2O_3 is total iron

[2] LOI: Loss on ignition

Table E2: Bulk rock XRF data of migmatitic biotite-orthogneiss; major elements in wt-%, trace elements in ppm.

Sample	Migmatitic biotite-orthogneiss											
	HvGr15	TeGr1	TeGr2	TeGr3	TeGr4	TeCh3	BoGr2	Or6	Or10	Or11	Or12	Piz2
SiO_2	66.31	64.16	66.99	67.69	66.69	67.82	59.93	65.21	63.66	70.17	65.94	68.01
TiO_2	0.64	0.72	0.45	0.38	0.62	0.48	0.87	0.61	0.72	0.35	0.5	0.46
Al_2O_3	16.2	16.58	15.82	16.5	15.93	15.35	18.59	16.46	17.28	14.88	16.09	15.72
Fe_2O_3[1]	4.57	5.09	3.94	2.44	4.47	4.14	6.24	4.48	5.06	2.67	4.39	3.6
MnO	0.09	0.09	0.07	0.04	0.05	0.08	0.09	0.07	0.07	0.06	0.08	0.05
MgO	1.89	1.37	1.44	0.86	1.21	1.63	1.74	1.5	1.33	0.66	1.69	0.95
CaO	3.25	3.7	3.19	2.95	3.21	2.85	4.51	3.61	3.72	2.36	3.79	3.2
Na_2O	4.25	4.43	3.81	4.09	4.11	3.46	4.33	3.82	4.34	3.56	3.62	3.84
K_2O	2.11	2.48	2.91	3.51	2.37	2.79	2.34	3.21	2.31	3.85	2.08	2.83
P_2O_5	0.17	0.26	0.18	0.15	0.19	0.12	0.42	0.23	0.26	0.12	0.15	0.16
Cr_2O_3	0	0	0	0	0	0	0	0	0	0	0.01	0
LOI[2]	0.46	0.49	0.65	0.93	0.58	0.71	0.64	0.47	1.12	0.55	1.1	0.49
Total	99.94	99.37	99.44	99.54	99.43	99.44	99.72	99.69	99.87	99.23	99.44	99.3
Rb	101	111	91	152	90	86	101	95	106	153	76	76
Ba	462	510	591	687	1004	648	591	1078	713	730	487	1229
Sr	320	289	246	392	319	251	385	346	378	230	298	301
Nb	18	23	10	9	16	11	18	12	17	14	12	8
Zr	197	324	154	212	355	159	300	236	330	179	184	245
Hf	4	6	4	5	7	5	6	6	7	5	5	7
Y	28	31	28	13	39	26	36	25	27	19	19	19
Ga	21	23	16	23	20	19	26	20	25	20	22	17
Zn	75	84	58	56	64	57	98	63	90	49	64	58
Cu	11	6	4	2	6	13	20	10	6	7	37	8
Ni	10	7	9	7	11	17	10	11	10	9	31	8
Co	12	7	9	6	8	8	13	8	13	11	6	9
Cr	15	6	16	1	8	28	8	11	10	8	40	5
V	54	67	57	26	53	56	86	68	67	33	65	43
Sc	11	14	8	6	9	11	16	10	9	5	9	9
La	32	56	20	35	120	34	28	29	53	37	50	42
Ce	49	107	26	46	197	42	62	34	93	56	85	38
Nd	21	42	13	20	73	19	26	16	37	24	34	17
Pb	16	15	14	43	17	20	19	12	14	20	13	14
Th	7	11	3	18	43	9	4	4	7	11	12	4
U	0	0	1	0	0	0	0	0	0	0	1	0

---

[1] Fe_2O_3 is total iron

[2] LOI: Loss on ignition

Table E3: Bulk rock XRF data of enclave-rich biotite orthogneiss and charnockite; major elements in wt-%, trace elements in ppm.

| Sample | **Enclave-rich biotite orthogneiss** | | | | | | **Charnockite** | | | | | |
	Sc13	PeGr3	DrGr2	DLOG1	Max2	Re4	SpCh1	ScCh1	ScCh2	ScCh3	RoCh1	RoCh4
SiO_2	66.45	67.17	70.58	67.47	67.53	70.59	65.75	72.39	62.28	61.49	66.35	69.38
TiO_2	0.58	0.50	0.29	0.48	0.44	0.33	0.61	0.28	0.72	0.72	0.55	0.42
Al_2O_3	15.98	16.27	15.21	16.01	16.04	15.08	16.05	14.28	18.87	18.38	16.21	15.83
Fe_2O_3[1]	4.12	3.70	2.24	3.54	3.37	2.27	5.42	2.14	5.41	5.75	4.81	3.21
MnO	0.06	0.06	0.04	0.05	0.06	0.05	0.11	0.01	0.06	0.07	0.09	0.07
MgO	1.03	1.50	0.83	0.91	1.26	0.90	2.22	0.51	1.55	1.68	1.56	0.94
CaO	3.02	3.49	2.22	3.26	2.95	2.22	3.27	1.48	4.60	4.78	3.48	3.05
Na_2O	3.77	4.78	4.06	3.60	4.73	3.79	3.18	2.51	4.10	4.08	3.44	3.89
K_2O	3.52	1.63	3.44	3.55	2.28	3.75	2.34	6.13	2.63	1.98	2.70	2.51
P_2O_5	0.27	0.17	0.09	0.16	0.22	0.05	0.18	0.12	0.36	0.34	0.19	0.11
Cr_2O_3	0.00	0.00	0.00	0.00	0.00	0.00	0.01	0.00	0.00	0.00	0.00	0.00
LOI[2]	0.62	0.60	0.37	0.49	0.75	0.47	0.47	0.31	0.24	0.29	0.49	0.31
Total	99.42	99.87	99.37	99.51	99.64	99.50	99.58	100.15	100.82	99.55	99.88	99.72
Rb	134	52	79	107	76	104	51	188	110	57	79	54
Ba	1173	662	879	1357	531	948	569	1468	674	656	806	593
Sr	327	388	353	306	365	271	251	270	384	366	275	322
Nb	18	4	7	14	9	9	20	7	18	13	16	12
Zr	306	170	115	296	90	195	165	174	335	344	199	242
Hf	6	4	4	6	3	6	4	5	8	7	6	6
Y	27	13	14	16	16	14	33	14	33	37	24	37
Ga	23	22	19	23	22	19	19	16	24	25	22	18
Zn	74	62	49	59	57	36	67	39	92	94	71	28
Cu	7	13	5	5	13	5	17	7	14	15	13	7
Ni	7	11	10	6	11	8	14	11	14	12	12	7
Co	8	10	6	7	5	8	10	6	9	9	8	6
Cr	5	11	8	6	10	5	38	8	17	17	17	7
V	45	52	24	46	44	32	85	24	72	77	64	28
Sc	9	7	4	15	7	5	12	7	15	17	9	10
La	49	11	26	56	16	39	20	17	29	35	24	24
Ce	79	11	24	75	28	53	20	0	44	67	38	45
Nd	32	8	12	30	14	23	11	0	20	27	17	20
Pb	21	10	18	13	15	23	14	24	14	12	15	17
Th	9	2	6	11	3	16	0	0	2	2	3	5
U	0	0	0	0	0	3	0	0	0	0	0	0

[1] Fe_2O_3 is total iron

[2] LOI: Loss on ignition

Table E4: Bulk rock XRF data of charnockite and leucogranite; major elements in wt-%, trace elements in ppm.

	Charnockite								Leucogranite			
Sample	PeCh6	TeCH5	BoGr1	Bo7	Conc7	Conc14	Pia8	Pia14	BiGr1	BiGr2	RoGr1	RoGr2
SiO_2	68.58	71.85	64.94	65.95	69.36	72.76	75.45	73.56	73.06	72.20	75.26	73.54
TiO_2	0.53	0.28	0.68	0.60	0.40	0.34	0.18	0.24	0.26	0.27	0.15	0.25
Al_2O_3	15.51	14.92	16.24	16.58	15.39	14.71	13.80	13.66	14.84	14.72	13.42	14.05
Fe_2O_3[1]	4.70	2.41	4.83	4.29	3.45	2.82	1.54	2.19	1.94	2.12	1.65	2.10
MnO	0.10	0.04	0.08	0.06	0.07	0.03	0.04	0.04	0.03	0.03	0.03	0.04
MgO	1.87	0.94	2.17	1.51	0.92	0.72	0.46	0.73	0.44	0.50	0.45	0.88
CaO	2.96	2.48	4.36	4.33	3.09	2.78	0.85	1.63	1.60	1.90	0.71	0.70
Na_2O	3.25	3.52	3.85	3.90	4.46	3.01	3.34	3.29	3.67	3.76	3.59	3.16
K_2O	2.83	2.80	2.20	1.78	1.88	2.30	4.63	4.46	3.56	3.03	3.83	4.40
P_2O_5	0.15	0.06	0.21	0.18	0.12	0.09	0.08	0.10	0.14	0.15	0.15	0.14
Cr_2O_3	0.01	0.00	0.00	0.00	0.00	0.00	0.00	0.00	0.00	0.00	0.00	0.00
LOI[2]	0.31	0.15	0.58	0.42	0.43	0.29	0.33	0.37	0.17	0.59	0.65	0.81
Total	100.79	99.46	100.14	99.60	99.57	99.86	100.69	100.27	99.73	99.26	99.90	100.07
Rb	71	50	55	26	24	37	181	77	102	73	241	282
Ba	723	1044	411	1459	1062	427	402	817	844	747	49	191
Sr	254	370	420	449	335	831	132	328	237	255	29	56
Nb	11	13	13	7	9	3	12	4	10	14	10	14
Zr	162	158	162	211	158	158	96	144	147	147	67	130
Hf	5	4	5	7	5	6	4	5	4	4	2	4
Y	34	20	23	12	18	18	30	9	11	15	18	20
Ga	18	18	19	19	17	19	17	15	22	21	21	21
Zn	64	20	67	64	45	61	36	34	51	39	42	49
Cu	12	6	7	8	4	4	2	1	3	3	5	3
Ni	16	8	14	12	10	9	10	6	9	3	6	8
Co	7	7	14	10	7	6	5	5	4	5	2	4
Cr	37	2	16	13	4	7	0	4	2	2	4	6
V	63	19	77	61	34	32	12	29	14	12	9	16
Sc	12	8	11	11	7	8	4	4	3	4	4	6
La	29	51	31	20	27	33	22	27	29	26	12	22
Ce	42	58	37	1	5	55	36	4	46	30	9	46
Nd	19	24	17	4	6	23	17	6	20	15	7	20
Pb	18	14	14	13	10	24	19	12	23	17	21	34
Th	4	19	3	1	3	15	11	0	9	8	5	10
U	0	0	0	0	0	0	0	0	0	0	4	4

[1] Fe_2O_3 is total iron

[2] LOI: Loss on ignition

Table E5: Bulk rock XRF data of leucogranite; major elements in wt-%, trace elements in ppm.

Leucogranite

Sample	RoGr3	PeGr2	PeGr2b	PeGr4	PeGr6	PeGr7	Pels1	DrGr1	DrGr3	HvOG3	HvOG5	HvGr 4	HvGr8
SiO_2	71.05	72.57	71.63	71.48	71.27	72.48	74.35	72.55	71.67	73.68	74.15	70.62	71.84
TiO_2	0.34	0.24	0.22	0.27	0.26	0.23	0.06	0.18	0.22	0.18	0.23	0.62	0.27
Al_2O_3	14.82	14.58	14.74	14.27	14.89	14.87	14.03	15.42	14.44	14.38	13.43	13.73	15.13
Fe_2O_3[1]	2.24	1.95	1.79	2.36	2.37	1.94	0.94	1.36	1.86	1.59	2.29	4.13	2.10
MnO	0.02	0.04	0.03	0.04	0.07	0.04	0.03	0.02	0.03	0.03	0.03	0.05	0.04
MgO	0.69	0.49	0.45	0.67	0.74	0.47	0.15	0.40	0.43	0.32	2.32	1.57	0.60
CaO	1.12	1.57	1.62	1.52	2.18	1.62	1.03	1.78	1.49	0.81	0.46	1.36	2.07
Na_2O	3.15	4.11	4.28	3.60	3.69	3.69	3.58	5.06	3.59	2.78	1.45	2.12	4.65
K_2O	5.13	3.45	3.43	4.31	3.33	3.25	5.04	2.04	3.39	5.05	3.73	3.90	2.29
P_2O_5	0.15	0.11	0.12	0.08	0.10	0.15	0.07	0.07	0.12	0.21	0.10	0.12	0.07
Cr_2O_3	0.00	0.00	0.00	0.00	0.00	0.00	0.00	0.00	0.00	0.00	0.00	0.00	0.00
LOI[2]	0.70	0.23	0.15	0.63	0.37	0.23	0.29	0.69	2.50	0.89	1.80	1.01	0.53
Total	99.41	99.32	98.46	99.23	99.28	98.97	99.56	99.58	99.73	99.92	99.97	99.22	99.58
Rb	159	67	68	129	109	91	100	44	97	217	131	128	78
Ba	526	706	710	688	439	693	622	444	880	197	231	758	513
Sr	186	244	263	151	177	255	171	433	262	80	55	188	340
Nb	13	10	10	14	16	10	2	3	10	12	7	13	9
Zr	144	139	125	186	110	136	50	102	135	74	144	249	143
Hf	3	4	4	5	4	4	2	4	4	3	4	6	5
Y	15	12	11	28	28	10	14	11	9	12	25	21	15
Ga	21	19	20	21	17	17	17	21	21	20	19	14	19
Zn	49	39	36	46	36	46	20	26	52	54	38	54	42
Cu	11	7	3	5	9	2	3	1	2	1	8	18	4
Ni	11	10	6	6	8	15	3	5	6	6	13	17	9
Co	6	5	4	4	4	0	4	0	3	7	5	8	5
Cr	16	3	1	4	9	6	1	2	1	6	18	32	6
V	27	13	12	24	25	13	6	13	13	12	18	60	16
Sc	5	4	2	6	6	3	2	4	4	3	2	10	4
La	36	32	33	36	24	34	15	15	36	8	26	44	30
Ce	52	45	34	63	23	42	0	12	66	23	64	83	54
Nd	22	20	16	26	12	19	4	8	27	12	26	33	23
Pb	43	14	15	22	27	18	27	13	24	39	16	32	16
Th	17	11	8	12	10	10	0	5	13	5	12	22	9
U	3	0	0	2	0	1	0	0	1	3	2	1	0

[1] Fe_2O_3 is total iron

[2] LOI: Loss on ignition

Table E6: Bulk rock XRF data of leucogranite and matrix of magmatic breccias; major elements in wt-%, trace elements in ppm.

	Leucogranite								Matrix of magmatic breccias			
Sample	TeGr5	Or9	Pia1	Pia2	Piz4	Re3	De1	Sa2	HvSi1	HvSi2	Si1	Si2
SiO_2	72.89	73.43	74.04	73.17	72.92	74.48	73.84	72.46	65.24	53.58	71.23	59.52
TiO_2	0.20	0.24	0.18	0.25	0.29	0.12	0.28	0.28	0.41	0.66	0.26	0.89
Al_2O_3	14.49	14.57	13.96	14.18	13.83	13.66	13.35	13.52	17.85	18.95	14.52	18.72
Fe_2O_3[1]	1.74	1.63	1.56	1.93	2.37	1.28	2.21	2.02	3.14	8.78	3.42	6.48
MnO	0.03	0.03	0.04	0.04	0.06	0.05	0.04	0.02	0.05	0.14	0.13	0.10
MgO	0.39	0.38	0.33	0.45	0.66	0.22	0.66	0.69	1.62	6.47	1.25	1.77
CaO	1.42	1.23	0.97	1.46	2.01	0.70	0.65	0.79	3.42	4.60	2.49	4.49
Na_2O	3.52	3.23	3.21	3.24	3.28	3.56	3.06	2.85	4.45	3.10	3.45	4.40
K_2O	3.69	4.53	4.85	4.46	4.20	4.34	4.95	6.16	2.69	1.93	2.16	2.42
P_2O_5	0.13	0.13	0.18	0.20	0.12	0.20	0.15	0.09	0.07	0.08	0.08	0.42
Cr_2O_3	0.00	0.00	0.00	0.00	0.00	0.00	0.00	0.00	0.01	0.03	0.00	0.00
LOI[2]	0.56	0.38	0.59	0.57	0.36	0.43	0.61	0.45	0.67	1.36	0.83	0.57
Total	99.05	99.78	99.92	99.96	100.10	99.04	99.80	99.33	99.63	99.70	99.83	99.78
Rb	102	198	198	184	154	269	299	158	110	94	52	103
Ba	840	774	478	530	524	140	225	892	751	479	583	594
Sr	238	198	150	202	195	50	52	189	343	389	228	379
Nb	10	10	13	18	11	13	13	7	12	10	6	19
Zr	113	116	93	103	144	68	142	134	130	148	163	287
Hf	4	4	4	4	5	2	5	5	5	5	4	6
Y	8	7	16	17	24	10	24	19	27	11	57	36
Ga	20	21	17	18	18	19	18	15	23	31	17	23
Zn	47	82	38	44	49	32	38	36	74	226	36	101
Cu	3	4	3	4	4	1	10	2	4	47	14	13
Ni	6	14	12	9	7	8	9	7	25	124	10	9
Co	5	6	5	3	6	0	4	4	15	30	11	13
Cr	2	8	2	2	4	6	7	3	47	234	24	10
V	10	11	11	13	28	10	15	20	51	98	39	88
Sc	4	2	3	3	6	2	6	3	6	18	11	18
La	33	49	23	24	29	12	21	33	25	31	24	28
Ce	47	77	32	35	25	7	30	46	19	39	26	61
Nd	21	31	15	16	13	7	15	20	11	18	13	26
Pb	23	30	24	26	39	26	22	32	24	16	19	17
Th	11	18	10	9	7	4	11	15	10	10	7	3
U	1	1	0	1	0	4	8	1	1	0	0	0

[1] Fe_2O_3 is total iron

[2] LOI: Loss on ignition

Table E7: Bulk rock XRF data of Augengneiss, migmatitic metapelites and amphibolite; major elements in wt-%, trace elements in ppm.

Sample	Augengneiss		Dykes		Migmatitic metapelites				Amphibolite	
	HvOG1	HvOG2	Pe32	PeBa2	PePel1	HvPe1	HvPe5	US9	RoBa2	HvBa5
SiO_2	69.41	69.02	43.56	57.44	57.40	41.97	65.26	54.30	47.44	46.24
TiO_2	0.61	0.68	1.20	0.57	0.98	1.62	1.19	1.26	2.80	3.32
Al_2O_3	14.80	14.54	20.59	8.54	22.08	27.23	17.12	23.39	14.02	13.71
Fe_2O_3[1]	3.58	4.00	12.15	8.30	8.58	12.19	8.28	10.82	14.10	18.18
MnO	0.04	0.05	0.16	0.17	0.16	0.13	0.11	0.11	0.25	0.30
MgO	1.02	1.11	4.60	12.14	2.20	3.49	2.43	3.41	6.69	6.37
CaO	1.64	1.93	11.12	8.10	0.39	0.54	0.39	0.36	9.67	9.26
Na_2O	2.68	3.33	2.37	1.38	1.24	1.05	0.96	0.56	2.89	0.76
K_2O	5.21	4.22	1.65	1.33	4.00	8.55	2.74	3.84	0.61	0.37
P_2O_5	0.12	0.24	0.94	0.16	0.07	0.05	0.06	0.05	0.51	0.43
Cr_2O_3	0.00	0.00	0.00	0.14	0.02	0.03	0.02	0.02	0.03	0.01
LOI[2]	0.57	0.59	0.99	1.55	2.71	2.93	0.97	1.59	0.42	1.15
Total	99.68	99.72	99.36	99.85	99.83	99.78	99.52	99.71	99.43	100.10
Rb	135	153	109	65	274	288	72	247	7	9
Ba	730	598	594	414	760	1063	769	625	85	99
Sr	176	184	829	170	88	102	78	44	208	113
Nb	15	20	5	7	21	29	24	26	22	15
Zr	267	306	63	99	215	330	481	215	249	225
Hf	6	7	4	3	6	9	10	5	6	6
Y	39	41	40	36	38	35	50	41	62	68
Ga	20	20	25	9	28	49	24	34	19	23
Zn	73	68	114	72	125	158	132	160	95	155
Cu	17	11	41	12	24	16	24	18	32	42
Ni	16	12	24	234	53	47	46	45	79	34
Co	9	10	26	46	18	19	24	27	41	50
Cr	16	16	31	945	109	178	106	143	224	41
V	43	47	234	183	125	209	149	168	346	480
Sc	8	9	29	39	19	20	16	23	41	49
La	51	53	22	22	64	80	66	87	20	7
Ce	109	124	70	48	108	162	144	171	57	48
Nd	42	47	29	21	42	61	55	64	24	21
Pb	45	35	8	6	25	21	22	14	7	9
Th	24	24	2	3	19	27	26	27	1	0
U	0	1	0	0	2	1	4	1	0	0

[1] Fe_2O_3 is total iron

[2] LOI: Loss on ignition

Table E8: Bulk rock XRF data of granulites; major elements in wt-%, trace elements in ppm.

Granulites

	Type A		Type B				Type C-coarse		Type C-fine		Type F	
Sample	BRE7	BRE13	BRE9	BRE10	BRE14	BRE15	GraG	ScGG	GraF	C.R.**	Conc12	Conc13
SiO_2	40.22	42.10	43.49	46.71	45.76	44.10	43.34	45.10	48.48	41.21	74.93	71.61
TiO_2	0.56	0.73	0.62	0.58	0.77	0.50	0.54	1.61	2.04	2.77	0.27	0.27
Al_2O_3	25.01	24.91	23.40	23.61	23.08	25.78	23.88	22.10	15.79	16.54	12.95	15.44
Fe_2O_3[1]	11.31	10.22	10.97	9.14	9.36	9.94	15.52	14.92	15.38	19.53	1.61	1.50
MnO	0.12	0.12	0.14	0.10	0.10	0.11	0.12	0.24	0.12	0.20	0.02	0.01
MgO	18.08	16.57	16.20	15.59	16.25	15.94	12.15	6.54	13.07	15.76	1.12	1.46
CaO	0.56	0.48	0.75	0.33	0.33	0.41	0.76	3.88	1.36	1.52	3.42	2.95
Na_2O	0.33	0.33	0.24	0.36	0.37	0.23	0.42	2.28	0.23	0.02	1.72	1.86
K_2O	2.55	2.54	2.39	2.64	2.96	1.89	1.47	1.95	2.43	1.87	3.05	3.97
P_2O_5	0.07	0.05	0.08	0.07	0.07	0.07	0.08	0.06	0.16		0.15	0.10
Cr_2O_3	0.00	0.00	0.00	0.00	0.00	0.00	0.00	0.06	0.05		0.01	0.00
LOI[2]	0.89	1.37	0.98	0.81	0.39	0.79	1.63	1.03	0.21		0.39	0.49
Total	99.72	99.42	99.25	99.93	99.42	99.76	99.93	99.79	99.35		99.62	99.65
Rb	27	25	28	23	25	19	30	111	45		67	98
Ba	331	304	292	266	280	300	177	511	148		615	834
Sr	59	41	77	67	45	57	52	265	41		1428	1413
Nb	12	16	12	20	23	7	9	21	11		7	4
Zr	0	0	2	3	0	1	2	395	3		129	123
Hf	132	146	103	134	163	108	110	8	123		6	6
Y	26	7	9	11	12	15	22	78	5		31	26
Ga	2	3	2	3	5	3	1	37	2		16	19
Zn	29	37	31	31	35	36	31	304	18		24	27
Cu	71	81	63	63	78	63	54	94	63		19	2
Ni	5	6	5	5	4	4	7	206	10		16	12
Co	10	8	9	9	5	4	40	58	180		6	8
Cr	19	20	16	21	16	22	27	387	56		53	14
V	6	13	9	9	13	26	6	262	315		30	48
Sc	45	60	50	51	50	50	77	34	174		7	1
La	97	24	54	53	49	94	73	37	45		43	36
Ce	44	9	20	25	20	39	30	104	19		110	112
Nd	233	289	244	279	282	144	85	39	130		41	42
Pb	46	8	20	16	18	39	37	0	26		31	24
Th	6	11	10	9	9	10	9	17	24		21	25
U	13	18	1	5	20	8	25	8	7		32	26

[1] Fe_2O_3 is total iron

[2] LOI: Loss on ignition

** C.R.: calculated residium

Table E9: Bulk rock XRF data of metalerzolith and websterite; major elements in wt-%, trace elements in ppm.

Sample	Metalerzolith				Websterite				
	HvUM1	HvUM2	DLUM1	SpUM1	BoUM1	Conc10	VaWh1	VaUM2	VaMa1
SiO_2	42.77	43.02	48.69	42.17	52.70	51.23	51.86	52.03	52.54
TiO_2	0.03	0.06	0.10	0.12	0.23	0.47	0.26	0.25	0.27
Al_2O_3	1.20	2.58	2.39	3.30	1.59	5.53	1.98	2.77	3.95
Fe_2O_3[1]	9.53	8.54	7.54	8.80	6.01	6.66	5.81	8.35	9.13
MnO	0.14	0.12	0.13	0.13	0.15	0.15	0.16	0.19	0.20
MgO	42.76	40.13	32.42	38.13	18.57	16.51	17.35	19.77	15.66
CaO	0.11	2.23	5.28	1.98	18.22	17.89	20.22	13.31	13.18
Na_2O	0.00	0.02	0.15	0.01	0.29	0.63	0.39	0.31	0.50
K_2O	0.02	0.01	0.04	0.02	0.14	0.13	0.05	0.21	0.33
P_2O_5	0.01	0.01	0.01	0.01	0.03	0.07	0.01	0.02	0.17
Cr_2O_3	0.30	0.37	0.42	0.38	0.45	0.33	0.53	0.13	0.14
LOI[2]	2.40	3.36	3.28	4.76	1.63	0.39	1.60	2.65	3.51
Total	99.59	100.73	100.64	100.07	100.04	100.03	100.26	100.03	99.59
Rb	0	0	0	0	12	3	1	11	21
Ba	0	2	1	0	19	30	24	40	63
Sr	1	3	26	12	29	236	53	33	93
Nb	1	1	0	1	1	2	0	1	6
Zr	6	7	8	11	31	50	24	32	44
Hf	2	1	2	1	2	3	3	1	2
Y	1	2	6	3	25	15	15	15	26
Ga	2	0	3	1	5	6	4	2	5
Zn	62	57	53	63	54	55	36	62	84
Cu	22	9	12	21	65	8	40	139	165
Ni	2578	2252	1559	2153	245	323	304	361	204
Co	127	111	82	108	38	48	43	65	61
Cr	2114	2652	2975	2712	3152	2245	3674	941	966
V	39	66	108	60	124	175	148	166	170
Sc	6	13	17	14	51	64	63	57	56
La	0	1	0	0	2	10	3	9	12
Ce	0	0	0	0	22	20	0	8	48
Nd	0	0	0	0	12	11	1	7	21
Pb	3	2	3	3	3	5	5	3	6
Th	3	0	0	1	0	0	2	0	2
U	0	0	0	0	0	0	0	0	0

[1] Fe_2O_3 is total iron

[2] LOI: Loss on ignition

Table E10: Bulk rock XRF data of mafic enclaves; major elements in wt-%, trace elements in ppm.

	Mafic enclaves					
Sample	E2	E3	PrE1	PrE2	DLE4	DLE6
SiO_2	49.07	48.17	46.86	53.23	52.39	59.61
TiO_2	0.76	0.31	2.61	1.10	0.72	0.60
Al_2O_3	16.80	20.10	14.53	15.76	10.44	14.93
FeO^{tot}	8.37	6.50	15.29	10.13	9.92	6.79
MnO	0.16	0.12	0.27	0.18	0.23	0.14
MgO	9.79	8.57	6.22	6.51	12.61	5.39
CaO	9.60	10.95	9.39	8.76	7.24	6.56
Na_2O	1.77	1.59	2.16	0.95	1.38	3.32
K_2O	2.25	2.20	1.80	2.37	3.04	1.80
P_2O_5	0.13	0.10	0.38	0.08	0.13	0.13
Cr_2O_3	0.05	0.01	0.01	0.03	0.06	0.02
NiO	0.02	0.00	0.01	0.01	0.01	0.00
LOI	1.48	1.30	0.72	0.99	1.55	0.88
Total	100.23	99.93	100.23	100.10	99.71	100.18
Rb	98	108	51	112	124	49
Ba	367	505	243	669	818	656
Sr	290	483	134	127	141	343
Nb	1	3	11	8	14	5
Zr	74	35	272	141	129	151
Hf	2	2	5	4	3	3
Y	22	14	62	47	49	41
Ga	16	19	21	21	17	17
Zn	84	79	128	99	146	99
Cu	4	7	8	8	23	9
Ni	128	30	46	50	42	34
Co	44	57	47	34	48	27
Cr	325	56	101	235	402	142
V	155	80	330	232	135	131
Sc	35	15	39	36	27	23
La	0	0	7	12	23	11
Ce	13	8	57	46	77	72
Nd	9	8	23	20	30	29
Pb	0	0	0	0	0	0
Th	0	0	1	5	3	2
U	9	11	8	8	8	10

[1] Fe_2O_3 is total iron

[2] LOI: Loss on ignition

Appendix F

LA-ICP MS Analysis

Table F1: LA-ICP MS trace element data (ppm) of migmatitic biotite-orthogeniss, enclave-rich biotite-granite and charnockite.

Sample	Migmatitic biotite-orthogneiss							Enclave-rich biotite-orthogneiss			Charnockite						
	PeGr5	HvGr15	TeGr2	TeGr4	BoGr2	Or6	Or10	PeGr3	DrGr2	Re4	SpCh1	ScCh3	RoCh1	BoGr1	Bo7	Conc14	Pia14
Cs μg/g	1	5	1	2	2	1	2	3	2	1	0	0	2	1	0	0	0
Rb μg/g	94	97	86	86	94	89	101	51	75	98	50	55	73	52	26	37	73
Ba μg/g	798	481	604	1015	608	1096	739	677	903	970	609	682	829	414	1493	438	858
Th μg/g	2	8	4	41	4	5	9	3	6	17	1	2	3	2	2	15	2
U μg/g	1	2	2	3	1	1	1	2	2	4	1	1	1	1	1	1	0
Nb μg/g	11	18	8	14	16	10	15	4	8	8	19	12	14	13	6	4	4
Ta μg/g	1	2	0	1	1	1	1	0	0	0	2	1	1	1	0	0	0
La μg/g	31	33	22	117	31	33	51	12	20	35	19	35	24	31	24	41	29
Ce μg/g	58	65	44	228	66	66	102	27	42	73	38	71	52	59	46	78	51
Pb μg/g	14	12	11	13	14	9	11	8	15	19	10	9	11	11	8	18	9
Pr μg/g	6	7	5	24	8	7	11	3	5	8	4	8	6	7	5	8	5
Sr μg/g	271	321	244	320	384	345	379	391	355	273	258	368	276	436	470	863	331
Nd μg/g	25	29	18	81	33	28	42	13	19	30	19	34	26	27	20	30	18
Zr μg/g	185	186	131	333	276	218	300	159	102	188	150	322	191	150	204	163	129
Hf μg/g	5	5	4	9	6	5	7	4	3	6	4	8	5	4	5	4	3
Sm μg/g	5	5	4	12	8	6	8	3	4	5	4	6	5	5	4	5	2
Eu μg/g	1	1	1	2	2	1	2	1	1	1	1	2	1	1	2	1	1
Gd μg/g	5	5	4	9	7	5	6	2	3	4	5	6	5	5	3	4	2
Tb μg/g	1	1	1	1	1	1	1	0	0	1	1	1	1	1	0	1	0
Dy μg/g	4	4	4	7	6	5	5	2	2	3	6	6	4	4	2	3	2
Ho μg/g	1	1	1	1	1	1	1	0	0	0	1	1	1	1	0	1	0
Er μg/g	3	2	3	3	3	2	2	1	1	1	3	3	2	2	1	1	1
Yb μg/g	3	2	2	2	2	2	2	1	1	1	3	2	2	2	1	1	1
Yb μg/g	25	24	24	33	30	21	24	11	13	12	27	31	21	19	10	16	9
Lu μg/g	1	0	0	0	0	0	0	0	0	0	0	0	0	0	0	0	0

Table F2: LA-ICP MS trace element data (ppm) of leucogranite, augengneiss, matrix of magmatic breccia and mafic enclaves.

Sample	Leucogranite				Augengneiss	Matrix	Mafic enclaves					
	BiGr1	RoGr3	PeLs1	Pia2	HVOG1	Si1	E2	E3	PrE1	PrE2	DLE4	DLE6
Cs $\mu g/g$	0	2	0	1	1	0	2	3	2	3	2	1
Rb $\mu g/g$	97	154	96	167	131	51	104	113	58	110	124	57
Ba $\mu g/g$	877	565	639	540	766	591	375	530	260	650	845	644
Th $\mu g/g$	11	18	0	11	24	8	1	0	1	6	3	1
U $\mu g/g$	1	4	0	2	2	1	1	1	1	2	1	0
Nb $\mu g/g$	10	11	2	15	13	5	2	4	13	9	15	5
Ta $\mu g/g$	1	1	0	1	0	0	0	0	1	1	0	0
La $\mu g/g$	36	37	14	26	53	25	8	5	19	16	23	22
Ce $\mu g/g$	72	80	27	53	112	50	18	11	46	35	56	46
Pb $\mu g/g$	17	36	20	20	39	14	4	4	4	4	3	5
Pr $\mu g/g$	8	9	3	6	13	5	2	1	6	4	8	6
Sr $\mu g/g$	239	192	173	200	178	230	298	493	146	132	149	334
Nd $\mu g/g$	31	35	9	25	49	19	12	6	30	19	33	26
Zr $\mu g/g$	132	132	44	93	248	138	57	23	258	133	117	125
Hf $\mu g/g$	4	4	1	3	7	4	2	1	6	4	3	3
Sm $\mu g/g$	5	7	1	5	10	4	3	1	8	5	7	6
Eu $\mu g/g$	1	1	0	1	1	1	1	1	3	1	1	1
Gd $\mu g/g$	4	6	1	5	8	4	3	1	9	5	7	5
Tb $\mu g/g$	1	1	0	1	1	1	0	0	1	1	1	1
Dy $\mu g/g$	2	4	2	4	7	6	2	1	8	6	6	5
Ho $\mu g/g$	0	1	0	0	1	2	0	0	2	1	1	1
Er $\mu g/g$	1	1	1	2	3	5	1	0	5	3	3	2
Yb $\mu g/g$	0	1	0	1	3	6	1	0	5	4	3	2
Yb $\mu g/g$	10	15	12	17	33	46	13	6	45	35	34	26
Lu $\mu g/g$	0	0	0	0	0	1	0	0	1	1	0	0

Appendix G

EMS Analysis

G.1 Mineral composition of representative phases in granulites and charnockites

G.1.1 Garnet composition

Table G.1.1
Representative garnet analyses

Sample	BRE7		BRE10		GraG		GraF		CodGra5		PiaGra1			Conc13	PiaMig1
Texture	Co	R	Co	R	Co	R	Co	R	Co	R	Co	R	Co_2	Co	Co
SiO_2	40.57	40.10	40.06	39.97	39.24	38.34	39.88	39.67	39.96	39.50	38.10	38.50	38.82	39.59	38.14
TiO_2	0.01	0.02	0.00	0.00	0.01	0.01	0.10	0.06	0.03	0.03	0.02	0.01	0.02	0.06	0.02
Cr_2O_3	0.00	0.01	0.02	0.00	0.03	0.00	0.07	0.06	0.00	0.01	0.01	0.00	0.00	0.01	0.00
Al_2O_3	23.20	23.04	22.97	22.70	22.18	22.01	22.18	22.32	22.66	22.71	21.74	22.26	22.21	22.26	21.56
FeO	21.40	23.28	22.43	23.77	24.33	26.71	23.04	25.21	23.03	23.52	27.82	28.44	28.23	22.55	31.32
Mno	0.26	0.70	0.62	0.57	0.32	0.46	0.60	0.46	0.73	0.89	1.23	0.90	1.58	0.44	2.24
MgO	15.13	13.14	14.27	12.62	13.13	11.09	10.93	10.53	12.89	12.42	10.06	9.83	9.47	11.60	6.25
CaO	0.75	1.40	0.91	1.06	1.03	1.27	4.18	2.65	1.78	1.71	0.73	0.78	0.75	3.29	1.65
Na_2O	0.02	0.01	0.04	0.01	0.02	0.02	0.00	0.01	0.01	0.02	0.00	0.00	0.04	0.00	0.00
K_2O	0.00	0.01	0.00	0.01	0.00	0.02	0.01	0.00	0.00	0.01	0.02	0.00	0.01	0.00	0.00
Tot	101.3	101.7	101.3	100.7	100.3	99.9	102.0	101.0	101.1	100.7	99.7	100.7	101.1	99.8	101.2
O	12	12	12	12	12	12	12	12	12	12	12	12	12	12	12
Si	2.97	2.96	2.95	2.99	2.94	2.92	2.99	2.99	2.97	2.95	2.94	2.94	2.96	2.99	2.97
Ti	0.00	0.00	0.00	0.00	0.00	0.00	0.01	0.00	0.00	0.00	0.00	0.00	0.00	0.00	0.00
Cr	0.00	0.00	0.00	0.00	0.00	0.00	0.00	0.00	0.00	0.00	0.00	0.00	0.00	0.00	0.00
Al	2.00	2.00	1.99	2.00	1.96	1.98	1.96	1.98	1.98	2.00	1.97	2.00	2.00	1.98	1.98
Fe^{2+}	1.24	1.36	1.26	1.46	1.37	1.52	1.40	1.57	1.35	1.37	1.64	1.70	1.71	1.39	1.96
Fe^{3+}	0.07	0.08	0.12	0.03	0.16	0.18	0.05	0.03	0.08	0.10	0.16	0.12	0.09	0.03	0.08
Mn	0.02	0.04	0.04	0.04	0.02	0.03	0.04	0.03	0.05	0.06	0.08	0.06	0.10	0.03	0.15
Mg	1.65	1.45	1.57	1.41	1.47	1.26	1.22	1.18	1.43	1.38	1.16	1.12	1.08	1.31	0.73
Ca	0.06	0.11	0.07	0.09	0.08	0.10	0.34	0.21	0.14	0.14	0.06	0.06	0.06	0.27	0.14
Na	0.00	0.00	0.01	0.00	0.00	0.00	0.00	0.00	0.00	0.00	0.00	0.00	0.01	0.00	0.00
K	0.00	0.00	0.00	0.00	0.00	0.00	0.00	0.00	0.00	0.00	0.00	0.00	0.00	0.00	0.00
Sum	8	8	8	8	8	8	8	8	8	8	8	8	8	8	8
X_{Mg}	0.56	0.50	0.53	0.49	0.49	0.43	0.46	0.43	0.50	0.52	0.39	0.38	0.37	0.52	0.26
$X_{Mg}*$	0.57	0.52	0.55	0.49	0.52	0.45	0.47	0.43	0.49	0.50	0.41	0.40	0.39	0.52	0.27
X_{pyr}	0.56	0.49	0.53	0.47	0.50	0.43	0.41	0.40	0.48	0.47	0.39	0.38	0.37	0.44	0.24
X_{alm}	0.42	0.46	0.43	0.49	0.47	0.52	0.47	0.52	0.46	0.47	0.56	0.58	0.58	0.47	0.66
X_{grs}	0.02	0.04	0.02	0.03	0.03	0.04	0.11	0.07	0.05	0.05	0.02	0.02	0.04	0.09	0.05
X_{sps}	0.01	0.02	0.01	0.01	0.01	0.01	0.01	0.01	0.02	0.02	0.03	0.02	0.02	0.01	0.05

Garnet: x(g) = Fe / (Fe + Mg); z(g) = Ca / (Ca + Fe + Mg); orthopyroxene: x(opx) = Fe / (Fe + Mg); y(opx) = x(Al,M1) = Al / 2; Q(opx) = 2 * (x(Fe,M2) – x(opx)); sapphirine: x(sa) = Fe / (Fe + Mg); y(sa) = x(Al,M1); spinel: x(sp) = Fe / (Fe + Mg); cordierite: x(cd) = Fe / (Fe + Mg); h(cd) = H_2O on hydroxil site; biotite: x(bi) = Fe / (Fe + Mg); y(bi) = x(Al,M1); Q(bi) = 3*(x - x(Fe,M2)); plagioclase: ca(pl) = Ca / (Ca + Na + K); k(pl) = K / (K + Ca + Na). Used activity models: garnet and biotite after White et al. (2007); orthopyroxene after Powell and Holland (1999); sapphirine after Kelsey et al. (2004); spinel and cordierite after Holland and Powell (1998); plagioclase after (Holland and Powell, 2003).

G.1.2   Orthopyroxene composition

Table G.1.2
Representative orthopyroxene analyses

Sample	BRE7				BRE10			GraG		GraF			CodGra5			PiaGra1	Conc13	PiaMig1
Texture	Co	R	Sym_1	Sym_2	Co	R	Sym	Co	R	Co	R	Sym	Co	R	Sym	Co	Co	Co
SiO_2	50.65	50.53	52.52	51.09	50.98	52.04	51.86	49.01	49.60	52.09	49.30	51.01	50.71	49.13	48.59	49.24	46.58	48.54
TiO_2	0.00	0.07	0.02	0.04	0.09	0.04	0.04	0.14	0.09	0.12	0.15	0.07	0.05	0.03	0.06	0.05	0.18	0.09
Cr_2O_3	0.00	0.01	0.00	0.03	0.00	0.03	0.00	0.00	0.00	0.00	0.05	0.14	0.00	0.00	0.00	0.00	0.00	0.00
Al_2O_3	8.72	6.49	5.35	5.87	8.82	5.17	5.35	9.19	5.80	4.15	8.11	5.04	4.91	7.22	8.25	6.57	9.83	4.53
FeO	12.07	17.64	16.39	17.93	10.99	17.22	17.27	16.13	20.10	19.40	19.65	19.97	17.89	19.19	19.33	21.65	23.46	28.62
Mno	0.12	0.22	0.15	0.19	0.07	0.18	0.15	0.08	0.10	0.10	0.11	0.12	0.29	0.35	0.30	0.27	0.26	0.92
MgO	27.86	25.13	26.04	24.84	28.73	25.85	25.52	25.07	23.63	24.22	22.61	23.27	25.42	23.67	23.30	21.63	19.55	17.12
CaO	0.07	0.05	0.05	0.08	0.14	0.03	0.06	0.12	0.07	0.13	0.07	0.08	0.12	0.08	0.10	0.06	0.07	0.15
Na_2O	0.00	0.00	0.01	0.01	0.01	0.01	0.02	0.00	0.00	0.00	0.00	0.00	0.02	0.01	0.01	0.13	0.00	0.00
K_2O	0.01	0.03	0.01	0.01	0.01	0.00	0.00	0.00	0.00	0.00	0.01	0.00	0.00	0.02	0.01	0.27	0.00	0.02
Tot	99.5	100.2	100.5	100.1	99.8	100.6	100.3	99.7	99.4	100.2	100.1	100.0	99.4	99.7	99.9	99.9	99.9	100.0
O	6	6	6	6	6	6	6	6	6	6	6	6	6	6	6	6	6	6
Si	1.80	1.83	1.88	1.85	1.79	1.87	1.87	1.77	1.83	1.90	1.80	1.88	1.85	1.80	1.77	1.82	1.74	1.86
Ti	0.00	0.00	0.00	0.00	0.00	0.00	0.00	0.00	0.00	0.00	0.00	0.00	0.00	0.00	0.00	0.00	0.01	0.00
Cr	0.00	0.00	0.00	0.00	0.00	0.00	0.00	0.00	0.00	0.00	0.00	0.00	0.00	0.00	0.00	0.00	0.00	0.00
Al(T)	0.20	0.18	0.12	0.15	0.21	0.13	0.13	0.23	0.18	0.10	0.20	0.12	0.15	0.20	0.23	0.18	0.26	0.14
Al(M)	0.16	0.10	0.11	0.10	0.16	0.09	0.10	0.16	0.08	0.08	0.15	0.10	0.06	0.11	0.13	0.11	0.17	0.07
Fe^{2+}	0.32	0.46	0.48	0.50	0.28	0.48	0.49	0.42	0.53	0.58	0.57	0.60	0.45	0.49	0.49	0.57	0.64	0.85
Fe^{3+}	0.04	0.07	0.01	0.04	0.04	0.04	0.03	0.07	0.09	0.01	0.03	0.02	0.09	0.10	0.10	0.09	0.09	0.07
Mn	0.00	0.01	0.00	0.01	0.00	0.01	0.01	0.00	0.00	0.00	0.00	0.00	0.01	0.01	0.01	0.01	0.01	0.03
Mg	1.47	1.35	1.39	1.34	1.51	1.38	1.37	1.35	1.30	1.32	1.23	1.28	1.38	1.29	1.27	1.19	1.09	0.98
Ca	0.00	0.00	0.00	0.00	0.01	0.00	0.00	0.01	0.00	0.01	0.00	0.00	0.01	0.00	0.00	0.00	0.00	0.01
Na	0.00	0.00	0.00	0.00	0.00	0.00	0.00	0.00	0.00	0.00	0.00	0.00	0.00	0.00	0.00	0.01	0.00	0.00
K	0.00	0.00	0.00	0.00	0.00	0.00	0.00	0.00	0.00	0.00	0.00	0.00	0.00	0.00	0.00	0.01	0.00	0.00
Sum	4	4	4	4	4	4	4	4	4	4	4	4	4	4	4	4	4	4
X_{Mg}	0.80	0.72	0.74	0.71	0.82	0.73	0.73	0.74	0.68	0.69	0.67	0.68	0.72	0.69	0.68	0.64	0.60	0.52
$X_{Mg}*$	0.82	0.75	0.74	0.73	0.84	0.74	0.74	0.76	0.71	0.70	0.69	0.68	0.75	0.73	0.72	0.68	0.63	0.54
y(Al)	0.18	0.14	0.11	0.13	0.18	0.11	0.11	0.20	0.13	0.09	0.18	0.11	0.11	0.16	0.18	0.14	0.22	0.10
A/AFM	0.17	0.13	0.11	0.12	0.17	0.10	0.11	0.18	0.12	0.09	0.16	0.10	0.10	0.15	0.17	0.13	0.19	0.10
Fe^{3+}/Fe^{tot}	0.14	0.13	0.02	0.08	0.13	0.08	0.06	0.14	0.15	0.02	0.06	0.03	0.17	0.16	0.17	0.14	0.12	0.08

Co – core of porphyroblast; R – rim of porphyroblast; Sym – symplectites. Fe^{3+} calculated after charge balance based on 4 cations.
X_{Mg} = Mg / (Mg + Fe^{tot}); $X_{Mg}*$ = X_{en} = Mg / (Mg + Fe^{2+}); y(Al) = (Al^{tot} / 2).

G.1.3   Sapphirine and spinel compositions

Table G.1.3
Representative sapphirine and spinel analyses

	Sapphirine							Spinel							
Sample	BRE7		BRE10	GraG	CodGra5	PiaGra1	Conc13	BRE7	BRE10		GraG		CodGra5	PiaGra1	Conc13
Texture	Co	R	Sym	Sym	Sym	Sym	Sym	In	In	Sym	In	Sym	Sym	Sym	Sym
SiO_2	14.02	13.81	13.10	12.57	13.26	12.75	13.69	0.03	0.17	0.20	0.06	0.14	0.02	0.05	0.00
TiO_2	0.02	0.05	0.06	0.03	0.02	0.01	0.01	0.00	0.03	0.02	0.02	0.02	0.01	0.01	0.05
Cr_2O_3	0.03	0.00	0.00	0.03	0.01	0.01	0.06	0.00	0.01	0.01	0.00	0.04	0.16	0.05	0.05
Al_2O_3	61.49	60.84	61.31	61.83	59.42	60.08	58.01	62.70	60.69	61.40	58.40	60.84	59.31	60.01	58.45
FeO	6.14	8.23	8.36	10.02	10.81	11.74	12.64	23.34	26.67	26.58	32.71	26.25	28.86	32.21	31.61
Mno	0.04	0.05	0.04	0.02	0.13	0.13	0.03	0.08	0.07	0.09	0.08	0.03	0.12	0.14	0.02
MgO	18.12	17.12	16.60	15.15	15.81	14.21	14.85	13.93	12.41	11.81	8.41	11.71	10.24	7.44	9.19
CaO	0.02	0.01	0.01	0.01	0.05	0.06	0.02	0.00	0.00	0.00	0.02	0.00	0.00	0.00	0.10
Na_2O	0.00	0.02	0.00	0.01	0.00	0.52	0.01	0.00	0.00	0.00	0.00	0.00	0.00	0.00	0.00
K_2O	0.00	0.00	0.01	0.00	0.01	0.17	0.00	0.01	0.00	0.00	0.00	0.00	0.00	0.02	0.01
Tot	99.9	100.1	99.5	99.7	99.5	99.7	99.3	100.1	100.1	100.1	99.7	99.0	100.3	99.9	99.5
O	10	10	10	10	10	10	10	4	4	4	4	4	4	4	4
Si	0.83	0.82	0.78	0.76	0.80	0.77	0.83	0.00	0.01	0.01	0.00	0.00	0.00	0.00	0.00
Ti	0.00	0.00	0.00	0.00	0.00	0.00	0.00	0.00	0.00	0.00	0.00	0.00	0.00	0.00	0.00
Cr	0.00	0.00	0.00	0.00	0.00	0.00	0.00	0.00	0.00	0.00	0.00	0.00	0.00	0.00	0.00
Al	4.27	4.25	4.32	4.38	4.22	4.28	2.17	1.94	1.91	1.93	1.90	6.00	1.91	1.95	1.89
Fe^{2+}	0.23	0.30	0.30	0.39	0.37	0.41	2.00	0.45	0.51	0.53	0.65	0.53	0.58	0.69	0.62
Fe^{3+}	0.07	0.11	0.12	0.11	0.18	0.19	0.48	0.06	0.08	0.06	0.10	0.06	0.08	0.05	0.11
Mn	0.00	0.00	0.00	0.00	0.01	0.01	0.16	0.00	0.00	0.00	0.00	0.00	0.00	0.00	0.00
Mg	1.59	1.51	1.48	1.36	1.42	1.28	0.00	0.55	0.49	0.47	0.35	0.47	0.42	0.31	0.38
Ca	0.00	0.00	0.00	0.00	0.00	0.00	1.35	0.00	0.00	0.00	0.00	0.00	0.00	0.00	0.00
Na	0.00	0.00	0.00	0.00	0.00	0.06	0.00	0.00	0.00	0.00	0.00	0.00	0.00	0.00	0.00
K	0.00	0.00	0.00	0.00	0.00	0.01	0.00	0.00	0.00	0.00	0.00	0.00	0.00	0.00	0.00
Sum	7	7	7	7	7	7	7	3	3	3	3	3	3	3	3
X_{Mg}	0.84	0.79	0.78	0.73	0.72	0.68	0.68	0.52	0.45	0.44	0.31	0.44	0.39	0.29	0.34
X_{Mg}*	0.87	0.84	0.83	0.78	0.79	0.76	0.74	0.55	0.49	0.47	0.35	0.47	0.42	0.31	0.38
Fe^{3+}/Fe^{tot}	0.24	0.27	0.28	0.22	0.33	0.31	0.25	0.11	0.14	0.10	0.13	0.10	0.12	0.07	0.13
A/AFM	0.70	0.70	0.71	0.71	0.70	0.72	0.70								

Co – cores; R – rims; Sym – symplectites; In – inclusions in garnet porphyroblasts; X_{Mg} = Mg / (Mg + Fe^{tot}); X_{Mg}* = Mg / (Mg + Fe^{2+}); A/AFM = Al / (Al + Fe^{2+} + Mg); Fe^{3+} calculated in sapphirine after charge balance based on 7 cations following the approach of Higgins *et al.* (1979) and in spinel after charge balance based on 3 cations.

G.1.4   Biotite, cordierite and plagioclase compositions

Table G.1.4
Representative biotite, cordierite and plagioclase analyses

Sample	Biotite								Cordierite					Plagioclase				
	BRE7	BRE10	GraG	GraF	CodGra5	PiaGra1	Conc13	PiaMig	BRE7	BRE10	GraG	GraF	CodGra5	GraF	CodGra5	PiaGra1	Conc13	PiaMig1
SiO_2	38.06	38.29	36.60	37.77	38.09	38.17	38.04	36.14	49.47	49.56	48.84	49.73	49.01	51.41	57.62	63.02	56.44	60.94
TiO_2	3.43	3.45	3.29	4.46	2.14	2.57	2.26	4.14	0.00	0.00	0.01	0.02	0.01	0.02	0.01	0.01	0.03	0.02
Cr_2O_3	0.00	0.00	0.00	0.05	0.05	0.01	0.00	0.02	0.01	0.00	0.01	0.00	0.02	0.00	0.01	0.00	0.00	0.00
Al_2O_3	17.15	16.53	17.14	15.75	16.55	16.15	18.42	15.10	33.87	33.36	32.33	33.30	33.20	30.13	25.92	22.52	27.34	23.88
FeO	9.29	9.86	11.86	11.02	9.98	10.75	11.47	18.88	2.89	2.93	3.69	3.30	3.15	0.07	0.12	0.03	0.06	0.08
Mno	0.01	0.01	0.01	0.01	0.05	0.06	0.00	0.21	0.03	0.03	0.02	0.02	0.06	0.01	0.01	0.01	0.00	0.01
MgO	18.33	18.15	16.49	16.89	18.71	17.79	15.98	11.85	11.97	11.86	11.52	11.69	11.82	0.00	0.00	0.00	0.00	0.00
CaO	0.01	0.00	0.00	0.03	0.00	0.01	0.01	0.00	0.01	0.02	0.01	0.02	0.02	13.43	8.53	4.02	9.50	5.54
Na_2O	0.34	0.22	0.27	0.23	0.14	0.10	0.17	0.09	0.10	0.09	0.09	0.07	0.06	3.76	6.30	8.51	5.95	7.62
K_2O	9.19	9.39	9.39	9.25	9.54	9.59	9.50	9.32	0.01	0.01	0.01	0.02	0.00	0.08	0.20	0.33	0.16	0.29
Tot	95.8	95.9	95.3	95.5	95.2	95.2	95.6	95.8	98.4	97.9	96.5	98.2	97.3	98.9	98.7	98.5	99.5	98.4
O	11	11	11	11	11	11	11	11	18	18	18	18	18	8	8	8	8	8
Si	2.49	2.51	2.45	2.51	2.52	2.54	2.51	2.49	4.97	5.00	5.02	5.01	4.98	2.36	2.62	2.84	2.55	2.76
Ti	0.17	0.17	0.17	0.22	0.11	0.13	0.11	0.22	0.00	0.00	0.00	0.00	0.00	0.00	0.00	0.00	0.00	0.00
Cr	0.00	0.00	0.00	0.00	0.00	0.00	0.00	0.00	0.00	0.00	0.00	0.00	0.00	0.00	0.00	0.00	0.00	0.00
Al	1.32	1.28	1.35	1.23	1.29	1.27	1.43	1.23	4.01	3.97	3.92	3.96	3.98	1.63	1.39	1.20	1.46	1.28
Fe^{tot}	0.51	0.00	0.67	0.00	0.55	0.60	0.63	1.09	0.24	0.25	0.32	0.28	0.27	0.00	0.01	0.00	0.00	0.00
Mn	0.00	0.54	0.00	0.61	0.00	0.00	0.00	0.01	0.00	0.00	0.00	0.00	0.01	0.00	0.00	0.00	0.00	0.00
Mg	1.79	0.00	1.65	0.00	1.84	1.76	1.57	1.22	1.79	1.78	1.76	1.76	1.79	0.00	0.00	0.00	0.00	0.00
Ca	0.00	1.77	0.00	1.67	0.00	0.00	0.00	0.00	0.00	0.00	0.00	0.00	0.00	0.66	0.42	0.19	0.46	0.27
Na	0.04	0.00	0.04	0.00	0.02	0.01	0.02	0.01	0.02	0.02	0.02	0.01	0.01	0.34	0.56	0.74	0.52	0.67
K	0.77	0.03	0.80	0.03	0.81	0.81	0.80	0.82	0.00	0.00	0.00	0.00	0.00	0.01	0.01	0.02	0.01	0.02
Sum	7.09	0.79	7.12	0.78	7.14	7.12	7.08	7.09	11.04	11.02	11.03	11.02	11.04	5	5	5	5	5
X_{Mg}	0.78	0.77	0.71	0.73	0.77	0.75	0.71	0.53	0.88	0.88	0.85	0.86	0.87					
X_{Ab}														0.34	0.57	0.78	0.53	0.70
X_{An}														0.66	0.42	0.20	0.47	0.28
X_{Or}														0.01	0.01	0.02	0.01	0.02

M – matrix; C – corona; X_{Mg} = Mg / (Mg + Fe^{tot}); X_{Ab} = Na / (Na + Ca + K); X_{An} = Ca / (Ca + Na + K); X_{Or} = K / (K + Na + Ca).

Appendix H

SHRIMP Analysis

Migmatitic biotite-orthogneiss (PeGr5)

Sample spot	U (ppm)	Th (ppm)	^{232}Th/^{238}U	^{206}Pb* (ppm)	%-^{206}Pb$_c$	^{207}Pb/^{206}Pb	±%	^{238}U/^{206}Pb	±%	1 ^{206}Pb*/^{238}U	±%	Age (Ma) ^{206}Pb/^{238}U	± error
Magmatic oscillatoric zircon domains													
PeGr5.1.1	1281	382	0.31	50.6	0.38	0.05333	1.6	21.75	1.3	0.0458	1.3	288.7	± 3.7
PeGr5.1.2	596	364	0.63	6.24	0.00	0.0523	4.6	81.96	0.96	0.0122	0.96	78.17	± 0.74
PeGr5.2.1	678	139	0.21	23.2	0.00	0.0521	2.3	25.09	0.54	0.03985	0.54	251.9	± 1.3
PeGr5.3.1	844	221	0.27	27	0.00	0.0505	2.2	26.87	0.74	0.03721	0.74	235.5	± 1.7
PeGr5.4.2	968	161	0.17	14.4	0.98	0.0501	5.7	57.8	2.2	0.01713	2.3	109.5	± 2.5
PeGr5.5.1	282	93	0.34	5.97	0.00	0.0535	7.3	40.6	2.8	0.02464	2.8	156.9	± 4.3
PeGr5.5.2	11724	1918	0.17	453	0.06	0.05158	0.82	22.24	1.7	0.04493	1.7	283.3	± 4.7
PeGr5.6.1	844	383	0.47	32.5	0.00	0.0532	3.3	22.34	1.9	0.0477	1.9	282.3	± 5.3
PeGr5.6.2	1114	184	0.17	25.3	0.85	0.0552	3.5	37.89	1.9	0.02616	2.1	166.5	± 3.4
PeGr5.7.1	683	106	0.16	25.9	0.41	0.0543	3.8	22.65	2	0.04397	2	277.4	± 5.4
PeGr5.7.2	1179	197	0.17	45.2	0.00	0.0535	2.6	22.4	1.8	0.04465	1.8	281.6	± 5
PeGr5.8.1	804	71	0.09	32.7	0.26	0.0512	3.1	21.1	1.9	0.04726	1.9	297.7	± 5.7
PeGr5.9.1	1796	43	0.02	72.7	0.18	0.0526	2.1	21.23	1.8	0.04701	1.8	296.1	± 5.2
PeGr5.10.1	1077	266	0.26	42.8	–	0.0522	2.9	21.63	1.8	0.04628	1.8	291.6	± 5.3
PeGr5.11.1	444	135	0.31	17.5	0.00	0.0534	4.4	21.84	2.2	0.0458	2.2	288.6	± 6.2
PeGr5.12.1	854	700	0.85	15.7	0.61	0.0518	6.4	46.72	2.1	0.02127	2.1	135.7	± 2.8
PeGr5.13.1	1212	386	0.33	47	–	0.0491	2.9	22.16	1.8	0.04531	1.8	285.6	± 5.2
PeGr5.14.1	1044	238	0.24	29.1	0.33	0.0537	3.5	30.82	2.6	0.03233	2.6	205.1	± 5.3
PeGr5.15.1	2577	331	0.13	107	0.00	0.05081	1.8	20.64	1.8	0.04845	1.8	305	± 5.3
Metamorphic zircon domains													
481	337	0.72	2.85	3.80	0.0653	11	145.3	3.3	0.00662	4	42.6	42.6	±1.7
1107	67	0.06	4.05	2.93	0.0471	6.7	234.6	1.4	0.004141	2.4	26.64	26.64	± 0.64

Pb$_C$ and Pb* indicate the common and radiogenic portions, respectively.
Common Pb corrected using measured ^{204}Pb.

Investigated zircons in sample PeGr5

Figure H.1: *CL-imaging of analysed zircon grains in sample PeGr5 showing the location of the spot analyses and the calculated age (uncorrected)*

Migmatitic biotite-orthogneiss (HvGr15)

Sample spot	U (ppm)	Th (ppm)	^{232}Th/^{238}U	^{206}Pb* (ppm)	%-^{206}Pb$_c$	^{207}Pb/^{206}Pb	± %	^{238}U/^{206}Pb	± %	1 ^{206}Pb*/^{238}U	± %	Age (Ma) ^{206}Pb/^{238}U	± error
Magmatic oscillatoric zircon domains													
HvGr15.1.1	203	86	0.44	8.09	1.24	0.0531	4.1	21.57	1.1	0.04579	1.2	288.6	± 3.4
HvGr15.1.3	5202	718	0.14	198	0.00	0.05193	0.88	22.557	0.28	0.04433	0.28	279.62	± 0.77
HvGr15.2.2	2885	1598	0.57	110	–	0.05152	1.5	22.5	0.96	0.04445	0.96	280.4	± 2.6
HvGr15.3.3	6618	1105	0.17	221	0.20	0.05281	1.1	25.753	0.37	0.03875	0.38	245.1	± 0.91
HvGr15.4.1	320	158	0.51	13.1	0.00	0.0509	4.5	21.03	0.93	0.04755	0.93	299.5	± 2.7
HvGr15.5.1	668	38	0.06	44.7	0.18	0.0566	2.5	12.85	1.9	0.0777	1.9	482.1	± 8.7
HvGr15.5.2	519	144	0.29	19.6	1.28	0.0529	3.9	22.69	2.1	0.04351	2.2	274.6	± 6
HvGr15.6.2	1929	385	0.21	78.7	0.00	0.0522	2	21.05	1.8	0.04752	1.8	299.3	± 5.2
HvGr15.7.2	4382	440	0.10	170	0.02	0.05332	1.3	22.08	1.7	0.04527	1.7	285.4	± 4.8
HvGr15.8.2	883	375	0.44	38.5	–	0.0481	3	19.72	2.6	0.051	2.7	320.5	± 8.3
HvGr15.9.2	319	196	0.63	11	0.36	0.0578	5.1	24.87	2.2	0.04006	2.3	253.2	± 5.6
HvGr15.10.2	805	83	0.11	43.2	0.40	0.0599	4.9	16	1.9	0.0622	1.9	389.2	± 7.1
HvGr15.10.3	2936	417	0.15	114	0.00	0.05263	1.7	22.2	1.7	0.04504	1.7	284	± 4.8
HvGr15.11.2	885	109	0.13	32.4	0.76	0.0544	3.2	23.45	2	0.04232	2	267.2	± 5.3
Metamorphic zircon domains													
HvGr15.1.2	451	34	0.08	2.72	2.30	0.0686	6.4	142.5	1.6	0.00686	2.2	44.08	± 0.97
HvGr15.1.4	1846	32	0.02	11.7	12.06	0.1605	5.5	136	2.8	0.00641	6.6	41.2	± 2.7
HvGr15.2.1	1067	6	0.01	4.77	0.00	0.0551	7.4	192.3	2	0.0052	2	33.43	± 0.67
HvGr15.2.3	1356	6	0.00	6.2	0.00	0.0525	7.2	188.1	2.6	0.00532	2.6	34.18	± 0.89
HvGr15.3.1	468	71	0.16	2.1	7.99	0.0598	7.6	191.3	1.8	0.00482	4.6	31	± 1.4
HvGr15.3.2	1183	12	0.01	4.91	1.81	0.0578	6.4	207	1.4	0.004746	1.8	30.52	± 0.56
HvGr15.4.2	873	7	0.01	4.46	0.00	0.0672	7.5	168.1	2.6	0.00595	2.6	38.2	± 1
HvGr15.5.3	530	16	0.03	4.5	0.00	0.0531	8.3	101.2	2.9	0.00988	2.9	63.4	± 1.9
HvGr15.7.1	699	32	0.05	3.67	3.41	0.0866	9.8	163.9	2.9	0.00588	3.6	37.8	± 1.4
HvGr15.8.1	631	8	0.01	2.85	3.07	0.0602	10	190	3	0.0051	3.5	32.8	± 1.2
HvGr15.9.1	155	58	0.39	0.819	0.00	0.119	14	162.6	5.1	0.00615	5.1	39.5	± 2
HvGr15.10.1	374	34	0.09	2.04	0.00	0.09	11	157.4	3.9	0.00635	3.9	40.8	± 1.6
HvGr15.11.1	275	30	0.11	1.39	0.00	0.0591	14	169.6	3.9	0.0059	3.9	37.9	± 1.5

Pb$_c$ and Pb* indicate the common and radiogenic portions, respectively.
Common Pb corrected using measured ^{204}Pb.

Investigated zircons in sample HvGr15

Figure H.2: *CL-imaging of analysed zircon grains in sample HvGr15 showing the location of the spot analyses and the calculated age (uncorrected)*

Migmatitic biotite-orthogneiss (TeGr2)

Sample spot	U (ppm)	Th (ppm)	^{232}Th/^{238}U	^{206}Pb* (ppm)	%-^{206}Pb$_c$	^{207}Pb/^{206}Pb	±%	^{238}U/^{206}Pb	±%	^{206}Pb*/^{238}U	±%	Age (Ma) ^{206}Pb/^{238}U	± error
Magmatic oscillatoric zircon domains													
TEGR2.1.3	2343	1009	0.44	92.8	–	0.05233	0.99	21.69	0.64	0.0461	0.64	290.5	±1.8
TEGR2.2.2	733	142	0.20	26.7	–	0.05118	1.7	23.59	0.87	0.0424	0.87	267.7	±2.3
TEGR2.5.2	1042	276	0.27	38.2	–	0.05151	1.4	23.42	0.82	0.04271	0.82	269.6	±2.2
TEGR2.6.2	882	164	0.19	31.7	–	0.05066	1.6	23.9	0.84	0.04184	0.84	264.2	±2.2
TEGR2.7.2	587	148	0.26	20.9	0.35	0.0509	3.8	24.18	0.85	0.04136	0.85	261.2	±2.2
TEGR2.8.2	1425	406	0.29	51.6	0.04	0.05159	1.4	23.75	0.69	0.0421	0.69	265.8	±1.8
TEGR2.9.2	681	120	0.18	24.4	–	0.0535	4.4	23.81	0.8	0.04201	0.8	265.3	±2.1
TEGR2.11.2	958	163	0.18	34.1	0.21	0.0517	2.6	24.22	0.85	0.04129	0.85	260.8	±2.2
Metamorphic zircon domains													
TEGR2.1.1	847	5	0.01	3.45	–	0.0579	8.6	209	1.6	0.004787	1.6	30.79	±0.48
TEGR2.2.1	1433	6	0.00	5.88	–	0.0516	6.7	209	1.1	0.004785	1.1	30.77	±0.33
TEGR2.3.1	234	1	0.01	1	4.20	0.027	77	209.5	3.3	0.00477	3.3	30.7	±1
TEGR2.4.1	838	7	0.01	3.49	1.70	0.0393	19	210	1.5	0.004762	1.5	30.63	±0.46
TEGR2.5.1	980	3	0.00	4	0.66	0.0453	13	211.9	1.4	0.004719	1.4	30.35	±0.43
TEGR2.6.1	405	3	0.01	1.68	2.73	0.041	36	212.8	2.4	0.0047	2.4	30.22	±0.74
TEGR2.7.1	383	2	0.00	1.56	–	0.078	19	206.7	2.7	0.00485	2.7	31.2	±0.85
TEGR2.8.1	513	2	0.00	2.12	0.00	0.0609	5.7	208.2	1.7	0.004803	1.7	30.89	±0.53
TEGR2.9.1	225	1	0.00	0.944	–	0.0705	12	203.3	2.9	0.00492	2.9	31.66	±0.92
TEGR2.10.1	1621	7	0.00	6.55	–	0.0517	5	211.8	1.1	0.004722	1.1	30.37	±0.33
TEGR2.11.1	308	1	0.00	1.27	1.70	0.05	26	212	2.6	0.00472	2.6	30.33	±0.8
TEGR2.1.2	877	38	0.04	4.29	1.63	0.0409	22	178.6	1.8	0.005599	1.8	36	±0.63

Pb$_c$ and Pb* indicate the common and radiogenic portions, respectively.
Common Pb corrected using measured ^{204}Pb.

Investigated zircons in sample TeGr2

Figure H.3: *CL-imaging of analysed zircon grains in sample TeGr2 showing the location of the spot analyses and the calculated age (uncorrected)*

Migmatitic biotite-orthogneiss (Or10)

Sample spot	U (ppm)	Th (ppm)	$^{232}Th/^{238}U$	$^{206}Pb^*$ (ppm)	%-$^{206}Pb_c$	$^{207}Pb/^{206}Pb$	±%	$^{238}U/^{206}Pb$	±%	$1\ ^{206}Pb^*/^{238}U$	±%	Age (Ma) $^{206}Pb/^{238}U$	± error
Magmatic oscillatoric zircon domains													
Or10.1.1	1456	24	0.02	40	0.00	0.05166	1.4	31.25	2.4	0.032	2.4	203	±4.8
Or10.1.2	600	214	0.37	24.6	–	0.05166	1.8	20.94	2.4	0.0478	2.4	300.9	±7.1
Or10.2.2	742	191	0.27	25	0.24	0.05382	1.5	25.53	2.5	0.03908	2.5	247.1	±6
Or10.3.2	569	221	0.40	19.5	0.27	0.0546	1.9	25.02	2.4	0.03985	2.4	251.9	±6
Or10.4.2	905	285	0.33	35	0.12	0.05333	1.4	22.21	2.4	0.045	2.4	283.6	±6.7
Or10.5.2	419	122	0.30	14	0.33	0.0545	2.2	25.66	2.5	0.03884	2.5	245.6	±6
Or10.6.2	885	534	0.62	31.6	0.07	0.05308	1.5	24.06	2.5	0.0415	2.5	262.3	±6.3
Or10.7.2	465	196	0.44	18.3	0.13	0.0527	2	21.82	2.5	0.0458	2.5	288.4	±6.9
Or10.8.1	347	63	0.19	12.9	0.00	0.0515	2.4	23.11	2.5	0.0433	2.5	273.1	±6.7
Or10.8.2	198	72	0.37	6.78	0.00	0.0538	3.2	25.11	2.6	0.0398	2.6	251.8	±6.4
Or10.9.2	573	129	0.23	22.8	0.12	0.05349	1.7	21.6	2.4	0.0462	2.4	291.3	±6.9
Metamorphic zircon domains													
Or10.2.1	240	11	0.05	1.02	2.88	0.0639	9.8	202.4	3.6	0.0048	3.9	30.9	±1.2
Or10.2.3	170	5	0.03	0.736	0.00	0.0471	11	198.2	3.7	0.00505	3.7	32.4	±1.2
Or10.3.1	210	7	0.03	0.979	4.03	0.0929	7.2	183.9	3.5	0.00521	4.3	33.5	±1.4
Or10.4.1	207	13	0.07	0.931	3.12	0.0716	8.3	190.8	3.5	0.00508	4.1	32.6	±1.3
Or10.5.1	326	11	0.03	1.45	1.85	0.0616	6.9	193.3	3.1	0.00508	3.4	32.7	±1.1
Or10.6.1	349	12	0.04	1.57	2.65	0.0592	7.1	191.6	3.2	0.00508	4	32.7	±1.3
Or10.7.1	219	14	0.06	0.95	0.00	0.0429	10	198	3.5	0.00505	3.5	32.5	±1.1
Or10.9.1	665	7	0.01	2.84	1.57	0.0619	4.8	201.2	2.8	0.00489	2.9	31.46	±0.9

Pb_c and Pb^* indicate the common and radiogenic portions, respectively.
Common Pb corrected using measured ^{204}Pb.

Investigated zircons in sample Or10

Figure H.4: *CL-imaging of analysed zircon grains in sample Or10 showing the location of the spot analyses and the calculated age (uncorrected)*

Enclave-rich biotite-orthogneiss (PeGr3)

Sample spot	U (ppm)	Th (ppm)	$^{232}Th/^{238}U$	$^{206}Pb^*$ (ppm)	$\%-^{206}Pb_c$	$^{207}Pb/^{206}Pb$	±%	$^{238}U/^{206}Pb$	±%	$^{206}Pb^*/^{238}U$	±%	Age (Ma) $^{206}Pb/^{238}U$	± error
Magmatic oscillatoric zircon domains													
PeGr3.1.2	372	42	0.12	27.1	0.00	0.0582	2.2	11.8	2.3	0.0848	2.3	525	± 12
PeGr3.1.4	567	86	0.16	40.1	0.59	0.0598	1.9	12.16	1.8	0.0817	1.8	506.5	± 8.8
PeGr3.2.2	436	76	0.18	27.1	0.75	0.067	3.9	13.82	1.8	0.0718	1.9	447.1	± 8.1
PeGr3.3.3	404	60	0.15	28.6	0.00	0.0583	2.2	12.15	1.8	0.0823	1.8	509.9	± 8.9
PeGr3.4.1	687	122	0.18	49.7	0.30	0.05869	1.6	11.88	1.8	0.084	1.8	519.7	± 9
PeGr3.5.1	428	65	0.16	31.2	0.00	0.0574	2	11.8	1.9	0.0847	1.9	524.3	± 9.7
PeGr3.6.2	419	69	0.17	29	0.00	0.0577	1.9	12.42	1.8	0.0805	1.8	499.4	± 8.7
PeGr3.8.2	392	56	0.15	24.9	0.55	0.0623	2.9	13.52	1.9	0.0735	2	457.4	± 8.7
PeGr3.9.2	574	82	0.15	36.4	0.53	0.058	2.5	13.55	1.9	0.0734	1.9	456.7	± 8.3
PeGr3.7.3	409	53	0.13	25.7	0.67	0.0578	2.4	13.71	1.9	0.0724	1.9	450.8	± 8.4
Metamorphic zircon domains													
PeGr3.1.1	918	99	0.11	3.78	2.85	0.0514	5.9	208.8	2.4	0.00466	2.8	29.94	± 0.83
PeGr3.2.1	291	51	0.18	1.21	17.18	0.065	9.6	207.5	2.8	0.00401	9.5	25.8	± 2.4
PeGr3.1.3	342	2	0.01	1.5	4.93	0.0585	9.3	195.5	2.6	0.00487	3.7	31.3	± 1.1
PeGr3.3.1	316	39	0.13	1.39	5.94	0.0579	9.7	195.5	2.5	0.00482	4	31	± 1.2
PeGr3.3.2	355	0	0.00	1.42	6.52	0.0495	11	214.8	2.6	0.00436	5.2	28	± 1.4
PeGr3.4.2	174	29	0.17	0.665	–	0.0465	18	225.3	3.7	0.00492	6.5	31.6	± 2.1
PeGr3.5.2	291	47	0.17	1.17	0.00	0.0512	10	214.7	2.5	0.00466	2.5	29.96	± 0.76
PeGr3.5.3	220	0	0.00	0.994	19.38	0.0577	10	190.4	2.6	0.00426	9.9	27.4	± 2.7
PeGr3.6.1	746	86	0.12	3.07	4.54	0.0478	6.7	208.7	2.1	0.00458	2.9	29.45	± 0.86
PeGr3.7.1	1622	134	0.09	6.54	0.00	0.0512	5	212.9	2	0.004696	2	30.2	± 0.61
PeGr3.7.2	1452	145	0.10	5.94	3.04	0.0503	4.3	209.9	2	0.00462	2.4	29.73	± 0.71
PeGr3.8.1	763	121	0.16	3.16	–	0.0476	6.5	207.7	2.2	0.00494	2.5	31.76	± 0.79
PeGr3.9.1	3956	213	0.06	16.8	1.42	0.0495	4.2	202.9	2	0.00486	2.2	31.26	± 0.68

Pb_c and Pb^* indicate the common and radiogenic portions, respectively.
Common Pb corrected using measured ^{204}Pb.

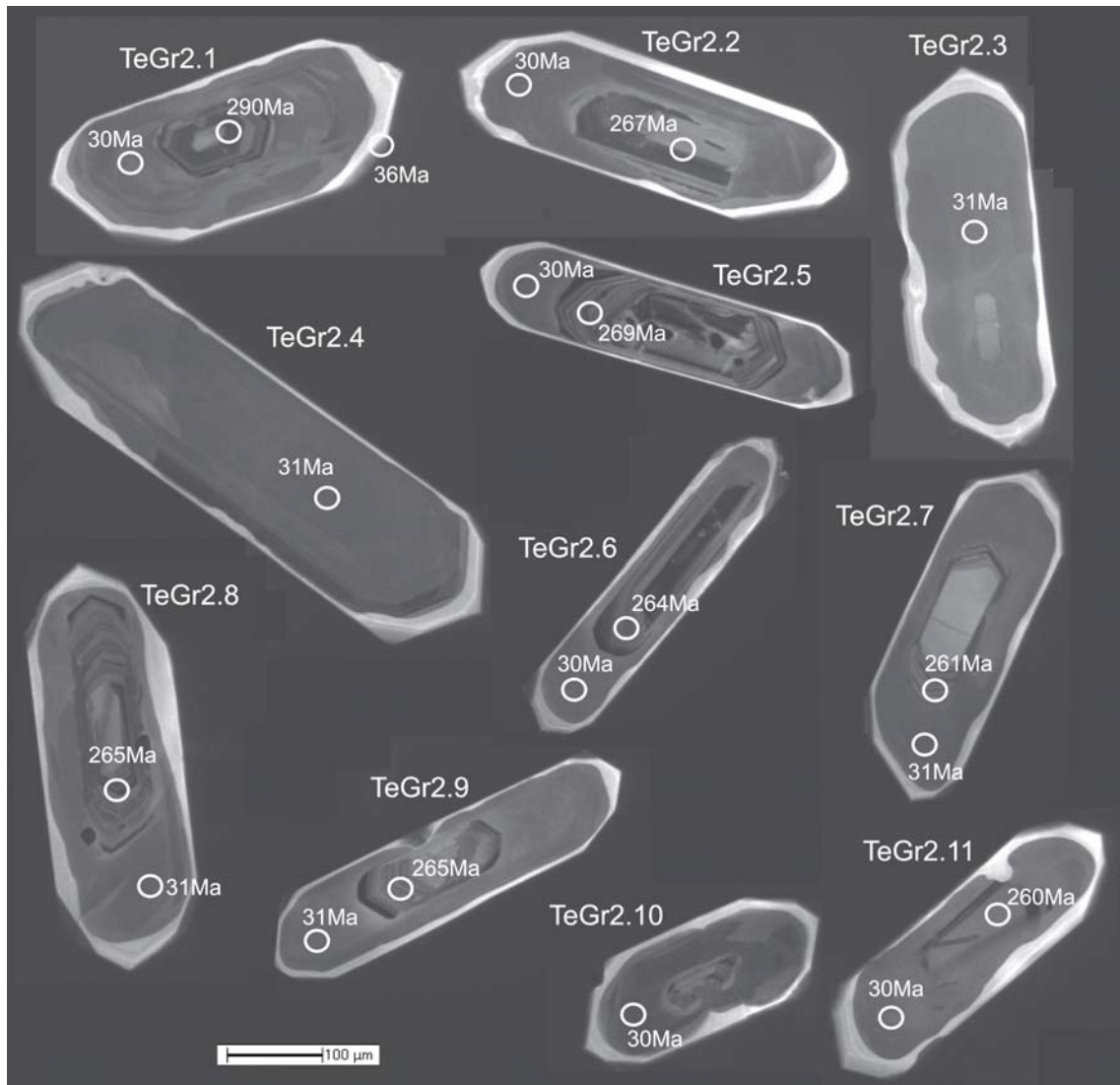**Investigated zircons in sample PeGr3**

Figure H.5: *CL-imaging of analysed zircon grains in sample PeGr3 showing the location of the spot analyses and the calculated age (uncorrected)*

Enclave-rich biotite-orthogneiss (Re4)

Sample spot	U (ppm)	Th (ppm)	^{232}Th/^{238}U	^{206}Pb* (ppm)	‰^{206}Pb$_c$	^{207}Pb/^{206}Pb	±%	^{238}U/^{206}Pb	±%	1 ^{206}Pb*/^{238}U	±%	Age (Ma) ^{206}Pb/^{238}U	± error
Magmatic oscillatoric zircon domains													
Re4.1.1	647	115	0.18	25.9	0.08	0.054	3.2	21.47	2.5	0.0465	2.5	293.3	± 7.1
Re4.2.1	237	110	0.48	9.02	0.25	0.0546	2.7	22.61	2.5	0.0441	2.5	278.3	± 6.9
Re4.3.1	530	403	0.79	21.7	0.13	0.05325	1.8	20.97	2.4	0.0476	2.4	300	± 7.1
Re4.4.1	1260	301	0.25	40.1	0.25	0.05389	1.3	27	2.4	0.03694	2.4	233.8	± 5.6
Re4.5.1	1408	303	0.22	90.6	0.44	0.06071	0.87	13.35	2.4	0.0746	2.4	464	± 11
Re4.7.1	228	50	0.23	15	0.09	0.0589	2.8	13.11	2.5	0.0762	2.5	473	± 12
Re4.8.2	282	130	0.48	8.61	0.50	0.0563	2.9	28.1	6.3	0.0354	6.3	224	± 14
Re4.9.1	128	19	0.15	9.43	0.20	0.0585	2.6	11.64	2.7	0.0857	2.7	530	± 14
Re4.11.2	433	15	0.04	15.3	–	0.0523	7	24.32	2.5	0.0412	2.5	260	± 6.3
Metamorphic zircon domains													
Re4.1.2	732	52	0.07	3.4	1.54	0.0541	4.8	184.8	2.7	0.00533	2.8	34.25	± 0.96
Re4.2.2	861	71	0.08	3.59	0.47	0.0495	4.5	205.7	2.7	0.00484	2.7	31.12	± 0.83
Re4.3.2	514	42	0.09	2.19	1.64	0.0542	5.3	201.1	2.8	0.00489	3	31.45	± 0.93
Re4.4.2	701	62	0.09	3.15	2.16	0.0604	5.5	191.5	2.7	0.00511	2.9	32.85	± 0.96
Re4.5.2	497	98	0.20	2.17	3.14	0.0759	4.8	196.5	2.8	0.00493	3.1	31.67	± 0.99
Re4.6.1	699	55	0.08	3.24	1.34	0.0587	4.5	185.5	2.7	0.00532	2.9	34.19	± 0.98
Re4.7.2	344	38	0.11	1.44	1.09	0.0598	6.2	205	3	0.00482	3.1	31.02	± 0.95
Re4.8.1	607	5	0.01	2.62	2.19	0.0614	4.8	199.4	2.7	0.0049	3	31.54	± 0.95
Re4.8.3	1921	91	0.05	9.14	3.52	0.0749	2.7	180.7	2.5	0.00534	2.7	34.33	± 0.92
Re4.9.2	1606	82	0.05	7.26	0.76	0.0511	5	190.2	2.6	0.00522	2.6	33.55	± 0.88
Re4.10.1	815	76	0.10	3.42	1.98	0.0588	4.3	204.7	2.7	0.00479	2.8	30.8	± 0.86
Re4.11.1	1057	102	0.10	4.35	0.35	0.0514	3.9	208.7	2.6	0.00477	2.6	30.71	± 0.8

Pb$_c$ and Pb* indicate the common and radiogenic portions, respectively.
Common Pb corrected using measured ^{204}Pb.

1
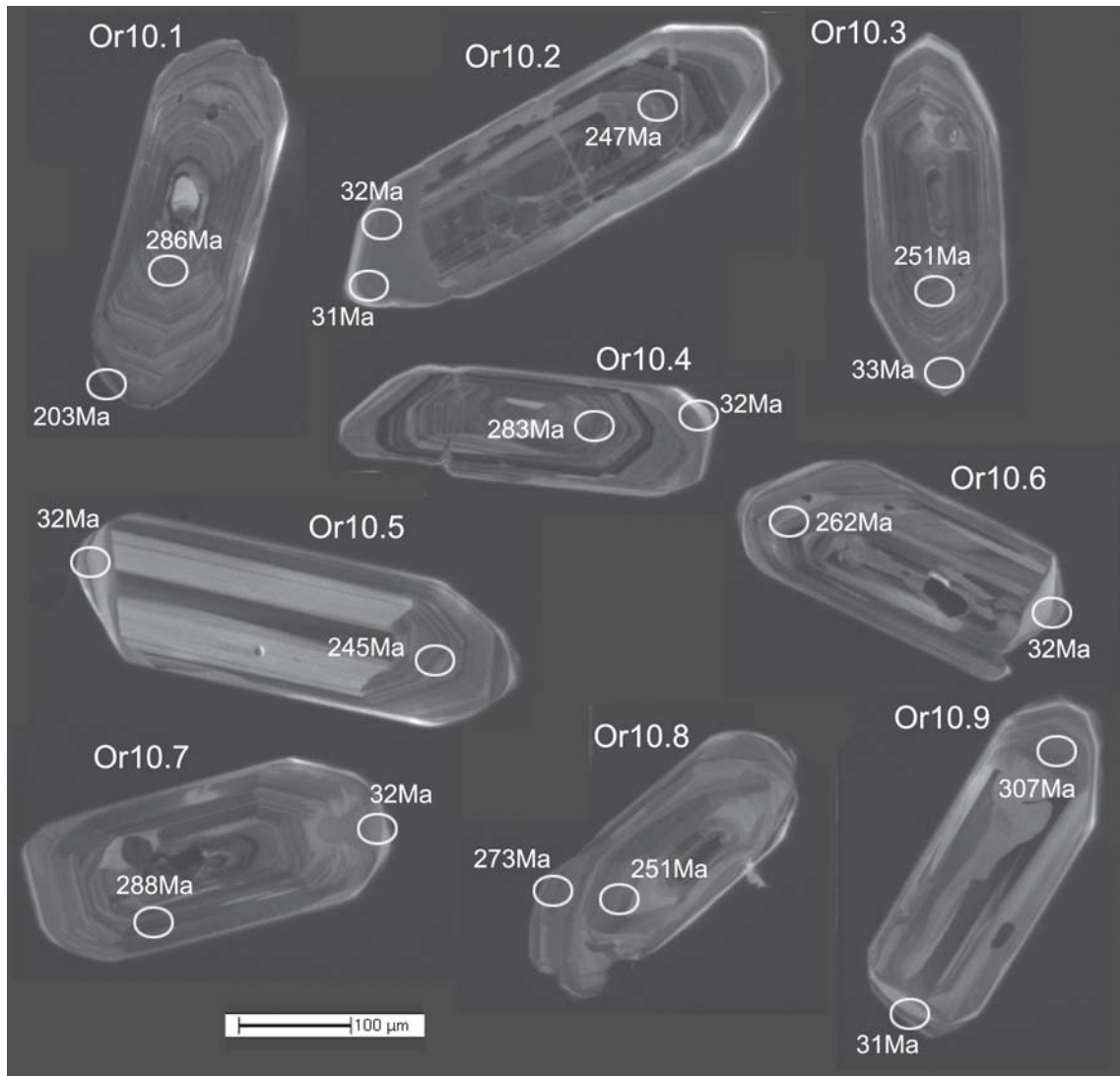
Investigated zircons in sample Re4

Figure H.6: *CL-imaging of analysed zircon grains in sample Re4 showing the location of the spot analyses and the calculated age (uncorrected)*

Charnockite (RoCh1)

Sample spot	U (ppm)	Th (ppm)	$^{232}Th/^{238}U$	$^{206}Pb^*$ (ppm)	$\%-^{206}Pb_c$	$^{207}Pb/^{206}Pb$	±%	$^{238}U/^{206}Pb$	±%	1 $^{206}Pb^*/^{238}U$	±%	Age (Ma) $^{206}Pb/^{238}U$	± error
Magmatic oscillatoric zircon domains													
RoCh1.1.1	372	108	0.30	10.7	0.03	0.0521	4.9	29.9	5.9	0.0334	5.9	212	±12
RoCh1.2.1	619	751	1.25	23.2	0.00	0.0504	3.2	22.89	1	0.04368	1	275.6	±2.8
RoCh1.3.1	842	179	0.22	34.6	0.00	0.0524	2.7	20.89	0.94	0.04788	0.94	301.5	±2.8
RoCh1.4.1	456	360	0.82	16.3	0.00	0.0539	3.3	24.07	1.2	0.04155	1.2	262.4	±3
RoCh1.5.1	2147	1968	0.95	66.1	0.06	0.05189	1.7	27.92	0.72	0.03579	0.73	226.7	±1.6
RoCh1.6.1	269	46	0.18	9.66	0.00	0.0525	4.6	23.9	1.6	0.04184	1.6	264.2	±4
RoCh1.7.1	4142	1246	0.31	146	0.07	0.05116	1.2	24.36	0.55	0.04102	0.55	259.2	±1.4
RoCh1.8.1	2674	390	0.15	77.9	0.10	0.0518	3.6	29.48	0.62	0.03389	0.62	214.8	±1.3
RoCh1.9.1	3197	1065	0.34	102	0.00	0.05127	1.5	26.81	0.66	0.0373	0.66	236.1	±1.5
RoCh1.10.2	1614	1310	0.84	57.8	0.22	0.0547	2	24	0.75	0.04158	0.76	262.6	±1.9
RoCh1.11.1	643	214	0.34	27.2	0.73	0.0525	4.5	20.26	1.2	0.04898	1.3	308.3	±3.9
Metamorphic zircon domains													
RoCh1.1.2	342	113	0.34	1.53	0.00	0.0626	12	191.8	3.1	0.00521	3.1	33.5	±1.1
RoCh1.2.2	478	14	0.03	2.76	1.79	0.0539	8	149	2.8	0.00659	2.9	42.3	±1.2
RoCh1.3.2	171	4	0.02	0.791	0.00	0.082	13	185.6	4.9	0.00539	4.9	34.6	±1.7
RoCh1.4.2	497	94	0.19	2.39	2.13	0.0601	8.2	178.5	2.6	0.00548	2.8	35.3	±1
RoCh1.5.2	203	9	0.05	0.714	6.28	0.088	12	245	5.5	0.00383	6.7	24.6	±1.7
RoCh1.6.2	552	92	0.17	5.96	0.90	0.0528	6.1	79.5	2.1	0.01246	2.1	79.8	±1.7
RoCh1.7.2	454	7	0.02	2.16	2.59	0.0579	9.4	180.5	3.4	0.0054	3.7	34.7	±1.3
RoCh1.8.2	685	11	0.02	3.22	2.02	0.0524	8.4	182.9	2.5	0.00536	2.8	34.44	±0.95
RoCh1.9.2	406	137	0.35	1.92	3.45	0.0684	10	181.3	3.2	0.00533	3.8	34.2	±1.3
RoCh1.10.1	707	15	0.02	3.15	0.00	0.0538	8.6	192.8	2.5	0.00519	2.5	33.35	±0.84

Pb_c and Pb^* indicate the common and radiogenic portions, respectively.
Common Pb corrected using measured ^{204}Pb.

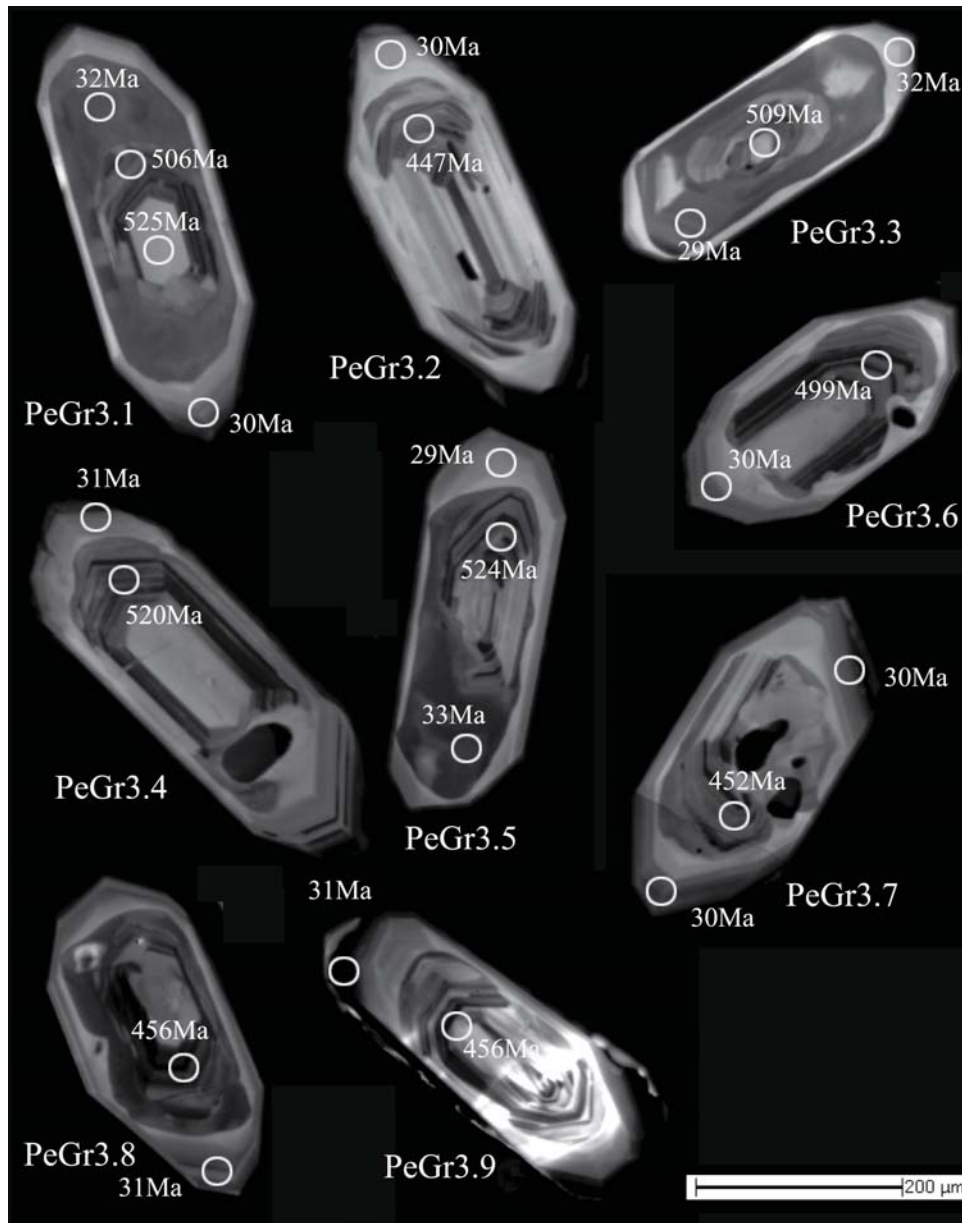**Investigated zircons in sample RoCh1**

Figure H.7: *CL-imaging of analysed zircon grains in sample RoCh1 showing the location of the spot analyses and the calculated age (uncorrected)*

Charnockite (SpCh1)

Sample spot	U (ppm)	Th (ppm)	^{232}Th/^{238}U	^{206}Pb* (ppm)	%^{206}Pb$_c$	^{207}Pb/^{206}Pb	±%	^{238}U/^{206}Pb	±%	^{1} ^{206}Pb*/^{238}U	±%	Age (Ma) ^{206}Pb/^{238}U	± error
Magmatic oscillatoric zircon domains													
SpCh1.1.1	1220	355	0.30	32.2	0.62	0.0526	2.9	32.55	0.95	0.03053	1	193.9	±1.9
SpCh1.1.2	977	741	0.78	37.7	0.55	0.0557	2.7	22.27	0.98	0.04465	1	281.6	±2.8
SpCh1.2.1	1265	692	0.57	35.4	–	0.053	3.2	30.67	1.1	0.03264	1.1	207.1	±2.2
SpCh1.3.1	351	180	0.53	13.5	1.11	0.0572	4.2	22.42	1.7	0.0441	1.8	278.2	±4.9
SpCh1.4.2	411	250	0.63	16.4	0.10	0.0521	4	21.62	1.4	0.04621	1.4	291.2	±4
SpCh1.5.2	1197	181	0.16	44.3	0.00	0.0521	4.5	23.23	1	0.04306	1	271.8	±2.7
SpCh1.6.2	294	137	0.48	11.2	0.61	0.0566	4	22.47	1.4	0.04423	1.5	279	±4
SpCh1.7.1	787	85	0.11	34.1	0.81	0.0609	2.2	19.82	10	0.05004	1.1	314.7	±3.3
SpCh1.8.2	1146	220	0.20	43.7	–	0.0517	2.4	22.55	0.88	0.04444	0.89	280.3	±2.4
SpCh1.9.2	299	137	0.47	8.41	1.34	0.0549	6	30.58	1.6	0.03226	2	204.7	±3.9
Metamorphic zircon domains													
SpCh1.1.3	643	9	0.01	2.96	3.69	0.0837	9.3	186.5	3.3	0.00516	4	33.2	±1.3
SpCh1.3.2	680	32	0.05	3.1	4.80	0.0843	7.6	188.4	2.7	0.00505	4	32.5	±1.3
SpCh1.2.2	2025	8	0.00	8.27	1.19	0.0529	5.6	210.3	1.6	0.004699	1.8	30.22	±0.54
SpCh1.4.1	932	8	0.01	3.91	0.00	0.0545	7.7	204.8	2.3	0.00488	2.3	31.4	±0.71
SpCh1.5.1	304	9	0.03	1.27	0.00	0.0761	12	205.6	4.8	0.00486	4.8	31.3	±1.5
SpCh1.6.1	661	16	0.03	3.1	10.03	0.125	6.9	183.2	2.9	0.00491	5.8	31.6	±1.8
SpCh1.7.2	1573	23	0.02	6.13	1.18	0.048	6.1	220.4	1.6	0.004484	1.9	28.84	±0.56
SpCh1.8.1	708	23	0.03	4.93	4.25	0.136	9.4	123.3	3.7	0.00776	4.7	49.8	±2.3
SpCh1.9.1	311	8	0.03	2.92	0.00	0.058	8.4	91.7	2.9	0.0109	2.9	69.9	±2

Pb$_c$ and Pb* indicate the common and radiogenic portions, respectively.
Common Pb corrected using measured ^{204}Pb.
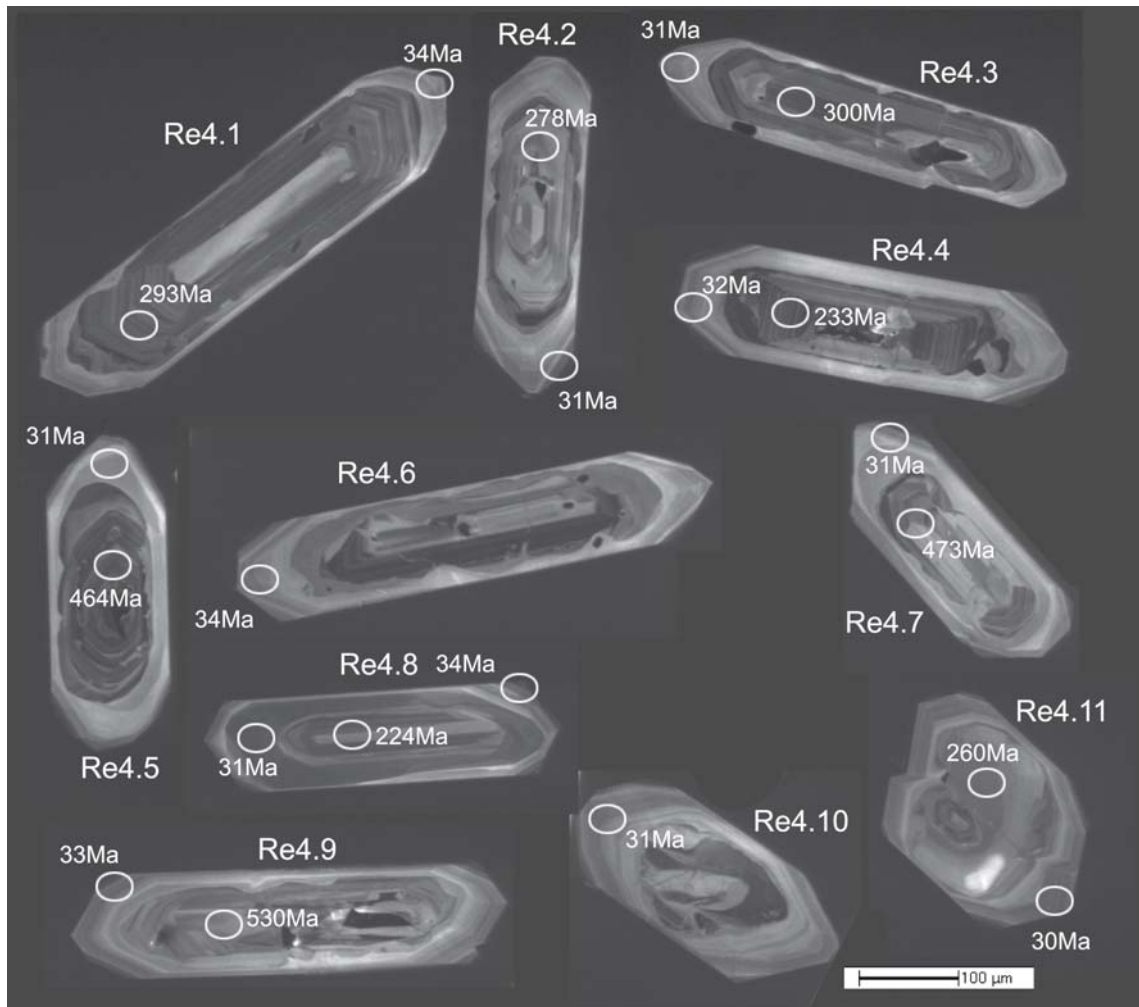
Investigated zircons in sample SpCh1

Figure H.8: *CL-imaging of analysed zircon grains in sample SpCh1 showing the location of the spot analyses and the calculated age (uncorrected)*

Charnockite (PeCh13)

Sample spot	U (ppm)	Th (ppm)	^{232}Th/^{238}U	^{206}Pb* (ppm)	%-^{206}Pb$_c$	^{207}Pb/^{206}Pb	± %	^{238}U/^{206}Pb	± %	1 ^{206}Pb*/^{238}U	± %	Age (Ma) ^{206}Pb/^{238}U	± error
Inherited cores													
PeCh13.3.2	975	338	0.36	62.0	0.00	0.0556	1.6	13.50	0.4	0.0741	0.4	461	2
PeCh13.5.2	247	230	0.96	70.5	0.06	0.1204	0.9	3.01	0.7	0.3315	0.7	1845	11
Magmatic oscillatoric zircon domains													
PeCh13.1.2	1105	729	0.68	41.0	0.14	0.0523	1.9	23.17	0.5	0.0431	0.5	272	1
PeCh13.2.2	749	523	0.72	28.9	0.35	0.0532	2.6	22.26	0.5	0.0448	0.6	282	2
PeCh13.3.3	969	154	0.16	37.3	0.17	0.0531	1.9	22.32	1.1	0.0447	1.1	282	3
PeCh13.4.2	545	92	0.17	20.5	0.22	0.0538	2.8	22.83	0.8	0.0437	0.8	276	2
PeCh13.5.3	1018	140	0.14	34.7	0.00	0.0514	1.8	25.22	0.5	0.0397	0.5	251	1
PeCh13.6.2	361	107	0.31	15.1	0.00	0.0525	2.9	20.62	0.8	0.0485	0.8	305	2
PeCh13.7.2	230	69	0.31	9.4	0.89	0.0597	3.7	21.08	1.1	0.0470	1.3	296	4
PeCh13.8.1	479	175	0.38	16.8	0.55	0.0564	2.8	24.56	0.9	0.0405	0.9	256	2
PeCh13.9.1	4965	918	0.19	129.8	0.11	0.0506	1.1	32.85	0.3	0.0304	0.3	193	1
PeCh13.11.1	717	277	0.40	27.7	-0.08	0.0501	2.2	22.21	0.6	0.0451	0.6	284	2
PeCh13.12.1	1019	649	0.66	34.1	0.20	0.0533	1.9	25.68	0.6	0.0389	0.6	246	1
Metamorphic zircon domains													
PeCh13.1.1	1789	20	0.01	7.1	0.00	0.0470	4.8	216.78	1.6	0.0046	1.6	30	0.5
PeCh13.2.1	2538	20	0.01	9.7	0.00	0.0461	4.1	225.12	0.9	0.0044	0.9	29	0.3
PeCh13.3.1	1489	31	0.02	5.8	0.00	0.0455	5.5	221.27	1.0	0.0045	1.0	29	0.3
PeCh13.4.1	1558	39	0.03	6.2	0.71	0.0526	5.2	216.10	1.0	0.0046	1.1	30	0.3
PeCh13.5.1	1099	46	0.04	4.4	1.92	0.0634	4.9	215.43	1.4	0.0046	2.0	29	0.6
PeCh13.6.1	1309	12	0.01	5.1	0.00	0.0508	5.0	219.42	1.1	0.0046	1.1	29	0.3
PeCh13.7.1	1533	31	0.02	6.0	0.00	0.0471	4.9	219.45	1.1	0.0046	1.1	29	0.3
PeCh13.10.1	4231	1866	0.46	75.5	0.23	0.0512	1.3	48.11	0.4	0.0207	0.4	132	1

Pb$_c$ and Pb* indicate the common and radiogenic portions, respectively.
Common Pb corrected using measured ^{204}Pb.

Investigated zircons in sample PeCh13

Figure H.9: *CL-imaging of analysed zircon grains in sample PeCh13 showing the location of the spot analyses and the calculated age (uncorrected)*

Charnockite (ScCh3)

Sample spot	U (ppm)	Th (ppm)	$^{232}Th/^{238}U$	$^{206}Pb^*$ (ppm)	$\%-^{206}Pb_c$	$^{207}Pb/^{206}Pb$	±%	$^{238}U/^{206}Pb$	±%	$1\ ^{206}Pb^*/^{238}U$	±%	Age (Ma) $^{206}Pb/^{238}U$	± error
Inherited cores													
ScCh3.2.2	387	49	0.13	23.5	0.31	0.0580	2.4	14.13	0.7	0.0705	0.8	439	3
ScCh53.8.2	2759	134	0.05	154.7	0.00	0.0553	0.9	15.33	0.3	0.0653	0.3	407	1
ScCh3.8.3	225	34	0.15	12.4	0.61	0.0584	3.3	15.55	1.0	0.0639	1.1	399	4
ScCh3.10.2	331	210	0.66	22.0	0.58	0.0592	2.4	12.91	0.7	0.0770	0.8	478	3
Magmatic oscillatoric zircon domains													
ScCh3.1.2	144	57	0.41	5.0	0.97	0.0586	4.9	24.55	1.3	0.0403	1.4	255	4
ScCh3.1.3	403	214	0.55	14.0	0.00	0.0517	3.2	24.64	0.9	0.0406	0.9	256	2
ScCh3.2.1	944	84	0.09	35.3	0.14	0.0534	2.0	22.95	0.6	0.0435	0.6	275	2
ScCh3.3.2	471	258	0.57	16.8	0.00	0.0544	3.8	24.02	0.8	0.0416	0.8	263	2
ScCh3.5.2	289	95	0.34	11.2	0.43	0.0564	3.5	22.18	1.0	0.0449	1.0	283	3
ScCh3.6.2	389	169	0.45	13.0	0.51	0.0554	3.2	25.68	0.8	0.0387	0.8	245	2
ScCh3.9.2	189	49	0.27	7.7	0.69	0.0578	4.2	20.96	1.2	0.0474	1.3	298	4
Metamorphic zircon domains													
ScCh3.1.1	36	1	0.03	0.2	0.00	0.1600	16.3	136.48	5.9	0.0073	5.9	47	3
ScCh3.3.1	114	3	0.03	0.6	0.00	0.1472	10.9	174.23	3.4	0.0057	3.4	37	1
ScCh3.4.1	28	8	0.31	0.1	0.00	0.1793	19.6	172.87	6.8	0.0058	6.8	37	3
ScCh3.5.1	62	21	0.35	0.3	0.00	0.1413	14.3	185.44	4.7	0.0054	4.7	35	2
ScCh3.6.1	67	5	0.08	0.7	21.90	0.4197	8.6	85.97	4.3	0.0091	17.6	58	10
ScCh3.7.1	97	42	0.44	0.4	0.00	0.1444	13.6	190.68	3.9	0.0052	3.9	34	1
ScCh3.7.2	441	195	0.46	4.0	3.30	0.0501	5.9	94.29	1.4	0.0103	2.4	66	2
ScCh3.8.1	397	13	0.04	1.7	3.31	0.0607	8.6	205.34	1.9	0.0047	2.7	30	1
ScCh3.9.1	133	7	0.06	0.8	0.00	0.1038	15.3	151.68	4.1	0.0066	4.1	42	2
ScCh3.10.1	51	1	0.02	0.3	0.00	0.2782	11.8	172.71	4.9	0.0058	4.9	37	2

Pb_c and Pb^* indicate the common and radiogenic portions, respectively.
Common Pb corrected using measured ^{204}Pb.
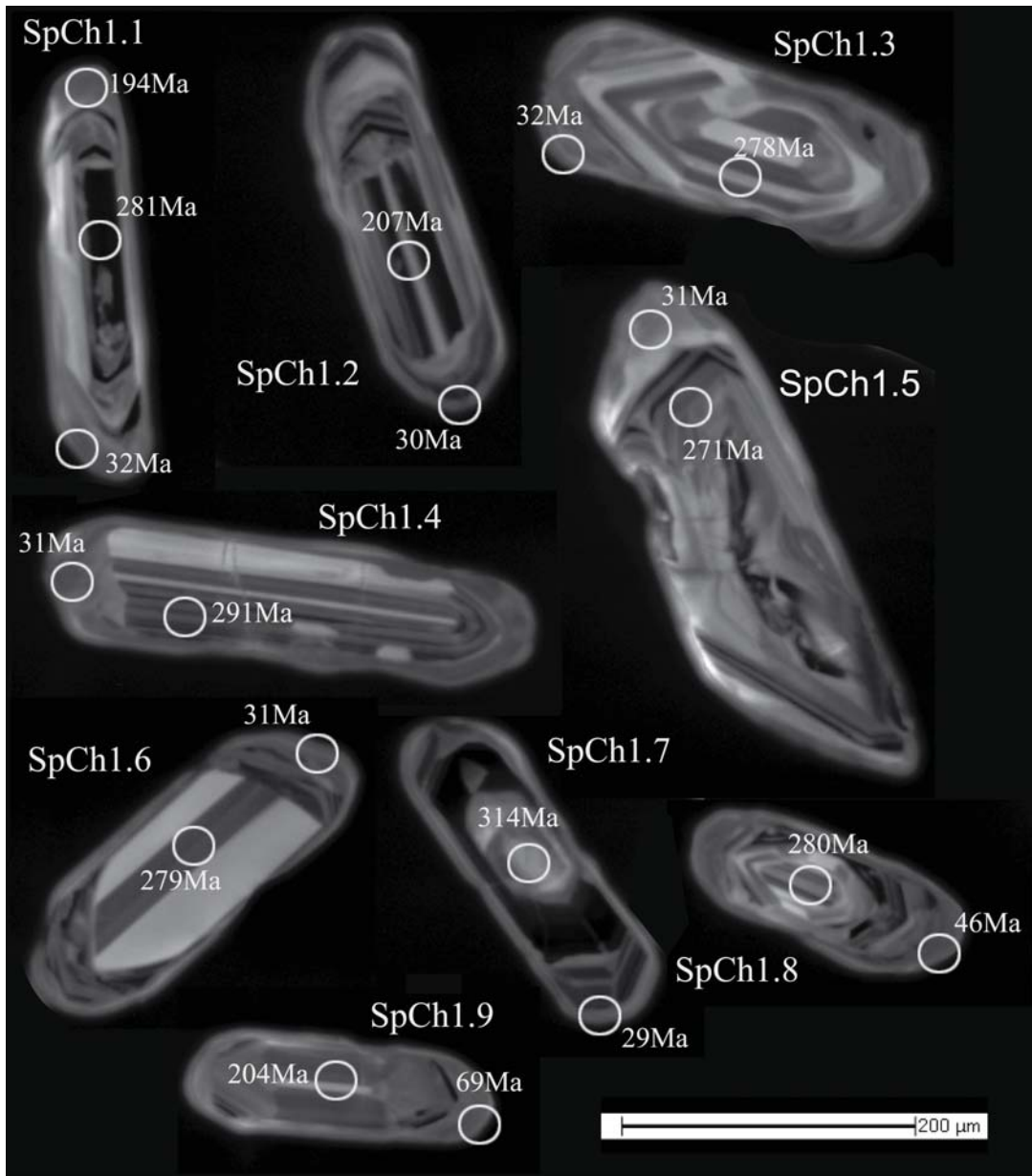
Investigated zircons in sample ScCh3
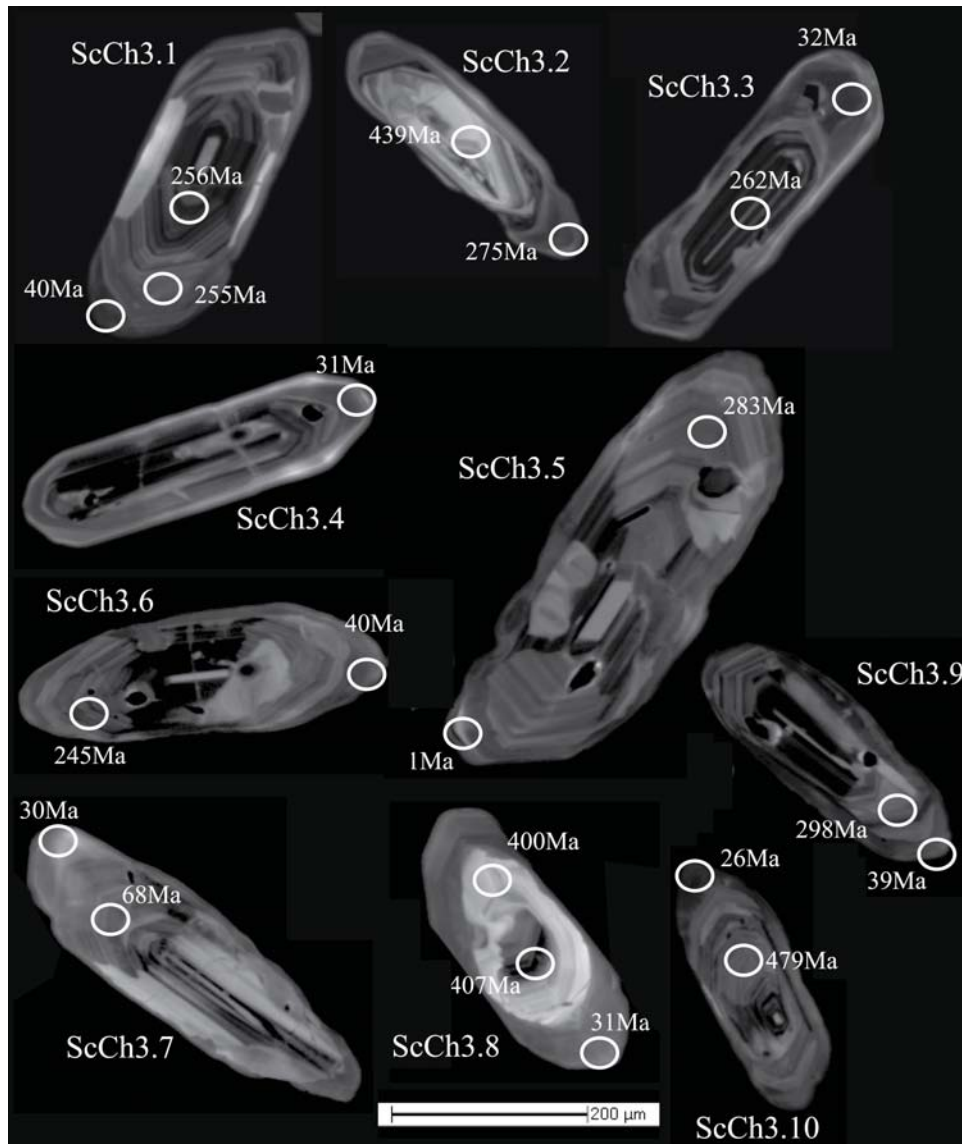
Figure H.10: *CL-imaging of analysed zircon grains in sample ScCh3 showing the location of the spot analyses and the calculated age (uncorrected)*

Leucogranite (BiGr1)

Sample spot	U (ppm)	Th (ppm)	^{232}Th/^{238}U	^{206}Pb* (ppm)	‰-^{206}Pb$_c$	^{207}Pb/^{206}Pb	± %	^{238}U/^{206}Pb	± %	^{1} ^{206}Pb*/^{238}U	± %	Age (Ma) ^{206}Pb/^{238}U	± error
Magmatic oscillatoric zircon domains													
BiGr1.1.1	1595	15	0.01	31.5	0.26	0.0489	2.9	43.56	1.7	0.02296	1.7	146.3	±2.5
BiGr1.1.2	90	39	0.45	3.51	–	0.0556	7	21.99	1.4	0.04548	1.4	286.7	±4
BiGr1.2.1	1606	7	0.00	54.2	–	0.0522	2	25.4	0.82	0.03937	0.82	249	±2
BiGr1.3.1	557	109	0.20	21.4	0.19	0.0527	2.6	22.43	0.79	0.04458	0.79	281.2	±2.2
BiGr1.3.2	738	340	0.48	24.9	0.02	0.05187	1.7	25.46	0.86	0.03928	0.86	248.4	±2.1
BiGr1.4.1	349	39	0.11	13.5	–	0.0538	3.6	22.16	0.97	0.04513	0.97	284.6	±2.7
BiGr1.5.1	897	208	0.24	33.5	–	0.05209	1.5	22.99	0.81	0.0435	0.81	274.5	±2.2
BiGr1.6.1	1246	39	0.03	43.8	0.08	0.05223	1.6	24.47	0.79	0.04086	0.79	258.2	±2
BiGr1.7.1	383	13	0.04	11	1.12	0.0556	11	30.18	1.7	0.03312	1.7	210	±3.6
BiGr1.7.2	211	78	0.38	8.27	0.28	0.054	3.9	21.94	1	0.04558	1	287.3	±2.8
BiGr1.8.1	1208	10	0.01	40.4	0.14	0.05179	1.8	25.76	0.7	0.03882	0.7	245.5	±1.7
BiGr1.8.2	258	156	0.63	10.2	–	0.0526	5	21.68	0.96	0.04613	0.96	290.7	±2.7
BiGr1.9.1	329	12	0.04	9.01	0.67	0.0513	8.1	31.57	1.2	0.03167	1.2	201	±2.3
BiGr1.10.1	178	110	0.64	6.46	0.76	0.05	7.2	23.88	1.1	0.04187	1.1	264.4	±2.9
BiGr1.11.1	948	39	0.04	34.5	0.07	0.05208	1.6	23.63	0.82	0.04232	0.82	267.2	±2.1
BiGr1.12.1	232	150	0.67	9.3	–	0.0527	3.2	21.42	0.99	0.04669	0.99	294.1	±2.8
BiGr1.13.1	207	104	0.52	8.51	0.35	0.0519	5.3	20.96	1.2	0.0477	1.2	300.4	±3.5
BiGr1.14.1	224	103	0.48	8.83	0.68	0.0498	7	21.92	1.1	0.04562	1.1	287.6	±3
BiGr1.15.1	311	186	0.62	11.6	0.39	0.0486	3.6	23.02	0.9	0.04344	0.9	274.1	±2.4
BiGr1.15.2	141	53	0.39	4.33	1.44	0.0492	19	28.3	4.4	0.0354	4.4	224	±9.6

Pb$_c$ and Pb* indicate the common and radiogenic portions, respectively.
Common Pb corrected using measured ^{204}Pb.

Investigated zircons in sample BiGr1

Figure H.11: *CL-imaging of analysed zircon grains in sample BiGr1 showing the location of the spot analyses and the calculated age (uncorrected)*

Leucogranite (Pia2)

Sample spot	U (ppm)	Th (ppm)	^{232}Th/^{238}U	^{206}Pb* (ppm)	%-^{206}Pb$_c$	^{207}Pb/^{206}Pb	± %	^{238}U/^{206}Pb	± %	1 ^{206}Pb*/^{238}U	± %	Age (Ma) ^{206}Pb/^{238}U	± error
Magmatic oscillatoric zircon domains													
Pia2.1.2	283	99	0.36	10.4	0.55	0.0508	6.8	23.41	1.1	0.04271	1.1	269.6	±2.8
Pia2.2.2	504	23	0.05	13.6	0.24	0.0502	4.5	31.85	1	0.03139	1	199.3	±2
Pia2.3.1	2168	88	0.04	78.4	0.02	0.05074	1.1	23.75	0.7	0.04211	0.7	265.9	±1.8
Pia2.4.2	164	66	0.42	3.41	0.42	0.0514	12	41.4	3.3	0.02415	3.3	153.8	±5
Pia2.5.2	384	162	0.44	15.6	0.04	0.0513	2.2	21.11	1	0.04738	1	298.4	±2.9
Pia2.6.2	797	39	0.05	21.4	0.19	0.052	3.7	32.11	0.94	0.03114	0.94	197.7	±1.8
Pia2.7.1	659	25	0.04	22.7	0.18	0.0522	3.2	25.06	0.95	0.03991	0.95	252.3	±2.3
Pia2.8.1	170	59	0.36	6.72	0.37	0.0528	4.8	21.83	1.1	0.04581	1.1	288.8	±3.2
Pia2.9.2	266	98	0.38	10.7	0.00	0.0529	2.9	21.47	1.4	0.04657	1.4	293.4	±3.9
Pia2.9.3	2715	31	0.01	96.6	0.02	0.05121	0.89	24.14	0.65	0.04143	0.65	261.7	±1.7
Metamorphic zircon domains													
Pia2.1.1	1129	7	0.01	4.7	–	0.0473	4.2	206.4	1.3	0.004845	1.3	31.16	±0.4
Pia2.1.3	1084	6	0.01	4.55	1.68	0.0461	14	208	1.4	0.004808	1.4	30.92	±0.44
Pia2.2.1	1301	8	0.01	5.83	–	0.0513	4.3	191.7	1.2	0.005216	1.2	33.54	±0.39
Pia2.4.1	1541	19	0.01	7.38	5.91	0.052	35	190.6	2.7	0.00524	2.7	33.69	±0.91
Pia2.5.1	602	2	0.00	2.48	–	0.0485	9.7	206.4	1.5	0.004846	1.5	31.17	±0.47
Pia2.6.1	1914	8	0.00	7.86	0.21	0.0482	4.7	209.7	0.98	0.004768	0.98	30.66	±0.3
Pia2.6.3	1319	8	0.01	5.49	0.66	0.0486	7.4	207.9	1.4	0.004809	1.4	30.92	±0.43
Pia2.9.1	2108	6	0.00	8.67	0.42	0.0457	6.8	209.8	1.1	0.004766	1.1	30.65	±0.33

Pb$_c$ and Pb* indicate the common and radiogenic portions, respectively.
Common Pb corrected using measured ^{204}Pb.

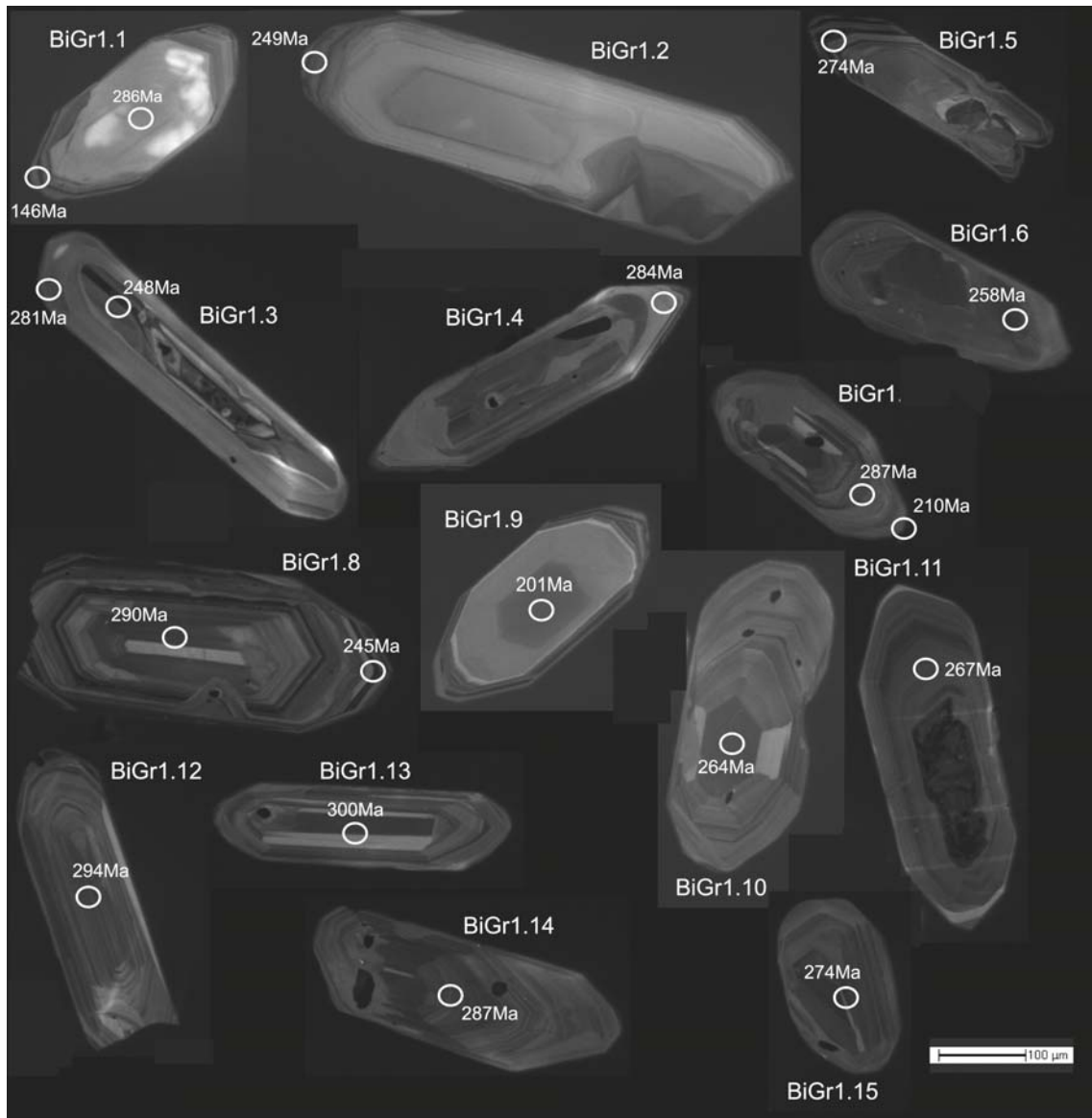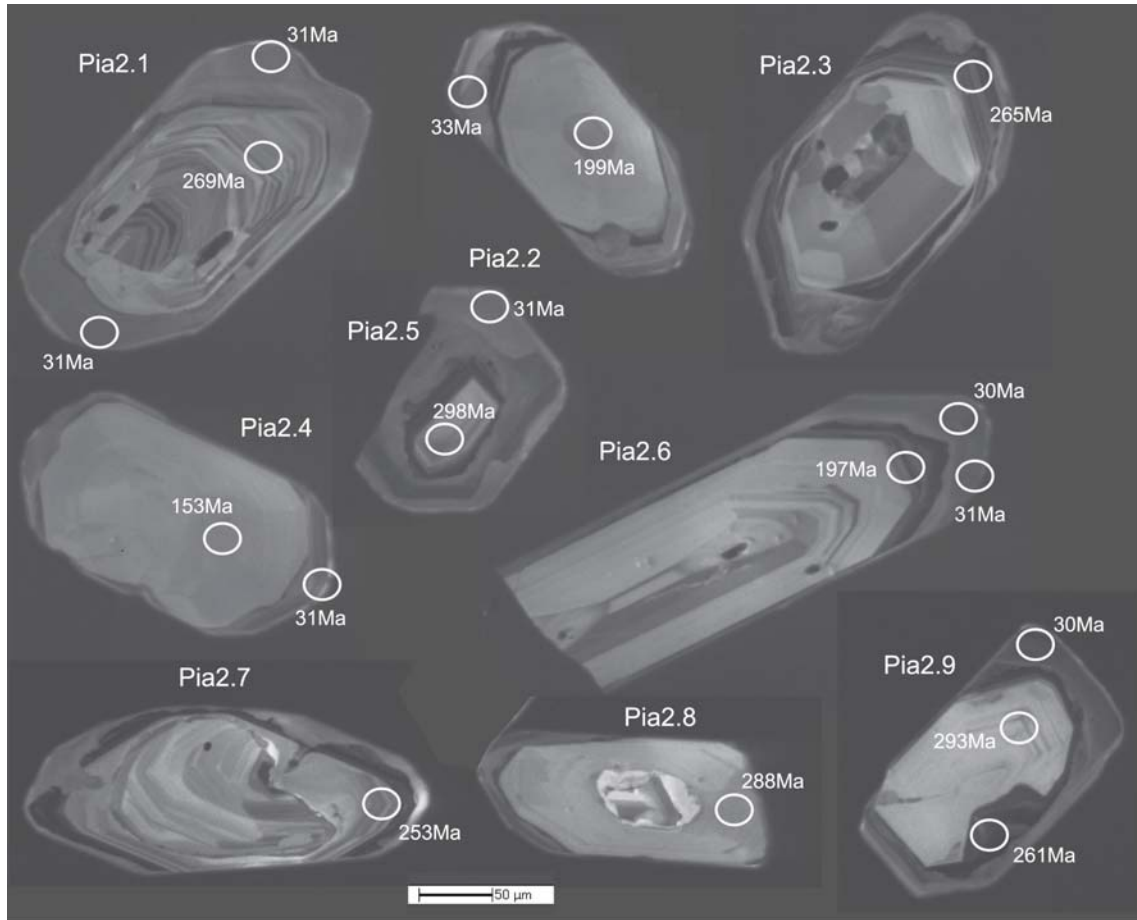**Investigated zircons in sample Pia2**

Figure H.12: *CL-imaging of analysed zircon grains in sample Pia2 showing the location of the spot analyses and the calculated age (uncorrected)*

Leucosome from migmatitic metapelites (PeLs1)

Sample spot	U (ppm)	Th (ppm)	^{232}Th/^{238}U	^{206}Pb* (ppm)	%-^{206}Pb$_c$	^{207}Pb/^{206}Pb	±%	^{238}U/^{206}Pb	±%	1 ^{206}Pb*/^{238}U	±%	Age (Ma) ^{206}Pb/^{238}U	± error
Magmatic oscillatoric zircon domains													
PeLs1.1.1	1189	28	0.02	39.4	0.00	0.0593	2	25.93	2.1	0.03857	2.1	243.9	± 5.1
PeLs1.2.1	644	134	0.21	48.2	0.21	0.0584	2.2	11.46	2.1	0.0871	2.1	538	±11
PeLs1.2.2	739	24	0.03	24.5	0.00	0.0514	3	25.9	2.1	0.03861	2.1	244.2	± 5.1
PeLs1.3.1	916	193	0.22	43.1	0.00	0.0584	3	18.25	2.1	0.0548	2.1	343.8	± 7
PeLs1.5.1	2021	118	0.06	122	–	0.05624	1.2	14.2	2.1	0.0705	2.1	439	± 9
PeLs1.6.1	151	121	0.83	6.11	0.00	0.0587	4.2	21.28	2.6	0.047	2.6	296.1	± 7.4
PeLs1.7.2	1371	199	0.15	31.9	0.20	0.0537	3.8	36.9	2.9	0.02704	2.9	172	± 4.9
PeLs1.9.2	2620	397	0.16	99.2	0.00	0.05589	1.3	22.69	2.1	0.04408	2.1	278.1	± 5.6
PeLs1.10.2	1085	783	0.75	42.2	0.27	0.0531	2.1	22.1	2.1	0.04513	2.1	284.5	± 6
PeLs1.11.1	468	5	0.01	7.61	3.33	0.0794	5.8	52.9	2.4	0.0183	2.9	116.9	± 3.4
PeLs1.12.1	1064	17	0.02	15.8	1.05	0.0551	3.4	58	2.2	0.01705	2.3	109	± 2.5
PeLs1.13.1	612	4	0.01	6.7	5.97	0.0604	5.2	78.5	3.2	0.012	4.2	76.9	± 3.2
PeLs1.14.1	1234	9	0.01	29	0.00	0.0612	3.7	36.57	2.4	0.02734	2.4	173.9	± 4.1
PeLs1.17.3	2160	116	0.06	119	–	0.05599	1.4	15.62	2.1	0.0641	2.1	400.8	± 8.1
PeLs1.5.3	3931	96	0.03	111	0.25	0.0516	1.9	30.41	2.1	0.0328	2.1	208	± 4.3
Metamorphic zircon domains													
PeLs1.1.2	567	50	0.09	2.42	8.65	0.0571	9.9	200.9	2.8	0.00456	7.2	29.3	± 2.1
PeLs1.3.2	1766	57	0.03	8.91	0.88	0.0497	4.9	170.3	2.3	0.00582	2.3	37.42	± 0.87
PeLs1.4.1	6454	47	0.01	53.6	0.40	0.0492	3.3	103.5	2.3	0.00963	2.3	61.8	± 1.4
PeLs1.5.2	5628	40	0.01	21.9	0.61	0.0491	3.6	221.1	2.2	0.0045	2.3	28.91	± 0.65
PeLs1.7.1	10222	11	0.00	41.5	0.13	0.0453	2.5	211.5	2.1	0.00472	2.1	30.37	± 0.64
PeLs1.8.1	1202	171	0.15	4.8	0.00	0.0494	5.6	215.3	2.4	0.00464	2.4	29.87	± 0.72
PeLs1.9.1	624	29	0.05	2.85	17.51	0.055	11	188.2	3.4	0.0044	12	28.3	± 3.5
PeLs1.10.1	954	20	0.02	4.02	4.73	0.0595	6.9	203.6	3.1	0.00468	4.2	30.1	± 1.3
PeLs1.15.1	1029	190	0.19	4.28	0.00	0.0505	7.7	206.4	2.7	0.00484	2.7	31.16	± 0.83
PeLs1.15.2	660	116	0.18	2.75	0.00	0.0632	8.9	205.7	2.8	0.00486	2.8	31.26	± 0.86
PeLs1.15.3	1255	194	0.16	4.84	0.00	0.0504	5.9	222.9	2.3	0.00449	2.3	28.85	± 0.67
PeLs1.8.2	954	137	0.15	3.95	0.00	0.0653	7	207.4	2.5	0.00482	2.5	31.01	± 0.79
PeLs1.16.1	5850	9	0.00	21.9	0.75	0.0545	5.2	229.6	2.5	0.00432	2.5	27.81	± 0.7
PeLs1.17.1	564	170	0.31	27.9	–	0.0514	4.5	17.39	4.8	0.0577	4.8	362	±17
PeLs1.17.2	4982	183	0.04	18.8	0.95	0.0473	4.1	227.1	3.7	0.00436	3.7	28.1	± 1

Pb$_c$ and Pb* indicate the common and radiogenic portions, respectively.
Common Pb corrected using measured ^{204}Pb.

Investigated zircons in sample PeLs1

Figure H.13: *CL-imaging of analysed zircon grains in sample PeLs1 showing the location of the spot analyses and the calculated age (uncorrected)*

Matrix of magmatic breccia (Sil)

Sample spot	U (ppm)	Th (ppm)	^{232}Th/^{238}U	^{206}Pb* (ppm)	%-^{206}Pb$_c$	^{207}Pb/^{206}Pb	±%	^{238}U/^{206}Pb	±%	1 ^{206}Pb*/^{238}U	±%	^{206}Pb*/^{238}U	±%	Age (Ma) ^{206}Pb/^{238}U	± error
Magmatic oscillatoric zircon domains															
Sil.1.2	1884	375	0.21	63.4	–	0.05164	1.2	25.51	0.82	0.03919	0.82	0.03919	0.82	247.8	±2
Sil.2.2	955	200	0.22	35	0.04	0.05201	1.6	23.44	0.86	0.04266	0.86	0.04266	0.86	269.3	±2.3
Sil.3.1	1995	200	0.10	34.1	0.14	0.0488	2.9	50.31	0.91	0.01987	0.91	0.01987	0.91	126.9	±1.1
Sil.5.2	521	130	0.26	20.4	0.19	0.0508	2.3	22.03	0.94	0.0454	0.94	0.0454	0.94	286.2	±2.6
Sil.6.2	231	124	0.55	7.01	0.08	0.0518	3.2	28.31	1.2	0.03532	1.2	0.03532	1.2	223.8	±2.6
Sil.7.2	653	182	0.29	25.4	0.05	0.0522	3.1	22.1	0.77	0.04525	0.77	0.04525	0.77	285.3	±2.1
Sil.8.2	678	246	0.38	22.7	0.20	0.0521	2.3	25.73	0.79	0.03886	0.79	0.03886	0.79	245.8	±1.9
Sil.9.2	1408	303	0.22	24.1	0.14	0.0499	2.1	50.28	0.77	0.01989	0.77	0.01989	0.77	126.94	±0.96
Sil.10.1	1550	110	0.07	26.2	0.79	0.0499	6.1	51.17	0.85	0.01954	0.85	0.01954	0.85	124.7	±1.1
Sil.12.1	988	46	0.05	16.3	0.17	0.0491	3.1	52.33	0.84	0.01911	0.84	0.01911	0.84	122	±1
Metamorphic zircon domains															
Sil.1.1	1058	6	0.01	4.24	–	0.0494	6	213.5	1.3	0.004684	1.3	0.004684	1.3	30.13	±0.38
Sil.2.1	294	14	0.05	1.33	4.86	0.075	26	199.4	3.1	0.00499	3.1	0.00499	3.1	32.08	±10
Sil.4.1	1071	22	0.02	4.46	1.95	0.035	20	210.2	1.4	0.004758	1.4	0.004758	1.4	30.6	±0.42
Sil.5.1	483	5	0.01	2.11	2.56	0.0397	23	201.7	1.9	0.004957	1.9	0.004957	1.9	31.87	±0.61
Sil.6.1	101	24	0.25	0.503	9.67	0.141	40	191	9.1	0.00508	9.1	0.00508	9.1	32.7	±3
Sil.6.3	526	28	0.05	2.1	–	0.075	28	206.8	3.3	0.00486	3.3	0.00486	3.3	31.2	±1
Sil.7.1	354	175	0.51	1.5	4.24	0.046	39	211.3	2.8	0.00473	2.8	0.00473	2.8	30.44	±0.86
Sil.8.1	2225	54	0.02	9	0.29	0.0485	5.6	213	0.96	0.004695	0.96	0.004695	0.96	30.19	±0.29
Sil.9.1	854	15	0.02	3.53	0.93	0.0449	13	209.8	1.4	0.004766	1.4	0.004766	1.4	30.65	±0.43
Sil.11.1	289	19	0.07	1.28	3.65	0.032	86	201.3	4	0.00497	4	0.00497	4	32	±1.3

Pb$_c$ and Pb* indicate the common and radiogenic portions, respectively.
Common Pb corrected using measured ^{204}Pb.

Investigated zircons in sample Si1

Figure H.14: *CL-imaging of analysed zircon grains in sample Si1 showing the location of the spot analyses and the calculated age (uncorrected)*

Augengneiss (HvOG1)

Sample spot	U (ppm)	Th (ppm)	^{232}Th/^{238}U	^{206}Pb* (ppm)	‰-^{206}Pb$_c$	^{207}Pb/^{206}Pb	±%	^{238}U/^{206}Pb	±%	1 ^{206}Pb*/^{238}U	±%	Age (Ma) ^{206}Pb/^{238}U	± error
Magmatic oscillatoric zircon domains													
HvOg1.1.1	389	56	0.15	4.18	52.46	0.491	3	79.9	2.7	0.0061	19	39.1	±7.5
HvOg1.1.2	495	132	0.28	16.9	0.00	0.0511	3.2	25.18	2.2	0.03972	2.2	251.1	±5.3
HvOg1.2.1	1229	83	0.07	43.3	0.00	0.05023	2	24.41	2.1	0.04096	2.1	258.8	±5.3
HvOg1.3.1	843	110	0.13	29.7	–	0.0503	2.5	24.38	2.1	0.04115	2.1	259.9	±5.5
HvOg1.4.1	1185	209	0.18	45	0.57	0.0531	2	22.61	2.1	0.04397	2.1	277.4	±5.7
HvOg1.5.1	1303	284	0.23	45.4	–	0.05224	1.9	24.63	2.1	0.04067	2.1	257	±5.3
HvOg1.6.1	1876	150	0.08	66.8	0.00	0.04971	1.6	24.11	2.1	0.04148	2.1	262	±5.3
HvOg1.7.1	1641	120	0.08	60.5	–	0.05094	1.8	23.3	2.1	0.04299	2.1	271.3	±5.5
HvOg1.8.1	2058	119	0.06	74.5	0.12	0.05075	1.5	23.74	2.1	0.04208	2.1	265.7	±5.4
HvOg1.9.1	1894	84	0.05	72	–	0.05069	1.6	22.6	2.1	0.0443	2.1	279.4	±5.7
HvOg1.10.1	2033	185	0.09	82.8	0.00	0.05169	1.5	21.09	2.1	0.04742	2.1	298.7	±6

Pb$_c$ and Pb* indicate the common and radiogenic portions, respectively.
Common Pb corrected using measured ^{204}Pb.
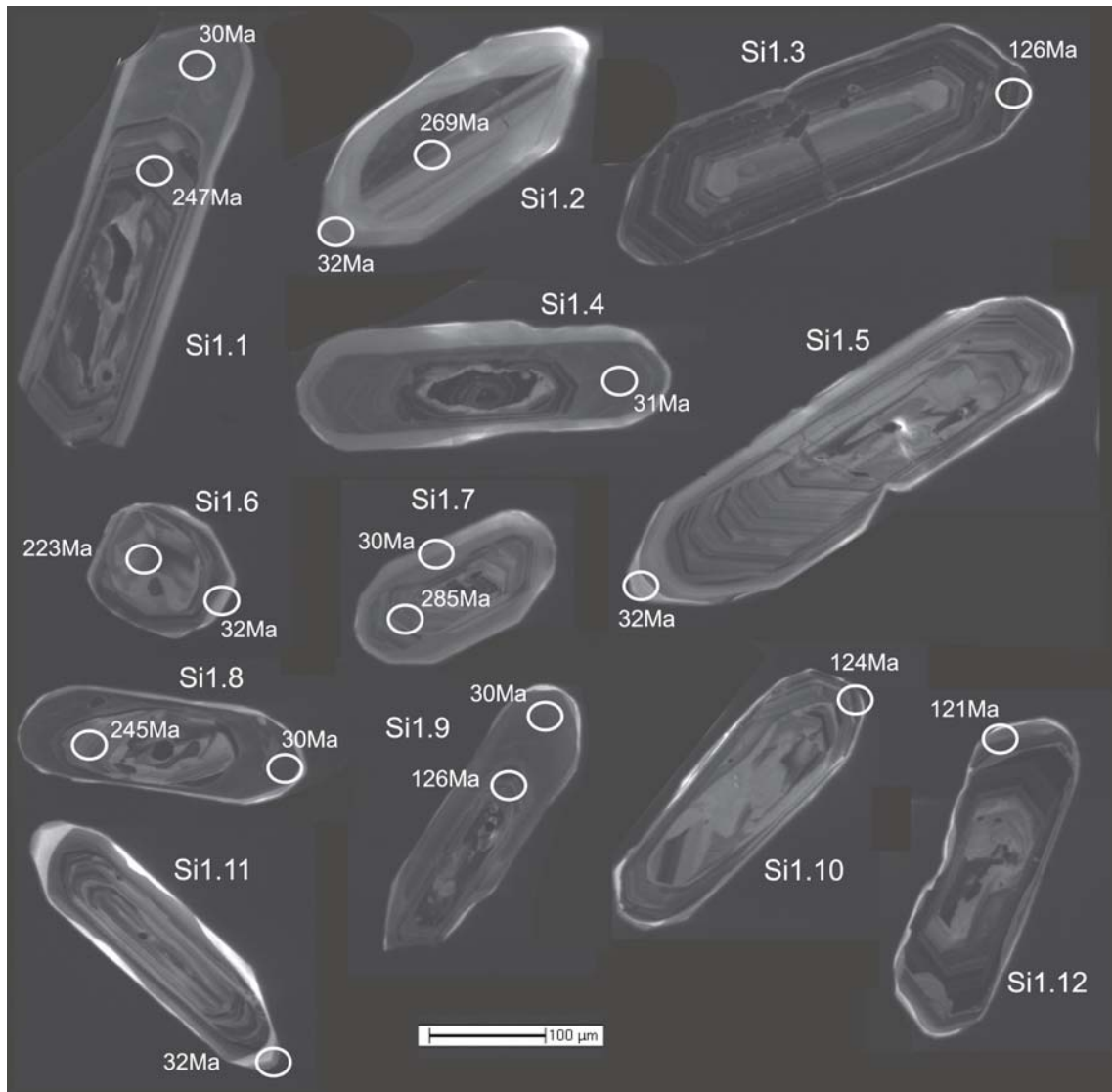
Investigated zircons in sample HvOG1
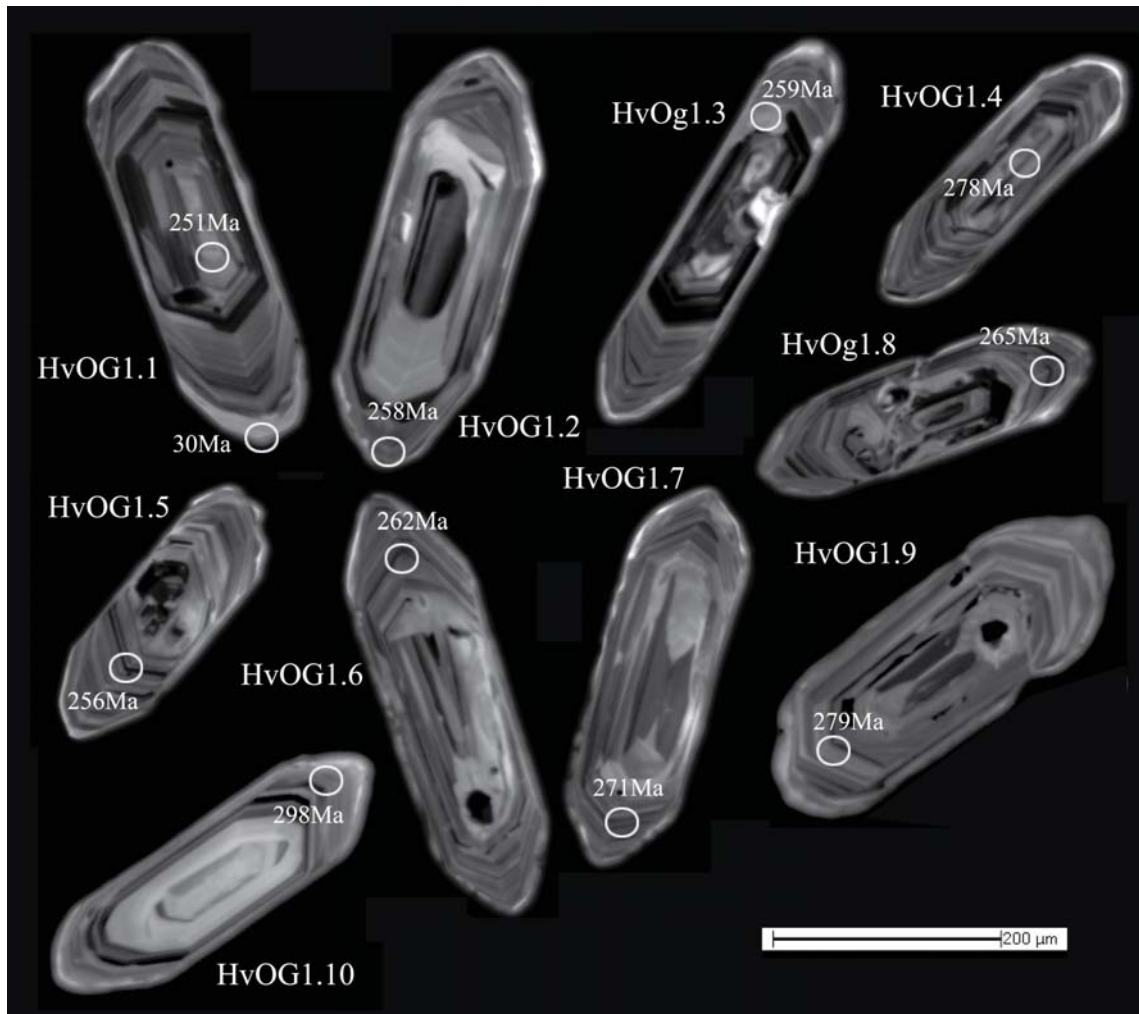
Figure H.15: *CL-imaging of analysed zircon grains in sample HvOG1 showing the location of the spot analyses and the calculated age (uncorrected)*

Appendix I

Geological map of the Gruf Complex

Chiavenna Unit

Metacarbonate

Amphibolite

Metaultramafite

Gruf Complex

Migmatic biotite-orthogneiss

Enclaves-rich biotite-orthogneiss

Charnockite

Leucogranite

Migmatitic paragneiss and micaschist

Amphibolite

Websterite to gabbronorite

Chlorite-spinel-enstatite-olivine fels

Calcsilicate

Aplite and pegmatite dykes

Bergell Intrusion

Bergell undifferentiated

Quaternary

Granulite (in-situ)

Granulite (not in-situ)

A-A' Profile location

Tambo Nappe

Micaschist

2 km

N

Appendix J

Detailed geological map around Bivacco Vaninetti

Geological map of the northern part of Val Codera

Gruf Complex

- Migmatitic biotite-orthogneiss
- Charnockite
- Leucogranite
- Migmatitic paragneiss and micaschist
- Amphibolite
- Websterite to gabbronorite
- Augengneiss
- Chl-spl-opx-ol fels

Bergell Intrusion

- Bergell undifferentiated
- Aplitic and pegmatitic dykes
- ★ Sapphirine-bearing granulite
- ★ Corundum-bearing micaschist

N

200 m

Biv. Vaninetti

la Tr...

Va d...

Piz d...

Pizzo Trubinasca

2998

2918

2701

2400

2214

a Tegiola

Siogia

Pizza...

763

764
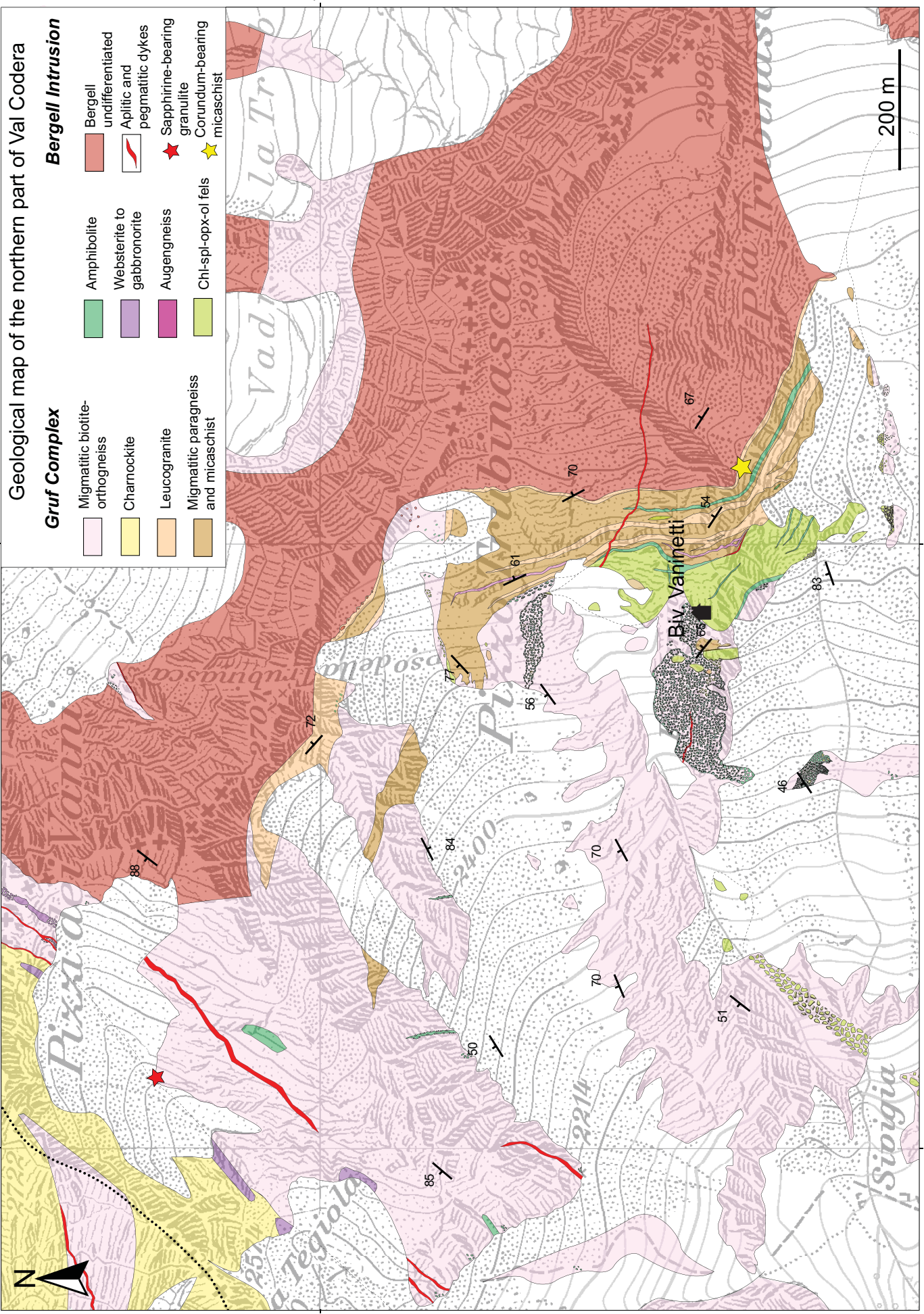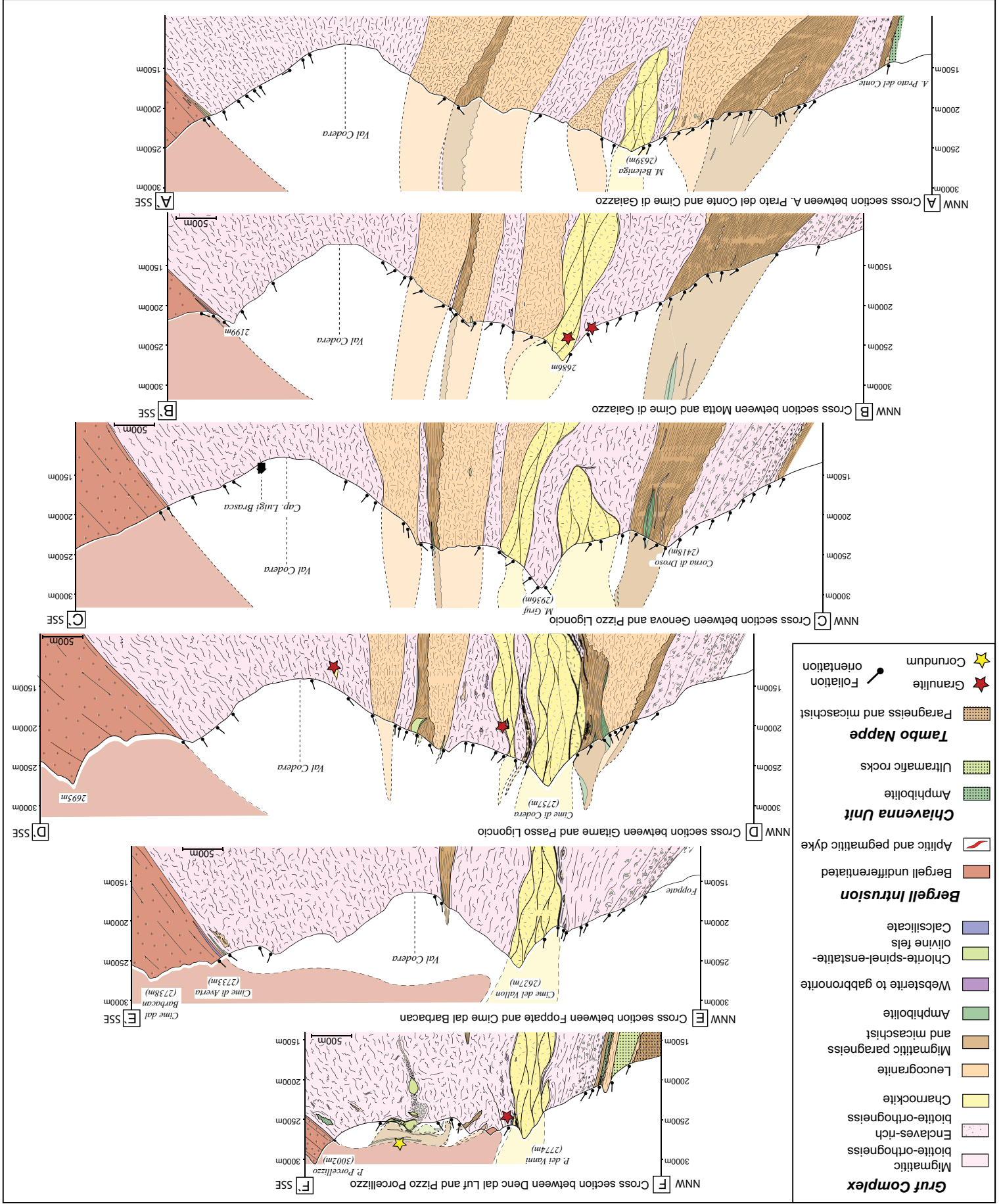
130

88 72 67 70 54 61 77 56 84 70 70 51 83 46 50 85 65

Appendix K

Cross sections

Cross section between A. Prato del Conte and Cime di Galazzo — **A** NNW / **A'** SSE

Cross section between Motta and Cime di Galazzo — **B** NNW / **B'** SSE

Cross section between Genova and Pizzo Ligoncio — **C** NNW / **C'** SSE

Cross section between Gitame and Passo Ligoncio — **D** NNW / **D'** SSE

Cross section between Foppate and Cime dal Barbacan — **E** NNW / **E'** SSE

Cross section between Denc dal Luf and Pizzo Porcellizzo — **F** NNW / **F'** SSE

Gruf Complex

- Migmatitic biotite-orthogneiss
- Enclaves-rich biotite-orthogneiss
- Charnockite
- Leucogranite
- Migmatitic paragneiss and micaschist
- Amphibolite
- Websterite to gabbronorite
- Chlorite-spinel-enstatite-olivine fels
- Calcsilicate

Bergell Intrusion

- Bergell undifferentiated
- Aplitic and pegmatitic dyke

Chiavenna Unit

- Amphibolite

Tambo Nappe

- Ultramafic rocks
- Paragneiss and micaschist

- Granulite — Corundum
- Foliation orientation

Curriculum Vitae

Personal Data

Name:	Andrea Galli
Date of Birth:	March 26, 1980
Place of Birth:	Bellinzona, Switzerland
Citizenship:	Swiss
Place of origin:	Mosogno, Switzerland
Current Address:	Via Serta 20, 6934 Bioggio, Switzerland

Education

09/1986 - 06/1991	Primary school in Bioggio (TI, Switzerland)
09/1991 - 06/1995	Secondary school in Agno (TI, Switzerland)
09/1995 - 07/1999	Grammar School in Lugano (TI, Switzerland)
10/1999 - 03/2005	ETH-Zürich: Dipl. Scienc. Nat. (Erdwissenschaften); Diploma Thesis "Strukturgeologie und Petrographie des Naret-Gebietes (Valle Maggia, Ticino)". Supervised by Prof. Neil Mancktelow and Dr. Eric Reusser
4/2006 - present	Ph.D. student, ETH-Zürich, Switzerland; supervised by Prof. Max W. Schmidt. Thesis: "Tectono-metamorphic evolution of the Gruf Complex (Swiss and Italian Central Alps)

Professional Experience

10/2003 - 03/2005	Student Assistant (Hilfsassistent); Institute for Mineralogy and Petrology, ETH-Zürich, Switzerland
12/2006 - 04/2007	Peregrine Metals Ltd. Mining exploration, San Juan, Argentina.

Zürich, October 2010   Andrea Galli